UNIVERSITÀ DEGLI STUDI FIRENZE

UNIVERSITÀ DI PISA

TECHNISCHE UNIVERSITÄT WIEN

DOTTORATO DI RICERCA IN

International Doctorate in Civil and Environmental Engineering

CICLO XXX

COORDINATORE Prof. Fabio Castelli

EVALUATION OF SATELLITE RAINFALL ESTIMATES FOR HYDROLOGIC AND GEO-HYDROLOGIC HAZARDS PREDICTION

Settore Scientifico Disciplinare: ICAR/07

Dottorando

Luca Ciabatta

Promotors: Prof. Dr. Claudio Tamagnini

Prof. Dr. Wolfgang Wagner

Dr. Luca Brocca

Judging Commission: Dr. Luca Brocca

Prof. Dr. Marco Borga

Prof. Dr. Renato Morbidelli

Prof. Dr. Wolfgang Wagner

Prof. Dr. Wouter Arnoud Dorigo

Prof. Dr. Robert Weber

Abstract

Satellite rainfall data are becoming available at high temporal and spatial resolution. The use of such data in ad-hoc developed modelling can extend hydrological applications to poorly instrumented areas. The use of remotely sensed information can provide also valuable insights about rainfall spatial variability, improving ground rainfall estimation. Despite the great availability of data, their use in hydrological practice is still very rare, with just few studies that have used such data for landslide hazard risk mitigation. In order to test the feasibility of using this kind of data for landslide prediction, a coupled hydrological-slope stability model has been developed and forced with remotely sensed information. Before that, several satellite rainfall products have been assessed through direct comparison with modelled and ground – based benchmarks and through hydrological validations, in order to highlight advantages and drawbacks of this source of information. Preliminary results showed that satellite rainfall data can be used with benefit in natural hazards mitigation, although the inherent errors related to the indirect nature of measurement have to be deeply assessed and corrected.

Abstrakt

Satellitenniederschlagdaten werden mit hoher zeitlicher und räumlicher Auflösung verfügbar. Die Verwendung solcher Daten in einer ad-hoc entwickelten Modellierung kann hydrologische Anwendungen auf schlecht instrumentierte Bereiche erweitern. Die Verwendung von Fernerkundungsinformationen kann auch wertvolle Einblicke in die räumliche Variabilität des Niederschlags liefern und die Niederschlagsschätzung verbessern. Trotz der großen Verfügbarkeit von Daten ist ihr Einsatz in der hydrologischen Praxis noch sehr selten, und nur wenige Studien haben solche Daten zur Risikominderung von Erdrutschen verwendet. Um die Machbarkeit der Verwendung dieser Art von Daten für die Erdrutschvorhersage zu testen, wurde ein gekoppeltes Hydrologie-Hang-Stabilitätsmodell entwickelt und mit Fernerkundungsinformation erzwungen. Zuvor wurden mehrere Satellitenregenprodukte durch direkten Vergleich mit modellierten und bodengestützten Benchmarks und hydrologischen Validierungen bewertet, um die Vor- und Nachteile dieser Informationsquelle aufzuzeigen. Vorläufige Ergebnisse zeigten, dass die Niederschlagsdaten aus dem Satelliten mit einem Nutzen bei der Minderung der Naturgefahren genutzt werden können, obwohl die inhärenten Fehler in Bezug auf die indirekte Natur der Messung tief eingeschätzt und korrigiert werden müssen.

To my family,

To Laura,

To my mentors,

To me

ACKNOWLEDGEMENTS

First of all, I wish to thank my supervisor, Prof. Claudio Tamagnini, for giving me this great opportunity. I wish to thank Prof. Wolfgang Wagner for hosting me at Vienna University of Technology and for teaching me to look at things from a different point of view. I wish to thank Luca for guiding me through this important phase and for his patience. Without the help of my mentors, this work would not have been possible. I'm really grateful to work with them.

I wish also to thank Sebastian, Christoph, Alexander, Christoph, Bernhard, Wouter, Livia, Alexandra, Daniel, Stefano, Angelika, Romina, Elsa, Felix and all the people of the Department of Geodesy and Geoinformation of TUWIEN for the help and support gave to me during my stay in Vienna.

I wish to thank my colleagues of Perugia for their help, their mathematical support and their understanding during these years.

I thank my friends, for being there when I am in need.

I thank my family, for being always ready to help me and calm me.

I thank my grandmother, for looking after me from above.

My last acknowledgement goes to Laura, for everything she did in the last years; for being my compass, my centre, for loving me, for bearing me, for standing by me.

TABLE OF CONTENTS

Table of contents 1
List of Figures 5
List of Tables 11
1. Introduction 14
1.1 Satellite rainfall estimation 15
1.2 Precipitation retrievals 24
VIS/IR methods 24
Passive microwave methods 24
Active microwave methods 25
Multi-sensor techniques 25
1.3 New bottom-up approach 33
1.4 Use of satellite rainfall data for landslide risk assessment and hydrological application 34
1.5 Purposes of the thesis 37
2. Assessment and validation of satellite rainfall products 39
2.1 Methodology development and testing over Italy 40
Study area 41
Datasets 43
Assessment strategy 48
Results 49
2.2 Validation on a global scale 67
Dataset 68
ESA CCI SM data preprocessing 69

SM2RAIN-CCI rainfall product generation 70

Results 72

3. Hydrological validation 80

3.1 Rainfall-runoff modelling over Italy 81

Study areas 82

Rainfall products 83

Bias correction 84

Mean areal rainfall 84

Integration scheme 84

MISDc rainfall-runoff model 85

Performance metrics 86

Results and discussions 87

4. Application of satellite rainfall data for landslides prediction 97

4.1 The coupled hydrological-stability distributed model for landslide risk assessment 98

Model description 99

Input data reading, pre-processing and memory allocation 100

The hydrological module 101

The stability module 105

4.2 Application of satellite-based rainfall data for slope analysis in Umbria region 107

Results of the application of the coupled hydrological-stability model 108

5. Conclusions 121

5.1 Satellite rainfall data validation and integration 122

5.2 Use of satellite rainfall data for flood estimation 122

5.3 Use of satellite rainfall data for landslide risk assessment 123

5.4 Final remarks 123

5.5 Next steps 123

6. Appendix 124

6.1 Validation over Australia 125

Study area 125

Rainfall datasets 129

Parameter values of rainfall estimation algorithms 131

Results 132

6.2 Validation over India 139

Study area 139

Satellite soil moisture and rainfall products 139

SM2RAIN algorithm 141

Merging procedure 141

Performance indices 141

Performance assessment 141

Categorical scores assessment 143

6.3 Rainfall-runoff modelling over the Mediterranean area 144

Datasets 146

Ground 146

Workflow 148

Results 150

6.4 Use of satellite rainfall data with empirical rainfall thresholds 158

Study area 158

Landslide and rainfall data 159

Algorithm for rainfall event reconstruction 160

Method for calculation and selection of ED rainfall thresholds 161

Results 162

7. References 168

8. Publications 185

LIST OF FIGURES

Figure 1.1 – Spatial distribution of monthly in-situ stations used for the creation of the Global Precipitation Climatology Centre (GPCC) in 2015. Modified by Schneider et al., (2017). ..15

Figure 1.2 – Schematic representation of Low Erath Orbit (LEO) and Geostationary (GEO) satellite orbit geometry. ..18

Figure 1.3 – Artistic view of the Meteosat Second Generation (MSG) 4 satellite orbiting in geostationary orbit. ..21

Figure 1.4 - Difference between conical (up) and cross-track (bottom) scanning technology (courtesy of National Center of Atmospheric Research http://www2.ucar.edu/). ..22

Figure 1.5 – Global Precipitation Measurement (GPM) Mission constellation satellites ..23

Figure 1.6 – Experimental early warning system for rainfall-induced landslides set up in Indonesia (Courtesy of Liao et al., 2010). ..35

Figure 1.7 – Global Landslide Hazard Assessment for Situational Awareness (LHASA) model framework. ..36

Figure 2.1 – Morphology of the study area. The letters indicate the boxes (highlighted in black) where the analysis of 5-day accumulated rainfall timeseries is carried out (Ciabatta et al., 2017)..41

Figure 2.2 – Cumulated observed rainfall for the period 2010-2013 over Italy. The data are obtained through the high quality ground network of the Italian Civil Protection Department (Modified from Ciabatta et al., 2015). ..42

Figure 2.3 – Noise map over Italy obtained through the ASCAT SM product (http://rs.geo.tuwien.ac.at/dv/ascat/). ..42

Figure 2.4 – Spatial distribution of the rain gauges used for obtaining the ground-based benchmark ..43

Figure 2.5 – Spatial distribution of SM2RAIN parameters (left) Z*, (middle) a, and (right) b, obtained in Ciabatta et al. (2015). ..46

Figure 2.6 - Spatial (a) and temporal (b) variability of the integration weights between CDRD-PNPR and SM2RASC during the 1st January–31st December 2011 period obtained in Ciabatta et al. (2017). ..47

Figure 2.7 - Boxplots of the correlation coefficient (R) between CDRD, PNPR and CDRD-PNPR and the observed rainfall dataset as a function of the number of 3-hour intervals with at least one satellite overpass during the validation period (2012-2014). Specifically, the black dots indicate the median values, the boxes the 25th and 75th 1008 percentiles while the whiskers the minimum and maximum values. ..50

Figure 2.8 - Boxplot reporting the performance scores [(left) R and (right) RMSE] obtained during the calibration period for (top) 1 day and (bottom) 5 days of accumulated rainfall. The box lines represent the 25th, 50th, and 75th percentiles, while the whiskers represent the max and min values. ..51

Figure 2.9 - Maps of R for 5 days of accumulated rainfall for (a) $SM2R_{ASC}$ (median R 5 0.62), (b) 3B42-RT (median R 5 0.6), (c) H05 (median R 5 0.53), (d) $SM2R_{ASC}$ +H05 (median R 5 0.68), and (e) $SM2R_{ASC}$ +3B42-RT (median R 5 0.71) during the validation period (2012–13) (Modified from Ciabatta et al., 2015). 53

Figure 2.10 - Maps of RMSE for 5 days of accumulated rainfall for (a) $SM2R_{ASC}$ (median RMSE 5 19.94 mm), (b) 3B42-RT (median RMSE 5 21.87 mm), (c) H05 (median RMSE 5 22.32 mm), (d) $SM2R_{ASC}$+H05 (median RMSE 5 18.32 mm), and (e) $SM2R_{ASC}$+3B42- RT (median RMSE 5 18.13 mm) during the validation period (2012–13). 54

Figure 2.11 - Pearson correlation coefficient (R [–], upper panel) and Root Mean Square Error (RMSE [mm], lower panel) maps for CDRD-PNPR (first column), $SM2R_{ASC}$ (second column) and CDRD-PNPR + $SM2R_{ASC}$ (third column) during the validation period (2012–2014) for 1 day of accumulated rainfall. 55

Figure 2.12 - Timeseries of 5-day cumulated rainfall for all analysed products for the four analysis boxes A, B, C and D shown in Figure 1.2 (from top to bottom). The text annotation indicates the Pearson correlation coefficient, R and Root Mean Square Error, RMSE (mm), values with respect to the observed rainfall. 56

Figure 2.13 - Spatial averages of categorical metrics, computed for 5 days of accumulated rainfall, for the analyzed rainfall products (SM2RASC, 3B42-RT, H05, SM2RASC+H05, and SM2RASC+3B42-RT) in the validation period (2012–13): (left) FAR, (middle) POD, and (right) TS for a 5-day rainfall accumulation threshold. An event is defined as a 5-day rainfall accumulation that exceeds a given percentile threshold of all 5-day accumulations observed for a given pixel over the analyzed period. 58

Figure 2.14 - Spatial average of False Alarm Ratio (FAR, left), Probability Of Detection (POD, middle) and Threat Score (TS, right) for the five analyzed products during the validation period (2012-2014) for different rainfall thresholds (1, 2, 4, 8, 16 and 32 mm/day). 58

Figure 2.15 - Monthly (top) correlation coefficient (R) and (bottom) Root Mean Square Error (RMSE) values for 5 days of accumulated rainfall for each analyzed product. 60

Figure 2.16 – POD vs FAR plot for each seasonal period considering 5 days of accumulated rainfall. The gray lines indicate TS values, the horizontal bars represent the standard deviation of POD, and the vertical bars represent the standard deviation of FAR for each analyzed percentile. 61

Figure 2.17 - Pearson correlation coefficient (R [–], upper panel), Root Mean Square Error (RMSE (mm), middle panel) and percentage BIAS (lower panel) for the five analyzed products on a seasonal scale during the whole validation period (2012–2014). 62

Figure 2.18 - Time series for the two selected pixels throughout the study area, showing (a), (b) bad integration results and (c), (d) good results in terms of the variation in RMSE after the integration. (a) Results for H05 and SM2RASC1H05 (RMSE values of 37.43 and 34.93 mm, respectively) and (b) results for 3B42-RT and SM2RASC13B42-RT (RMSE values of 26.08 and 25.59 mm, respectively) for 5 days of accumulated rainfall. (c) Results for H05 and SM2RASC+H05 (RMSE values of 46.91 and 21.30 mm, respectively) and (d) results for

3B42-RT and SM2RASC+3B42-RT (RMSE values of 41.24 and 21.26 mm, respectively). 63

Figure 2.19 - Cumulated rainfall maps for some important rainfall events in the study period listed in Table 2.4. The first column represents the observed rainfall data, while the other five columns the maps obtained by the satellite rainfall products considered in the study. The color bar refers to the cumulated rainfall [mm] over the time period considered for each case in Table 2.4. 65

Figure 2.20 – Data mask used for remove areas (red areas) characterized by issues in the soil moisture retrieval. 70

Figure 2.21 - Analysis framework 72

Figure 2.22 – Hovmoller plot showing the spatial-temporal data availability, in percentage of the total annual available data (upper panel) and the mean daily rainfall (lower panel) of the SM2RAIN-CCI rainfall data set for different latitude bands. 73

Figure 2.23 – Global Pearson correlation (left) and Root Mean Square Difference (right) maps obtained between GPCC-FDD and the SM2RAIN-CCI rainfall data set for 5-day accumulated rainfall during the periods 1998-2001 (upper panel), 2002-2006 (middle panel) and 2007-2013 (lower panel). 74

Figure 2.24 – Correlation maps for 5 days of accumulated rainfall (left column) and differences in mean annual rainfall (right column) obtained by comparing (from top to bottom) SM2RAIN-CCI and GPCC (a), SM2RAIN-CCI and TRMMRT (b), SM2RAIN-CCI and CMORPH (c), SM2RAIN-CCI and ERA-Interim (d) and SM2RAIN-CCI and MSWEP (e) at 1° of spatial resolution. 75

Figure 2.25 – Mean Monthly Rainfall estimated by GPCC-FDD (blue line) and the new CCI-derived rainfall data set (red line) over the six analysis boxes throughout North America (A), South America (B), Europe (C), Sahel (D), Asia (E), India (F) and Australia (G) during the period 1998-2013. The blue lines draw the Mean Monthly Rainfall estimated by GPCC-FDD when both a ground-based and a SM-derived rainfall estimate is available. 76

Figure 2.26 – Yearly boxplots for the correlation coefficients (R) and Root Mean Square Differences (RMSD, in mm) between SM2RAIN-CCI and MSWEP obtained on a global scale at 0.25° spatial resolution during the period 1998-2015. For each box, the red line represents the median values, the blue box the 25th and 75th percentile, while the black dotted whiskers extend to the most extreme data points. 77

Figure 2.27 – Correlation coefficient (left) and Root Mean Square Difference (RMSD, right) box plots obtained by comparing SM2RAIN-CCI (in red), TRMMRT (in green), CMORPH (in blue), ERA-Interim (in black) and MSWEP (in magenta) with gauge-based data sets over Europe (top), India (middle) and Australia (bottom). 78

Figure 3.1 – Geographical location and elevation of the a) Tanaro River basins, b) Brenta River basin, c) Tiber River basin and d) Volturno River basin (not in scale). 82

Figure 3.2 - Schematization of the MISDc rainfall-runoff model with the representation of the simulated hydrological processes. 85

Figure 3.3 - Comparison of observed and simulated discharge obtained by forcing MISDc model with ground observed rainfall for Brenta (up-left), Tanaro (up-right), Tiber (bottom-left) and Volturno (bottom-right) basins, during the entire analysis period (2010-2013). 88

Figure 3.4 - Observed and simulated hydrographs obtained by forcing MISDc model with TMPA data before (upper panel) and after (lower panel) bias correction and model recalibration. . 90

Figure 3.5 - Comparison of observed and simulated daily discharge obtained by forcing MISDc model with the two satellite rainfall products SM2RASC and TMPA for Brenta (up-left), Tanaro (up-right), Tiber (bottom-left) and Volturno (bottom-right) basins, during the entire analysis period (2010-2013). 91

Figure 3.6 - Comparison of observed and simulated daily discharge obtained by forcing MISDc model with the two integrated rainfall products SM2RASC+OBS and TMPA +OBS for Brenta (up-left), Tanaro (up-right), Tiber (bottom-left) and Volturno (bottom-right) basins, during the entire analysis period (2010-2013). 93

Figure 3.7 - Nash-Sutcliffe efficiency index (NS) percentage variation obtained by forcing MISDc model with SM2RAIN derived rainfall (SM2RASC), TMPA 3B42-RT product (TMPA) and the integrated products between the observed and satellite rainfall data (SM2RASC+OBS and TMPA+OBS) during calibration (blue squares) and validation (green rumbles). The text boxes show the percentage variations in NS obtained for TMPA during the validation period that exceed the axis limit. 94

Figure 3.8 - Performance scores obtained during the flood events simulations over the Tanaro (TA), Brenta (BR), Tiber (TI) and Volturno (VO) basins by forcing MISDc model with observed data (OBS, solid green line), SM2RAIN derived rainfall (SM2RASC, dashed red line), TMPA data (TMPA, dashed blue line), integrated product between SM2RASC and OBS data (SM2RASC+OBS, dashed black line) and integrated product between TMPA and OBS data (TMPA+OBS, dashed magenta line). Nash-Sutcliffe efficiency index (NS, upper panel), percentage error in peak discharge (EQp, middle panel) and percentage error on direct runoff volume (Ev, bottom panel). In the upper panel graph, the y-axis is truncated to 0 for visualization purposes..... 95

Figure 4.1 – Planar(A) and sectional (B) view of the analysis mesh..... 99

Figure 4.2 – Visual representation of the d8 algorithm 101

Figure 4.3 – Visual representation of water fluxes considered in the coupled hydrological-stability model. 102

Figure 4.4 – Schematic representation of infinite slope..... 105

Figure 4.5 – Study area (left) and slope angles (right)..... 108

Figure 4.6 – Flow direction layer obtained during the preprocessing step. The colors refer to a direction, as displayed in the direction coding inset. 109

Figure 4.7 – Soil textural map for Umbria region (Modified from Brocca et al., 2016c). 109

Figure 4.8 – Spatial distribution of soil textures over the study area..... 110

Figure 4.9 – Angle of internal friction (upper panel) and cohesion (lower panel) values for the study area. 111

Figure 4.10 – Soil saturation profile for a cell simulated by the hydrological module 112

Figure 4.11 – Correlation maps obtained by comparing GROUND and SAT soil moisture simulations with ASCAT SWI estimates for the first (A, C) and second (B, D) soil layers. 113

Figure 4.12 – Soil moisture time series for 3 randomly selected pixels over the analysis, obtained through GROUND (red dashed line), SAT (blue dashed line) and SWI ASCAT (green solid line). For each time series the spatial localization is provided along with the temporal correlation (R). 114

Figure 4.13 – Spatial localization of the 3 landslide events used for the assessment of stability conditions by using GROUND and SAT model runs. The colorbar is referred to the slope angles obtained during the previous steps. 115

Figure 4.14– Soil moisture and Factor of Safety time series for three landslides events within the study area obtained by forcing the model with ground rainfall data 117

Figure 4.15 – Soil moisture and Factor of Safety time series for the three landslides events analyzed in this work obtained by forcing the model with satellite rainfall data. 119

Figure 6.1 - Climatology of the study area expressed as mean daily rainfall rate (mm/d) in the investigated period (from 15 January 2010 to 30 November 2013) obtained by the AWAP data set. The four letters indicate the 1° boxes for which the monthly rainfall time series are shown in Figure 6.6. Black areas represent the zones in which AWAP data are not available. 127

Figure 6.2 - Diagram of the input-output data, algorithms, and processing step carried out in the study for estimating and correcting rainfall through SMOS soil moisture observations. Note that TMPA 3B42 and AWAP data sets are used for parameter calibration/estimation and products validation, respectively. 128

Figure 6.3 - (left column) Pearson's correlation maps between AWAP-observed accumulated rainfall and TMPA 3B42RT product. (right column) Correlation ratio maps between the correlation obtained by comparing the four different SMOS-derived products (SM2RAIN, SM2RAIN+3B42RT, API-mod, and SMART) with AWAP observed rainfall and the correlation obtained with TMPA 3B42RT (left column); red pixels indicate degradation (lower correlations), whereas blue pixels an improvement (higher correlations). The analysis period is from 14 January 2010 to 30 November 2013, and the top (bottom) rows show results for 1 day (5 day) accumulated rainfall. Black areas represent the zones in which AWAP data are not available. 135

Figure 6.4 - As in Figure 6.3 but for the root-mean-square error (RMSE). Red pixels indicate degradation (higher RMSE), whereas blue pixels indicate an improvement (lower RMSE). 136

Figure 6.5 - POD (Probability of Detection) versus FAR (False Alarm Ratio) plots for (a, d) 10th, (b, e) 50th, and (c, f) 90th percentile and for 1 day (Figures 6a–6c) and 5 days (Figures 6d–6f) accumulated rainfall. The contour lines indicate TS (Threat Score) values, the horizontal (vertical) bars represent the standard deviation of POD (FAR), and the square is the median value. Squares represent the median POD (FAR) over all pixels for the 10th, 50th, and 90th

percentiles at that pixel. Optimal performances are for FAR = 0, POD = 1, and TS = 1. Percentiles represent the rainfall threshold used for the computation of the scores. Therefore, low (high) percentiles indicate the product capability to detect high (low) rainfall intensities. 137

Figure 6.6 - Time series of monthly rainfall obtained from observations (AWAP), the real-time TMPA product (3B42RT), and the SMOS-derived products (SM2RAIN, SM2RAIN+3B42RT, API-mod, and SMART) for the four boxes shown in Figure 6.1 (R: Pearson's correlation coefficient; RMSE: root-mean-square error). 138

Figure 6.7 - Box plot of summary statistics for 1-day rainfall estimates grouped by rainfall intensity, i.e., <5 mm (drizzle events), 5-15 mm (moderate rainfall events), >15 mm (heavy rainfall events), computed on the ground observed data in India. Note that y-axis have different ranges to better visualize the differences in the performance between datasets. In the box plots the min/max, 25/75° percentiles and the median values are shown (R: Pearson correlation coefficient; ubRMSE: unbiased Root Mean Square Error, BIAS: mean error). 143

Figure 6.8 - Box plot of the categorical metrics POD (Probability of Detection), FAR (False Alarm Ratio) and TS (Threat Score) values, for daily rainfall estimates grouped by rainfall intensity, i.e. >0 mm, >5 mm and >15 mm, and computed on the ground observed data in India. In the box plots the min/max, 25°/75° percentiles and the median values are shown. 144

Figure 6.9 - Study basins and relative ANSE index obtained by considering E-OBS rainfall dataset in the calibration period. For each catchment, the related dots vary in dimension depending on the area. 145

Figure 6.10. Performances in terms of ANSE (Nash–Sutcliffe efficiency for high-flow conditions) and KGE (Kling-Gupta efficiency, for medium flow conditions) of the different parent (a, b) and integrated (c, d) rainfall products in reproducing the observed discharge for all the study catchments in the calibration (thin boxplot) /validation period (thick boxplot). Cross symbols represent outlier values, the bold numbers indicate the mean values for each rainfall product..... 151

Figure 6.11 Performances in terms of ANSE (Nash–Sutcliffe efficiency for high-flow conditions) and KGE (Kling-Gupta efficiency, for medium flow conditions) of the different parent (a, b) and integrated (c, d) rainfall products in reproducing the observed discharge for all the study catchments in the calibration (thin boxplot) /validation period (thick boxplot). Cross symbols represent outlier values, the bold numbers indicate the mean values for each rainfall product..... 153

Figure 6.12 - Comparison in terms of ANSE index: performances of integrated versus parent satellite rainfall products/E-OBS data (first column/ second column) in reproducing observed discharge data. Blue dots and the red diamonds refer to calibration/validation periods, numbers indicate the basins as listed in Table 6.9..... 156

Figure 6.13 - Discharge time series for some study catchments obtained by forcing MISDc model through E-OBS, TMPA and TMPA+SM2RCCI rainfall products. For sake of visualization, for each basin only short time windows on the validation period are shown. 157

Figure 6.14 - Map of Italy showing the distribution of the rainfall-induced landslides in the period 2008-2014 (white dots). 158

Figure 6.15 - Maps of Pearson correlation between ground-based rainfall observations and (a) SM2RASC, (b) 3B42-RT, (c) CMORPH and (d) PERSIANN satellite rainfall products. .. 163

Figure 6.16 - Empirical cumulative distribution function (ECDF) of (a) the rainfall duration D and (b) the cumulated rainfall E of the reconstructed rainfall events for OBS (green curves), SM2RASC (red curves), 3B42-RT (blue curves), CMORPH (magenta curves) and PERSIANN (black curves) data sets. Inset tables list relevant quantile values of D and E. 164

Figure 6.17 - Example of ED rainfall thresholds calculated using RE^* at exceeding probabilities from 1% (T_1) to 50% (T_{50}) for the OBS data set. Grey dots are the (D, E) pairs. 164

Figure 6.18 - Rainfall duration vs. cumulated event rainfall conditions in Italy in the period 2008-2014, compared with thresholds at 50% (T50%) exceedance probability level (dashed black lines) for (a) OBS, (b) SM2RASC, (c) 3B42-RT, (d) CMORPH and (e) PERSIANN. Legend: TP, True Positives; TN, True Negative; FP, False Positive; FN, False Negative.. 165

Figure 6.19 - Values of the POD, POFD and HK skill scores at varying the threshold non-exceedance probability for the five data sets. Values in red are those which maximize HK. 166

Figure 6.20 - ROC curves built by skill scores obtained varying the threshold exceedance probability for OBS (green), SM2RASC (red), 3B42-RT (blue), CMORPH (magenta) and PERSIANN (black) data sets. Horizontal and vertical bars represent the range of variation of POFD and POD for the 100 runs in which RE^* are randomly selected. 167

LIST OF TABLES

Table 1.1 - Summary of publicly available precipitation estimates from precipitation gauge data. Adapted from the IPWG International Precipitation Working Group (http://www.isac.cnr.it/~ipwg/). 16

Table 1.2 - Summary of the main important instrument used for the retrieval of precipitation from space for quasi-operational, quasi-global precipitation estimates from a single satellite sensor type. 20

Table 1.3 - Summary of publicly available, precipitation estimates that are produced by combining input data from several satellite sensor types. Adapted from the IPWG International Precipitation Working Group (http://www.isac.cnr.it/~ipwg/). 30

Table 1.4 - Summary of publicly available precipitation estimates that are produced by combining input data from several sensor types, including satellite sensors and precipitation gauges. Adapted from the IPWG International Precipitation Working Group (http://www.isac.cnr.it/~ipwg/). 32

Table 2.1 – Main features of the analyzed satellite rainfall products 48

Table 2.2 - Median R, median RMSE (mm), and pixels with a significant correlation (p-value, 0.01) for each analyzed product (%), during the calibration and validation periods, considering 1 and 5 days of accumulated rainfall (std dev is given in parentheses) (Modified by Ciabatta et al., 2015). 52

Table 2.3 - Statistics of continuous (Pearson correlation, R, Root Mean Square Error, RMSE and BIAS), and categorical performance median scores (Probability Of Detection, POD, False Alarm Ratio, FAR and Threat Score, TS) of the different analyzed products during the validation period 2012–2014. (Modified from Ciabatta et al., 2017). 55

Table 2.4 - Rainfall events occurred in Italy within the period 2011–2014 for the case studies analysis. For each event, the maximum cumulated rainfall, calculated during the rainfall event, is reported. 64

Table 2.5 – Available sensors and temporal intervals considered for the SM2RAIN algorithm application. 71

Table 3.1 - Main characteristics of the investigated basins: gauging station, drainage area, Mean Annual Rainfall (MAR), Mean Annual Temperature (MAT), average elevation (in m a.s.l.) and average slope (in °). 83

Table 3.2 – Correlation coefficients (R) and Root Mean Square Error (RMSE) for the analysed satellite products ($SM2R_{ASC}$ and TMPA) against observed rainfall during the calibration (CAL) and validation (VAL) periods. 87

Table 3.3 - Nash-Sutcliffe efficiency (NS), correlation coefficient (R) and percentage volume error (E_v) obtained by forcing MISDc hydrologic model with observed, satellite ($SM2R_{ASC}$ and TMPA) and integrated ($SM2R_{ASC}$+OBS and TMPA+OBS) rainfall data, during the calibration (2010-2011) and validation (2012-2013) periods. In bold font the best performance scores of each basin are reported while the scores are in italic font if better than those obtained with ground observed rainfall (OBS). The highest performance of the integrated $SM2R_{ASC}$+OBS product for Brenta, Tanaro and Tiber river basins is evident. 89

Table 3.4 - Integration coefficient (K) for the considered basins by using as model input the integrated products between the observed and satellite products (SM2RASC+OBS and TMPA+OBS). 92

Table 4.1 – Values of hydraulic parameters used for the hydrological module according to Rawls et al. (1982). 110

Table 4.2 – Date of occurrence and coordinates of the landslide events occurred within the study area. 115

Table 6.1 - Summary statistic of the calibration parameters of each method; (s: Standard Deviation; 25th and 75th: Percentiles) 132

Table 6.2 - Summary statistics of the spatial distribution of performance scores of the different satellite rainfall products in the comparison with AWAP data. 134

Table 6.3 - Main characteristics of the satellite soil moisture products employed in this study. 140

Table 6.4 - Main characteristics of the study basins. 146

Table 6.7 - Main characteristics of the satellite datasets used in this study. 147

Table 6.8 - ANSE index obtained by forcing MISDc hydrological model with E-OBS and satellite (TMPA, CMOR, PERS) rainfall data during the calibration and the validation periods. In bold font the best performances score for each basin are reported while the scores are in italic font if better than those obtained with ground observed data (E-OBS). 152

Table 6.9 - ANSE index obtained by forcing MISDc hydrological model with integrated satellite rainfall data during the calibration and the validation periods. In bold font the best performances score for each basin are reported while the scores are in italic font if better than those obtained with ground observed data (E-OBS). 155

1.INTRODUCTION

In this Chapter, a brief introduction related to rainfall estimation from space is given, together with the aims of this work of thesis. The first part describes the most common used methods for rainfall estimation, along with their main limitations and advantages. In the second part, retrieval algorithm from space are described. In this part state-of-the-art approaches and a new method for rainfall estimation are reported. The third part present a brief review of the use of satellite rainfall data for landslide risk assessment. In the last part of the Chapter, the purposes of this work of thesis are presented.

1.1 Satellite rainfall estimation

Rainfall plays a key role in many fields, such as natural hazard assessment, drought management, weather forecasting, agriculture, and disease prevention (Dinku et al. 2007). Obtaining accurate rainfall estimates is of paramount importance, as precipitation data act as main driver for several applications. Due to the high spatial and temporal variability of rainfall, its estimation is a challenging task. Traditionally, rainfall is estimated through ground monitoring networks (rain gauges and weather radars), through short-range forecasts from Numerical Weather Prediction (NWP) models and through satellite observations. In the following a brief explanation of the methods will be provided, focusing on the advantages and the drawbacks of each approach.

Rain gauges are generally assumed as the most accurate method to estimate rainfall, providing the most direct measurement of point precipitation. Despite the high quality of rainfall estimates obtained through rain gauges, this source of information is impacted by the variable network density throughout the world (Rudolf and Schneider 2005). Indeed, Kidd et al., (2017) reported that the number of stations available with sub-daily temporal sampling over land is just 64000 throughout the world. As it can be seen in ***Figure 1.1***, most of the ground stations are located in Europe and over the USA, limiting the use of observed rainfall data on a global scale. Examples of ground based rainfall dataset are the Global Precipitation Climatology Centre (GPCC) first guess daily product (Schamm et al., 2013), provided by the German Meteorological Service (Deutscher Wetterdienst, DWD) and the CPC Unified Gauge-based Analysis of Global Daily Precipitation (Chen et al. 2008a, 2008b, https://climatedataguide.ucar.edu/climate-data/cpc-unified-gauge-based-analysis-global-daily-precipitation) provided by the National Center for Atmospheric Research (NCAR). The dataset is constructed over the global land areas. Gauge reports from over 30,000 stations are collected from multiple. The daily analysis is constructed on a 0.125° grid over the entire global land areas, and released on a 0.5° grid over the global domain for a period from 1979 to the present (Xie, 2011). Some of gauge-based rainfall datasets are listed in ***Table 1.1***.

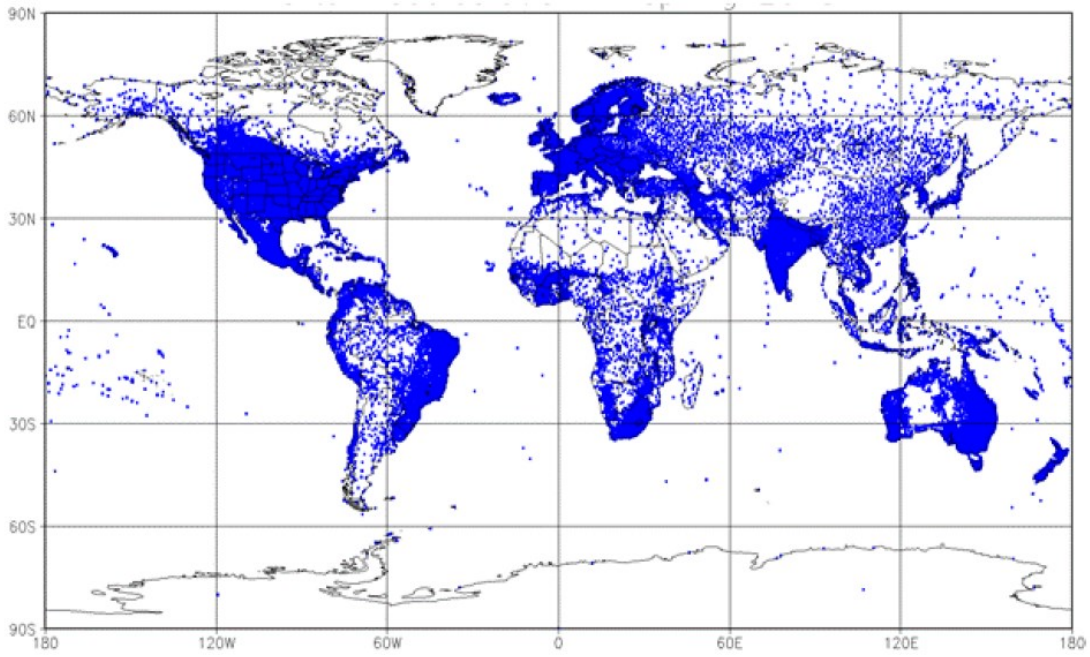

Figure 1.1 – Spatial distribution of monthly in-situ stations used for the creation of the Global Precipitation Climatology Centre (GPCC) in 2015. Modified by Schneider et al., (2017).

Raingauges estimates are also impacted by the limited spatial representativeness of the data (Kidd et al., 2012) and by under-catch phenomena due to wind around the gauge orifice (Peterson et al., 1998).

Algorithm	Input data	Space/time res.	Areal coverage/start date	Latency	Producer
APHRODITE Water Resources	~12,000 gauges	0.25°, 0.5°/daily	Eurasia/1951-2007	-	APHRODITE Project
CPC Unified Gauge-based Analysis of Global Daily Precip.	> 30,000 gauges	0.5°/daily	Global/1979-2005	-	NOAA/NWS CPC
	> 17,000 gauges real-time	0.5°/daily	Global/2006	1 day	NOAA/NWS CPC
CRU Gauge	~10,000 gauges (anomaly interpolation)	2.5°x3.75°, 5°/monthly	Global/1900 - 1998	-	CRU at U. East Anglia
CRU TS 3.10.01 Gauge	~10,000 gauges	0.5°/monthly	Global/1901 - 2009	1-2 years	CRU and BADC
Dai Gauge Dataset 2	~4,000 gauges (anomalies rel. to 1950-1979)	2.5°/monthly	Global regions with data/1850 - 1996	-	NCAR
GHCN+CAMS Gauge	~3,800 gauges (SPHEREMAP)	2.5°/monthly	Global/1979	1 week	NOAA/NWS CPC
GPCC Monitoring	~8,000 gauges	1°,2.5°/monthly	Global/1986-2006 V. 1; 2007 V. 4	2 months	DWD GPCC
GPCC Full Data Reanalysis Version 6	~67,200 gauges	0.5°,1°,2.5°/ monthly	Global/1901-2010	-	DWD GPC
GPCC VASClimo Version 1.1	~9,000 gauges	0.5°,1°,2.5°/ monthly	Global/1950-2000	-	DWD GPCC
GPCC First Guess		1°/daily	Global/2009	-	DWD GPCC

Table 1.1 - Summary of publicly available precipitation estimates from precipitation gauge data. Adapted from the IPWG International Precipitation Working Group (http://www.isac.cnr.it/~ipwg/).

Another useful source of ground rainfall data relies in ground weather radars. These instruments provide a spatial estimation of rainfall through the use of microwave radiation, operating at C- (4-8 GHz), S- (2-4 GHz), X- (8-12 GHz) and K-band (18-27 GHz). The weather radar broadcast an energy impulse and then measures the reflected energy back to the antenna. The reflected energy can be linked to raindrops and hail. Besides the high costs related to setting up and maintenance of such instruments, a ground weather radar is impacted by several issues: 1) the backscattered radiation depends upon the drop size distribution, which can vary considerably across the range of precipitation regimes, 2) range effects due to 'lifting' of the beam, so that precipitation may be undetected and, 3) false returns from ground objects (Kidd and Huffman. 2011). Due to these limitations, radar data are often merged with rain gauge observations in order to provide a more accurate estimate of precipitation, such as the National Centers for Environmental Prediction (NCEP) Stage IV product available over the US (Seo et al., 1998).

NWP models provide rainfall estimates using satellite and ground observations of atmospheric variables (temperature, moisture, pressure) as input in order to solve the equations of atmospheric motions. This allows to predict rainfall (and other quantities) in a short-range. Among NWP models, one can identify analysis, reanalysis (that assimilate observed information), Global Circulation Models (GCM) and Regional Circulation Models (RCM), used for climate studies. An example of reanalysis dataset is the European Centre for Medium range Weather Forecast (ECMWF) ERA-Interim product (Dee et a., 2011), providing several atmospheric and surface variables estimates (e.g., pressure, air temperature, volumetric water content, to name a few) over a grid of 0.77° every 6 hours. Very recently, ECMWF developed a new version of ERA Interim reanalysis product, named ERA5. The new dataset covers the period 1950 to present, providing atmospheric and surface variables at 31 km of spatial resolution on a hourly basis. The main limitations of such datasets are the relative coarse spatial resolution (0.77° for ERA-Interim) and the high computational demand needed to solve the atmospheric motion equations globally. The datasets are available from ECMWF (https://www.ecmwf.int/en/research/climate-reanalysis/browse-reanalysis-datasets).

A way to overcome some of the issues and limitations related to the different source of rainfall estimates described above could rely on satellite based observations. Satellite estimates of precipitation can be derived from a range of observations from many different sensors. In the following, a background of the most important satellite sensors used for the retrieval of precipitation will be provided along with the different retrievals algorithm that exploit a combination of these sensors and (in some cases) ground data. Large part of the text that will follow is a summary of three important review papers in the field of precipitation measurement (Kidd and Huffman, 2011, Kidd and Levizzani 2011, Serrat-Capdevila et al. 2014). For further details, the reader is referred to these papers.

Meteorological satellites can be divided in to two broad categories: Geostationary (GEO) satellites and Low Earth Orbiting (LEO) satellites, which include polar-orbiting satellites (***Figure 1.2***). ***Table 1.2*** summarizes the main instrumentation used for the estimation of precipitation, covering both visible (VIS) and infrared (IR) sensors and those in the microwave (MW) region of the spectrum.

Figure 1.2 – Schematic representation of Low Erath Orbit (LEO) and Geostationary (GEO) satellite orbit geometry. Modified from satellites4everyone.co.uk.

GEO satellites orbit the Earth about 35 800 km above the Equator such that they orbit at the same rate as the Earth turns, appearing stationary relative to a location over the surface. Each GEO satellite is able to view about one third of the Earth's surface, but due to increasing scan angle towards the extremities of the imagery degrading the usability of the data.

Five operational GEO satellites are required to ensure full West – East (and ~70 N to 70 S) coverage. From their position, they are able to provide imagery on a frequent and regular basis (e.g., VIS and IR sensors with nominal resolutions of 1 km × 1 km and 4 km × 4 km, respectively, acquiring images every 30 min).

Sensor	Acronym meaning	Satellite	Channels	Bands	Resolution (km)	Sampling	Orbit	Type	Scanning method
AVHRR	Advanced very high resolution radiometer	NOAA/MetOp	5	VIS-IR	1	Twice daily	LEO	Imager	Cross track
SEVIRI	Spinning Enhanced Visible and Infrared Imager	MSG (Meteosat Second Generation)	11	VIS-IR	1–3	15 min	GEO	Imager	Geostationary
GOES	Geostationary Operational Environmental Satellite	GOES	5	VIS-IR	1–4	30 min	GEO	Imager	Geostationary
AMSU A/B	Advanced microwave Sounding Unit	NOAA/MetOp	5	23.8–183	20–50	Twice daily	LEO	Sounder	Cross track
MHS	Microwave Humidity Sounder	NOAA/MetOp	5	89–190	17–50	Twice daily	LEO	Sounder	Cross track
AMSR	Advanced microwave Scanning radiometer	NASA Aqua	12	6–85	5–25	Twice daily	LEO	Imager	Conical Scanner
SSM/I	Special Sensor Microwave Imager	DMSP (Defense Meteorological	7	PMW 19–85	12.5–25	Twice daily	LEO	Imager	Conical Scanner

		Satellite Program (DMSP)							
SSMIS	Special Sensor Microwave Imager-Sounder	DMSP	11	19–183	13–45	Twice daily	LEO	Imager-Sounder	Conical Scanner
TMI	TRMM microwave imager	TRMM	9	10–85	5–25	Twice 2-days	LEO	Imager	Conical Scanner
GMI	GPM microwave Imager	GPM core Observatory NASA/JAXA	13	10-183	5–25	Twice 2-days	LEO	Imager	Conical scanner
PR	Precipitation radar	TRMM	1	13.6 (Ku)	5	Twice 3 days	LEO	Radar	Conical scanner
CPR	Cloud profiling radar	CloudSat	1	94	1.4	Once 16 days	LEO	Radar	Conical scanner
DPR	Dual precipitation radar	GPM core Observatory NASA/JAXA	2	13.6 (Ku), 35.5(Ka)	5 (250 m in height)	Twice 2 days	LEO	Radar	Conical scanner

Table 1.2 - Summary of the main important instrument used for the retrieval of precipitation from space for quasi-operational, quasi-global precipitation estimates from a single satellite sensor type.

Notable examples of GEO satellites are the Meteosat Second Generation (MSG, ***Figure 1.3***) satellites operated by the European Organization for the Exploitation of Meteorological Satellites (EUMETSAT), two U.S. operated Geostationary Operational Environmental Satellite (GOES).

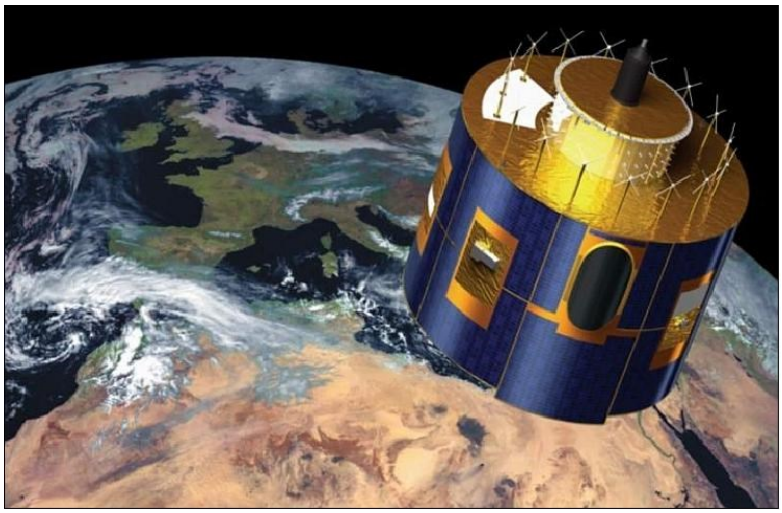

Figure 1.3 – Artistic view of the Meteosat Second Generation (MSG) 4 satellite orbiting in geostationary orbit (https://directory.eoportal.org/web/eoportal/satellite-missions/m/meteosat-second-generation).

LEO satellites generally cross the Equator at the same local time on each orbit, providing about two overpasses per day. These satellites carry a range of instruments capable of precipitation retrievals, including multi-channel VIS/IR sensors, and passive microwave (PMW). Sensors typically include both multichannel VIS and IR sensors and PMW sounders and imagers. Imagers provide a two-dimensional array of pixels from which an image of instantaneous precipitation may be produced. The typical scanning technology for these sensors is the conical scanning. Sounders, measure the vertical distributions of atmospheric parameters such as temperature, pressure, water vapor, and composition from multispectral information. Due to their characteristics (built to obtain vertical information of atmosphere variables) they have a lower spatial resolution when used for collecting information at the surface and do not own information on polarization. Typical scanning technology for sounders is the cross track scanning. The latter has the advantage of large scan width but the resolution degrades as one moves toward the edges (e.g., from 45 km at nadir to 75 km at the edge of the swath, see ***Figure 1.4***).

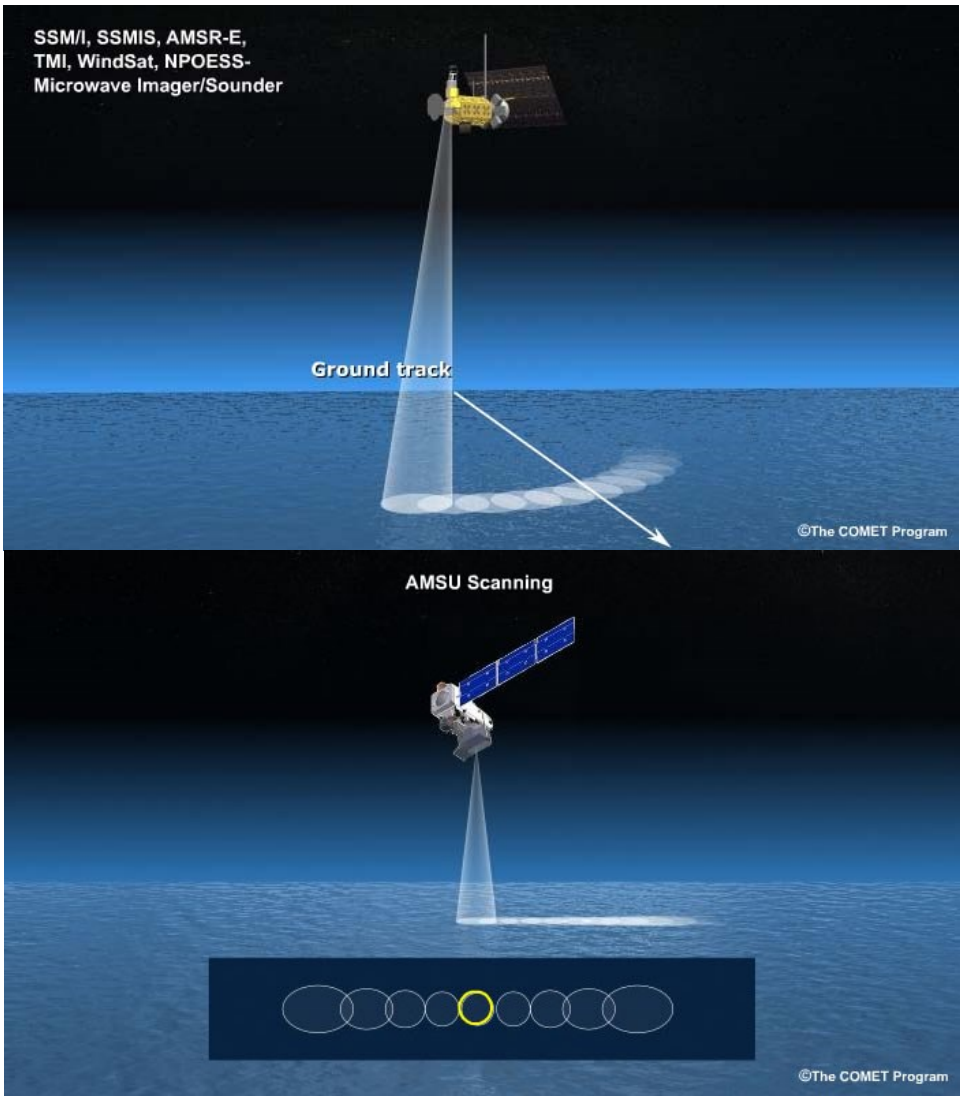

Figure 1.4 - Difference between conical (up) and cross-track (bottom) scanning technology (courtesy of National Center of Atmospheric Research http://www2.ucar.edu/).

Current operational and non-operational polar-orbiting satellites used for the retrieval of precipitation include the National Oceanic and Atmospheric Administration (NOAA) series of satellites with NOAA-19, the EUMETSAT's MetOp series, the Defense Meteorological Satellite Program (DMSP) series of satellites and the National Aeronautics and Space Administration (NASA) and the Japanese Aerospace Exploration Agency (JAXA) satellites.

Notable examples of the sensors installed on these satellites are the Special Sensor Microwave/Imager (SSM/I) installed on the DMSP series of satellites. It provides observations from 18 to 85 GHz, the latter being particularly useful for rainfall estimation over land. The AQUA satellite includes the PMW Advanced Microwave Scanning Radiometer-Earth Observing System (EOS) (AMSR-E) which provides measurements across the microwave spectrum from 6 to 85 GHz at resolutions up to 5 km at the highest frequency. Operational PMW observations useful for precipitation estimation have relied upon the cross-track Advanced Microwave Sounding Unit (AMSU on NOAA-19) and the Microwave Humidity Sounder (MHS) instruments that provide

information at higher frequencies, between 23.8 and 190 GHz.

The Tropical Rainfall Measuring Mission (TRMM), launched in 1997, was the first dedicated precipitation satellite and is key in the development and improvement of satellite rainfall estimation techniques. It carries a range of instruments which allow direct comparisons to be made between VIS, IR, PMW and active microwave observations. The Precipitation Radar (PR) was the first spaceborne precipitation radar, capable of sampling precipitation both vertically and horizontally, although with a limited swath of 210 km. Other instruments include the TRMM Microwave Imager (TMI), the Visible and InfraRed Scanner (VIRS), and the Lightning Imaging Sensor (LIS). The non sun-synchronous nature of its orbit allows samples across the full diurnal cycle to be made.

The Global Precipitation Measurement (GPM) Mission launched in 2014 is an international satellite mission to provide next-generation observations of rain and snow worldwide every three hours through a constellation of satellites. The mission carries advanced instruments for precipitation measurements from space. The foundation of the GPM mission is the Core Observatory satellite. Data collected from the Core satellite serves as a reference standard that unify precipitation measurements from research and operational satellites launched by a consortium of GPM partners in the United States, Japan, France, India, and Europe. The GPM constellation (***Figure 1.5***) of satellites can observe precipitation over the entire globe every 2-3 hours.

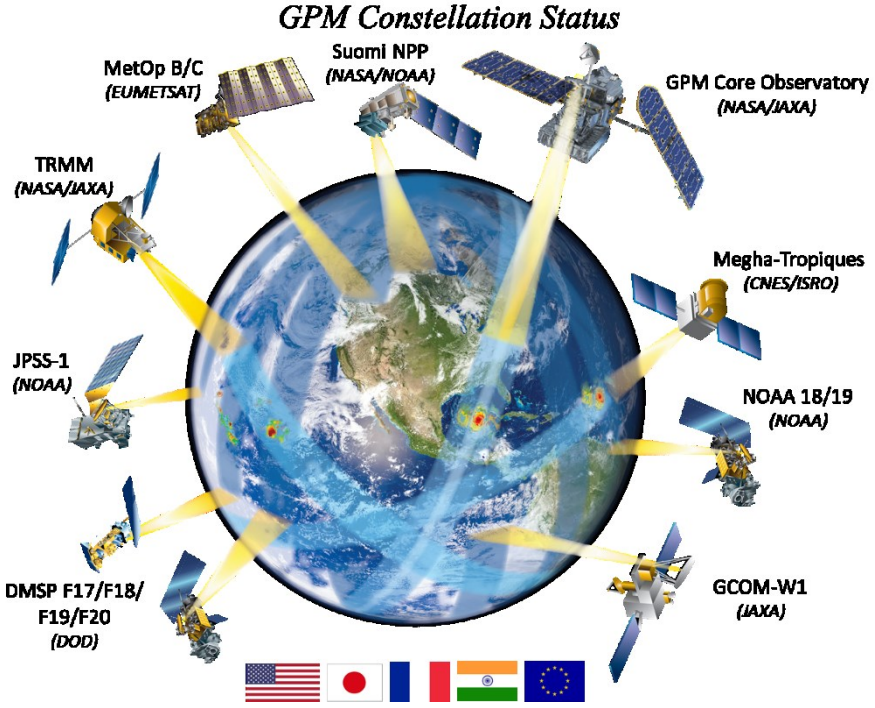

Figure 1.5 – Global Precipitation Measurement (GPM) Mission constellation satellites (https://pmm.nasa.gov/image-gallery/gpm-constellation).

The Core satellite measures rain and snow using two science instruments: the GPM Microwave Imager (GMI) and the Dual-frequency Precipitation Radar (DPR). The GMI captures precipitation intensities and horizontal patterns, while the DPR provides insights into the three dimensional structure of precipitating particles. Together these two instruments provide a database of

measurements against which other partner satellites' microwave observations can be meaningfully compared and combined to make a global precipitation dataset (http://www.nasa.gov/mission_pages/GPM/).

1.2 Precipitation retrievals

VIS/IR methods

In the visible (VIS) part of the electromagnetic spectrum, clouds appear relatively bright against the surface of the Earth due to their high albedo. Rainfall can be inferred from VIS images since bright clouds tend to be thick, and thick clouds are more likely to be associated with rainfall. However, the relationship between brightness and rainfall is poor and consequently VIS imagery is usually only used in conjunction with other observations.

IR imagery that measures the thermal emissions from objects is potentially more useful, and is available at night and day. Heavier rainfall tends to be associated with larger, taller clouds with colder cloud tops. By observing cloud top temperatures, a simple rainfall estimate can be derived trough Cold-Cloud duration techniques (CCD). CCD techniques relate the occurrence of cold clouds to the surface rainfall, such as the Global Precipitation Index (GPI; Arkin and Meisner, 1987). The GPI assigns a constant rain-rate (3 mm/h) to the fraction of clouds below a set threshold (235 K). However, the indirectness of the relationship between rainfall and cloud temperature along with the significant variations of such relationship during the lifetime of a rainfall event, between different rain systems, and between climatological regimes reduce the accuracy of rainfall IR estimates.

Passive microwave methods

The radiation emitted by Earth in the spectrum of microwave may be passively sensed by radiometers. This radiation is primarily attenuated by the presence of precipitation-sized particles. Two processes can be used to identify precipitation: emission from rain droplets which lead to an increase in PMW radiation and scattering caused by precipitating ice particles which leads to a decrease in PMW radiation.

The background radiometric signal over water is low and constant, therefore additional emissions from precipitation can be used to identify and quantify the rainfall using low-frequency channels (<20 GHz). Over land, the surface has a much higher background emissivity hence emissions from hydrometeors cannot be reliably measured. Here, scattering caused by ice particles, resulting in a decrease in received radiation at high- frequencies (>35 GHz), must be used.

Since the observed PMW brightness temperatures (Tb) generally have a non-unique response to rainfall intensity, multi-channel approaches are the norm. These techniques for the retrieval of precipitation can be divided in two broad groups: empirically derived and physically derived techniques.

In particular, physical techniques minimize the difference between modelled and the observed radiation. More successful physical techniques use a priori databases of which compare the satellite observations with model-generated atmospheric profiles. A noteworthy example of these techniques is the Goddard Profiling technique (GPROF; Kummerow et al., 2001) which has evolved to ensure

consistency between the physical retrievals from the TRMM PR and TMI PMW Tbs through the use of cloud resolving models. Artificial Neural Network (ANN) are also used to derive relationships between the satellite passive microwave observations and surface rainfall but are mostly used in conjunction with other type of information (Sorooshian et al. 2000, Sanò et al., 2016).

High-frequency PMW observations from, for example, the AMSU-B instrument, provide additional information and the ability to retrieve precipitation over problematic surface backgrounds, such as coastlines and snow/ice (Kongoli et al., 2007). Chen and Staelin (2003) constructed one of the first global techniques to exploit these sounding channels to derive precipitation rates at 15- and 50-km resolution from the Atmospheric Infrared Sounder (AIRS), AMSU and the Humidity Sounder for Brazil using an ANN.

The main drawback of PMW-based techniques is that observations are currently only available from LEO satellites, typically resulting in two observations per day per satellite. Moreover, the retrieval of precipitation using PMW observations has always represented a problem over coastal areas; often techniques omit retrievals over the coastline, or use a less optimum technique (Kidd, 1998).

Active microwave methods

Active MW techniques, although considered the most direct method of precipitation estimation are specifically designed for retrieving precipitation characteristics.

Despite this, radar technology for spaceborne precipitation estimation is limited primarily to the TRMM PR and then to GPM DPR. For the retrieval of precipitation, these systems rely upon the interpretation of the backscattered radiation from precipitation, which is broadly proportional to the number of precipitation-sized particles and therefore the intensity. The DPR provides three-dimensional information about precipitation particles derived from reflected energy by these particles at different heights within the cloud system. The two frequencies of the DPR also allow the radar to infer the sizes of precipitation particles and offer insights into a storm's physical characteristics with an increase accuracy in the estimation of light rainfall.

Multi-sensor techniques

Retrievals from a single sensor have the relative advantage of processing simplicity, but the VIS/IR lack the directness of the PMW and the PMW lack the frequency sampling of the VIS/IR. To this end, a growing number of techniques are developed to exploit the synergy between the polar-orbiting PMW retrievals (infrequent, more direct) with the geostationary observations (frequent, less direct).

Techniques that generate calibration curves to map IR radiances to other data sets (such as the PMW) are generally termed "blended" algorithms (e.g. Turk et al., 2000). One example, is the TRMM Multi-Satellite Precipitation Analysis (TMPA; Huffman et al., 2007) which ingests data from PMW imaging and sounding sensors and geostationary IR data with adjustments made for the different satellite retrievals before combining them into a single precipitation product.

Other techniques have used ANNs to derived precipitation estimates through combining information from multi-channel and multi-sensor observations like the Precipitation Estimation

from Remotely Sensed Information using Artificial Neural Network (PERSIANN; Hsu et al., 1997).

The above techniques are ultimately limited by the indirectness of the IR to sense rainfall itself. However, the IR data can provide a reasonable measure of cloud movement, which can then be used to advect or morph the more direct PMW data between the successive satellite overpasses. Examples of current state-of-the-art methodologies are the Climate Prediction Center Morphing technique (CMORPH; Joyce et al., 2004) and the Global Satellite Mapping of Precipitation (GSMaP; Kubota et al., 2007). The main drawback of this methodology is that the retrieved cloud motion might not necessarily represent the true motion of the precipitation at the surface, particularly if changes in the surface precipitation pattern occur between the infrequent PMW overpasses.

For many applications the combination of all available data sets is ideal, incorporating products derived from the various satellite observations, gauge data sets and, where available, surface radar data. In this framework, various combination schemes are developed like the Global Precipitation and Climatology Project (GPCP) precipitation product (Huffman et al., 1997, Adler et al., 2003), which generates a largely homogeneous global precipitation product or the Climate Prediction Center Merged Analysis of Precipitation (CMAP; Xie and Arkin, 1997), which merges satellite IR along with gauge and re-analyses data from the NCEP and NCAR.

Recently, the GPM mission in coordination with the Goddard Earth Sciences Data and Information Services Center (GES DISC) released the Integrated Multi-satellitE Retrievals for GPM (IMERG) which merges precipitation estimates from passive microwave sensors, geo-IR, and monthly surface precipitation gauge analysis data (where available) to provide half-hourly and monthly precipitation estimates and related fields on a 0.1° lat./long grid over the domain 60°N-S.

Some of the main satellite precipitation products currently produced are summarized in ***Table 1.3*** and ***Table 1.4***, showing satellite-only and gauge-corrected rainfall estimates, respectively.

Algorithm	Input data	Space/time grid	Areal coverage/start date	Update frequency	Latency	Producer
AIRS AIRG2SSD	AIRS , AMSU, HSB sounding retrievals	Level 2G swath/orbit segments	Global/Sept. 2002	Daily	1 day	NASA/GSFC GES DISC
AIRS AIRX3STD, AIRX3ST8, AIRX3STM	AIRS, AMSU, HSB sounding retrievals	1°/daily, 1°/8-day, 1°/monthly	Global/Sept. 2002	Daily, 8-day, monthly	1 day	NASA/GSFC GES DISC
CMORPH	TMI, AMSR-E, SSM/I, SSMIS, AMSU, MHS, IR vectors	8 km/30-min	50°N-S/1998	Daily	18 hours	NOAA/CPC
CMORPH V1.0 RAW	TMI, AMSR-E, SSM/I, SSMIS, AMSU, MHS, IR vectors	0.25°/3-hourly	50°N-S/1998	Daily	18 hours	NOAA/CPC
GPM Imerg	Satellites used in the TMPA, CMORPH and PERSIANN-CCS	10 km – 0.5 hours	Global - 60°N-S/Mar 2014	30-min (early run)	6 hours (early run)	NASA/GSFC PPS
GPM Imerg	Satellites used in the TMPA, CMORPH and	10 km – 0.5 hours	Global - 60°N-S/Mar 2014	30-min	18 hours	NASA/GSFC PPS

	PERSIANN-CCS			(late run)	(late run)	
GSMaP-NRT	TMI, AMSR-E, SSM/I, SSMIS, AMSU, IR vectors	0.1°/hourly	60°N-S/Oct. 2007	1 hour	4 hours	JAXA
GSMaP-MWR	TMI, AMSR-E, AMSR, SSM/I, IR vectors	0.25°/hourly, daily, monthly	60°N-S/1998-2006	-	-	JAXA
GSMaP-MVK	TMI, AMSR-E, AMSR, SSM/I, SSMIS, AMSU, IR vectors	0.1°/hourly	60°N-S/2000 (currently 2003-2008 data available)	Monthly	Reprocess now; will become operational	JAXA
GSMaP-MVK+	TMI, AMSR-E, AMSR, SSM/I, AMSU, IR vectors	0.1°/hourly	60°N-S/2003-2006	-	-	JAXA
MPE	Meteosat 7, 8, 9, 10 IR and SSM/I, SSMIS	MFG: original pixels/30-min	Indian Ocean 8°W-122°E, 65°N-S	30-min	10 min	EUMETSAT
		MSG: original pixels/15-min	Europe/Africa 79°W-E, 8165°N-S	15-min	10 min	
NRL Real Time	SSM/I- & F16/SSMIS-	0.25°/hourly	40°N-S/ July 2000	Hourly	3 hours	NRL Monterey

	cal IR (Prob.-Matching Method)					
PERSIANN	(TMI, AMSR-E, SSM/I, SSMIS, AMSU, MHS)-cal. IR	0.25°/30-min	60°N-S/ March 2000	Hourly	1 day	UC Irvine
PERSIANN-CCS	Grid Geo-IR	0.04°/30-min	60°N-S/2003	None	1 hour	UC Irvine
PR-OBS-3	SSMIS, AMSU/MHS, MSG-IR	5 km/15 min	Europe/Jan 2009	15 min	15 min	HSAF
PR-OBS-4	SSMIS, AMSU/MHS, MSG-IR	8 km/30 min	Europe/Nov 2011	1 hour	3 hours	HSAF
TCI (3G68)	PR, TMI	0.5°/hourly	Global - 37°N-S/ Dec. 1997	Daily	4 days	NASA/GSFC PPS
TOVS	HIRS, MSU sounding retrievals	1°/daily	Global/1979-April 2005	Daily	1 month	NASA/GSFC 610
TRMM Real-Time HQ Version 7 (3B40RT)	TMI, SSM/I, SSMIS, AMSR-E, AMSU, MHS	0.25°/3-hourly	Global - 70°N-S/Mar. 2000	3 hours	9 hours	NASA/GSFC PPS
TRMM Real-Time	MW-VAR (IR)	0.25°/hourly	Global - 50°N-S/Mar.	1 hour	9 hours	NASA/GSFC PPS

VAR Version 7 (3B41RT)			2000			
TRMM Real-Time HQVAR Version 7 (3B42RT)	HQ, MW-VAR (IR)	0.25°/3-hourly	Global - 50°N-S/Mar. 2000	3 hours	9 hours	NASA/GSFC PPS

Table 1.3 - Summary of publicly available, precipitation estimates that are produced by combining input data from several satellite sensor types. Adapted from the IPWG International Precipitation Working Group (http://www.isac.cnr.it/~ipwg/).

Algorithm	Input data	Space/time grid	Areal coverage/start date	Update frequency	Latency	Producer
CAMS/OPI	CMAP-OPI, gauge	2.5°/monthly	Global/1979	Monthly	5 days	NOAA/NWS CPC
CMAP	OPI, SSM/I, SSMIS, GPI, MSU, gauge, model	2.5°/monthly	Global/1979 - Oct. 2010	Seasonal	3 months	NOAA/NWS CPC
	OPI, SSM/I, GPI, MSU, gauge, model	2.5°/pentad	Global/1979 - Sept. 2009	Seasonal	3 months	NOAA/NWS CPC
	OPI, SSM/I, GPI, gauge	2.5°/pentad-RT	Global/2000	Pentad	1 day	NOAA/NWS CPC

CMORPH V1.0 BIAS-CORRECTED	TMI, AMSR-E, SSMI, SSMIS, AMSU, MHS, IR vectors, CPC Gauge, GPCP Pentad	0.25°/3-hourly	50°N-S/1998	Daily	18 hours	NOAA/CPC
CMORPH V1.0 BLENDED	TMI, AMSR-E, SSMI, SSMIS, AMSU, MHS, IR vectors, daily gauge	0.25°/3-hourly	50°N-S regional/1998	Daily	18 hours	NOAA/CPC
GPCP One-Degree Daily (Version 2.2)	SSMI- & SSMIS-TMPI (IR), TOVS, AIRS, GPCP monthly	1°/daily	Global - 50°N-50°S/Oct. 1997 - now	Monthly	3 months	NASA/GSFC 612
GPCP pentad (Version 1.1)	OPI, SSM/I, GPI, MSU, gauge, GPCP monthly	2.5°/5-day	Global/1979 - 2008	Seasonal	3 months	NOAA/NWS CPC
GPCP Version 2.2 Satellite-Gauge (SG)	GPCP-OPI, gauge 1/79-7/87, 12/87, thereafter SSMI- & SSMIS-AGPI (IR), gauge, TOVS, AIRS	2.5°/monthly	Global/1979 - 2010	Monthly	2 months	NASA/GSFC 612
GPM Imerg	Satellites used in the TMPA, CMORPH and	10 km – 0.5 hours	Global - 60°N-S/Mar 2014	Monthly	3 Months	NASA/GSFC PPS

	PERSIANN-CCS			(final run)	(final run)	
PERSIANN-CDR	GRIDSAT-IRWIN, GPCP Monthly Precipitation	0.25°/daily	60°N-S/1980	Monthly	2 months	UC Irvine
PR-OBS-5	PR-OBS-3, gauge, radar, NWP	5 km/3-hour	Europe/Jan 2009	3 hours	0.5 hours	H SAF
RFE	GPI, NOAA-SSM/I, gauge	10 km/daily	Africa/Oct 2000	Daily	6 hours	NOAA/NWS CPC
		10 km/daily	South Asia/Apr 2001	Daily	6 hours	NOAA/NWS CPC
TRMM Plus Other Data (3B43 Version 7)	TCI, TMI, SSMI, SSMIS, AMSR-E, AMSU, MHS, MW-VAR (IR), gauge	0.25°/monthly	Global - 50°N-S/Jan 1998	Monthly	2 months	NASA/GSFC PPS
TRMM Plus Other Satellites (3B42 Version 7)	TCI, TMI, SSMI, SSMIS, AMSR-E, AMSU, MHS, MW-VAR (IR), gauge	0.25°/3-hourly	Global - 50°N-S/Jan 1998	Monthly	2 months	NASA/GSFC PPS

Table 1.4 - Summary of publicly available precipitation estimates that are produced by combining input data from several sensor types, including satellite sensors and precipitation gauges. Adapted from the IPWG International Precipitation Working Group (http://www.isac.cnr.it/~ipwg/).

1.3 New bottom-up approach

All the sensors and algorithms described above refer to the so-called "top-down" approach (Brocca et al. 2015), in which information obtained by sensing the top of clouds (or within the clouds) are used to estimate rainfall. Another promising and innovative approach consists in using satellite-based soil moisture (SM) observations as an indirect signature of the rainfall dynamic in order to correct and/or to directly estimate precipitation fallen at ground. Various authors have proposed a method to estimate rainfall from in-situ or satellite based SM products (Crow et al., 2007, 2009; Pellarin et al., 2009, 2013; Brocca et al., 2013, 2014; Wanders et al. 2015; Zhan et al. 2015). Among them, the SM2RAIN algorithm developed by Brocca et al. (2014) allows to directly estimate rainfall from SM observations. The algorithm is based on the inversion of the soil water balance equation:

$$\frac{Z^* ds(t)}{dt} = p(t) - e(t) - g(t) - r(t) \tag{1.1}$$

Where Z^* is the soil water capacity (soil depth times soil porosity), $s(t)$ is the soil relative saturation, t is the time and p, e, g and r are the precipitation, evapotranspiration, drainage and surface runoff rates, respectively. The drainage rate is calculated by the relationship proposed by Famiglietti and Wood (1994):

$$g(t) = as(t)^b \tag{1.2}$$

Where a and b are two parameters describing the non-linearity between SM and drainage. By neglecting $r(t)$ and $e(t)$ during a rainfall event (Brocca et al., 2015) and solving ***Eq. 1.1*** for precipitation, one can obtain:

$$p(t) = Z^* \frac{ds(t)}{dt} + as(t)^b \tag{1.3}$$

With Z^*, a and b that have to be estimated through calibration. The algorithm allows to estimate the accumulated rainfall fallen at ground by knowing the difference in SM between to measurements (obtained through satellite sensors, in-situ stations or by models). The algorithm suffers the main limitations to not be able to estimate rainfall when the soil is close to saturation, as no variations of SM can be observed in such conditions after a rainfall event. On the other hand, SM2RAIN has proven to be able to correctly estimate the amount of rainfall fallen at ground, which is of paramount importance for hydrological applications. The algorithm is applied and tested both on a local (Brocca et al., 2013; 2015; 2016a; 2016b, Ciabatta et al., 2015; 2017a, Massari et al., 2014, Tarpanelli et al., 2017) and on a global scale (Brocca et al., 2014, Koster et al., 2017, Ciabatta et al., 2018) to several in-situ and satellite SM datasets. Alongside with the rainfall estimation capabilities, the integration between SM-derived and state-of-the-art rainfall products is tested. The integration allows to obtain a unique, superior rainfall product through very simple nudging schemes. As way of example in Ciabatta et al. (2017a), SM-derived rainfall, obtained through the application of SM2RAIN to the ASCAT SM product (Wagner et al., 2013), is integrated with a product obtained through PMW remotely sensed information. The results showed that the limitations of the two approaches (top-down and bottom-up) are compensated in the integrated product. In this respect,

the integration allows to improve the estimation of accumulated rainfall through SM2RAIN, while the state-of-art satellite rainfall product allows a better estimation of high intensity rainfall during close to saturation conditions.

1.4 Use of satellite rainfall data for landslide risk assessment and hydrological application

Despite the large availability of satellite rainfall data and their increasing spatial/temporal coverage and accuracy, their use for hydrological applications is still very scarse. The reasons for this could rely on: 1) the coarse spatial/temporal resolution of the provided satellite products; 2) the inherent BIAS contained in every estimate; 3) the latency own by the product before been collected by the end-users (Serrat-Capdevilla et al., 2014); 4) a general and unjustified skepticism regarding satellite data in the hydrologist community.

If one makes a research on the literature available on the use of satellite rainfall data for hydrological applications, the result would be that the majority of the studies are carried out at the basin scale for flood simulations, mainly in developing countries. On the other hand, just few studies provided some guidelines in order to use satellite rainfall products for hydrological applications. For instance, Artan et al. (2007) used the NOAA Climate Prediction Center (CPC) product for Famine Early Warning System (FEWS, Xie and Arkin, 1997) to drive a physically-based semi-distributed hydrologic model over four basins in Asia and Africa. They found that satellite rainfall products (SRPs) can be used to force a hydrologic model provided that the recalibration of the model parameter values is carried out. Harris et al. (2007) used TMPA 3B42 real-time product to drive a hydrologic model over a catchment in Kentucky finding that a BIAS correction is needed before using real-time satellite data in flood forecasting. Stisen and Sandholt (2010) forced a distributed hydrologic model over the Senegal River Basin with different SRPs: TMPA 3B42 V6, CPC MORPHing technique (CMORPH, Joyce et al., 2004), CPC FEWS v.2, PERSIANN and a local product based on CCD relationship. They found that the SRPs need a BIAS correction because of the differences in the estimates of the analyzed products (e.g., the number of rainy days and the recorded intensity). Camici et al., 2018 stated that BIAS correction and specific model recalibration are mandatory steps, even if not always sufficient to achieve good performance, mainly in small basins. They also stated that a simple integration between state-of-the-art and SM-derived products allows to obtained results even better than those obtained by using observed data. In this respect, Massari et al. (2014) showed that a simple integration between ground observed data and satellite rainfall provided better performance in terms of flood simulation for 3 out 4 basins with respect to use ground rainfall data only.

With respect to landslide risk assessment, just a handful of studies uses satellite rainfall data. Hong et al. (2006; 2007) set up an experimental monitoring system for rainfall-induced landslides using TMPA 3B42v6 product. The precipitation data were linked to a landslide susceptibility map in order to identify the location and timing of the earth movement and the associated risk. The model was applied to 74 landslide events during the period 1998-2006 with satisfactorily results. Although satellite rainfall data have their own limitations, the authors stated that “this may form a starting point for developing an operational early warning system for rainfall-induced landslides around the globe”.

Ray and Jacobs (2007), Ray et al., (2010) and Liao et al., (2010; 2012) used TMPA rainfall

estimates to force a land-surface model in order to assess the stability conditions over 4 areas throughout the globe. They stated that satellite rainfall data can be a valuable source of information and a valid input for such applications. More in details, Liao et al., (2010; 2012) developed an experimental early warning system based on several satellite information. The model framework is reported in ***Figure 1.6***.

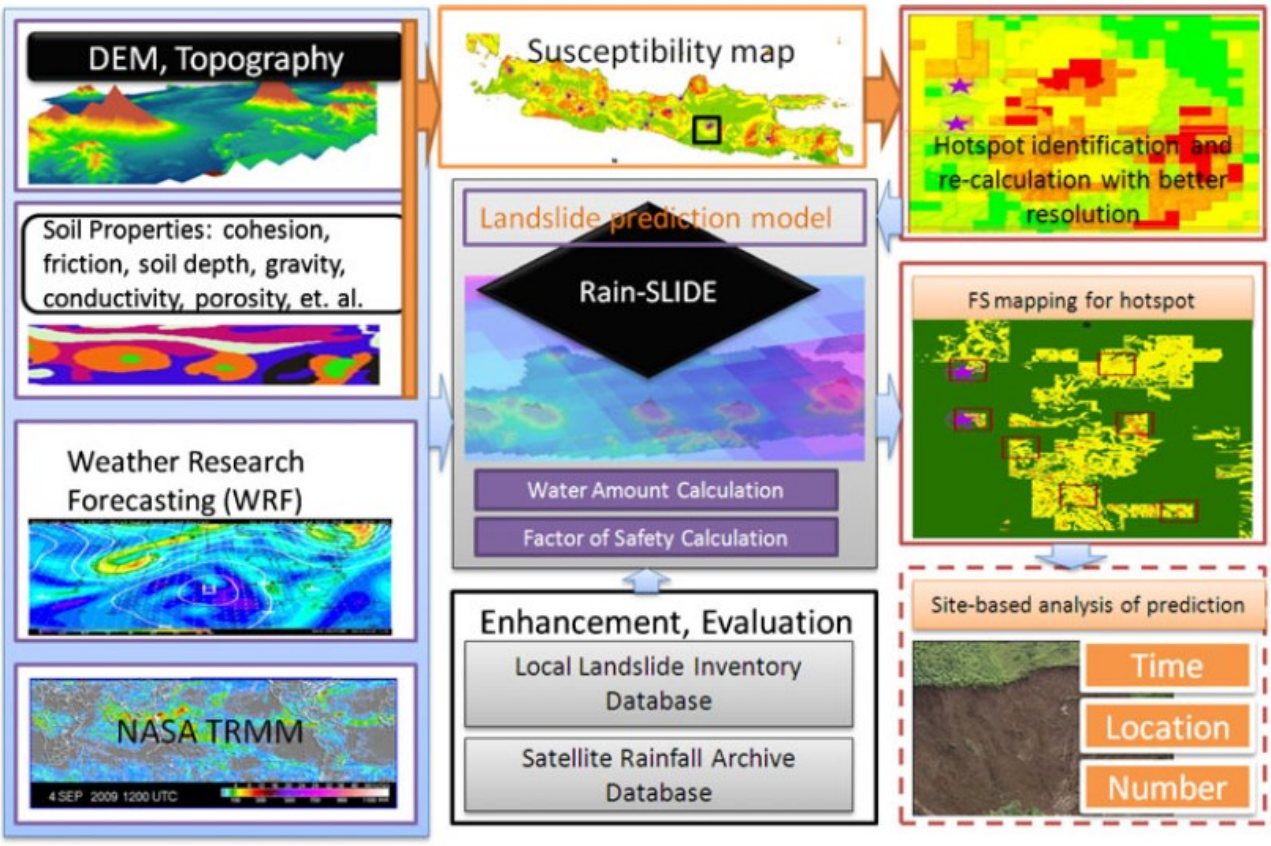

Figure 1.6 – Experimental early warning system for rainfall-induced landslides set up in Indonesia (Courtesy of Liao et al., 2010).

As it can be seen in ***Figure 1.6***, satellite rainfall estimates are used to force the Rain-SLIDE model. The model's outputs are then linked to susceptibility maps in order to predict landslide events at the site scale. The authors drawn the conclusions that despite the limitations of each early warning system and the satellite rainfall estimates, the proposed framework was able to identify real events occurred in the study area, enabling researchers to develop operational early warning systems at the regional scale. Posner and Georgakakos (2015) instead defined a rainfall-soil moisture threshold for El Salvador by forcing a hydrologic model with the Global Hydro-Estimator (GHE, Scofield and Kuligowsky, 2003). The satellite data are used to simulate the soil moisture conditions associated with occurred landslide events, underlining the beneficial effect of coupling hydrologic modelling to landslide early warning systems.

A different approach was used by Farahmand and AghaKouchak (2013), who used PERSIANN rainfall estimates and 581 landslide events (Kirschbaum et al., 2010) to train a Support Vector Machine (SVM). The SVM is used to classify, through a binary classifier, between landslide events (value of 1) and non-landslides events (value of 0), by considering rainfall, slope, land cover and land use and observed landslide events. The model provided very good results, with just 2% of false

alarms and 7% of missed events, but needed to be calibrated and trained with specific data.

Up to now, one of the only operational satellite-based early warning system is represented by the global Landslide Hazard Assessment for Situational Awareness (LHASA, Kirschbaum et al., 2011; 2015; 2016; Stanley and Kirschbaum, 2017; Kirschbaum and Stanley, 2018; https://pmm.nasa.gov/applications/global-landslide-model). The framework of the model is reported in ***Figure 1.7***. The model is based on TMPA (and now GPM) rainfall real-time estimates. The model computes the Antecedent Rainfall Index based on the following equation:

$$ARI = \frac{\sum_{t=1}^{n} w_t p_t}{\sum_{t=1}^{n} w_t} \tag{1.4}$$

where t is the number of days before the running date, n is the length of the time window use for the ARI estimation, p_t is the rainfall amount at day t and w_t is defined by $w_t=t^{-\alpha}$. In Stanley and Kirschbaum (2017) n was set to 7 and α to 0.5 after calibration. One of the most important component of this model is a susceptibility map. The map was created starting from combining information from elevation, geology, roads and infrastructures and forest cover. The map considers 5 different levels of susceptibility (very low, low, moderate, high and very high). If the 7-day precipitation is unusually high, the susceptibility map is used to discriminate if the landslide risk of the analyzed pixel is low, moderate or high.

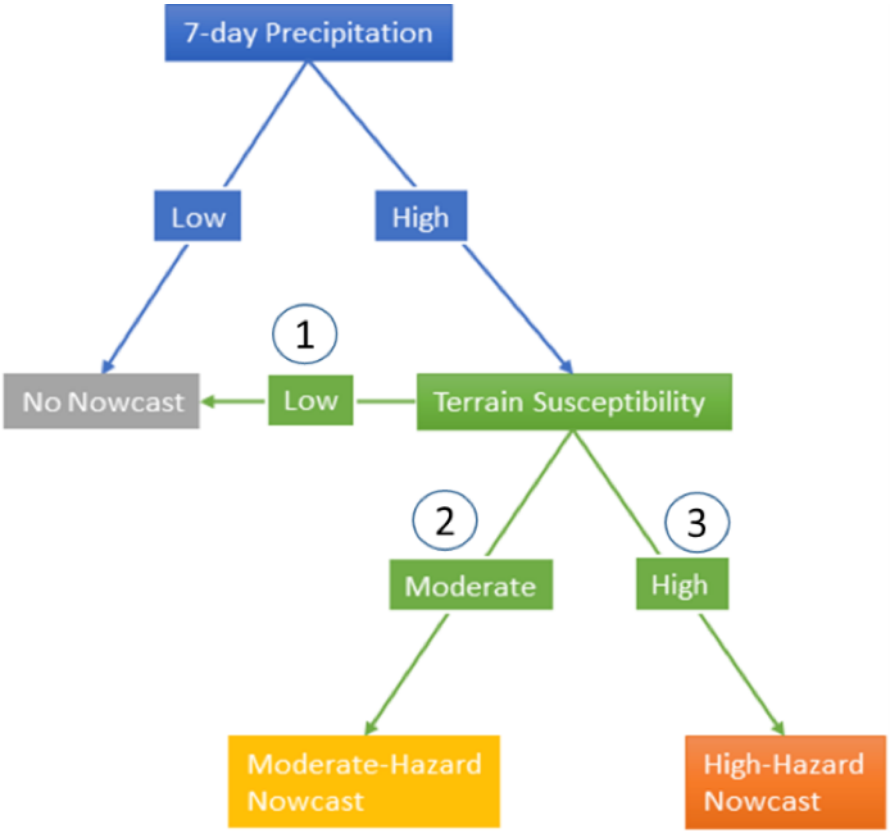

Figure 1.7 – Global Landslide Hazard Assessment for Situational Awareness (LHASA) model framework. (https://pmm.nasa.gov/applications/global-landslide-mode)

Very recently, Rossi et al., (2017) defined rainfall thresholds over Umbria region by using observed and satellite rainfall data obtained through TMPA products. The authors stated that the general underestimation of precipitation provided by the remotely sensed estimates is reflected in lower rainfall thresholds with respect to the ones obtained by considering rain gauge data. One the most recent application of satellite rainfall data to landslide risk assessment is the one proposed by Brunetti et al. (2018). In this work, the authors evaluated the capabilities of TMPA 3B42RT, CMORPH, PERSIANN real-time data and SM-derived rainfall estimates in terms of predicting the spatial-temporal occurrence of landslide events over the Italian territory during the period 2008-2014. Specifically, for all the analyzed products, an empirical cumulated rainfall – rainfall duration (ED) threshold is estimated by analyzing more than 1400 landslide events. The ED thresholds were then used to estimate several skill scores for the assessment of the products. The results showed that satellite-based rainfall estimates generally underestimated precipitation amount with respect to the ground-based dataset used for comparison. However, this aspect is not an issue for the development of an early warning system, as it could reflect in a lower ED threshold.

On this basis, it could be stated that satellite rainfall products are able to be used for such applications, taking advantages of the short latency of the real-time products. More details about this application can be found in Appendix 1.

1.5 Purposes of the thesis

Worldwide, rainfall-induced landslides occur every year causing fatalities, considerable damage and relevant economic losses with approximately 300 million people are estimated to be exposed to landslides (Dilley et al., 2005). Italy is one of the countries most prone to landslide risk (Guzzetti et al., 2005) and where the population is heavily affected, with about 20 % of the national territory characterized by hydrogeological risk (ISPRA, 2015). In the 50-year period 1964–2013, 1354 people died due to landslides (Salvati et al., 2014), while in the period 2010-2014, 566 landslides events caused 55 fatalities. Moreover, climate changing is expected to exacerbate the impact of landslides, mostly due to the increase in heavy rainfall (Fischer and Knutti, 2015; Ciabatta et al., 2016; Gariano and Guzzetti, 2016). In order to mitigate landslide risk, early warning systems for the prediction of rainfall-induced failures were developed in several countries based on different approaches and input datasets (Keefer et al., 1987; Baum and Godt, 2010; Ponziani et al., 2012; Rossi et al., 2012; Lagomarsino et al., 2013; Kirschbaum et al., 2015; Segoni et al., 2015; Piciullo et al., 2016, Stanley and Kirschbaum, 2017). Basically, the proposed early warning systems cited above use two main approaches: 1) definition of specific rainfall duration-intensity thresholds; 2) development of a physically-based model specifically designed for the study area. While the first approach has the main advantage to be easily implemented and used operationally, it requires high quality rainfall data. Another limiting issue is the problem to extend the threshold over larger areas, due to the high spatial variability of predisposing factors related to the triggering of landslides (mainly topography and geotechnical parameters). On the other hand, physically-based models have the advantages to fully describe the characteristics of the investigated slope, but they required a deep knowledge of the site with respect to the parameters needed to run the model itself. Also in this case, this approach is not applicable on large scale. The purposes of the present work are the develop and test a physically-based model for the assessment of the landslide hazard by using also satellite data as input, in order to reduce the computational demand of this approach. The present

work is a collection of papers published in peer-reviewed journal, showing the results and the insights found during the research period by the Author.

At first, a thorough validation of state-of-the-art satellite rainfall and SM products was carried out over Italy. The rainfall data obtained by classical satellite products as well as the SM-derived precipitation obtained through the application of SM2RAIN to SM products, are compared to high quality information obtained by ground network (Ciabatta et al., 2015; 2017; 2018) (Chapter 2).

Moreover, the capabilities of such products as input in rainfall-runoff models is tested over several basins in Italy and Europe (Ciabatta et al., 2016a). Along with the performance of the single products, the integration between top-down and bottom-up rainfall products is deeply tested, showing higher skills than the parent products alone (Chapter 3).

The developed stability model structure is discussed in Chapter 4. There, a detailed description of the components of the model and of the equations used for assess the slope stability over the study area are reported, along with the use of satellite rainfall data as input for the stability module, over a small study area in Italy.

Chapter 5 presents the main conclusions of the present work and an outline for future research and applications.

Appendix 1 collects all the supplementary material produced during this research. More in details, the evaluation of SM2RAIN-derived and state-of-the-art satellite rainfall products over larger areas (Brocca et al., 2016b and Tarpanelli et al., 2017) are reported along with the application of SM2RAIN to a sensor not used to retrieve SM (Brocca et al., 2016a). The findings of Camici et al. (2018) about hydrological modelling over the Mediterranean area carried out by considering several satellite rainfall products are described, underlining the feasibility and the beneficial effect of integrating SM2RAIN-derived rainfall with classical precipitation products. The last part of this section reports the results obtained by Brunetti et al. (2018) about the use of satellite rainfall data in order to define empirical ED thresholds over Italy.

2.ASSESSMENT AND VALIDATION OF SATELLITE RAINFALL PRODUCTS

In this Chapter, the assessment of satellite rainfall products carried out over Italy, India, Australia and on a global scale, is described. More in details, the study areas, the products, the modelling chains used for such analysis will be explained. The first study area is the Italian territory, for which the results of validation of several rainfall products (obtained through top-down and bottom-up approaches) was carried out against high quality observed rain gauge data. The integration between rainfall products will be also described. After the description of the results obtained over Italy, the results obtained on a global scale will be presented.

2.1 Methodology development and testing over Italy

This section will present the results of the comparison and integration of satellite rainfall products over Italy. The assessment allowed to characterize satellite rainfall products performances over the complex territory of Italy both in time and in space. The section is based on the following two publications:

Ciabatta, L., Brocca, L., Massari, C., Moramarco, T., Puca, S., Rinollo, A., Gabellani, S., Wagner, W. (2015). Integration of satellite soil moisture and rainfall observations over the Italian territory. Journal of Hydrometeorology, 16(3), 1341-1355.

Ciabatta, L., Marra, A.C., Panegrossi, G., Casella, D., Sanò, P., Dietrich, S., Massari, C., Brocca, L. (2017). Daily precipitation estimation through different microwave sensors: verification study over Italy. Journal of Hydrology, 545, 436-450.

Study area

The study area is the Italian territory, spreading between 47° N and 36° S of latitude and between 6° E and 18° E of longitude (Pantelleria and Lampedusa islands are not taken into account as too small to be recognize within a satellite field of view). The territory is characterized by the Alps mountain range (along the West-East direction) in the Norther part of the country, and by the Apennines mountain range from North to South. ***Figure 2.1*** shows the elevation map of Italy.

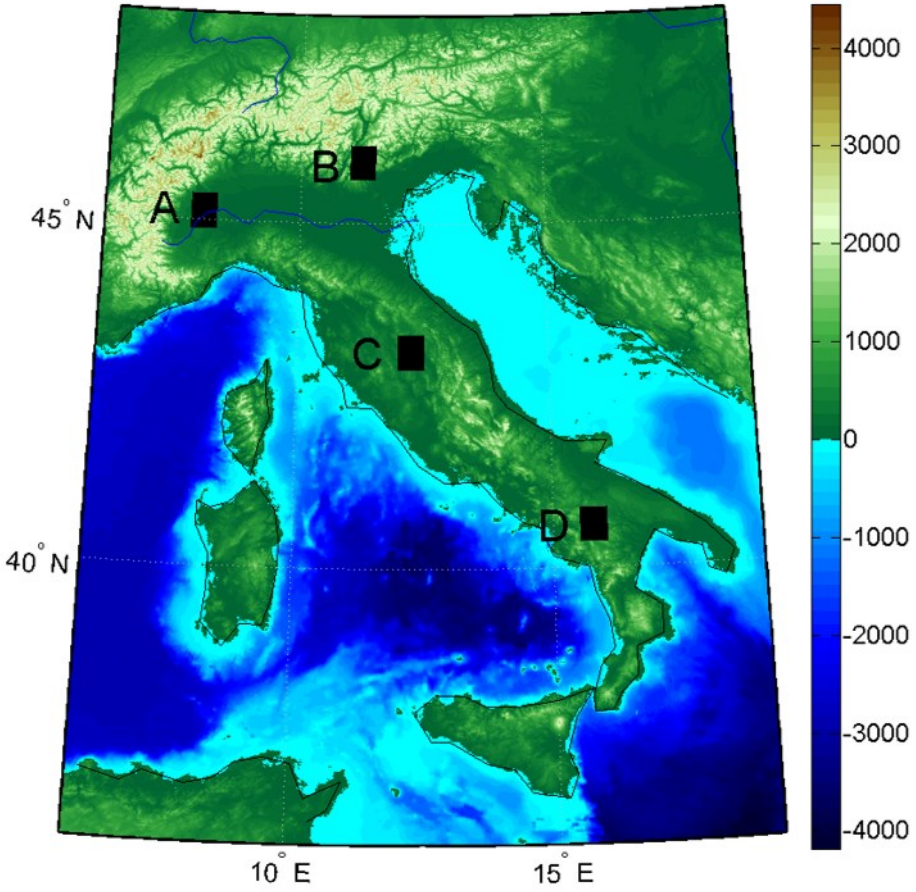

Figure 2.1 – Morphology of the study area. The letters indicate the boxes (highlighted in black) where the analysis of 5-day accumulated rainfall timeseries is carried out (Ciabatta et al., 2017).

The territory is mainly hilly expect for the Po river valley in the northern part of the country. The presence of the two mountain ranges strongly influences the rainfall pattern and impacts the satellite retrievals due to orographic effects. As it can be seen in ***Figure 2.2***, showing the cumulated rainfall over Italy for the period 2010-2013, two sectors are characterized by intense rainfall regimes. This is due to the effect of Alps and Apennines to block the hydrometeors causing intense precipitation in that areas.

The impact of topography can be observed also in the satellite retrievals over the study area. ***Figure 2.3*** draws the mean monthly noise associated to ASCAT SM retrievals over Italy.

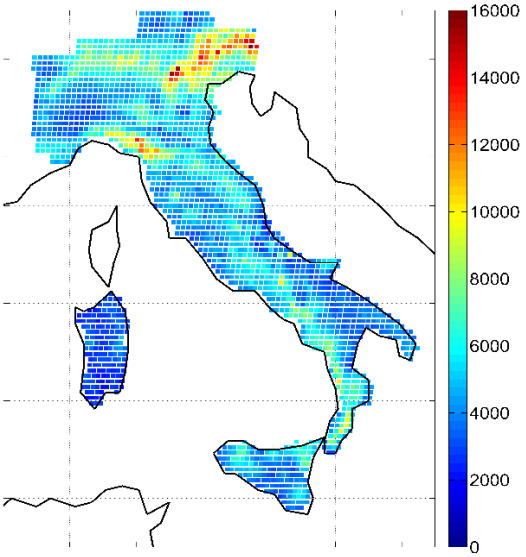

Figure 2.2 – Cumulated observed rainfall for the period 2010-2013 over Italy. The data are obtained through the high quality ground network of the Italian Civil Protection Department (Modified from Ciabatta et al., 2015).

As it can be seen, high error values (blueish and reddish areas) are associated with high topographic complexity (the Alps and part of the Apennines). The error maps are provided by the Vienna University of Technology (TUWIEN) through the ASCAT Soil Moisture Data Viewer (http://rs.geo.tuwien.ac.at/dv/ascat/). In those areas, the satellite retrievals could be challenging and the obtained estimates should be used carefully.

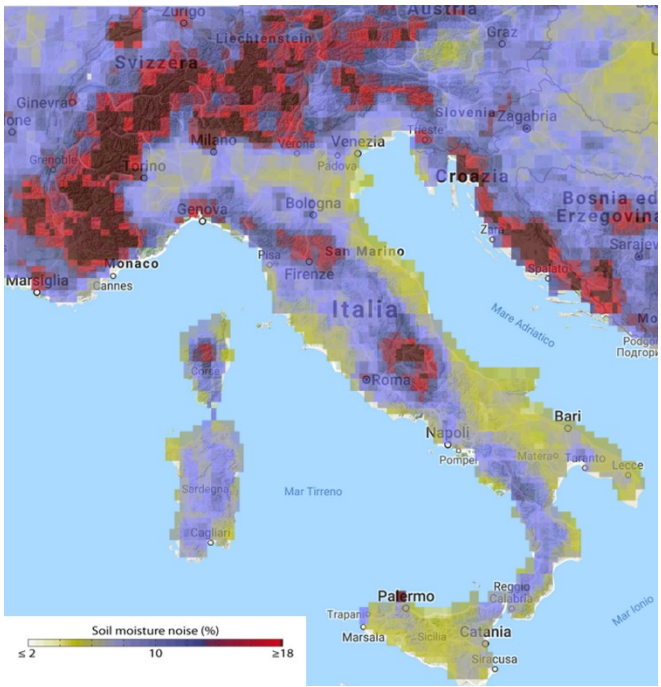

Figure 2.3 – Noise map over Italy obtained through the ASCAT SM product (http://rs.geo.tuwien.ac.at/dv/ascat/).

Datasets

Ground-based rainfall dataset

A ground-based rainfall dataset is used as a benchmark. The observed rainfall dataset is obtained by the measurements of more than 3000 rain gauges over the Italian territory spatially interpolated using the Random Generator of Space Interpolations from Uncertain Observations (GRISO; Pignone et al. 2010) algorithm. GRISO is a derivation of the most known kriging method, so it is also based on the geostatistical approach and the use of the semivariogram for generating the spatial structure of the interpolated field. The main innovations are the possibility of using different semivariograms per gauge at the same time and of reducing the computational time with respect to kriging. The spatial distribution of the rain gauges is drawn in ***Figure 2.4***.

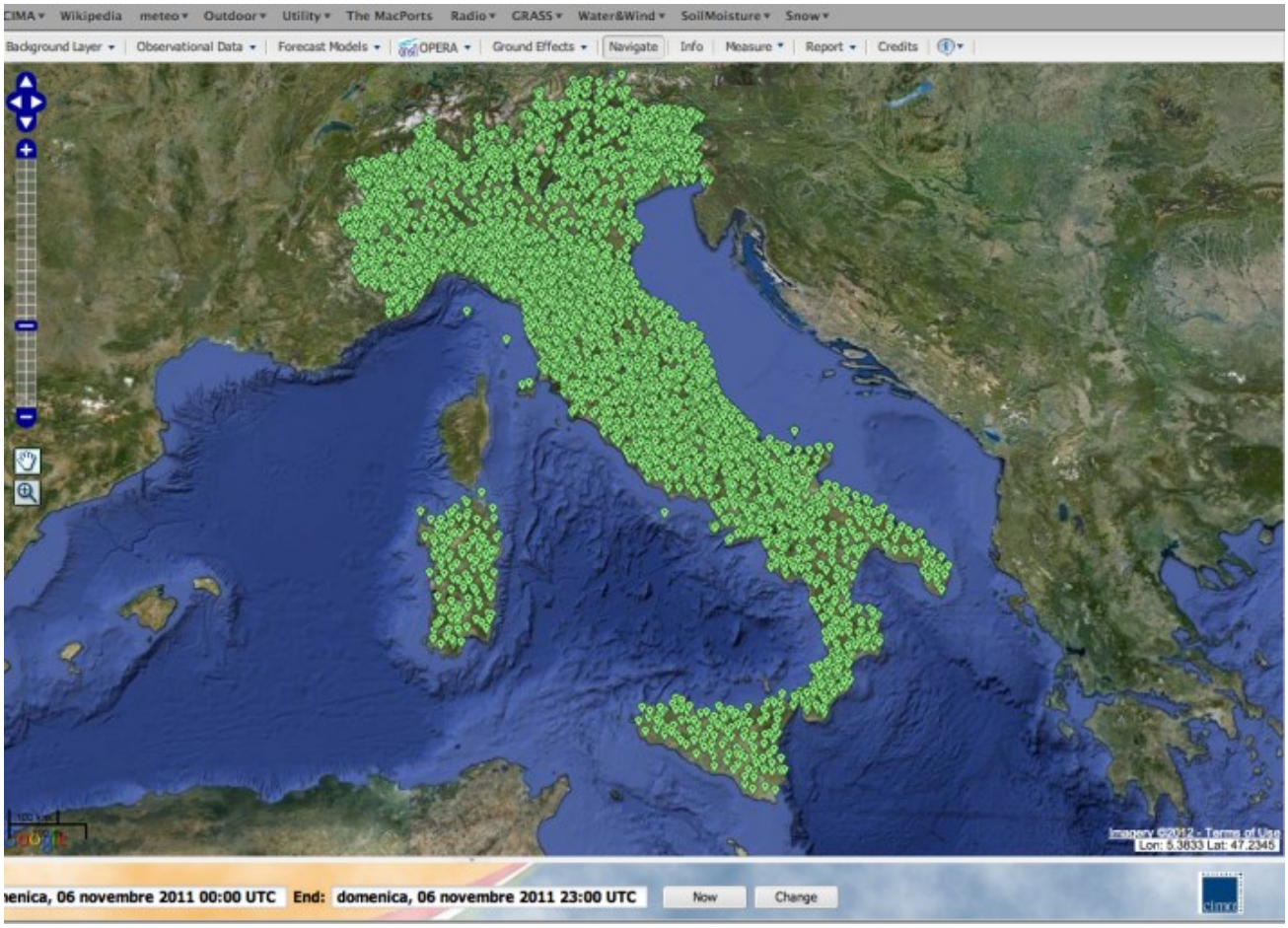

Figure 2.4 – Spatial distribution of the rain gauges used for obtaining the ground-based benchmark (courtesy of CIMA).

This dataset provides hourly rainfall observations throughout the Italian territory over a grid defined within GRISO. In this work, grids with spacing of 12.5 km (Ciabatta et al. 2015) and 25 km (Ciabatta et al., 2017) are used. The daily observed product is obtained by summing the hourly data from 0000 to 2400 UTC + 1 h. A ground-based benchmark is used benchmark because, besides the fact they are used worldwide, they are used operationally by Italian Civil Protection Service for hazard forecast and management; therefore, the satellite rainfall dataset performances are evaluated in such kinds of applications.

Satellite rainfall products

In this section, a brief introduction to the satellite rainfall products will be provided. The readers are referred to Chapter 1 for the acronyms, sensors and retrieval algorithms. The H05 product is provided by EUMETSAT within the Satellite Application Facility on support to operational hydrology and water management (H-SAF) project. The product is based on frequent precipitation measurements as retrieved by blending LEO MW-derived precipitation rate measurements and GEO IR imagery. As stated before, the LEO PMW rainfall estimates are obtained through cross-track and conical scanners, characterized by lower spatial/temporal resolution but higher accuracy. The IR data are obtained by GEO satellites, like the MSG. This kind of sensors provides frequent measurements over the covered area, with high spatial resolution. This product provides daily rainfall data with a spatial resolution of about 5 km over the full-disk area (http://hsaf.meteoam.it/overview.php). In this study, the period 2010-2013 is considered. The TMPA 3B42-RT, version 7 (http://trmm.gsfc.nasa.gov), combines rainfall estimates from various satellite sensors. The multisatellite platform uses the TRMM Microwave Imager (TMI), the Special Sensor Microwave Imager (SSM/I) on board the Defense Meteorological Satellite Program (DMSP) satellites, AMSR-E, and the Advanced Microwave Sounding Unit-B (AMSU-B) on board the National Oceanic and Atmospheric Administration (NOAA) satellite series. In addition, the TMPA product also uses GEO IR data through a constellation of GEO satellites. The 3B42-RT product is provided by the National Aeronautics and Space Administration (NASA) with a temporal resolution of 3 h and a spatial resolution of 0.25° for the 50° north–south latitude band. The cumulated daily rainfall is obtained by simply summing the eight 3-h time windows every day. It should be noted that TMPA data are provided within a time window of 90 min from the nominal time (0000, 0300, . . . , 2100 UTC) while the observed rainfall dataset is delivered in local time, that is, UTC + 1. Therefore, the daily cumulated rainfall product from TMPA represents the total rainfall starting, and ending the next day, at 2330 UTC, with only 30 min of delay with respect to the other products. Such a delay can be considered negligible, especially when taking into account longer accumulation intervals. All the products described above are used along with the SM-derived rainfall, described in the following, for assess their quality over the Italian territory by considering a grid with 12.5 km of spacing and 5 days of accumulated rainfall during the period 2010-2013.

In Ciabatta et al. (2017), three different satellite rainfall products are used. One is the Cloud Dynamics and Radiation Database algorithm (hereinafter CDRD, Casella et al., 2013, Mugnai et al., 2013a, b, Sanò et al., 2013), a physically-based Bayesian approach for the conically scanning radiometers originally developed for SSMIS (on board the three DMSP F16, F17 and F18 satellites in the time frame of this study). The second one is the Passive microwave Neural network Precipitation Retrieval algorithm (hereinafter PNPR) for cross-track scanning radiometers (Mugnai et al., 2013a, b, Sanò et al., 2015a), originally developed for the cross-track scanning AMSU/MHS radiometers (on board the MetOp-A, MetOp-B, NOAA-18, and NOAA-19 satellites in the time frame of this study). Both CDRD for SSMIS and PNPR for AMSU-A/MHS are used operationally within the EUMETSAT H-SAF program and provided as H01 and H02 instantaneous precipitation rate products (Mugnai et al., 2013a). The algorithms, originally optimized for the European and Mediterranean regions, are recently extended to other regions (i.e., Africa and Southern Atlantic) to provide precipitation products for the full MSG disk area (Panegrossi et al., 2014). Towards the full exploitation of the GPM constellation of MW radiometers, a new version of CDRD for AMSR-2, and PNPR for ATMS are recently released within H-SAF (Sanò et al., 2015b, 2016). The third one

is a combination of all SSMIS and AMSU-A/MHS observations, hereinafter CDRD-PNPR. These last three datasets are characterized by a spatial resolution of 0.25° and a daily temporal resolution. The performance of these products are evaluated during the period 2011-2014.

Soil moisture-derived rainfall

The SM data are obtained by backscattering retrievals from the ASCAT sensor (C-band scatterometer operating at 5.4GHz) on board the MetOp-A and B satellites. In this study the Water Retrieval Package (WARP), version 5.51, is used for estimating SM from backscatter measurements. The product has a nearly daily temporal resolution for the study area and a spatial resolution of about 25 km (resampled to 12.5 km; Wagner et al. 2013; http://rs.geo.tuwien.ac.at/products/), provided as soil moisture product H109 by the EUMETSAT H-SAF. In order to reduce the effect of noise in the estimated precipitation, an exponential filter was first applied to SM retrievals. The exponential filter (Albergel et al., 2008) requires a single parameter, the characteristic time length (T), to be calibrated. In the original formulation, the exponential filter allows to estimate the root-zone soil moisture conditions of a deeper layer starting from surface observations. The T- value takes into account all the factors affecting the temporal variability of soil moisture, e.g. hydraulic properties, evaporation, and soil layer thickness. The use of such a filter on one hand increases the considered soil layer thickness, thus affecting Z^* parameter, while, on the other hand, reduces the noises contained in the surface soil moisture time series. Because of the variable temporal resolution of the SM product, all the SM data are interpolated in time at 0000 UTC + 1 h each day. This step allows to compare all the datasets considered in the study in a consistent manner, that is, the daily cumulated rainfall from 0000 to 2400 UTC +1 h is obtained for each product. SM-derived rainfall (hereinafter SM2RASC) is estimated at 12.5 km (Ciabatta et al., 2015) and 25 km (Ciabatta et al., 2017) of spatial resolution.

The calibration of SM2RAIN parameters for both studies are carried out during the period 2010-2011. ***Figure 2.5*** draws the spatial distribution of the SM2RAIN parameters obtained in the Ciabatta et al. (2015). As it can be noticed, Z^* parameter shows the highest values in those areas characterized by an intense rainfall regime, as shown in ***Figure 2.5***. The a parameter shows the higher variability throughout the Italian territory, with the highest values along the coastline. This ‘‘coast effect’’ could be due to satellite issues at the water-land interface. The b parameter shows the highest values in northern Italy, mainly over the Alps. The variation patterns of these two parameters are in good agreement with the noise map drawn in ***Figure 2.3***, that is, the higher the uncertainty on SM retrieval, the higher parameter values needed to produce rainfall that contrasts the satellite noise. Similar patterns can be observed for the SM2RAIN parameters calibration carried out in Ciabatta et al. (2017a). Z^* shows higher values due to the introduction of the exponential filter applied to the ASCAT SM data before applying SM2RAIN. This prepocessing step related the SM time series to a deeper soil layer, resulting in higher Z^* values than the ones obtained in Ciabatta et al. (2015).

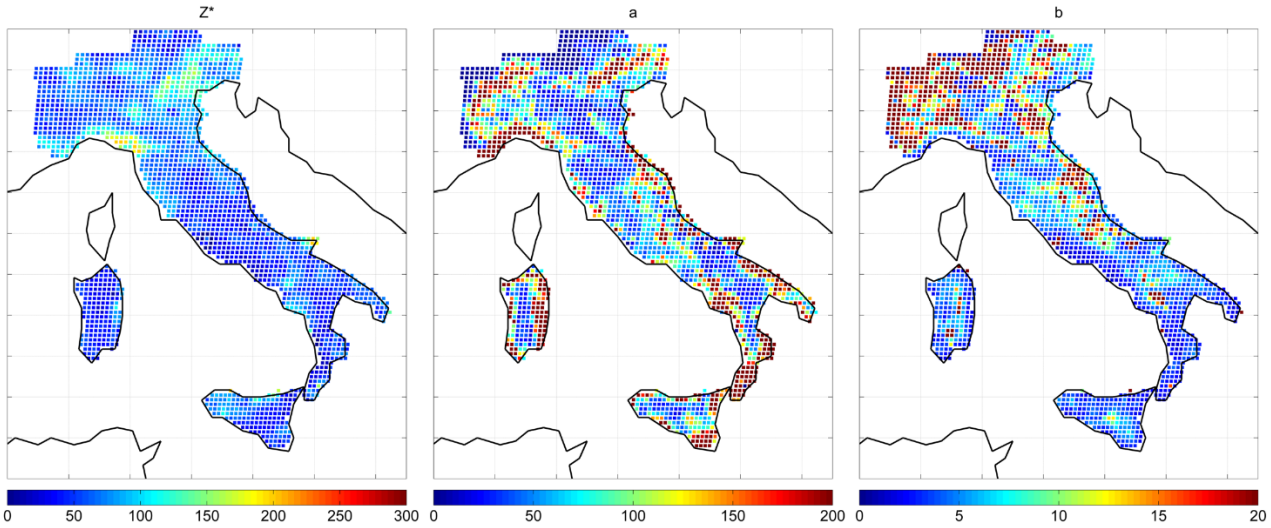

Figure 2.5 – Spatial distribution of SM2RAIN parameters (left) Z, (middle) a, and (right) b, obtained in Ciabatta et al. (2015).*

Integrated rainfall datasets

Along with state-of-the-art satellite rainfall products and SM-derived precipitation, the integration of the top-down and bottom-up approaches is evaluated. To this end, the following nudging scheme is used:

$$P_{\text{int}} = P_{bu} + w(P_{td} - P_{bu}) \tag{2.1}$$

Where P_{int} is the integrated rainfall product, P_{bu} is the SM-derived rainfall, P_{td} is the rainfall obtained through top-down approach and w is the integration weight, ranging from 0 and 1. The integration weight is estimated by minimizing the RMSE between observed and integrated rainfall considering 5 days of accumulated rainfall in Ciabatta et al. (2015) while the equation proposed by Kim et al. (2015) is used in Ciabatta et al. (2017a):

$$w = \frac{\rho_{bu-R} - \rho_{bu-td}\rho_{td-R}}{\rho_{td-R} - \rho_{bu-td}\rho_{bu-R} + \rho_{bu-R} - \rho_{bu-td}\rho_{td-R}} \tag{2.2}$$

where ρ_{P1P2} is the correlation between datasets P1 and P2 that can be the bottom-up (bu), top-down (td) and reference (R) rainfall products. The integration weights are estimated on a monthly scale in the calibration period and then applied to CDRD-PNPR and SM2RASC during the validation period in order to obtain the integrated product CDRD-PNPR + SM2RASC. ***Figure 2.6*** shows the estimated integration weights over the Italian territory during the calibration period.

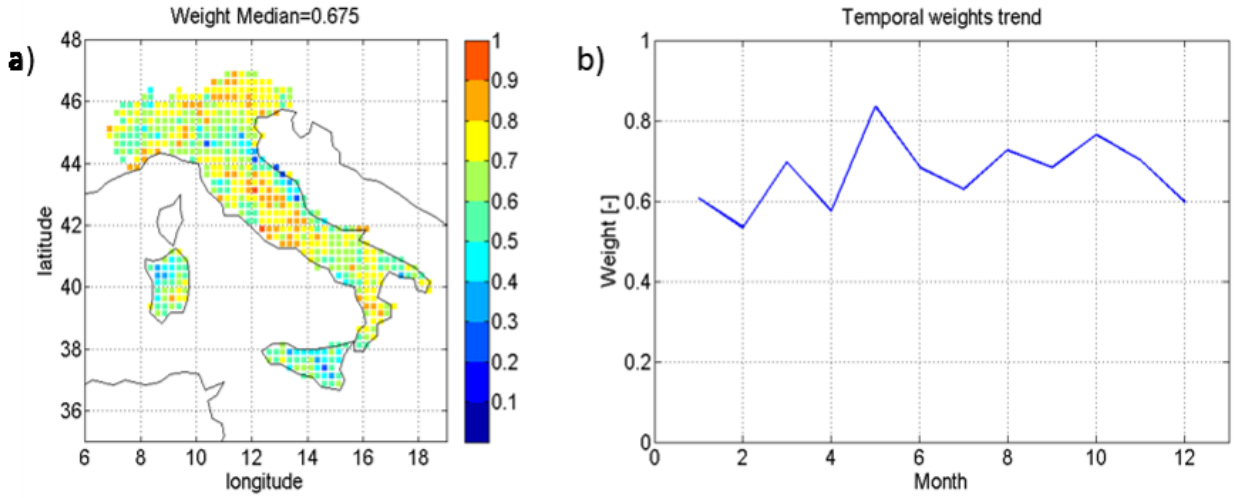

Figure 2.6 - Spatial (a) and temporal (b) variability of the integration weights between CDRD-PNPR and SM2RASC during the 1st January–31st December 2011 period obtained in Ciabatta et al. (2017).

After the calibration of the integration weights, a median value of 0.675 was obtained. This means that, on average, more weight is given to the CDRD-PNPR product. The limited calibration period (one year) could impact the representation of the relative error between the parent products. Therefore, the calibration of integration weights between top-down and bottom-up products should be performed on a longer period and more often. As it can be seen in ***Figure 2.6***, the lowest values (higher weight to SM2RASC) are located mainly over Sardinia and Sicily islands, central Italy along the coast of the Adriatic Sea, Po Valley and Apulia region. The temporal pattern of spatially averaged weights (***Figure 2.6b***) shows an increase of w values during the period from May to October, while during the winter season (from November to April) lower weights are obtained. However, the limited period used to compute the monthly weights might affect the reliability of their temporal variability. This is in good agreement with the results obtained by Ebert et al. (2007) showing that satellite rainfall products seem to work better during the summer season.

After the SM2RAIN algorithm and integration weights calibration, the two studies analysed a total of 9 satellite rainfall products over the Italian territory. ***Table 2.1*** summarises the main features of the analysed products.

Dataset	Spatial Resolution	Temporal Resolution	Period
OBS	12.5/25 km	Daily	2010-2013/2011-2014
H05	5 km	Daily	2010-2013
3B42-RT	0.25°	3-hourly	2010/2013

CDRD	0.25°	3-hourly	2011-2014
PNPR	0.25°	3-hourly	2011-2014
CDRD-PNPR	0.25°	3-hourly	2011-2014
SM2RASC	12.5/25 km	Daily	2010-2013/2011-2014
H05+SM2RASC	12.5 km	Daily	2010-2013
3B42RT+SM2RASC	12.5km	Daily	2010-2013
CDRD-PNPR+SM2RASC	0.25°	Daily	2011-2014

Table 2.1 – Main features of the analyzed satellite rainfall products

Assessment strategy

The assessment of the analysed rainfall products is carried out over the Italian territory on a pixel-by-pixel basis by considering two different rainfall accumulation intervals, daily and 5-days. The quality is evaluated by using several performance indexes, both statistical and categorical. The Pearson's correlation coefficient (R) and, Root Mean Square Error (RMSE) and BIAS are calculated over the study area to assess the agreement between ground-based and satellite-based rainfall dataset. Three different categorical scores are used to test the skills of each product in correctly identify a rainfall event. More in details, the Probability of detection (POD), the False Alarm Ratio (FAR) and the Treat Score (TS) are calculated for different rainfall classes. This allowed also to assess the quality of the satellite rainfall products as a function of rainfall intensities.

The categorical scores are defined as follow:

$$POD = \frac{H}{H + M} \tag{2.3}$$

$$FAR = \frac{F}{F + H} \tag{2.4}$$

$$TS = \frac{H}{H + F + M} \tag{2.5}$$

Where H represents the number of rainfall events successfully estimated (hits), M is the number of the missed events, and F is the number of no-rain events erroneously predicted as events (false alarms). For each given rainfall class, a rainfall event is scored as hit, miss, or false depending on

how the observed and estimated rainfall behave with respect to that threshold: hit if they both reach it, miss if only the observed rainfall reaches it, false if only the estimated rainfall reaches it. All the categorical scores range between 0 and 1, with 1 as perfect score for POD and TS, while FAR has a perfect score of 0. Two different approaches are used in the two studies; in Ciabatta et al. (2015) categorical scores are estimated for each percentile of the distribution of the OBS dataset, while in Ciabatta et al. (2017) they are estimated for 1, 2, 4, 8, 16 and 32 mm/day.

The same assessment strategy is applied to large scale validation study carried out over Australia (Brocca et al., 2016a), over India and Italy (Tarpanelli et al., 2017) and on a global scale (Ciabatta et al., 2018).

Results

Impact of satellite overpasses on top-down products performance

In this section, the impact of the number of satellite overpasses available throughout the day on the daily rainfall estimates derived from the top-down products is analysed. For each day and for each grid point, the satellite daily rainfall is associated to the number of 3-hour intervals (i.e., 00:00 – 03:00 UTC, 03:00 438 – 06:00 UTC, …, 21:00 – 24:00 UTC, hereafter "time slots") covered by at least one satellite overpass. The number, ranging from 1 to 8, is used to split the satellite datasets in 8 classes (as a function of the number of time slots covered with overpasses used to compute the daily rainfall estimate). The correlation coefficient R between the three top-down daily rainfall products CDRD, PNPR and CDRD-PNPR and the observed dataset is computed as a function of the class number (corresponding to the number of covered time slots). Only classes with sample size greater than 200 are used in this analysis. The results are shown in ***Figure 2.7***. As it can be seen, an increase in the number of time slots with at least one overpass provides an increase in R for each analysed product. CDRD daily rainfall is derived from a lower number of satellite overpasses, (mainly 3 and 4 time slots are covered), while PNPR daily rainfall is associated to more frequent overpasses (4 to 6 time slots are covered). The integration of the CDRD and PNPR rainfall rate estimates in the CDRD-PNPR daily rainfall product allows to have better temporal sampling of the precipitation throughout the day, with most of the satellite overpasses covering 6 to 7 time slots. This analysis clearly shows how the MW daily rainfall estimates based on top-down approaches are impacted not only by the number of overpasses available, but also by their temporal distribution throughout the day. The integration of multiple sensors provides a more reliable daily rainfall product. For instance, the median R increases from values lower than 0.5 when 3 (or less) time slots are covered, to values greater than 0.6 for 6 (or more) time slots covered.

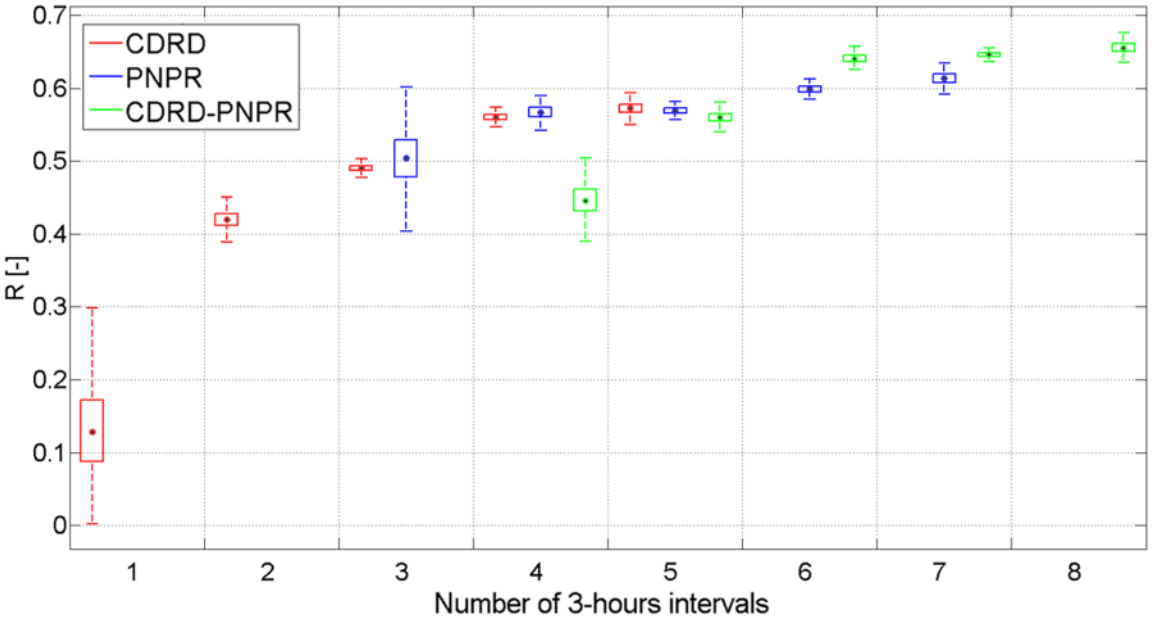

Figure 2.7 - Boxplots of the correlation coefficient (R) between CDRD, PNPR and CDRD-PNPR and the observed rainfall dataset as a function of the number of 3-hour intervals with at least one satellite overpass during the validation period (2012-2014). Specifically, the black dots indicate the median values, the boxes the 25th and 75th 1008 percentiles while the whiskers the minimum and maximum values. (Modified from Ciabatta et al., 2017).

Assessment during the calibration period

The assessment of the satellite-based rainfall products over the Italian territory provided good results. In this respect, all the analysed products showed good capabilities in estimating rainfall during the period 2010-2013 and 2011-2014. ***Figure 2.8*** shows the results obtained in Ciabatta et al. (2015) during the calibration period (2010-2011) for the five rainfall products (two top-down, one bottom-up and two integrated) in terms of R and RMSE for 1- and 5-day of accumulated rainfall.

The lower performance scores obtained for 1 day of accumulated rainfall depend on several factors: 1) at a daily time step, the noise of ASCAT soil moisture data has a strong impact on the estimated rainfall through SM2RAIN algorithm; 2) the ASCAT soil moisture data are not always available for every day; and 3) the SM2RAIN algorithm is found to perform satisfactorily when applied with a time resolution 3–4 times longer than the resolution of soil moisture data, even when applied with in situ observations (Brocca et al., 2013).

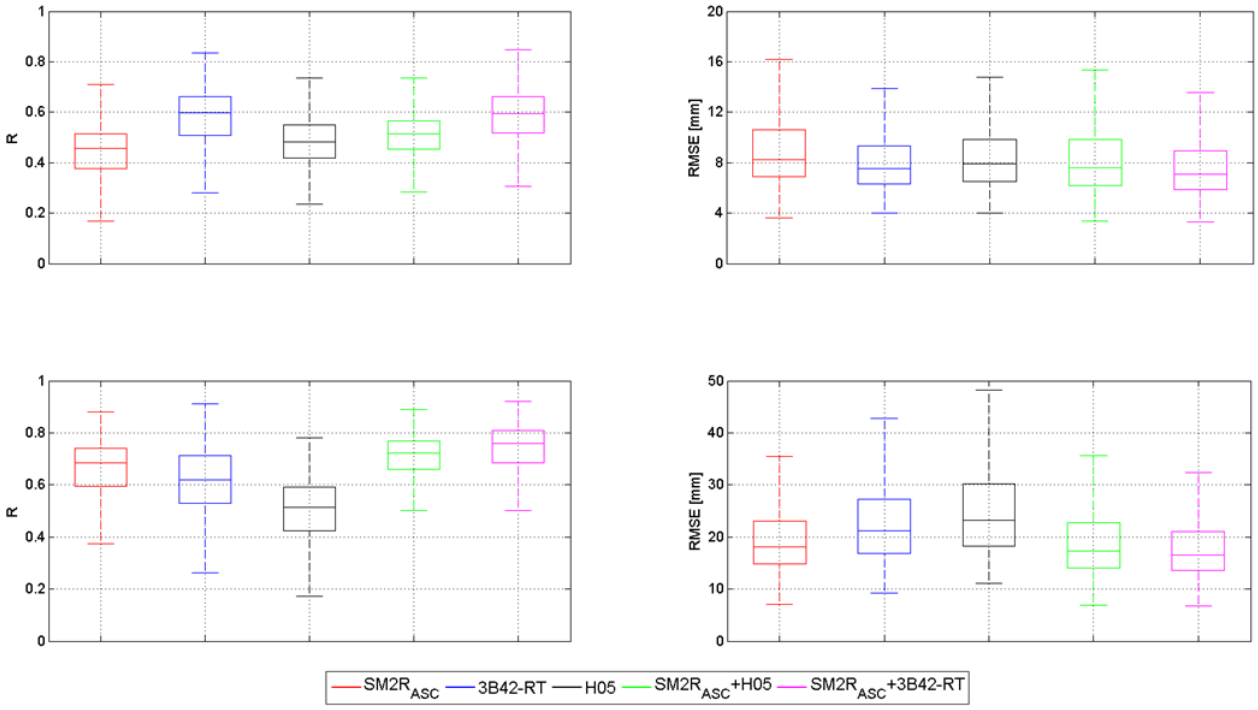

Figure 2.8 - Boxplot reporting the performance scores [(left) R and (right) RMSE] obtained during the calibration period for (top) 1 day and (bottom) 5 days of accumulated rainfall. The box lines represent the 25th, 50th, and 75th percentiles, while the whiskers represent the max and min values (Ciabatta et al., 2015*).*

Indeed, the change in the storage over a day cannot be related solely to the rainfall, and the use of daily satellite soil moisture observations may lead to errors in daily rainfall estimation. By computing the total rainfall over 5 days, more accurate results can be obtained thanks to an averaging effect. When more accurate and temporally dense satellite SM data are available (e.g., through merging of retrievals from different sensors), more accurate results, even at the daily time scale, are expected. Concerning the integrated products, results for 1 day of accumulated rainfall show a slight improvement. By way of example, R for SM2RASC+H05 shows an increase of 6% with respect to H05, while there is no noticeable difference considering the SM2RASC+3B42-RT product. This is probably due to the lower correlation of SM2RASC with respect to 3B42-RT. However, in terms of RMSE, there is a reduction of 4% and 6% for both SM2RASC+H05 and SM2RASC+3B42-RT compared to the parent satellite rainfall products. For 5 days of accumulated rainfall, the improvement due to the integration is evident and significant; the integrated products show the highest median R values (0.72 and 0.76 for SM2RASC+H05 and SM2RASC+3B42-RT, respectively), with an increase of nearly 41% and 23% compared to the parent products (i.e., H05 and 3B42-RT). In terms of RMSE (for 5 days of accumulated rainfall), the integrated products show a reduction of about 25% and 21% compared to the satellite rainfall datasets with the best results for SM2RASC+3B42-RT (with a median RMSE of 16.60 mm).

Assessment during the validation period

After the SM2RAIN calibration during the period 2010-2011, the parameters are applied to ASCAT SM data during the validation periods: 2012-2013 (Ciabatta et al., 2015) and 2012-2014 (Ciabatta et al., 2017). ***Table 2.2*** indicates that for 1 and 5 days of accumulated rainfall the validation results are

consistent to those obtained in calibration, showing only a little deterioration of the performance scores with respect to the calibration. In particular, significant improvements are obtained for 1 and 5 days of accumulated rainfall of the integrated products with respect to the parent products. The results for 5 days of accumulated rainfall deserve more attention. In this case, the correlation maps in ***Figure 2.9*** show good correlation against ground data in all cases. In particular, 3B42-RT results are 1) consistent with those found by Chen et al. (2013), Brocca et al. (2014), and Stampoulis and Anagnostou (2012) at mid latitude; 2) slightly lower than those of SM2RASC; and 3) better than H05.

Product	Calibration			Validation	
	1 day	5 days		1 day	5 days
	Median R				
$SM2R_{ASC}$	0.45 (0.12)	0.68 (0.14)		0.43 (0.13)	0.62 (0.16)
H05	0.48 (0.09)	0.51 (0.12)		0.50 (0.10)	0.54 (0.11)
3B42-RT	0.60 (0.11)	0.62 (0.12)		0.57 (0.12)	0.60 (0.13)
$SM2R_{ASC}$+H05	0.51 (0.09)	0.72 (0.10)		0.51 (0.11)	0.68 (0.11)
$SM2R_{ASC}$+3B42-RT	0.59 (0.11)	0.76 (0.11)		0.57 (0.12)	0.71 (0.10)
	Median RMSE				
$SM2R_{ASC}$	8.27 (3.66)	18.01 (7.95)		8.71 (4.05)	19.94 (10.97)
H05	7.93 (3.61)	23.22 (11.95)		8.25 (3.68)	22.32 (12.41)
3B42-RT	7.51 (3.10)	21.16 (10.05)		7.80 (3.44)	21.87 (11.60)
$SM2R_{ASC}$ +H05	7.62 (3.64)	17.36 (8.24)		7.86 (4.03)	18.32 (11.56)
$SM2R_{ASC}$ +3B42-RT	7.06 (3.34)	16.60 (7.71)		7.47 (3.83)	18.13 (10.91)
	Pixels with p value < 0.01				
$SM2R_{ASC}$	96%	95%		96%	94%
H05	97%	97%		95%	97%
3B42-RT	97%	97%		97%	96%
$SM2R_{ASC}$ +H05	97%	97%		97%	97%
$SM2R_{ASC}$ +3B42-RT	97%	97%		97%	97%

Table 2.2 - Median R, median RMSE (mm), and pixels with a significant correlation (p-value, 0.01) for each analyzed product (%), during the calibration and validation periods, considering 1 and 5 days of accumulated rainfall (std dev is given in parentheses) (Modified by Ciabatta et al., 2015).

The integration of the products improves the performance, causing an increase in median R from 0.60 to 0.71 for 3B42-RT and from 0.54 to 0.68 for H05. It is interesting to note that R maps highlight areas where the SM2RASC product provides less accurate results because of topographic

complexity (the Alps and Apennines chains), while both 3B42-RT and H05 products show lower performance in southern Italy. With respect to 3B42-RT performance, Stampoulis and Anagnostou (2012) found similar results. Therefore, the integration involves a substantial improvement in the product performance with an increase, during the validation period, in SM2RASC+H05 (SM2RASC+3B42-RT) median R value of about 26% (18%) with respect to the H05 (3B42-RT) product.

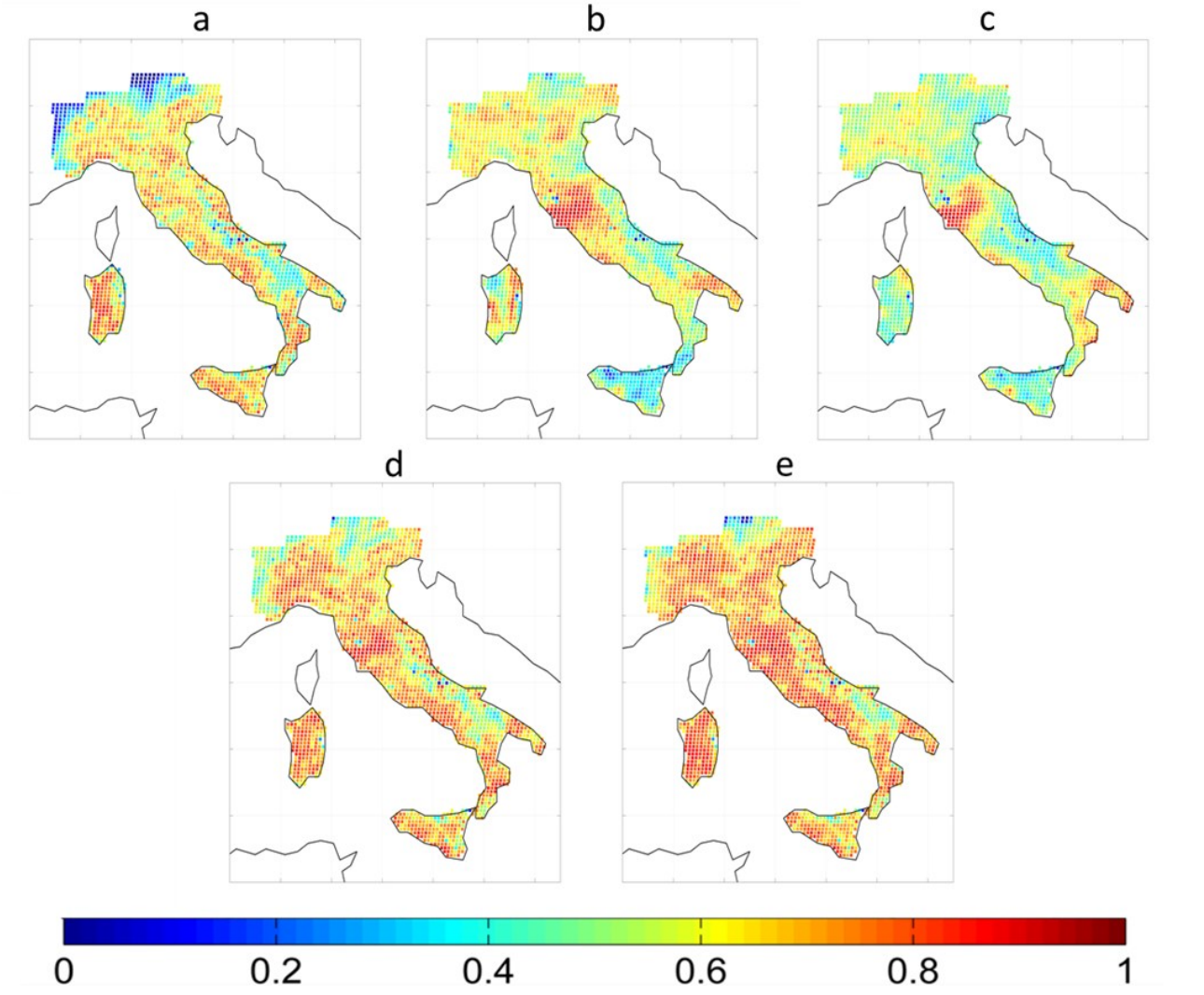

Figure 2.9 - Maps of R for 5 days of accumulated rainfall for (a) SM2R$_{ASC}$ (median R 5 0.62), (b) 3B42-RT (median R 5 0.6), (c) H05 (median R 5 0.53), (d) SM2R$_{ASC}$ +H05 (median R 5 0.68), and (e) SM2R$_{ASC}$ +3B42-RT (median R 5 0.71) during the validation period (2012–13) (Modified from Ciabatta et al., 2015).

For assessing the reliability of the analysis in terms of correlation, the percentage of pixels (over 2043) with a p value < 0.01 (significant correlation) are calculated and reported in ***Table 2.2***. The high percentage (>94%) of the pixels having a significant correlation confirms the analysis reliability. In particular, the pixels showing a p value <0.01 are mainly located over the Alps and the Gran Sasso massif for the SM2RASC product, while H05 and 3B42-RT products show pixels with a p value <0.01 over southern Italy and the mountainous regions, as might be expected by looking the correlation maps (***Figure 2.9***). In ***Figure 2.10***, the RMSE maps for the validation period

are shown. Median values of 19.94, 21.87, 22.32, 18.32, and 18.13mm are obtained for SM2RASC, 3B42-RT, H05, SM2RASC+H05, and SM2RASC+3B42-RT, respectively.

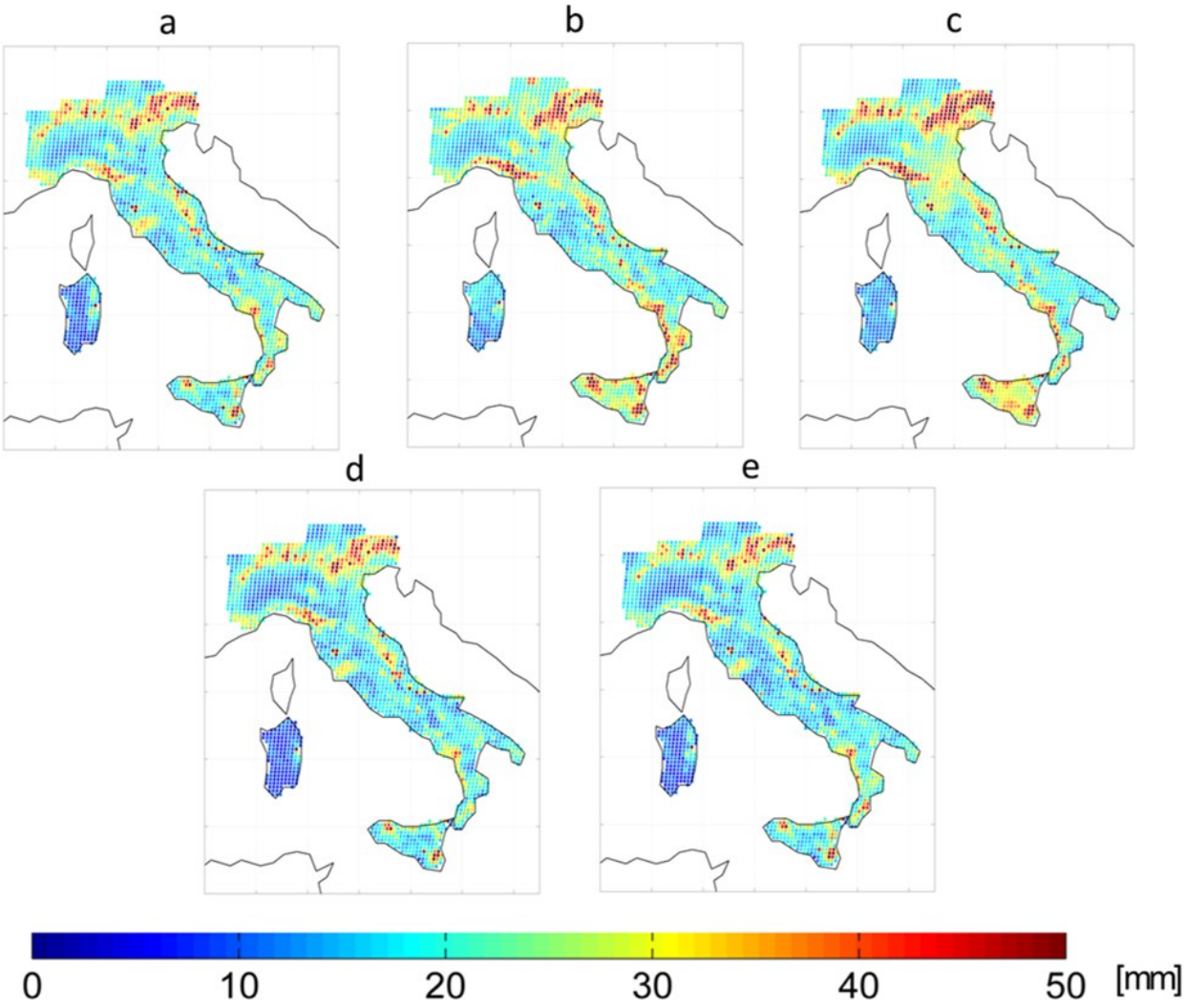

Figure 2.10 - Maps of RMSE for 5 days of accumulated rainfall for (a) $SM2R_{ASC}$ (median RMSE 5 19.94 mm), (b) 3B42-RT (median RMSE 5 21.87 mm), (c) H05 (median RMSE 5 22.32 mm), (d) $SM2R_{ASC}$+H05 (median RMSE 5 18.32 mm), and (e) $SM2R_{ASC}$+3B42- RT (median RMSE 5 18.13 mm) during the validation period (2012–13). (Modified from Ciabatta et al., 2015)

The five analysed rainfall products in Ciabatta et al. (2017) are evaluated during the independent validation period 2012–2014. The comparison is carried out pixel-by-pixel by using the gauge-observed rainfall dataset as benchmark. ***Table 2.3*** and ***Figure 2.11*** summarize the results in terms of R and RMSE. As it can be seen, all the analysed products provide quite good results. More in detail, CDRD and SM2RASC show worse performances in terms of R (median values of 0.57 and 0.58, respectively), while PNPR and CDRD-PNPR provide better R-values (median values of 0.61 and 0.68, respectively). The integrated product CDRD-PNPR + SM2RASC outperforms the other datasets with a median R-value of 0.71.

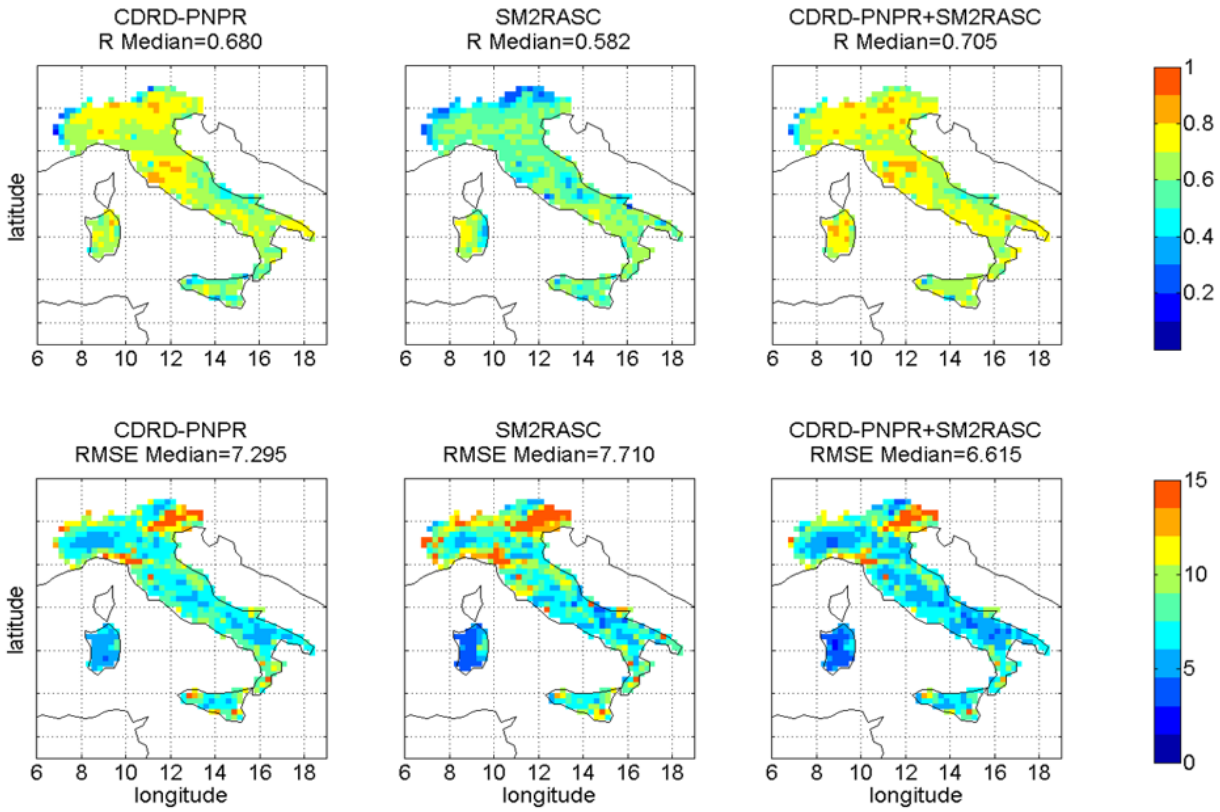

Figure 2.11 - Pearson correlation coefficient (R [–], upper panel) and Root Mean Square Error (RMSE [mm], lower panel) maps for CDRD-PNPR (first column), $SM2R_{ASC}$ (second column) and CDRD-PNPR + $SM2R_{ASC}$ (third column) during the validation period (2012–2014) for 1 day of accumulated rainfall. (Modified from Ciabatta et al., 2017).

In terms of RMSE, CDRD shows the highest values (median values of 10.97 mm), probably due to the limited number of satellite overpasses over the study area (see previous section). PNPR, CDRD-PNPR and SM2RASC provide similar performances with median values of about 7.70 mm.

Product	R (-)	RMSE (mm)	BIAS (%)	POD	FAR	TS
CDRD	0.57	10.97	3.65	0.36	0.12	0.34
PNPR	0.61	7.78	-23.5	0.53	0.17	0.48
CDRD-PNPR	0.68	7.3	-12.09	0.58	0.17	0.51
$SM2R_{ASC}$	0.58	7.71	-3.76	0.60	0.39	0.42
CDRD-PNPR+$SM2R_{ASC}$	0.71	6.62	-8.22	0.75	0.34	0.54

Table 2.3 - Statistics of continuous (Pearson correlation, R, Root Mean Square Error, RMSE and BIAS), and categorical performance median scores (Probability Of Detection, POD, False Alarm Ratio, FAR and Threat Score, TS) of the different analyzed products during the validation period 2012–2014. (Modified from Ciabatta et al., 2017).

The integrated product CDRD-PNPR + SM2RASC provides the significantly lower values, i.e., the best performance, with a median RMSE of 6.62 mm, showing a reduction of errors of about 15% over north-western, central and southern Italy with respect to the parent products. Overall, the integrated product (CDRD-PNPR+ SM2RASC) shows the highest performance scores throughout

the Italian territory (see ***Figure 2.11***), both in terms of R and RMSE. For the BIAS (see ***Table 2.3***), CDRD slightly overestimates rainfall on average, while the other four datasets show a general underestimation of rainfall. In order to visualize the agreement of the analysed products with the observed data, ***Figure 2.12*** shows the timeseries over the whole validation period of the 5-day (for the sake of better visualization) cumulated rainfall calculated for four different areas (A, B, C, and D) corresponding to the 4 grid boxes highlighted in black in ***Figure 2.1***.

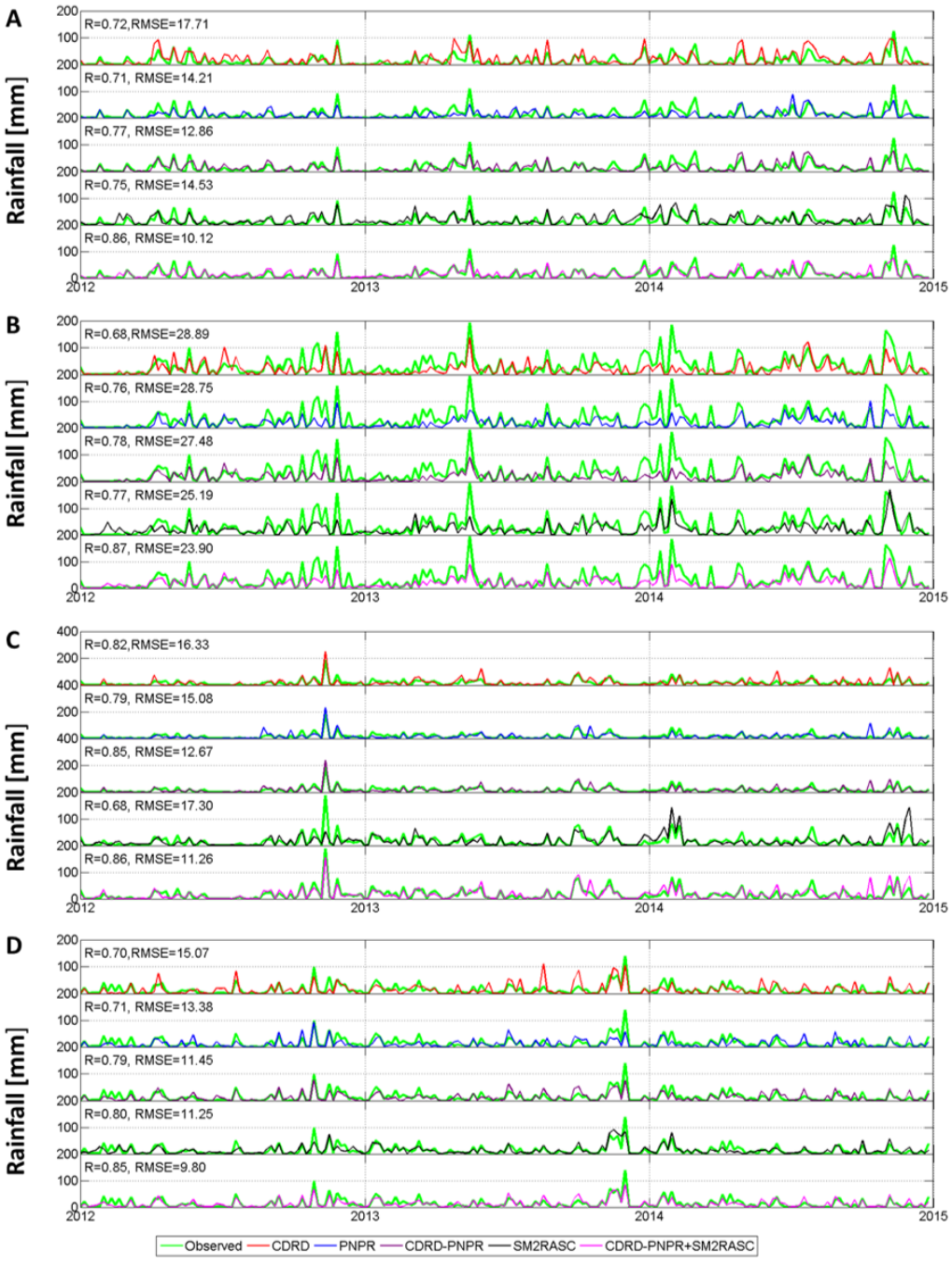

Figure 2.12 - Timeseries of 5-day cumulated rainfall for all analysed products for the four analysis boxes A, B, C and D shown in Figure 1.2 (from top to bottom). The text annotation indicates the Pearson correlation coefficient, R and Root Mean Square Error, RMSE (mm), values with respect to the observed rainfall. (Modified from Ciabatta et al., 2017).

All the products reproduce well the observed patterns, although some limitations can be noticed. Over box A (northwestern Italy), PNPR, CDRD-PNPR, SM2RASC and the integrated product underestimate rainfall, especially during the most intense events (for example the 9–13 October 2014 flood in Liguria and Piedmont regions, see the CASE STUDIES section). CDRD reproduces better the observed trend, with a general overestimation. Box B (northeastern Italy) highlights a different scenario: all the analysed products are characterized by high RMSE values (more than 23 mm) and almost all the intense events are largely underestimated. The underestimation is particularly evident during the winter months (especially for the winter season of 2013–2014) when the occurrence of snowfall (or the presence of snow at the surface) is more likely (in January–February 2014 record snowfall season was registered in the north-eastern Alpine region, partly included in Box B). In presence of snowfall, with a frozen or snow-covered background, the satellite precipitation estimate is affected by large uncertainty. It is worth noting that in snowfall conditions also the raingauge measurements used as benchmark are affected by large errors. The underestimation is noticeable also in other periods, for example in May of 2013 when very intense precipitation occurred in northern Italy for an extended period of time, and a big flood hit several areas in Veneto, included in Box B (May 16–19, 2013). While the top-down approaches might not be able to correctly capture the orographic enhancement of the precipitation in this area (orographic precipitation is associated to larger uncertainty in the PMW top-down approaches), the SM2RASC underestimates the precipitation because of soil conditions close to saturation. Box C (central Italy) shows an intense rainfall event at the end of 2012 (associated to flood occurred in Tuscany on 10–12 November 2012) that is not identified by SM2RASC, likely because of the soil conditions close to saturation, while it is well captured by the top-down products. The top-down products work very well in this region, with R values higher than 0.79. The timeseries over box D shows a general overestimation of CDRD, mainly in 2012 and 2013. PNPR, CDRD-PNPR and SM2RASC perform quite similarly, underestimating rainfall during the analysis period and not identifying the most intense rainfall event at the end of 2013 (flood in Apulia region on November 30-December 2, 2013). Finally, it is worth underlining that also in this analysis, the integrated product CDRD-PNPR + SM2RASC shows the highest performance scores, both in terms of R and RMSE, for all the investigated boxes.

Categorical scores assessment

In Ciabatta et al. (2015), the POD, FAR, and TS values are computed by considering percentile thresholds based on the observed rainfall distribution at each pixel. The results for 5 days of accumulated rainfall are displayed in ***Figure 2.13***. The figure shows that the 3B42-RT product has the lowest FAR and POD, probably because of the difficulty in estimating light rainfall, while H05 has the highest values of POD, mainly when considering the first percentiles. The integrated products generally outperform the parent products, providing a small reduction of FAR for higher percentiles (>70th percentile) and an increase in the detection of rainfall events (i.e., POD) for nearly all the considered thresholds. Consequently, higher TS values are obtained from the integrated products for >50th percentiles, that is, for higher rainfall rates that are more of interest for hydrological applications addressing flood and landslide prediction.

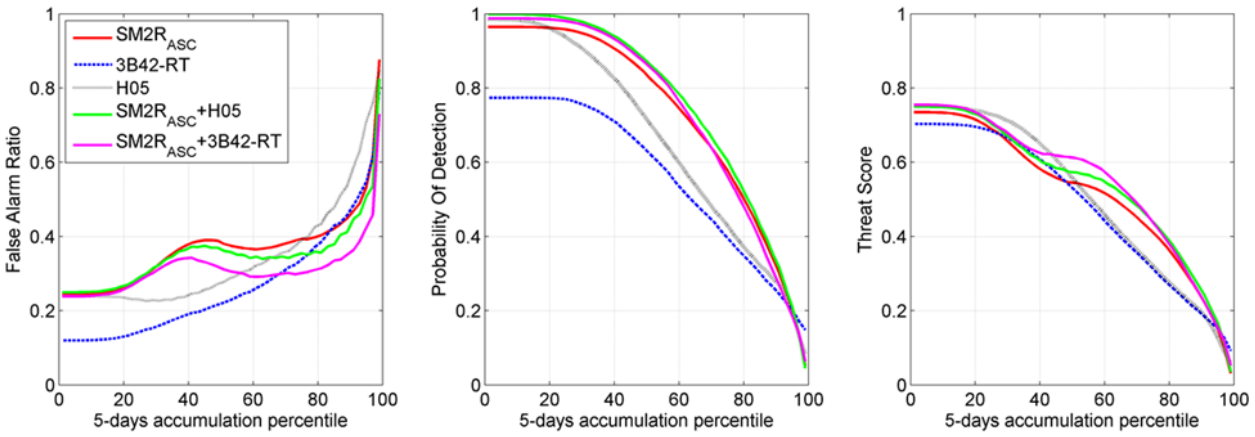

Figure 2.13 - Spatial averages of categorical metrics, computed for 5 days of accumulated rainfall, for the analyzed rainfall products (SM2RASC, 3B42-RT, H05, SM2RASC+H05, and SM2RASC+3B42-RT) in the validation period (2012–13): (left) FAR, (middle) POD, and (right) TS for a 5-day rainfall accumulation threshold. An event is defined as a 5-day rainfall accumulation that exceeds a given percentile threshold of all 5-day accumulations observed for a given pixel over the analyzed period. (Modified from Ciabatta et al., 2015).

Conversely, in Ciabatta et al. (2017), the categorical scores are evaluated by considering rainfall thresholds of 1, 2, 4, 8, 16 and 32 mm/day during the validation period (2012-2014). ***Figure 2.14*** shows the spatially averaged scores obtained for the different rainfall products (see also ***Table 2.3***, last three columns). For each rainfall threshold (based on observed rainfall data), the number of identified, missed and erroneously predicted events is estimated.

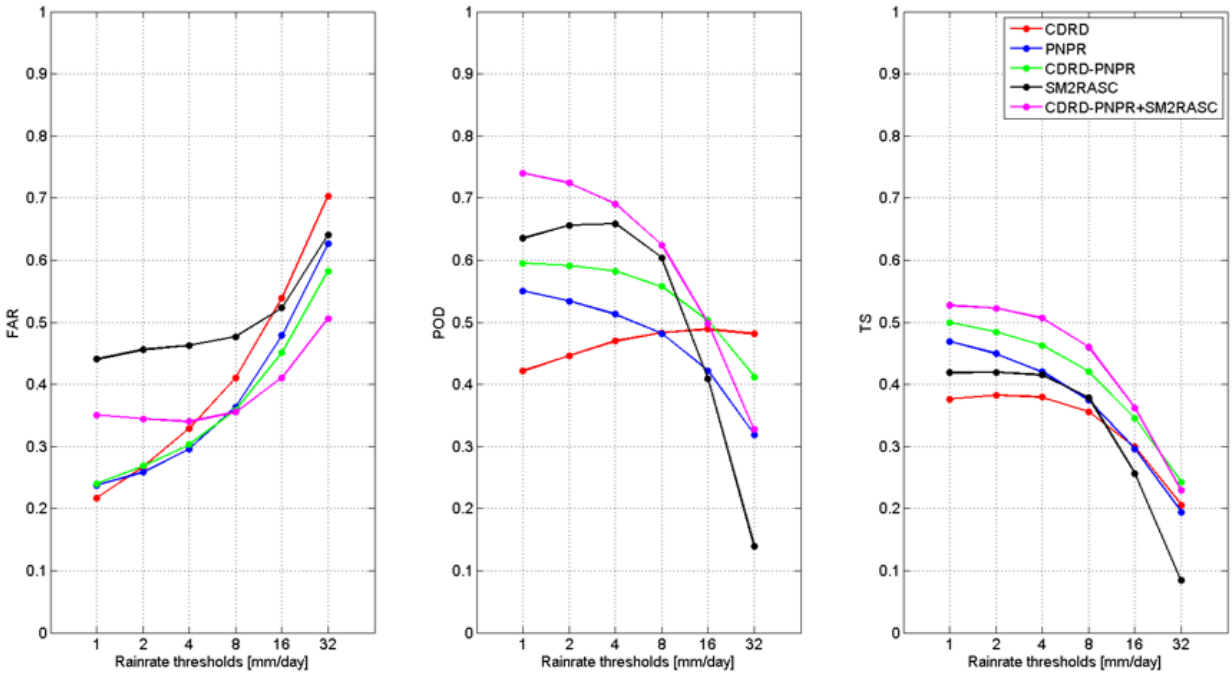

Figure 2.14 - Spatial average of False Alarm Ratio (FAR, left), Probability Of Detection (POD, middle) and Threat Score (TS, right) for the five analyzed products during the validation period (2012-2014) for different rainfall thresholds (1, 2, 4, 8, 16 and 32 mm/day). (Modified from Ciabatta et al., 2017)

All the rainfall datasets show similar trends with CDRD that provides the lowest FAR, POD and TS mainly when considering rainfall classes below 4 mm. PNPR shows FAR, POD ad TS very close to those obtained by analysing CDRD-PNPR, with better performance than CDRD alone. SM2RASC provides the highest FAR (up to 0.50) for rainfall classes below 8 mm and the lowest POD and TS for the rainfall thresholds of 16 and 32 mm/day. The FAR values could be explained in terms of noise in the SM satellite data, i.e. the small variations in SM could be related to the impact of noise on the satellite retrieval more than to SM variations due to rainfall. POD values, instead, are impacted by soil conditions close to saturation during intense rainfall events. The integrated product CDRD-PNPR+SM2RASC in general provides the best scores, with the lowest FAR for rainfall classes above 8 mm/day, the highest POD for rainfall classes below 8 mm/day (up to 0.73) and the best TS for nearly all the rainfall classes.

Temporal variability of the products performance

The temporal variability of the product performance is investigated by estimating R and RMSE values on a monthly scale in order to evaluate their trends during the entire period (2010–13). Specifically, for each month, the temporal R and RMSE values are computed by appending the time series of each pixel. ***Figure 2.15*** shows a general agreement between the analyzed products: SM2RASC, SM2RASC+3B42-RT, and SM2RASC+H05 show R values between 0.38 and 0.82. The other two products show more pronounced fluctuations in R value, between 0.13 and 0.75. All products show poor performance values during the winter months (Tian et al. 2009). In terms of RMSE, all the considered rainfall products have a similar pattern, with higher values (up to 50mm) during winter months and lower values during summer months (due to the RMSE dependency on rainfall amount).

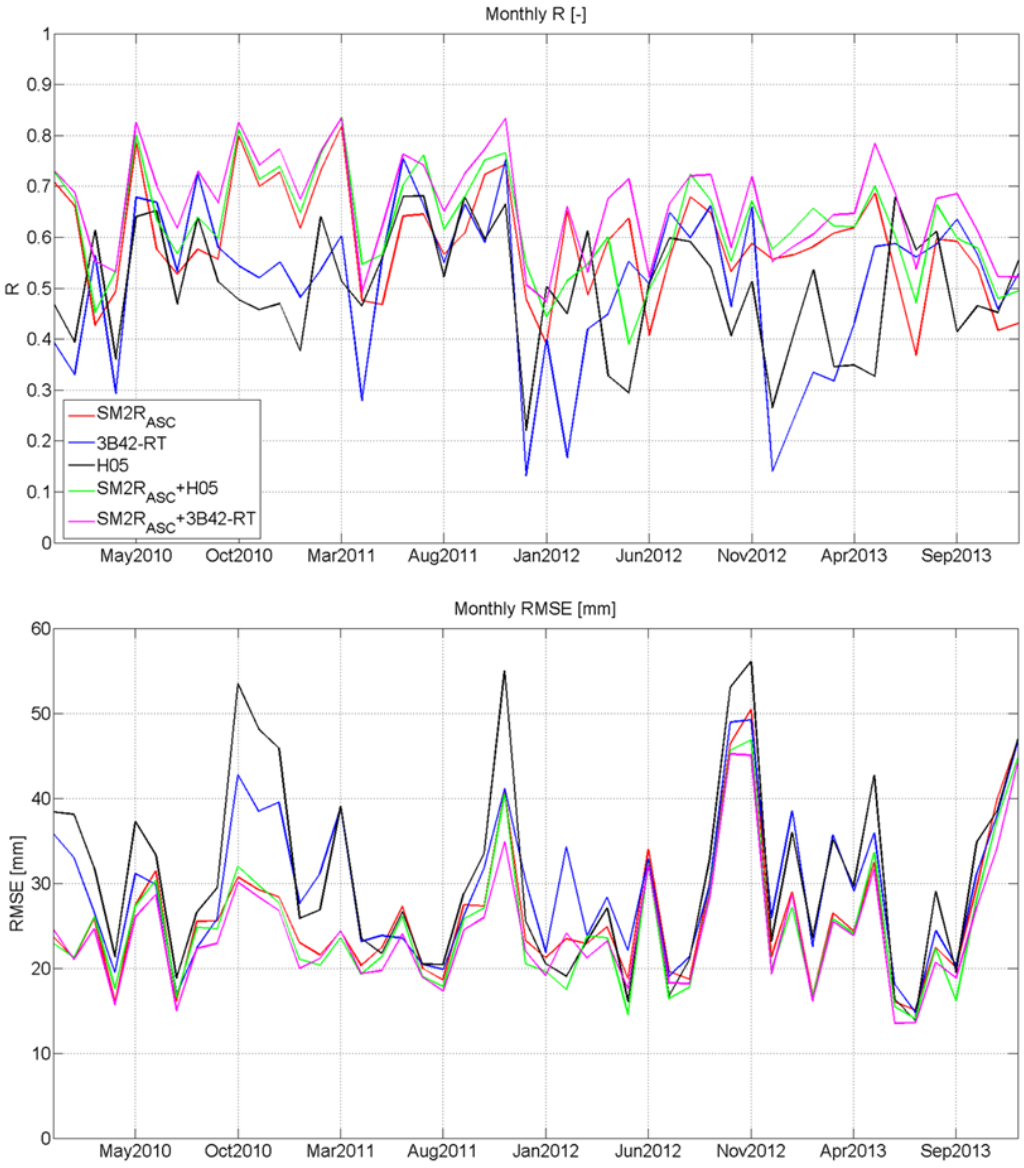

Figure 2.15 - Monthly (top) correlation coefficient (R) and (bottom) Root Mean Square Error (RMSE) values for 5 days of accumulated rainfall for each analyzed product. (Modified from Ciabatta et al., 2015)

The temporal analysis is also carried out by considering each individual season, that is, the entire analysis period is split into four different time ranges according to season. For spring the months of March–May (MAM) are considered, for summer June–August (JJA), for fall September–November (SON), and for winter December–February (DJF). For each period POD, FAR, and TS values are calculated (considering 5 days of accumulated rainfall) and averaged in space (over the 2043 grid points) and in time (every performance score presents four values, one for each year of the analysis period). In this way, one value per season is obtained. In ***Figure 2.16***, the POD and FAR values are plotted for each season, considering the 10th and 90th percentile thresholds.

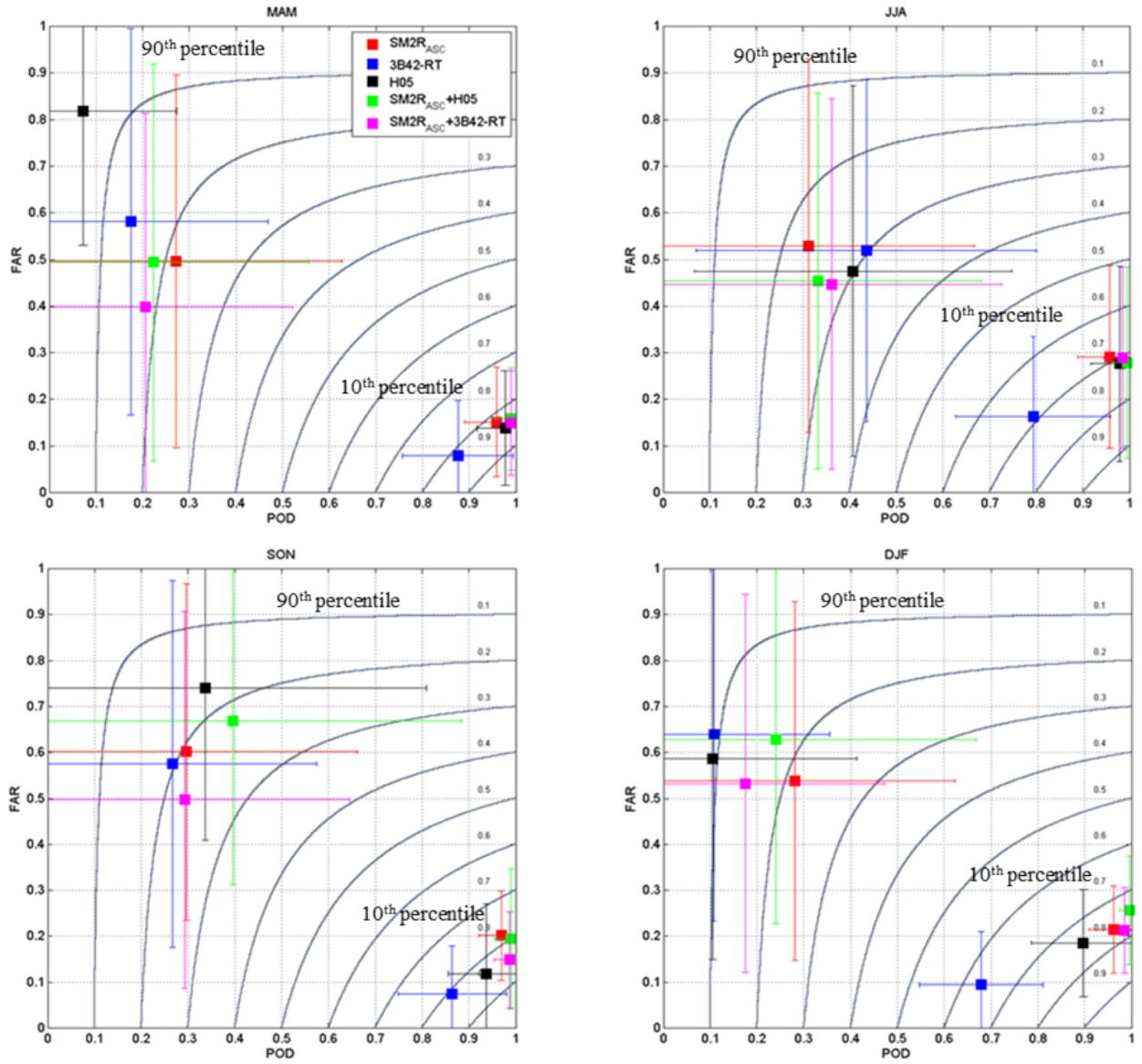

Figure 2.16 – POD vs FAR plot for each seasonal period considering 5 days of accumulated rainfall. The gray lines indicate TS values, the horizontal bars represent the standard deviation of POD, and the vertical bars represent the standard deviation of FAR for each analyzed percentile. (Modified from Ciabatta et al., 2015)

Specifically, in ***Figure 2.16***, the closer a point is to the lower-right corner of the plot, the better the performance is. By contrast, the proximity of a point to the upper-left corner suggests worse performance. On this basis, a downward and/or rightward variation implies an improvement. In terms of TS, ***Figure 2.16*** highlights that all the rainfall products perform better during the JJA and SON period than during MAM and DJF, mainly for the 90th percentile. The parent products (i.e., H05 and 3B42-RT) show the lowest performance during the MAM and DJF periods, probably because of the tendency of these products to underestimate light rainfall (Kidd and Levizzani 2011). In Ciabatta et al. (2017), the seasonal analysis is carried out during the validation period (2012-2014), by estimating R, RMSE and BIAS for the five analyzed products (***Figure 2.17***). In terms of R, CDRD, PNPR and CDRD-PNPR show an increasing trend from DJF to SON. This pattern is in

agreement with Ebert et al. (2007), who found that satellite rainfall products work slightly worse during winter with respect to the rest of the year. SM2RASC provides higher scores during MAM period, i.e., in correspondence with the drying period. In fact, during this period, the SM time series show a decreasing trend due to higher evapotranspiration and plant water demand. The performances of SM2RASC are comparable with those obtained with CDRD. Again, the integrated product outperforms the other datasets during all the seasons. With respect to RMSE, all the rainfall datasets show an increase in the errors during SON, due to the more intense rainfall regime. As highlighted by the previous analysis, CDRD shows the highest RMSE, while PNPR, CDRD-PNPR and SM2RASC have similar values. Also in this case, CDRD-PNPR + SM2RASC has the lowest RMSE values during all the seasons. In terms of BIAS, it can be seen that CDRD underestimates rainfall (about -25%) during DJF, while it overestimates precipitation during JJA (about +25%). This trend provides the almost ‘‘unbiased” rainfall estimates obtained during the validation period (see ***Table 2.1***). PNPR and CDRD-PNPR overestimate rainfall during JJA, while underestimate rainfall during the other three seasons (up to -50% and -45%, respectively, during DJF). SM2RASC underestimates rainfall from March to November with maximum value of -15% during JJA. SM2RASC is found to provide the lowest BIAS (in magnitude) throughout the four seasons. The integration between CDRD-PNPR and SM2RASC provides more accurate rainfall estimates with respect to top-down products but less accurate with respect to SM2RASC. Indeed, due to the high values of the integration weights (***Eq. 2.2***), the performance of the CDRD-PNPR + SM2RASC is impacted mainly by the BIAS of CDRD-PNPR.

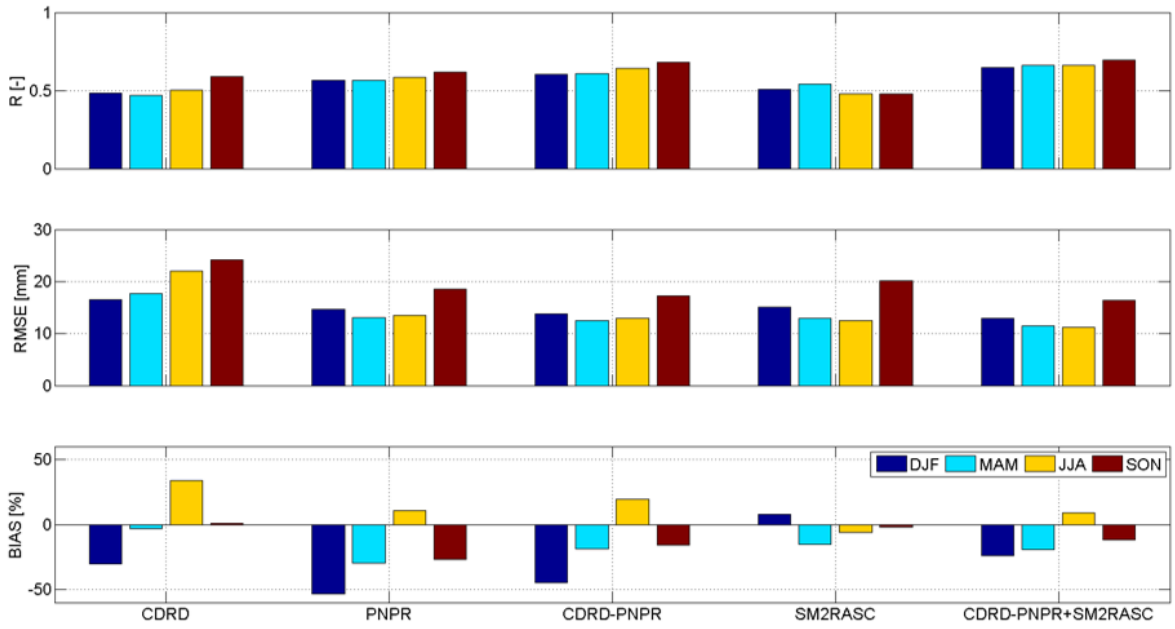

Figure 2.17 - Pearson correlation coefficient (R [–], upper panel), Root Mean Square Error (RMSE (mm), middle panel) and percentage BIAS (lower panel) for the five analyzed products on a seasonal scale during the whole validation period (2012–2014). Ciabatta et al. (2017).

Case studies

To visualize the temporal variability of rainfall products, two representative time series are reported in ***Figure 2.18***. Specifically, two pixels are selected throughout the study area, in order to show good and bad integration results in the calibration and validation period. The pixels are chosen by

considering the RMSE difference between the parent and the integrated products for 5 days of accumulated rainfall during the calibration period. ***Figures 2.18a*** and ***2.18b*** show the bad integration results with RMSE values equal to 25.59 and 34.93mm for the SM2RASC+3B42-RT and SMR2ASC+H05 products, respectively, while the parent products (i.e., 3B42-RT and H05) provide RMSE values equal to 26.08 and 37.43mm. As can be seen from the plot, the integrated products' time series are characterized by a general underestimation during both the calibration and validation periods.

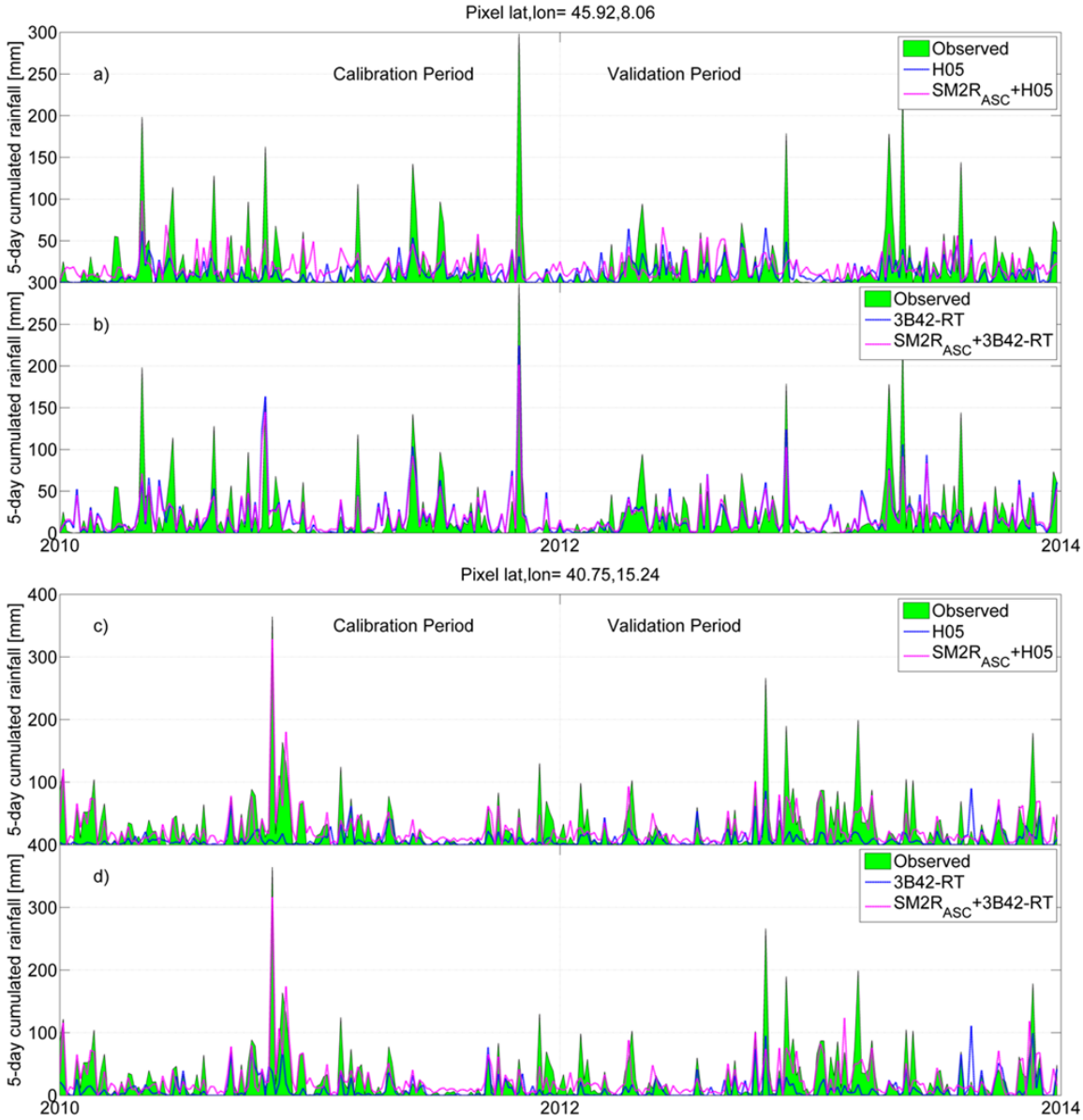

Figure 2.18 - Time series for the two selected pixels throughout the study area, showing (a), (b) bad integration results and (c), (d) good results in terms of the variation in RMSE after the integration. (a) Results for H05 and SM2RASC1H05 (RMSE values of 37.43 and 34.93 mm, respectively) and (b) results for 3B42-RT and SM2RASC13B42-RT (RMSE values of 26.08 and 25.59 mm, respectively) for 5 days of accumulated rainfall. (c) Results for H05 and SM2RASC+H05 (RMSE values of 46.91 and 21.30 mm, respectively) and (d) results for 3B42-RT and SM2RASC+3B42-RT (RMSE values of 41.24 and 21.26 mm, respectively). (Modified from Ciabatta et al., 2015)

The pixel is chosen over a mountainous area where the parent products are affected by many factors, such as the presence of snow/frozen soil and complex topography, and they do not provide good performance separately. As a result, their integration does not yield a satisfactory score. In contrast, ***Figures 2.18c*** and ***2.18d*** plot the time series for the good integration results. The RMSE values for the integrated products are 21.26 and 21.30mm, for SM2RASC+3B42-RT and SMR2ASC+H05, respectively, while the parent products show nearly double RMSE values equal to 41.24 and 46.91mm. ***Figures 2.18c*** and ***2.18d*** show a general agreement between the observed and the integrated products, confirming the capability of the SM2RAIN method to correctly estimate rainfall and the usefulness of the proposed integration procedure that allowed for a more reliable rainfall dataset by partially overcoming the satellite issues related to light rainfall estimation. In Ciabatta et al. (2017), 6 case studies are analyzed by comparing the spatial patterns of rainfall provided by the five rainfall products with respect to the observed benchmark. The first two cases refer to the year 2011, included in the calibration period of SM2RASC and of the integration coefficient (***Eq. 2.2***) used for CDRD-PNPR + SM2RASC. The other four cases refer to rainfall events occurred in the four areas selected for the timeseries analysis, and already evidenced in the analysis of ***Figure 2.12***. Details about the selected case studies are reported in ***Table 2.4***. The results are shown in ***Figure 2.19***, where the maps of the cumulated rainfall obtained from each product for the time frame corresponding to each event are shown. All the analysed products reproduce the observed rainfall fields with some limitations.

Event #	Date	Area (Box)	Maximum cumulated rainfall (mm)
1	15–18 March 2011	North and Central Italy (A, B, C)	239.07
2	5–8 November 2011	Northern Italy, Campania, Sardinia (A, B)	417.06
3	10–12 November 2012	Central (Tuscany) (C)	442.26
4	16–19 May 2013	North-east (Veneto) (B)	351.01
5	30 November–2 December 2013	South (Apulia) (D)	248.88
6	9–13 October 2014	North-west (Liguria-Piedmont) (A)	349.71

Table 2.4 - Rainfall events occurred in Italy within the period 2011–2014 for the case studies analysis. For each event, the maximum cumulated rainfall, calculated during the rainfall event, is reported.

The underestimation of rainfall is the most common issue that heavily affects the retrieval, in particular by SM2RASC in cases of extensive floods (i.e., the 10–12 November 2012 flood in Central Italy, and the 16–19 May 2013 flood in Veneto), and PNPR, CDRD-PNPR (and to a less extent by CDRD) in the north-east and in the Alpine regions (i.e., 15–18 March 2011 and 16–19 May 2013). In other cases, the top-down approaches (CDRD, or PNPR or CDRD-PNPR) are able to identify quite well the areas of heavy precipitation (i.e., in the north-west in the 5–8 November 2011 and in the 9–13 October event), although in some cases overestimation by CDRD is evident (i.e., Sardinia and Central Italy on 5–8 November 2011). By integrating all the available information, CDRD-PNPR+SM2RASC provides rainfall estimates closer to the observed ones, during almost all the analyzed events. Only for the fourth event (16–19 May 2013), rainfall is

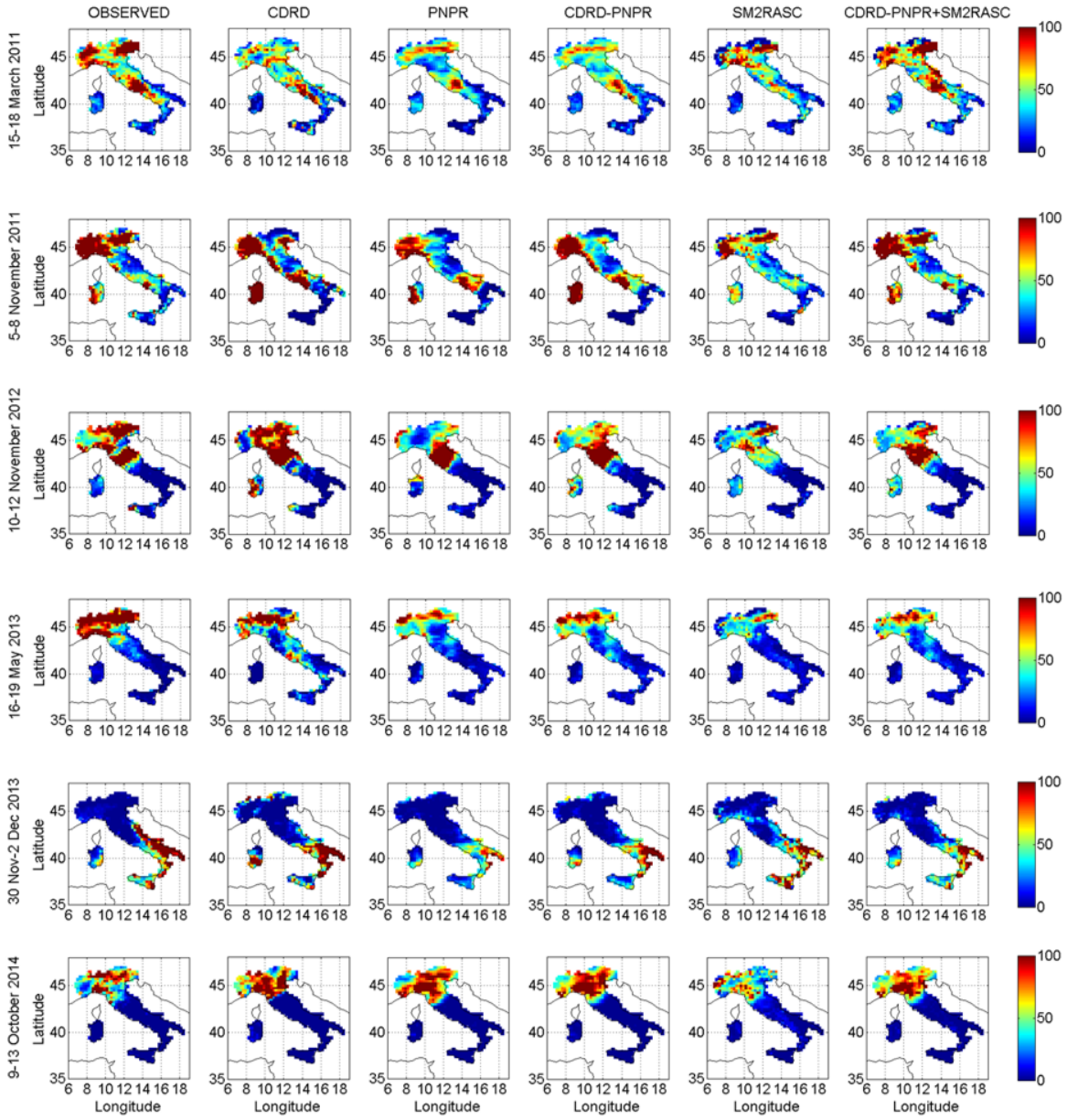

Figure 2.19 - Cumulated rainfall maps for some important rainfall events in the study period listed in Table 2.4. The first column represents the observed rainfall data, while the other five columns the maps obtained by the satellite rainfall products considered in the study. The color bar refers to the cumulated rainfall [mm] over the time period considered for each case in Table 2.4. (Modified from Ciabatta et al., 2017)

underestimated also by the integrated product, as already discussed in the analysis of ***Figure 2.12***. It is worth noting the good agreement with the observations of the integrated product for the two 2011 events (1 and 2 in ***Table 2.4***), showing the importance of the calibration procedure on SM2RASC and on the computation of the weights in ***Eq. 2.2*** for the integration of SM2RASC with CDRD-PNPR. The presented case studies highlight the benefits due to the integration in different rainfall regimes.

2.2 Validation on a global scale

This section shows the results of the assessment on a global scale a new derived SM-derived rainfall product. Specifically, the SM2RAIN algorithm is applied to the ESA Climate Change Initiative (CCI) SM products in order to obtain a long-term rainfall dataset. This section is based on the publication:

Ciabatta, L., Massari, C., Brocca, L., Gruber, A., Reimer, C., Hahn, S., Paulik, C., Dorigo, W., Kidd, R., Wagner, W. (2018). SM2RAIN-CCI: a new global long-term rainfall data set derived from ESA CCI soil moisture. Earth System Science Data, 10, 267-280.

Dataset

Rainfall datasets

In the study, five state-of-the-art rainfall products including models, satellite-based and ground-based observations are intercompared with the new SM2RAIN-CCI data set. In particular, the two following products are considered as benchmark:

1) the Global Precipitation Climatology Centre Full Data Daily (GPCC-FDD) product (Schamm et al., 2015), available at 1° spatial sampling during the period 1988-2013 (ground based data set) at daily temporal resolution, used for calibrating SM2RAIN;

2) Multi-Source Weighted-Ensemble Precipitation (MSWEP, Beck et al., 2017), available from 1st January 1979 to 31st December 2015 at 0.25° spatial sampling on a daily basis (combination of models, ground measurements and satellite observations), used as independent benchmark for the yearly global analysis.

Three rainfall data sets are additionally used for cross-comparison with the SM2RAIN-CCI product:

1) TMPA 3B42RT (hereinafter referred to as TRMMRT), available from 1st March 2000 to present at 0.25° spatial resolution for the ± 50° latitude band every 3 hours (only satellite);

2) Climate Prediction Center Morphing Technique (CMORPH, Joyce et al., 2004) raw data (hereinafter referred to as CMORPH), available from 1st January 2000 to present at 0.25° spatial resolution for the ± 60° latitude band every 3 hours (only satellite);

3) ERA-Interim reanalysis product, available from 1st January 1978 to present at 0.77° spatial sampling on a daily basis (Dee et al., 2011) (reanalysis).

Due to the different spatial sampling and coverage (both in space and in time), the assessment is carried out during the period 1998-2013 for the ± 50° latitude band (due to data availability TRMMRT and CMORPH are considered starting from 2000). A more detailed description of the analysed rainfall products is reported below. For TRMMRT, CMORPH and ERA-Interim data, the reader is referred to the previous sections.

The GPCC-FDD data set is a gauge-based product. The number of stations used in the data set varies throughout the years. In total, data from more than 60000 stations are used. GPCC-FDD is provided on a global scale over a grid with 1° spatial sampling and on a daily basis. The product is available for the period 1988-2013. Here, GPCC-FDD is used as benchmark because it is completely independent from any satellite data and it does not contain any missing values (Herold et al., 2017). For further details, the reader is referred to Schamm et al. (2015).

MSWEP is a recently developed rainfall data set that combines precipitation information from several sources, including GPCC-FDD, TRMMRT, CMORPH and ERA-Interim. The estimates obtained through satellite sensors, global models and in-situ stations are merged by the use of integration weights. The product is available from 1979 to 2015 with a spatial sampling of 0.25°. More information about MSWEP can be found in Beck et al. (2016).

Satellite soil moisture data

The ESA CCI (http://www.esa-soilmoisture-cci.org/) provides long-term SM data sets for the period 1978-2015 (Liu et al., 2011; Dorigo et al., 2015; Dorigo et al., 2017). The products are

provided on a global scale with a spatial sampling of 0.25° with daily temporal sampling in three different configurations. The passive microwave product (hereinafter referred to as "PASSIVE") is provided for the period 1978-2015 and it is generated by merging SM products derived from the Scanning Multichannel Microwave Radiometer (SMMR, operating at 6.6 and 10.7 GHz, Owe et al., 2001), the Special Sensor Microwave Imager (SSM/I, operating at 19.35 GHz, Owe et al., 2008), the TRMM Microwave Imager (TMI, operating at 10.65 GHz and above, Gao et al., 2006), the Advanced Microwave Scanning Radiometer - Earth Observing System (AMSR-E, operating at 6.9 and 10.65 GHz, Owe et al. 2008) and its successor AMSR2 (operating at 6.93, 7.3 and 10.65 GHz), WindSat (operating between 6.8 and 37 GHz, Li et al., 2010 and Parinussa et al., 2012) and the ESA Soil Moisture and Ocean Salinity mission (SMOS, Kerr et al., 2012). Although the PASSIVE data set is obtained by considering some of the sensors used for creating the TMPA products, this will not impact the comparison between TRMMRT and SM2RAIN-CCI as different microwave frequency are taken into account for rainfall estimation. The Active data set (hereinafter referred to as "ACTIVE") is provided for the period 1991-2015 and it is generated by merging active microwave satellite retrievals from the European Remote Sensing satellites (ERS-AMI, operating at 5.3 GHz) and from the Advanced Scatterometer (ASCAT, operating at 5.255 GHz, Wagner et al., 2013) onboard the Metop-A and -B satellites. The third data set (hereinafter referred to as "COMBINED") is obtained by merging the ACTIVE and PASSIVE products. The merging of the individual data sets is performed by means of a weighted averaging which is parameterized using a triple collocation (TC, Stoffelen, 1998) approach (Gruber et al., 2017). In this study, we consider the ESA CCI SM product at version v03.2. For further details regarding the ESA CCI SM product development, sensors availability and performances the reader is referred to Liu et al., (2011; 2012), Dorigo et al., (2015; in 2017) and Wagner et al., (2012).

ESA CCI SM data preprocessing

Before applying SM2RAIN algorithm the following preprocessing steps are applied to the ESA CCI SM data sets. A static mask (***Figure 2.20***) is used to mask out periods with high frozen soil and snow probability, rainforest areas and areas with high topographic complexity. The latter two are provided within the ESA CCI SM data portal. Notice that deserts are particularly challenging for SM retrieval from active instruments. Therefore, we use the passive data set only in such areas, which typically provides more reliable retrievals over desert areas (Dorigo et al., 2010). Moreover, a dynamic mask is applied to SSM data on a daily basis in order to remove observations characterized by issues in the retrieval (frozen soil, dense vegetation). This mask is provided alongside with each of the ESA CCI SM products. After the application of the dynamic mask, many temporal gaps are found within the SM time series. In order to reduce the data gaps, the time series are interpolated to 00:00 UTC.

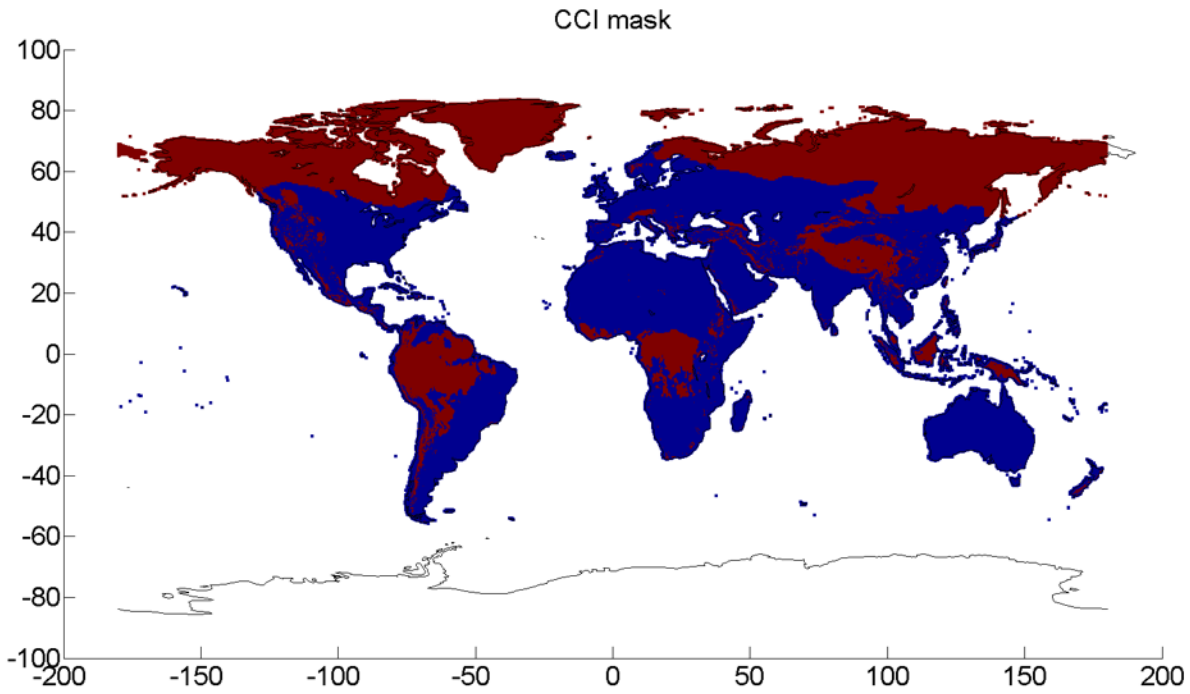

Figure 2.20 – Data mask used for remove areas (red areas) characterized by issues in the soil moisture retrieval.

A maximum data gap of three days is considered for the temporal interpolation. Data gaps larger than three days are left empty, i.e., no rainfall estimation is carried out within these intervals. Prior to 1998, the SM data sets are characterized by a low temporal coverage and a reduced data quality (Dorigo et al., 2015). Thus, the SM2RAIN-CCI product is generated only for the period 1998-2015. The original ACTIVE and PASSIVE CCI SM data sets are read and preprocessed by using routines developed in Python® language by the TUWIEN Remote Sensing Research Group (Ciabatta et al., 2016b). After the preprocessing steps, the ESA CCI SM data are ready to be used as input in SM2RAIN.

SM2RAIN-CCI rainfall product generation

The SM2RAIN parameters are obtained by minimizing the Root Mean Square Difference (RMSD) between the 5-day estimated rainfall and the GPCC-FDD data during three calibration periods 1998-2001, 2002-2006, 2007-2013 on a pixel-by-pixel basis. We considered 5-day of accumulation to reduce the amount of data and speed-up the calibration step. The use of different calibration periods relies on the different data and sensors that we used for building the ACTIVE and PASSIVE SSM data sets (***Table 2.5***, see also Dorigo et al., 2012). The calibration is performed on a pixel-by-pixel basis separately for ACTIVE and PASSIVE. SM2RAIN was also applied to the COMBINED SSM data set, but we observed a reduction of performance with respect to the individual ACTIVE and PASSIVE products (not shown), hence the COMBINED SSM data set is not considered here.

Sensor (Active/Passive)	Temporal interval
AMI-WS / SSMI & TMI	1998-01-01 to 2002-06-30
AMI-WS / AMSR-E	2002-07-01 to 2006-12-31
ASCAT-A & ASCAT B / AMSR-E & Windsat & SMOS & AMSR2	2007-01-01 to 2013-12-31
AMI-WS / SSMI & TMI & AMSR-E	1992-01-01 to 2006-12-31
ASCAT-A & ASCAT-B / AMSR-E & Windsat & SMOS & AMSR2	2007-01-01 to 2013-12-31

Table 2.5 – Available sensors and temporal intervals considered for the SM2RAIN algorithm application.

In order to match the different spatial resolutions of the considered data sets, GPCC-FDD was regridded to the 0.25° CCI grid by using the griddata function implemented in MATLAB® R2012a, through linear interpolation. After the application of SM2RAIN to the ACTIVE and PASSIVE SM data sets, the two obtained rainfall products are integrated through:

$$P_{SM2RAIN-CCI} = kP_{ACT} + (1-k)P_{PAS} \tag{2.6}$$

where PACT and PPAS are the two rainfall data sets obtained through the application of SM2RAIN to the ACTIVE and the PASSIVE SM data sets, respectively, and PSM2RAIN-CCI is the final SM2RAIN-CCI rainfall data set. The integration weights (k) are estimated through (Kim et al., 2015):

$$k = \frac{\rho_{AB} - \rho_{AP} * \rho_{AB}}{\rho_{PB} - \rho_{AP} * \rho_{AB} + \rho_{AB} - \rho_{AP} * \rho_{PB}} \tag{2.7}$$

Where ρ is the Pearson correlation coefficient between two data sets with the subscript A, P and B denoting the ACTIVE, the PASSIVE and the benchmark (GPCC-FDD in this case) rainfall estimates, respectively. When one of the two data sets (PACT or PPAS) is not available at a certain

location (e.g., due to unfavourable retrieval conditions), then only the available one is used for the generation of the combined rainfall product. The workflow is depicted in ***Figure 2.21***.

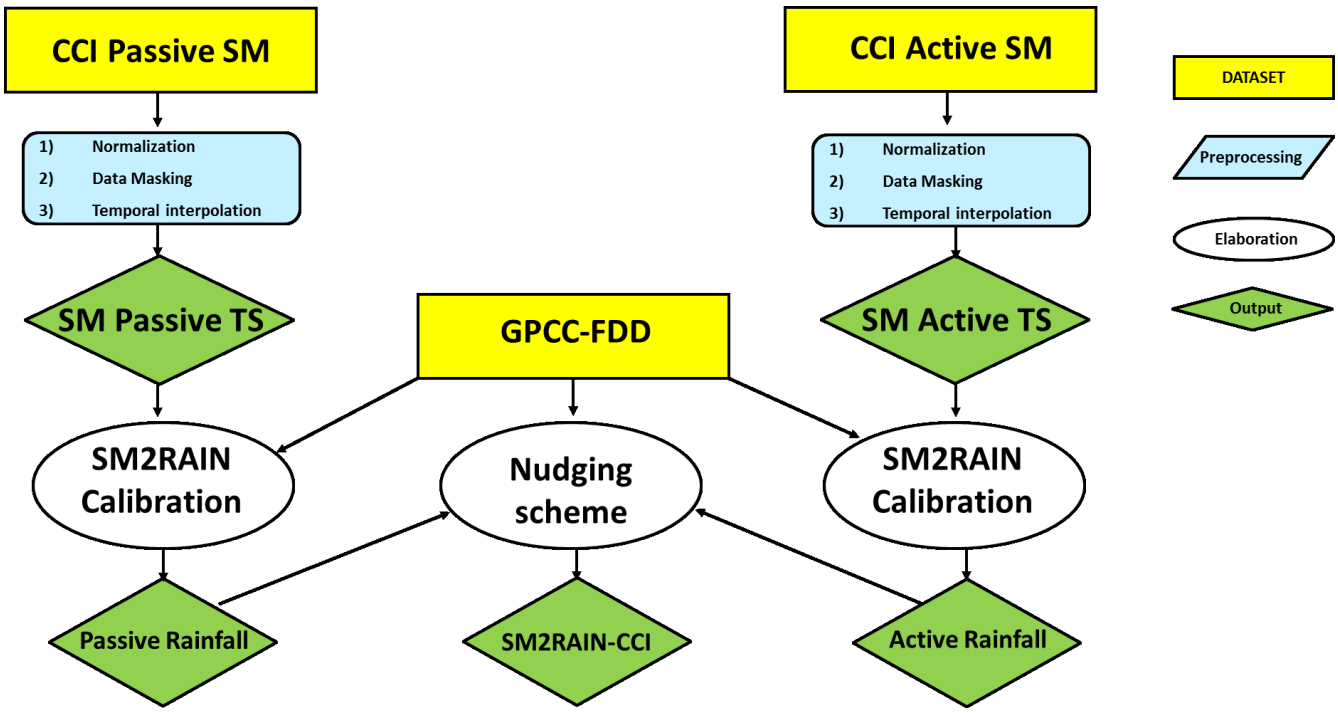

Figure 2.21 - Analysis framework

Results

SM2RAIN-CCI performance

The SM2RAIN-CCI rainfall data set is available from 1st of January 1998 to 31st December 2015 with daily temporal resolution. The data are provided over a 0.25° grid on a global scale, given the native spatial resolution of SM observation of 25 and 50 km. The spatio-temporal coverage is reported in ***Figure 2.22***. As it can be seen, there is an increase of available data after 2002 and 2007, corresponding to the start of the AMSR-E and ASCAT operations, respectively. Before 2002, the ESA CCI SM products are characterized by a small amount of data, due to longer revisit times of the used satellites. Before that date, the rainfall estimates obtained through SM2RAIN should be used with caution because of the likelihood of missing precipitation events. The lack of data over tropical areas and at high latitudes is due to the application of the mask described above. ***Figure 2.22*** also shows the mean daily rainfall for the SM2RAIN-CCI data set during the analysis period. As it can be seen, an increase in the daily values can be observed after 2007, especially over the tropical areas, where the seasonality is well reproduced, due to the higher number of satellite overpasses.

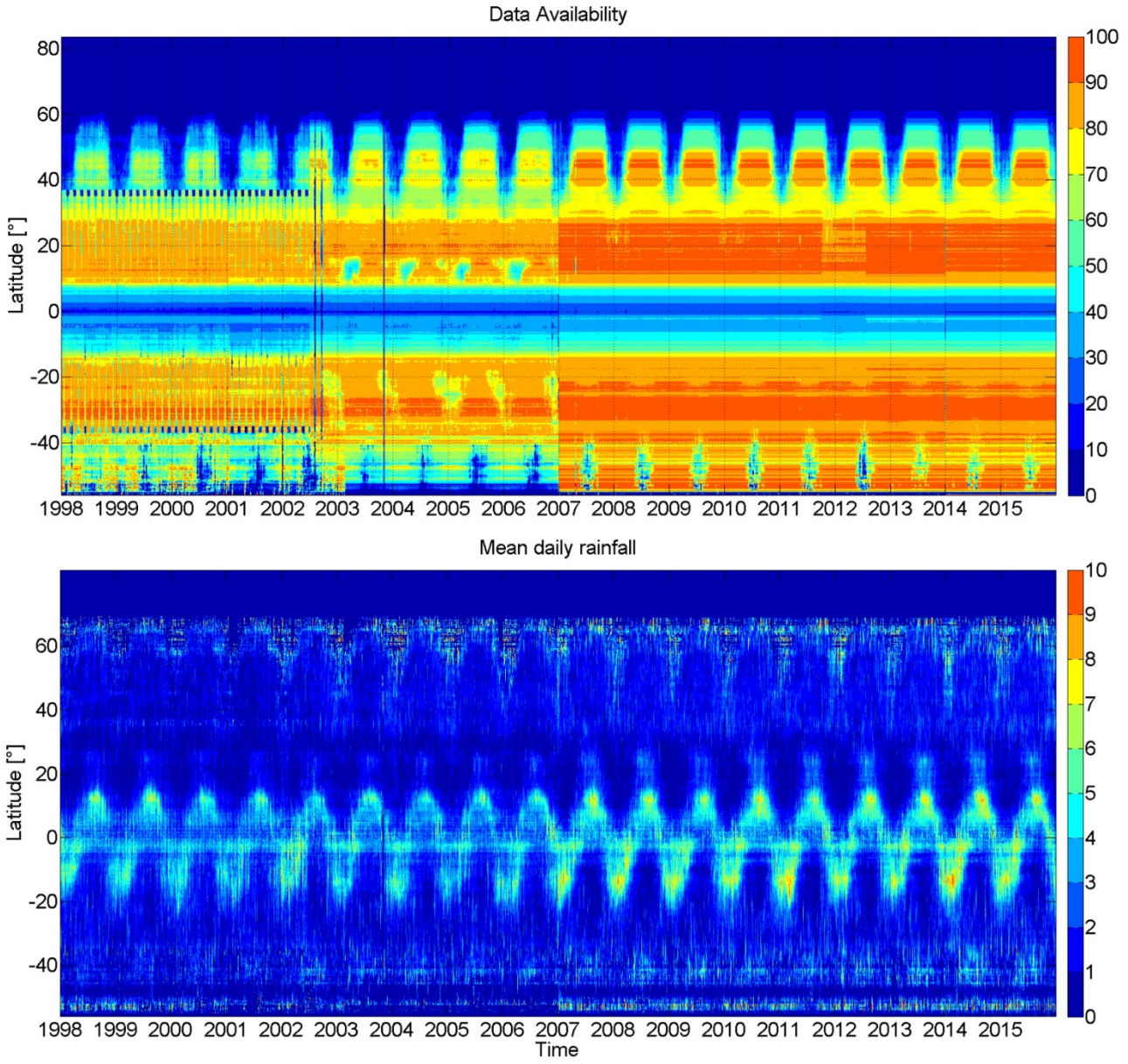

Figure 2.22 – Hovmoller plot showing the spatial-temporal data availability, in percentage of the total annual available data (upper panel) and the mean daily rainfall (lower panel) of the SM2RAIN-CCI rainfall data set for different latitude bands.

When compared to the GPCC-FDD rainfall data set, SM2RAIN-CCI shows relatively good performance for 5-day rainfall accumulation both in terms of correlation and RMSD, as drawn in Figure 36 for the ±50° latitude bands during the three calibration periods at 1° of spatial resolution, in order to perform a fair comparison with the benchmark. SM2RAIN-CCI rainfall shows relatively good agreement with GPCC-FDD, especially over Africa, Australia, India and South America in terms of correlation (R). The RMSD pattern is related to the rainfall regimes. The highest values are located in those regions characterized by high total annual precipitation, e.g. tropical areas. The comparison also provides better performance for the 2007-2013 period than for the 1998-2001 and 2002-2006 periods due to the better temporal coverage of the ESA CCI SM products and their improved accuracy (Dorigo et al., 2015). As it can be seen in ***Figure 2.23***, the median R (RMSD) obtained for the 1998-2001 calibration period is 0.54 (10.94 mm), while for the 2007-2013 period, a

median value of 0.65 (9.6 mm) is obtained. Indeed, due to the nature of the SM2RAIN algorithm, more frequent satellite overpasses are expected to provide more reliable rainfall estimates. SM2RAIN-CCI shows a lower performance over the Sahara Desert and at high latitudes, due to lower SM data quality over these regions. ***Figure 2.23*** also displays the lower performances obtained for the eastern US. A similar performance pattern was also found by Massari et al. (2017) who calculated global correlation of different rainfall data sets by applying the Extended TC (McColl et al., 2014) analysis. A cross-comparison of SM2RAIN-CCI with GPCC, TRMM, CMORPH, ERA-Interim and MSWEP is reported in ***Figure 2.24***. The Figure displays the 1°x1° (± 50°) correlation maps of 5 day of accumulated rainfall (on the left) and the differences in the mean annual rainfall (on the right) between SM2RAIN-CCI and the other rainfall data sets. The difference in the mean annual rainfall are calculated by subtracting the mean annual rainfall of each data set to the one provided by SM2RAIN-CCI. The analysis shows that SM2RAIN-CCI rainfall estimates are in good agreement with the state-of-the-art data sets both in terms of R and mean annual rainfall. Non-negligible differences can be observed over the Sahara Desert, Eastern US, South America, the tropical area and over Europe, where SM2RAIN-CCI provides a smaller amount of rainfall than the other rainfall data sets. On the other hand, very good performance can be observed over Africa, Brazil, western US, India and Australia, both in terms of R and mean annual rainfall.

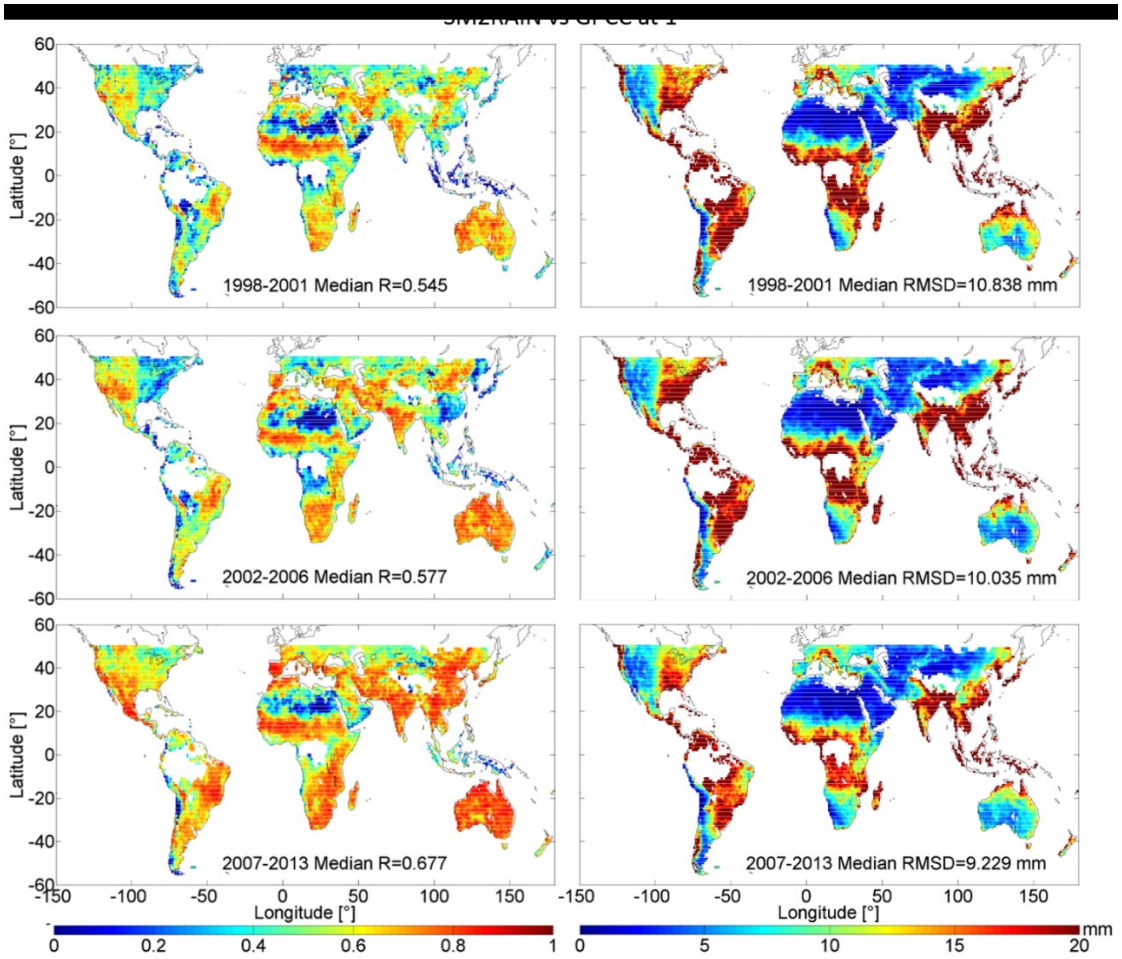

Figure 2.23 – Global Pearson correlation (left) and Root Mean Square Difference (right) maps obtained between GPCC-FDD and the SM2RAIN-CCI rainfall data set for 5-day accumulated rainfall during the periods 1998-2001 (upper panel), 2002-2006 (middle panel) and 2007-2013 (lower panel).

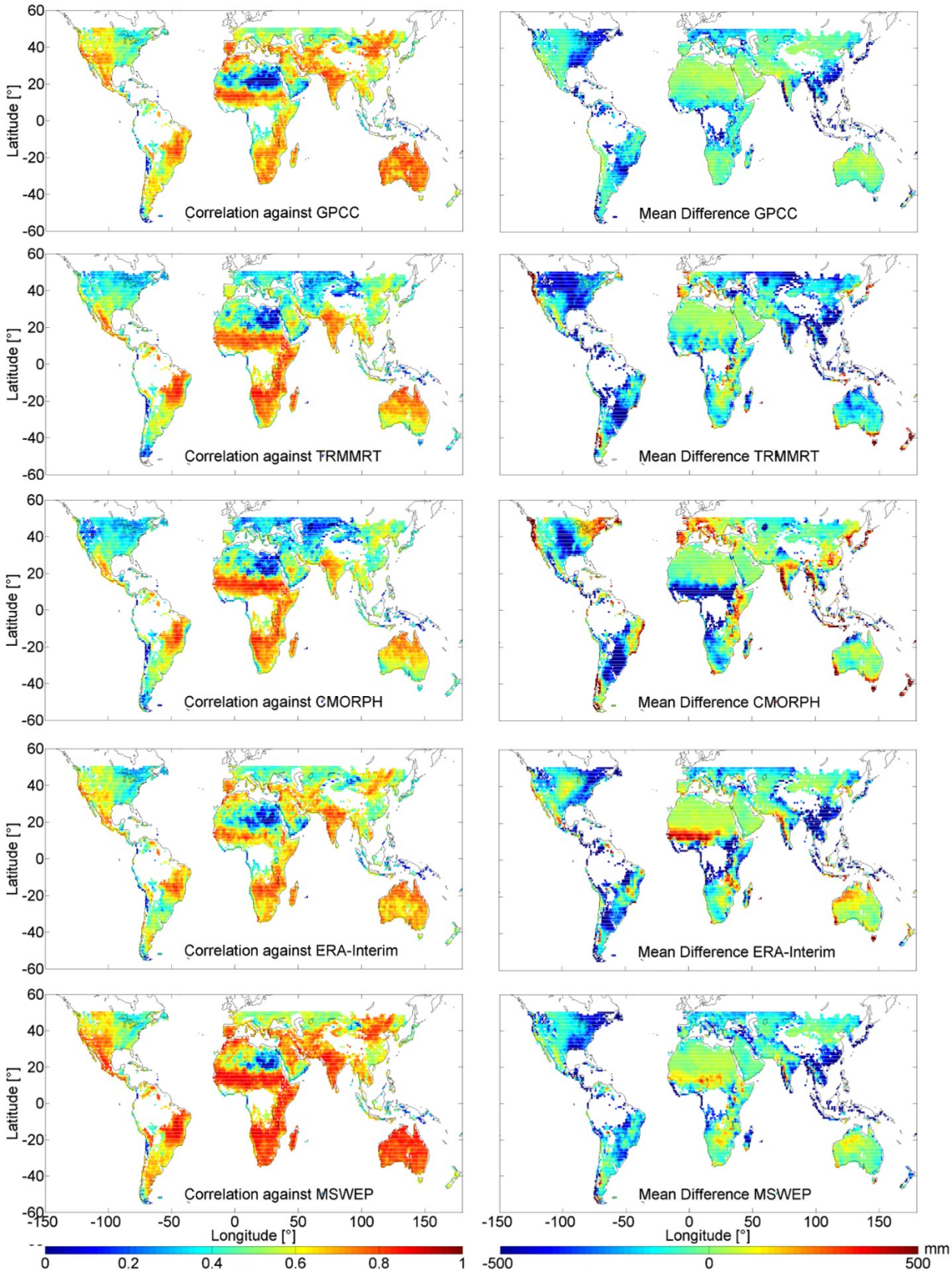

Figure 2.24 – Correlation maps for 5 days of accumulated rainfall (left column) and differences in mean annual rainfall (right column) obtained by comparing (from top to bottom) SM2RAIN-CCI and GPCC (a), SM2RAIN-CCI and TRMMRT (b), SM2RAIN-CCI and CMORPH (c), SM2RAIN-CCI and ERA-Interim (d) and SM2RAIN-CCI and MSWEP (e) at 1° of spatial resolution.

Seven macro-regions worldwide are selected to check the capability of the SM2RAIN-CCI in estimating rainfall under different climatic conditions. Therefore, mean monthly rainfall (MMR) was computed from GPCC-FDD and SM2RAIN-CCI during the period 1998-2013 within these regions, illustrated as green boxes in ***Figure 2.25***. From ***Figure 2.25***, one can see that the temporal rainfall patterns agree well in all considered macro-regions. SM2RAIN-CCI provides a general underestimation before 2007, due to the increased number of data gaps. Indeed, if the GPCC-FDD MMR is estimated only when SM observations are available (i.e. when both GPCC-FDD and SM2RAIN-CCI provide a rainfall estimate), the two estimates are very close to each other, for the entire analysis period.

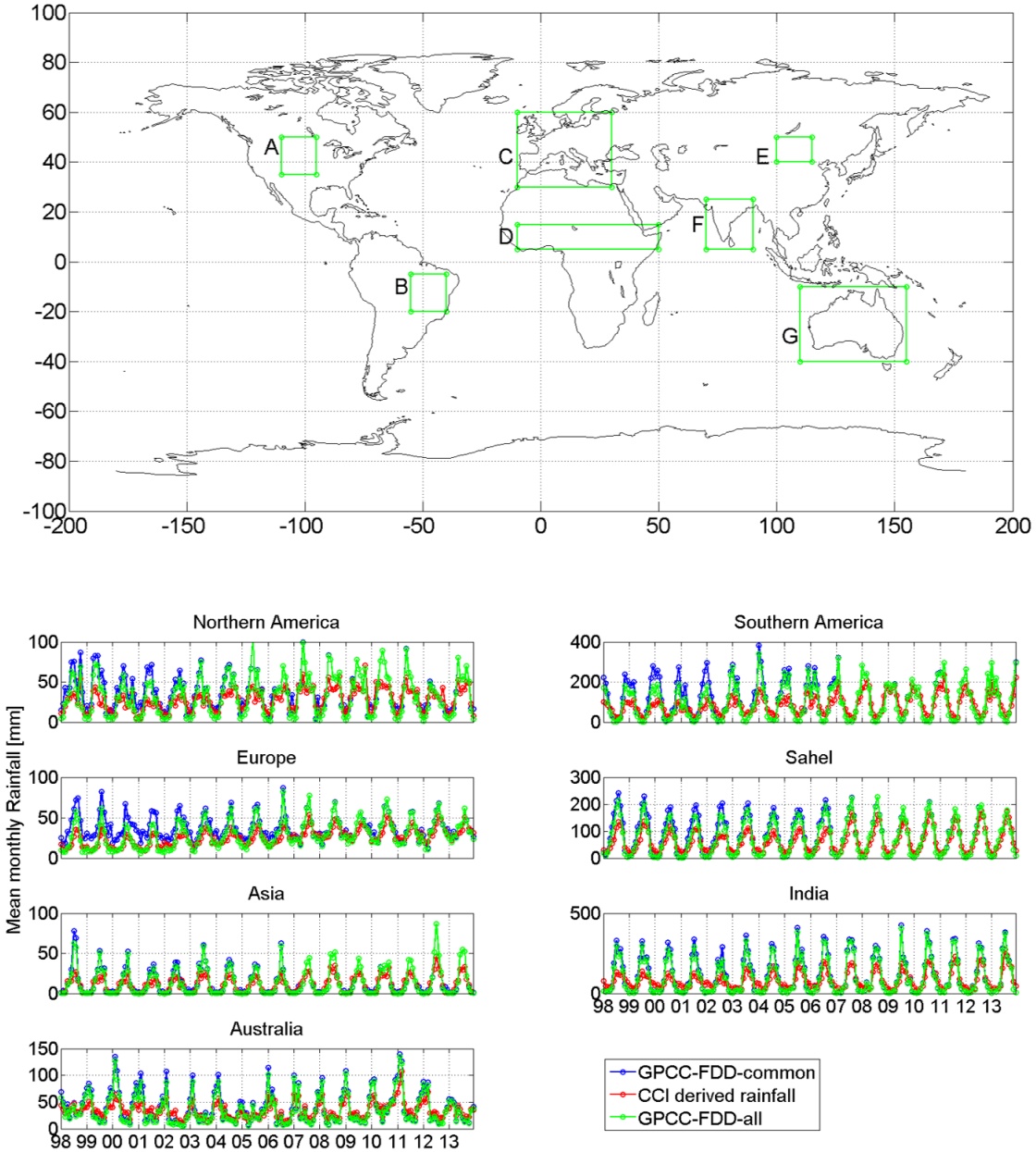

Figure 2.25 – Mean Monthly Rainfall estimated by GPCC-FDD (blue line) and the new CCI-derived rainfall data set (red line) over the six analysis boxes throughout North America (A), South America (B), Europe (C), Sahel (D), Asia (E), India (F) and Australia (G) during the period 1998-2013. The blue lines draw the Mean Monthly Rainfall estimated by GPCC-FDD when both a ground-based and a SM-derived rainfall estimate is available.

SM2RAIN-CCI performance over time

Figure 2.26 shows box plots of R and RMSD values between SM2RAIN-CCI and MSWEP on a yearly scale. The use of an independent benchmark removes the effect of the algorithm calibration against GPCC-FDD data set and (partly) the effect of in situ stations density on the benchmark reliability. The comparison is carried out over the ± 50° latitude band. The SM2RAIN-CCI rainfall product generally agrees well with MSWEP. An increasing trend in the performance can be observed over time during the analysis period, highlighting the impact of data availability on estimation uncertainty. The most significant improvements can be observed in 2003 and 2007, corresponding to the start of AMSR-E and ASCAT operations, respectively. ***Figure 2.35*** shows that the SM2RAIN-CCI product provides the lowest R (0.57) during 2001 and the highest (0.80) during 2013. Similar patterns are found for the RMSD score. The improvements are not just recognizable in the median values, but also in the spread of R and RMSD values within each year.

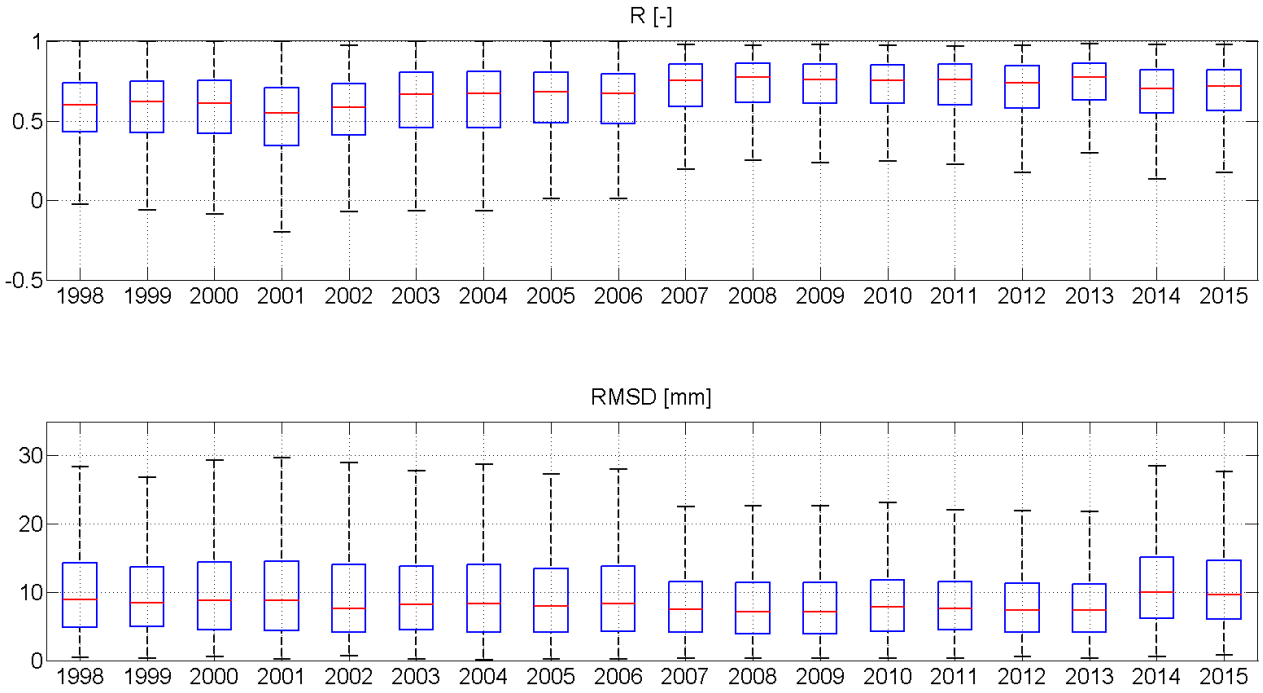

Figure 2.26 – Yearly boxplots for the correlation coefficients (R) and Root Mean Square Differences (RMSD, in mm) between SM2RAIN-CCI and MSWEP obtained on a global scale at 0.25° spatial resolution during the period 1998-2015. For each box, the red line represents the median values, the blue box the 25th and 75th percentile, while the black dotted whiskers extend to the most extreme data points.

Regional scale assessment

For the regional scale assessment, three macro-areas with a high rain gauge station density are selected, which are Europe, India, and Australia. SM2RAIN-CCI estimates are compared against data from these ground-based measurements on the 0.25° scale. The comparison over Europe is carried out by considering the so-called E-OBS rainfall data set (Haylock et al., 2008) as benchmark. This data set provides daily rainfall estimates over the European area at 0.25° spatial resolution starting from 1950. The estimates are obtained by interpolating via a three-step kriging procedure rainfall values from gauge stations over Europe. For this analysis, we consider the region between -9.875°W and 24.875°E longitude and between 28.125°N and 59.875°N latitude. Due to the TRMM orbit geometry, the considered TRMMRT data set covers only the area between

28.125°N and 49.875°N latitude. The analysis is carried out during the period 2002-2015, in order to avoid to consider partly the data calibrated during the period 1998-2001. ***Figure 2.27*** shows R and RMSD statistics against E-OBS for 5 days accumulated rainfall. As can be seen, SM2RAIN-CCI provides a median R lower than 0.5, close to that provided by TRMMRT and CMORPH. All rainfall products show a large variability in terms of R, ranging between -0.4 and almost 1. In terms of RMSD, all the products show median values close to 10 mm, with values ranging approximately between 5 and 20 mm. ERA Interim provided very good performance, both in terms of R and RMSD, due to the use of dense meteorological networks in Europe that guarantees good performance of the ERA-Interim reanalysis product. It is worth noting that ERA-Interim does not use raingauge data, but only other meteorological variables. MSWEP provided the best performance over Europe, due to the merging of different rainfall products. In general, SM2RAIN-CCI performs quite well in southern Europe (Italy, Spain and southern France). In central and northern Europe, observations are subject to a high selective masking of frozen soil and snow, which reduces the temporal observation density and hence also the SM2RAIN retrieval accuracy.

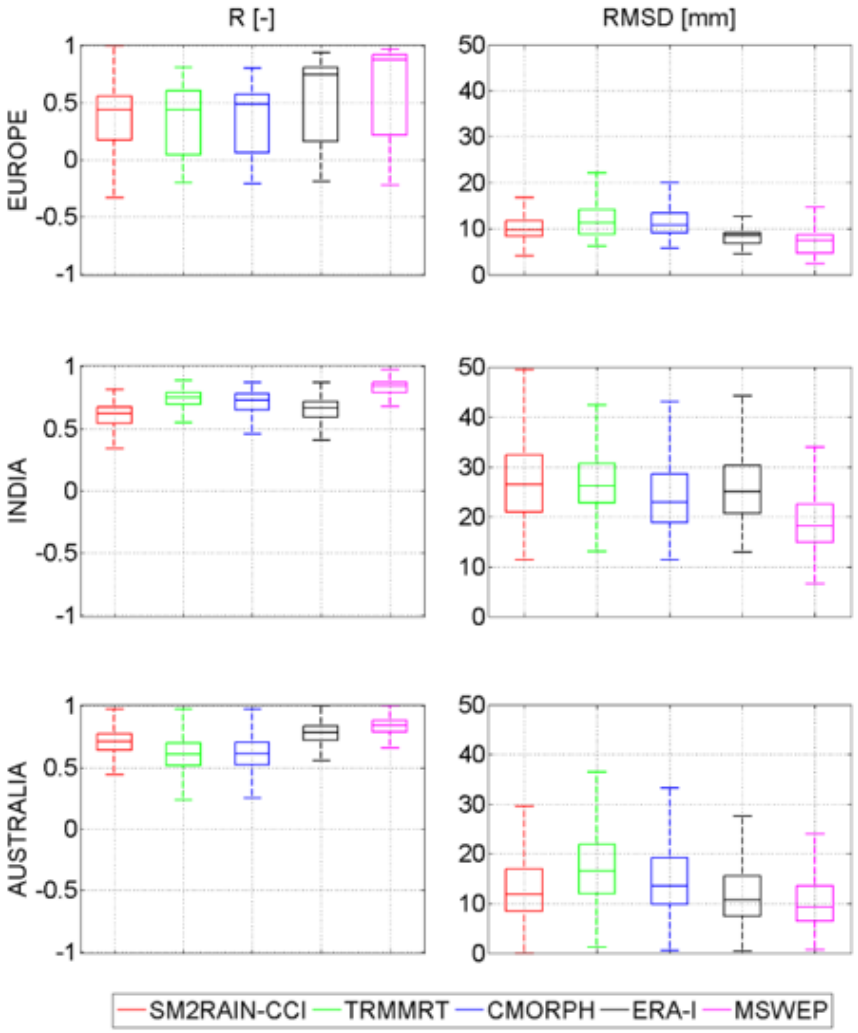

Figure 2.27 – Correlation coefficient (left) and Root Mean Square Difference (RMSD, right) box plots obtained by comparing SM2RAIN-CCI (in red), TRMMRT (in green), CMORPH (in blue), ERA-Interim (in black) and MSWEP (in magenta) with gauge-based data sets over Europe (top), India (middle) and Australia (bottom).

The analysis over India is carried out during the period 2002-2015 using observed rainfall data provided by the India Meteorological Department (IMD). The considered region spans from 70°E to 90°E longitude and from 5°N to 25°N latitude. As can be seen in ***Figure 2.27***, R values are generally higher than those obtained over Europe, most likely due to the strong seasonal signal. The SM2RAIN-CCI data set shows a median R of 0.60, which is slightly lower than that achieved by TRMMRT, CMORPH, ERA Interim and MSWEP. In terms of RMSD, values are generally higher than over Europe, which result from the larger annual precipitation amount. SM2RAIN-CCI performs very well over India, and is less reliable along the coast and in the Northern parts of the country due to the impact of the Himalaya.

Over Australia, the Australian Water Availability Project (AWAP) observed rainfall data during the period 2010-2013 is used as benchmark. The analysis box spans from 120°E to 160°E longitude and from 10°S to 40°S latitude. The analysis shows very good results both in terms of R and RMSD (***Figure 2.27***). SM2RAIN-CCI provides a median R of 0.71 which is higher than that obtained with TRMMRT and CMORPH. Moreover, R values are consistently higher than 0.5 in the entire macro-region. In terms of RMSD, median value of 11.90 mm is obtained for SM2RAIN-CCI, while TRMMRT and CMORPH provided median values of 16.56 mm and 13.52 mm, respectively. The large variability of errors is related to the different rainfall regimes in Australia, i.e. tropical climate in the northern sector and drier conditions in the inland part. In tropical rainfall regimes, the SM2RAIN algorithm is often subject to close-to-saturation soil conditions, which lead to a general underestimation of precipitation. Results are consistent with those of Tarpanelli et al., (2017) over India.

3.HYDROLOGICAL VALIDATION

The hydrological validation of satellite rainfall products is carried out over some basins in Italy, to further assess their quality and reliability. The use of satellite-based rainfall data in the hydrological modeling is a challenging task, as rainfall estimation is impacted by several factors (see previous sections). These errors have a significant impact on the hydrological simulation and propagates forward in time for several months. As a result, any short period in which rainfall estimates are less accurate produces remarkable errors in the simulation of discharge through rainfall-runoff modeling. While a large amount of work is carried out to quantify these errors, comparatively, little work is done to quantify the implications of these errors on derived predictions of hydrological models. Because of the strong nonlinearities of hydrological models, precipitation errors can be amplified or dampened in flood simulations and this response likely depends upon the interactions between the model itself and the quality of the underlying satellite rainfall product. In order to quantify the impact of satellite rainfall data into hydrological modeling, the use of ad-hoc model recalibration, bias correction, and rainfall integration are tested over river basins characterized by different morphologic features, size, geographical areas and climatic conditions.

3.1 Rainfall-runoff modelling over Italy

This section shows the performance of satellite rainfall products over four basins in Italy. A semi-distributed model is forced with TMPA 3B42RT and SM2RAIN derived rainfall data. The simulated discharge time series are then compared with observed data in order to assess the feasibility of using remotely sensed information. The integration of ground- and satellite-based rainfall data is investigated as well. the following section is based on the publication:

Ciabatta, L., Brocca, L., Massari, C., Moramarco, T., Gabellani, S., Puca, S., Wagner, W. (2016a). Rainfall-runoff modelling by using SM2RAIN-derived and state-of-the-art satellite rainfall products over Italy. International Journal of Applied Earth Observation and Geoinformation, 48, 163-173.

Study areas

Four basins throughout the Italian territory are considered in this analysis, specifically the Brenta, the Tanaro (Northern Italy), the Tiber (Central Italy) and the Volturno (Southern Italy) basins. The elevation maps reported in ***Figure 3.1***, and the main features listed in ***Table 3.1***, highlight the differences between the basins: Tanaro is the biggest basin and is characterized by a mountainous area upstream and a large flood plain downstream. Brenta is the smallest one, mainly mountainous and it is characterized by the highest rainfall regime (see ***Table 3.1***). These two first basins are characterized by mountainous areas where snow fall might occur during winter. Tiber basin is characterized by a quite large flood plain in the central area of the basin surrounded by hills and it has the lowest rainfall regime.

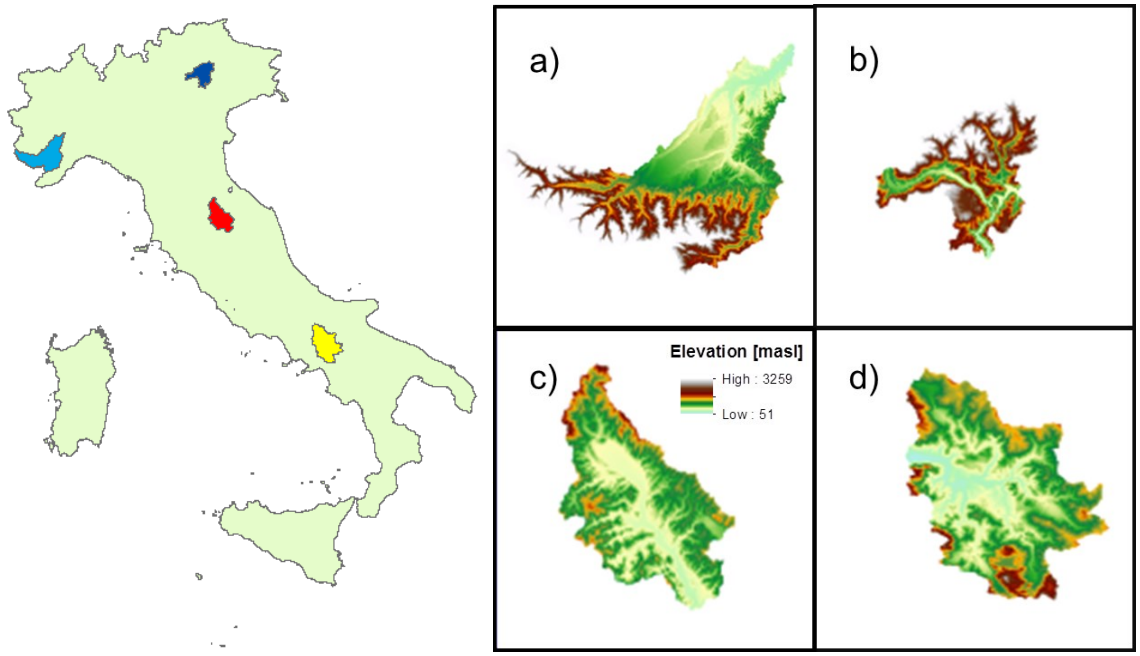

Figure 3.1 – Geographical location and elevation of the a) Tanaro River basins, b) Brenta River basin, c) Tiber River basin and d) Volturno River basin (not in scale).

Volturno basin is mainly flat with the presence of some low elevation mountains in the southern part of the basin. The basins are selected in four sectors of the Italian territory (North-Eastern, North-Western, Central and Southern Italy) in order to investigate different physiographic and climatic conditions. Moreover, basin selection is driven from the availability of good quality meteorological and discharge observations (based on the study by Massari et al., 2015), and from the suitability of the employed hydrological model, MISDc, as it does not incorporate a snow melting module.

Basin	Gauging station	Area (km^2)	MAR (mm)	MAT (°C)	Average altitude (m a.s.l.)	Average slope (°)
Tanaro	Asti S. Martino	3229.7	1125	8.94	1025	15.59
Brenta	Berzizza	1506.3	2123.8	7.04	1239	22.53
Tiber	Ponte Felcino	1879	967.76	13.22	518	10.76
Volturno	Solopaca	2578.8	1208.1	13.33	543	8.80

Table 3.1 - Main characteristics of the investigated basins: gauging station, drainage area, Mean Annual Rainfall (MAR), Mean Annual Temperature (MAT), average elevation (in m a.s.l.) and average slope (in °).

Rainfall products

Ground-based rainfall, temperature and discharge data at hourly temporal resolution are provided by the Italian hydrometeorological network of the National Civil Protection Department. For a complete description of the observed dataset, the reader is referred to Massari et al. (2015). Specifically, the observed rainfall dataset is provided by the interpolation of more than 3000 raingauges throughout the Italian territory (Ciabatta et al., 2015).

The SRPs considered in this study are the TMPA 3B42-RT product (Huffman et al., 2007), hereinafter TMPA, and the dataset obtained by applying the SM2RAIN algorithm (Brocca et al., 2013; 2014) to the Advanced SCATterometer (ASCAT) SM data (Wagner et al., 2013), hereinafter $SM2R_{ASC}$.

The TMPA product combines rainfall estimates from various satellite sensors. The multi-satellite platform uses TRMM Microwave Imager (TMI), the Special Sensor Microwave Imager (SSM/I) onboard Defense Meteorological Satellite Program (DMSP) satellites, the Advanced Microwave Scanning Radiometer-Earth Observing System (AMSR-E) and the Advanced Microwave Sounding Unit-B (AMSU-B) onboard the National Oceanic and Atmospheric Administration (NOAA) satellites. In addition, the TMPA product also uses geostationary (GEO) satellite infra-red (IR) data, characterized by higher spatial and temporal resolution than the Microwave (MW) sensors, through a constellation of GEO satellites. The TMPA product is provided by the National Aeronautics and Space Administration (NASA, http://trmm.gsfc.nasa.gov/) with a temporal resolution of 3 hours and a spatial resolution of 0.25° for the ± 50° North-South latitude band. Although a gauged corrected TMPA 3B42 product version is also available, in this study such product is not used in order to evaluate the feasibility of using SRPs in an operational framework, i.e., for real-time flood forecasting.

The second dataset is obtained by the application of the SM2RAIN algorithm (Brocca et al., 2013, 2014; Ciabatta et al., 2015) to the Surface Soil Moisture (SSM) product obtained from ASCAT (Wagner et al., 2013), a scatterometer operating at 5.3 GHz onboard MetOp A and B satellites. Specifically, the Water Retrieval Package (WARP) 5.51 product is used in this study to estimate rainfall from SM data. The product has a resolution of 25 km (resampled at 12.5 km, Wagner et al., 2013) and is provided within the H-SAF project (http://hsaf.meteoam.it). For more details about SM2RAIN algorithm, the reader is referred to (Brocca et al., 2013, 2014; Ciabatta et al., 2015),

while a first application using the algorithm SM2RAIN for flood prediction through in situ SM data can be found in Massari et al. (2014). In this study, the same SM2RAIN-derived product as considered in Ciabatta et al. (2015) is employed.
Both SRPs and the observed rainfall data are remapped over a grid with spacing of 12.5 km, using the nearest neighbor algorithm. As described in Ciabatta et al., (2015), the selected spacing is a compromise between the resolution of the different rainfall datasets and it was found to not significantly affect the results. The one-day cumulated rainfall at 00:00 UTC+1 for each analyzed dataset is considered in this study. Although TMPA data are provided within a time window ± 90 minutes from the nominal time (0000,0300,…,2100 UTC), all the remaining data are released in local time, i.e. UTC +1. This allows to compare TMPA data with the other datasets with only 30 minutes of delay.
In order to match the different temporal resolutions, the analysis is carried out at a daily time scale, and hence, the mean observed discharge, mean temperature and the accumulated rainfall during one day are computed and considered in the sequel.

Bias correction

In order to take into account, the systematic errors due to the indirect measurement of rainfall by satellite sensors (Kucera et al., 2013), a bias correction is applied to each SRP. The applied correction allows to match the mean and the standard deviation of SRPs with the observed rainfall data. The correction applied in this study is expressed by:

$$P_{corr} = \left(\frac{P_{sat} - \overline{P_{sat}}}{\sigma_{sat}} \right) \sigma_{obs} + \overline{P_{obs}} \tag{3.1}$$

where P_{corr} is the bias corrected SRP, P_{sat} is the original SRP, $\overline{P_{sat}}$ is the temporal mean of SRP, σ_{sat} is the standard deviation of SRP, $\overline{P_{obs}}$ is the temporal mean of observed rainfall, and σ_{obs} is the standard deviation of observed rainfall. This formulation, originally applied by Draper et al. (2009) and Brocca et al. (2011a) to satellite SM data, is simple to implement in an operational framework and allows to correct the bias of SRPs. The correction is applied in the calibration period before the computation of the mean areal rainfall. In the validation period, the same correction is applied without changing the correction coefficients.

Mean areal rainfall

The mean areal rainfall for each basin is obtained by considering the contribution of each pixel inside the basin by using the following equation:

$$P_A = \sum_{i=1}^{N} \frac{p_i a_i}{A_{tot}} \tag{3.2}$$

where P_A is the mean areal rainfall amount, p_i is the rainfall for the pixel i within a polygon of area a_i that represents the portion of the basin area covered by the pixel i, and A_{tot} is the total basin area.

Integration scheme

The integration of satellite and ground observed rainfall datasets is carried out by using the following nudging scheme:

$$P_{\text{int}}(t) = P_{sat}(t) + K\left[P_{obs}(t) - P_{sat}(t)\right] \tag{3.3}$$

where t is the time, P_{int} is the integrated rainfall, P_{sat} is the satellite rainfall, P_{obs} is the observed rainfall, and K is the weight factor that ranges between 0 and 1. For K=1, only the observed rainfall is considered, while for K=0 only the satellite products are used as input into the model. The K-values are obtained through calibration, by maximizing the Nash-Sutcliffe efficiency index (NS) between the observed and simulated discharge during the calibration period.
To sum up, a total of 5 different rainfall datasets are used in this study:

1. Observed rainfall (hereinafter OBS);
2. Bias corrected SM2RAIN-derived rainfall dataset ($SM2R_{ASC}$);
3. Bias corrected TMPA 3B42-RT (TMPA);
4. Integrated rainfall dataset between OBS and $SM2R_{ASC}$ (hereinafter $SM2R_{ASC}$+OBS);
5. Integrated rainfall dataset between OBS and TMPA (hereinafter TMPA+OBS).

MISDc rainfall-runoff model

The lumped version of the continuous and semi-distributed rainfall-runoff model MISDc (***Figure 3.2***), proposed by Brocca et al. (2011b) is adopted here. MISDc is a single layer model and it was specifically developed for flood forecasting purposes, as a consequence it may have limitations in reproducing accurately the low flow conditions which in turn may determine volume errors in the long-term comparison between observed and simulated discharge. MISDc couples a routing module with a single layer soil water balance module (Brocca et al., 2008). Soil water balance is based on the following equation:

$$\frac{dW(t)}{dt} = [p(t) - p_e(t)] - e(t) - g(t) \tag{3.4}$$

where $W(t)$ is the soil water content at time t, $p(t)$, $p_e(t)$, $e(t)$ and $g(t)$ are the rainfall, effective rainfall, actual evapotranspiration and percolation rates, respectively.

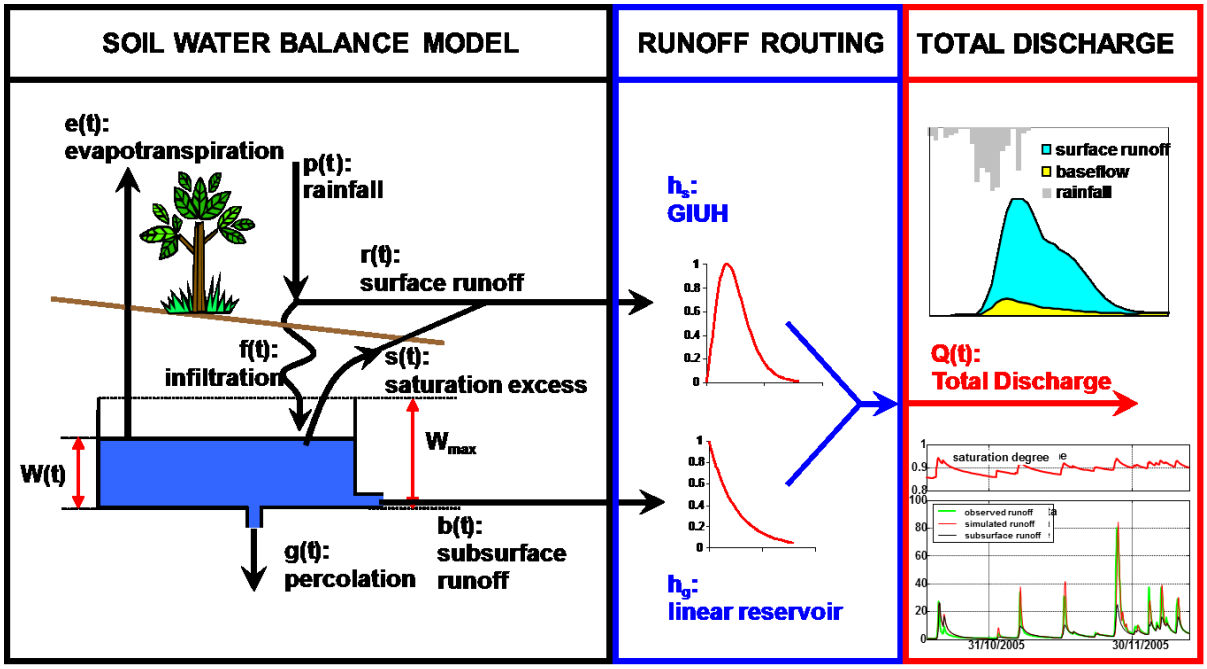

Figure 3.2 - Schematization of the MISDc rainfall-runoff model with the representation of the simulated hydrological processes.

In ***Eq. 3.4***, *e(t)* is calculated as a linear function between the potential evaporation, that is estimated via the Blaney and Criddle relation modified by Doorembos and Pruitt, (1977), and the soil saturation. The non-linear relation proposed by Famiglietti and Wood (1994) is used for the computation of the percolation rate, *g(t)*. The rainfall excess, $p_e(t)$, is calculated by using the well-known Soil Conservation Service–Curve Number (SCS-CN) method for estimation of losses incorporating the relationship between soil saturation and the parameter *S* (soil potential maximum retention) of the SCS-CN method as proposed by Brocca et al. (2009). Three different components contribute to generate discharge: the surface runoff, the saturation excess and the subsurface runoff component. The first two are summed and routed to the outlet by the Geomorphological Instantaneous Unit Hydrograph (GIUH). The subsurface runoff is transferred to the outlet section by a linear reservoir approach. For both routing schemes, the lag time is evaluated by the relationship proposed by Melone et al. (2002). Full details on model equations are already given in Brocca et al. (2009; 2011) and, hence, are not repeated here. The MATLAB® code of the model is freely available at: http://hydrology.irpi.cnr.it/download-area/midsc-code/.
MISDc uses 8 parameters, i.e., the maximum soil water capacity, the pore size distribution index, the saturated hydraulic conductivity, the fraction of percolated water that generates baseflow, the lag-area relationship coefficient, a correction parameter for the evapotranspiration, the initial abstraction coefficient of the SCS-CN method and the coefficient of the relationship relating SM to the initial condition of the SCS-CN method. As input data, the model needs continuous rainfall and temperature timeseries. The calibration step is carried out in MATLAB® environment by using a standard gradient-based automatic optimization method (Bober, 2013) and the maximization of the Nash-Sutcliffe efficiency index is considered as objective function.

Performance metrics

The assessment of the model performances, driven by ground rainfall observations and SRPs, is carried out in terms of Nash-Sutcliffe efficiency (*NS*), correlation coefficient (*R*) and percentage volume error (E_v). *NS* is often used for hydrological modelling assessment and it ranges between -∞ and 1. The closer the index is to 1, the better the performance is. *NS* index is defined as:

$$NS = 1 - \frac{\sum_{t=1}^{n}\left(Q_{obs} - Q_{sim}\right)^2}{\sum_{t=1}^{n}\left(Q_{obs} - \overline{Q_{obs}}\right)^2} \tag{3.5}$$

where Q_{obs} and Q_{sim} are the observed and simulated discharge at time *t*, while $\overline{Q_{obs}}$ is the temporal mean of observed discharge.
The percentage volume errors, E_v, is expressed by the following equation:

$$E_v = \frac{\sum_{t=1}^{n} Q_{obs} - \sum_{t=1}^{n} Q_{sim}}{\sum_{t=1}^{n} Q_{obs}} 100 \tag{3.6}$$

Positive E_v values indicate discharge underestimation while negative ones, an overestimation. The performance metrics are calculated during both the calibration and validation period, for each rainfall input dataset.

For each basin, the most significant flood events are extracted in order to assess the capability of the considered rainfall datasets in reproducing the flood hydrograph, volume and peak at the event-scale. The evaluation is carried out by considering the indexes described above, computed for each flood event, and by using the percentage error in peak discharge, expressed by the following equation:

$$E_{Qp} = \frac{\max(Q_{obs}) - \max(Q_{sim})}{\max(Q_{obs})} \tag{3.7}$$

A negative error highlights overestimation, while a positive value means underestimation.

Results and discussions

The hydrological validation of satellite rainfall datasets is described for both the calibration and the validation period, for each of the 5 rainfall datasets, and over the 4 selected basins considered in the study.

Rainfall datasets comparison

First, an intercomparison of rainfall datasets is carried out in order to evaluate the quality of input data used to drive MISDc model. This analysis is carried out by considering *R* and the root mean square error (*RMSE*) between the daily ground and the satellite mean areal rainfall during the calibration and the validation periods. Results, reported in ***Table 3.2***, show a satisfactorily agreement between the ground and satellite derived rainfall datasets. SM2R$_{ASC}$ provides lower performance scores than TMPA: this is probably due to the algorithm calibration procedure, based on 5 days of accumulated rainfall (Ciabatta et al., 2015). All the analysed datasets provide *R* values higher than 0.48 and quite low *RMSE* values. The higher *RMSE* values over Brenta basin are due to the high rainfall regime and the presence of mountains that might affect the satellite retrievals accuracy. The obtained results are in line with those showed by Ciabatta et al. (2015) who obtained median *R* values over the Italian territory equal to 0.44 and 0.59 for SM2R$_{ASC}$ and TMPA, respectively, for 1 day of accumulated rainfall. Moreover, similar results are also obtained by Stampoulis and Anagnostou (2011) and Nikolopoulos et al. (2013) who evaluated the real-time TMPA product over Northern Italy.

	SM2R$_{ASC}$				**TMPA**			
Basin	**CAL**		**VAL**		**CAL**		**VAL**	
	R	***RMSE***	***R***	***RMSE***	***R***	***RMSE***	***R***	***RMSE***
Brenta	0.56	14.97	0.49	14.91	0.70	12.78	0.66	13.55
Tanaro	0.60	7.56	0.48	6.96	0.79	5.94	0.69	6.52
Tiber	0.54	7.00	0.49	7.66	0.71	5.73	0.83	9.25
Volturno	0.63	6.10	0.60	5.80	0.64	6.07	0.63	5.78

Table 3.2 – Correlation coefficients (R) and Root Mean Square Error (RMSE) for the analysed satellite products (SM2R$_{ASC}$ and TMPA) against observed rainfall during the calibration (CAL) and validation (VAL) periods.

Discharge simulation with ground observed rainfall

The performance scores obtained by forcing MISDc model with OBS are assessed in order to evaluate the model capability in reproducing observed discharges and are used as benchmark to highlight any increase (or deterioration) in model accuracy when using SRPs.

Figure 3.3 shows the simulated discharge timeseries obtained by forcing MISDc with OBS data. As it can be seen, the model is able to reproduce the observed discharge well, showing *NS* values of 0.72, 0.76, 0.77 and 0.86 during the calibration period (2010-2011) for Brenta, Tanaro, Tiber and Volturno basins, respectively. During the validation period (2012-2013), the simulations provide *NS* values of 0.76, 0.68, 0.52 and 0.77 with only a slight deterioration of model performance. In terms of correlation, the model provides *R* values greater than 0.86 (0.77) during the calibration (validation) period. For what concerns the errors in volume, MISDc simulations provide E_v values lower than 23% in calibration and lower than 15% during the validation step. These not negligible errors in volume are partly due to the difficulties of the model in reproducing the low flows and to the objective function used for model calibration (maximization of *NS*) that is mainly addressed for the reproduction of high flows. In addition, as it can be noticed by ***Figure 3.3***, some discharge peaks are not correctly identified, as over Brenta basin during the calibration period and over Tanaro in 2011. These errors might be due to different causes, for example the inaccuracy of input observations and the modelling structure, to the effect of spatial variability that is neglected here, and to the daily time step used for the simulation that could be not fully appropriate for fast responding basins.

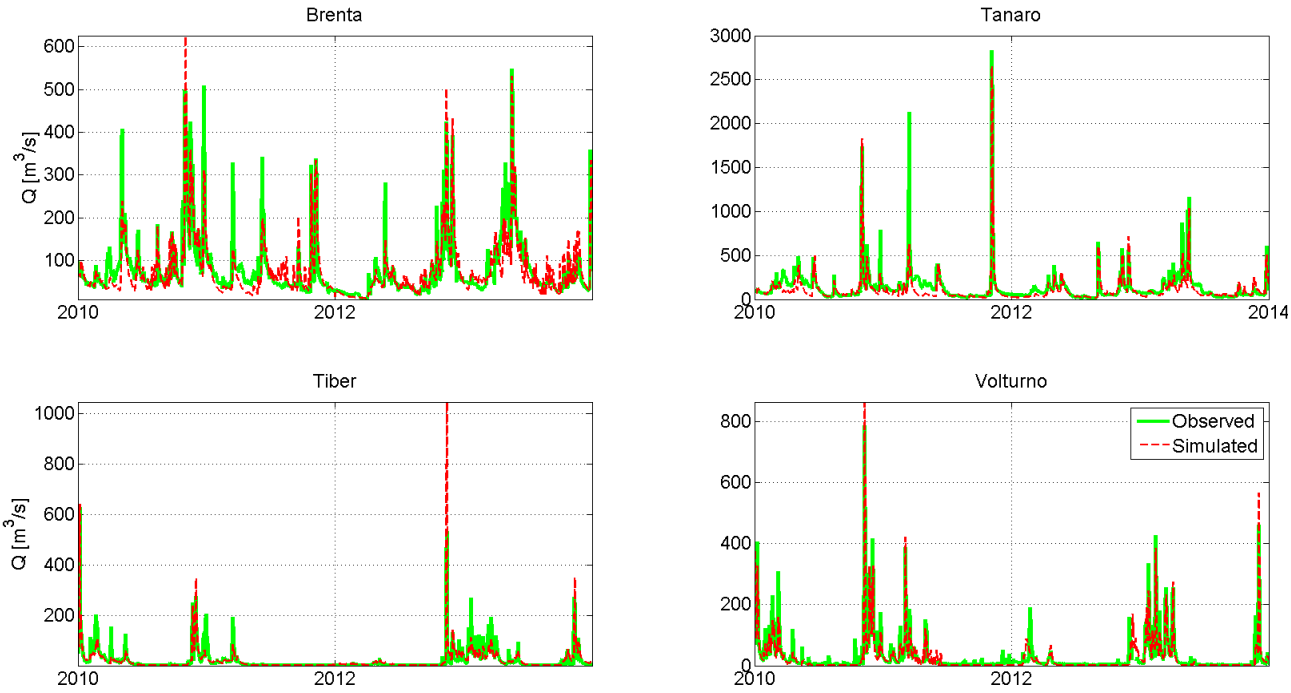

Figure 3.3 - Comparison of observed and simulated discharge obtained by forcing MISDc model with ground observed rainfall for Brenta (up-left), Tanaro (up-right), Tiber (bottom-left) and Volturno (bottom-right) basins, during the entire analysis period (2010-2013).

Despite these limitations, MISDc confirms its good capability in simulating floods, also in different physiographic and climatic conditions in Italy, thus representing an useful tool for testing the

potential added-value of SRPs for flood forecasting. All the performance scores obtained with each rainfall product, for the calibration and validation period, are summarized in ***Table 3.3***.

Basin	Calibration (2010-2011)			Validation (2012-2013)		
	NS	***R***	***E_v (%)***	***NS***	***R***	***E_v (%)***
OBS						
Brenta	0.72	0.86	6	0.76	0.88	4
Tanaro	0.76	0.89	23	0.68	0.83	11
Tiber	0.77	0.88	16	0.52	0.77	-15
Volturno	**0.86**	**0.93**	14	**0.77**	**0.88**	**5**
SM2R$_{ASC}$						
Brenta	0.63	0.73	*-2*	0.52	0.73	-4
Tanaro	0.60	0.78	***13***	0.48	0.70	*-10*
Tiber	0.66	0.81	***3***	0.48	0.70	***-1***
Volturno	0.63	0.79	*-3*	0.48	0.72	-32
TMPA						
Brenta	0.32	0.60	9	0.20	0.49	6
Tanaro	0.76	0.89	*19*	-0.22	0.49	*-4*
Tiber	0.53	0.73	16	-0.23	0.42	-27
Volturno	0.37	0.61	*6*	0.07	0.36	36
SM2R$_{ASC}$+OBS						
Brenta	***0.78***	***0.89***	***1***	***0.79***	***0.88***	-5
Tanaro	***0.78***	0.89	*21*	***0.71***	***0.85***	*9*
Tiber	***0.81***	***0.90***	*10*	***0.74***	***0.86***	*-6*
Volturno	0.77	0.88	***1***	0.63	0.82	-34
TMPA+OBS						
Brenta	*0.77*	*0.88*	*3*	0.74	0.87	**-4**
Tanaro	*0.79*	***0.90***	*20*	0.47	0.73	***3***
Tiber	*0.77*	0.88	17	0.36	*0.81*	*-14*
Volturno	0.75	0.87	*5*	0.61	0.81	-26

Table 3.3 - Nash-Sutcliffe efficiency (NS), correlation coefficient (R) and percentage volume error (E_v) obtained by forcing MISDc hydrologic model with observed, satellite (SM2R$_{ASC}$ and TMPA) and integrated (SM2R$_{ASC}$+OBS and TMPA+OBS) rainfall data, during the calibration (2010-2011) and validation (2012-2013) periods. In bold font the best performance scores of each basin are reported while the scores are in italic font if better than those obtained with ground observed rainfall (OBS). The highest performance of the integrated SM2R$_{ASC}$+OBS product for Brenta, Tanaro and Tiber river basins is evident.

Discharge simulation with satellite rainfall products

Before introducing the bias correction and recalibration steps into the workflow, discharge simulations are carried out by using the raw SRPs. By way of example, ***Figure 3.4*** shows the

observed and simulated hydrographs for Tanaro basin obtained by forcing MISDc with TMPA rainfall dataset without and with the application of the bias correction step.

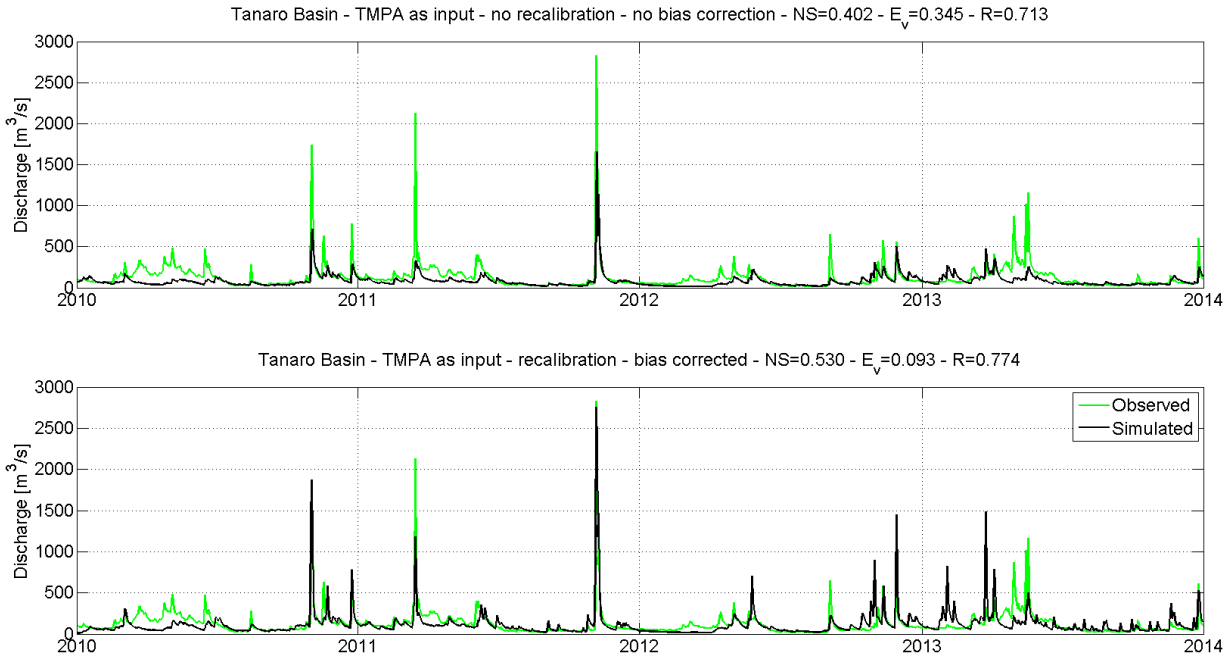

Figure 3.4 - Observed and simulated hydrographs obtained by forcing MISDc model with TMPA data before (upper panel) and after (lower panel) bias correction and model recalibration.

As it can be seen, if the model is forced with bias corrected data and after the recalibration, higher performances are obtained. Indeed, the obtained performance scores, before and after the bias correction and the model recalibration, increase from *NS*=0.40, *R*=0.71 and E_v=35%, to *NS*=0.53, *R*=0.77 and E_v=9%. Although the improvement is not so significant, the effect of the two pre-processing steps is evident. In most of the cases (results not shown for brevity) the simulations carried out by using corrected data provide higher performance scores than those obtained by using the raw data. Exceptions are found for the Brenta and Tanaro during the validation period for TMPA and for Brenta and Volturno during the calibration period for $SM2R_{ASC}$. These results may be due to the high variability of the rainfall regime from year to year which would need a dynamic correction of the bias or its more frequent recalibration. On this basis, the correction of the bias is in general beneficial but may also provide additional uncertainties in case the rainfall presents a high non-stationary character. Moreover, it is obtained that after the recalibration, all the parameter values remained into a physically acceptable range of variation thus ensuring the consistency of the hydrological simulations. The small but consistent improvement in hydrological model performance after bias correction of TMPA product (and model recalibration) is also obtained by Artan et al. (2007) for two sub-basins of Mekong River in South Asia, Stisen and Sandhot (2010) for the Senegal River basin in West Africa, Tarnavsky et al. (2013) in Senegal and Tunisia, and Zhao et al. (2015) in the Weihe River basin in China. Therefore, due to the overall improved performances, in the following we show only results in which SRPs bias is corrected through ground observations and the model parameter values are recalibrated for each SRP (in the calibration period).
The comparison between observed and simulated discharge obtained by using TMPA and $SM2R_{ASC}$ as input is reported in ***Figure 3.5***. Although a general agreement between observed and simulated

discharge is recognizable, some peaks are not identified (mainly in the Brenta basin) or overestimated (Tanaro and Tiber basins) likely due to errors in the SRPs used here as input data.

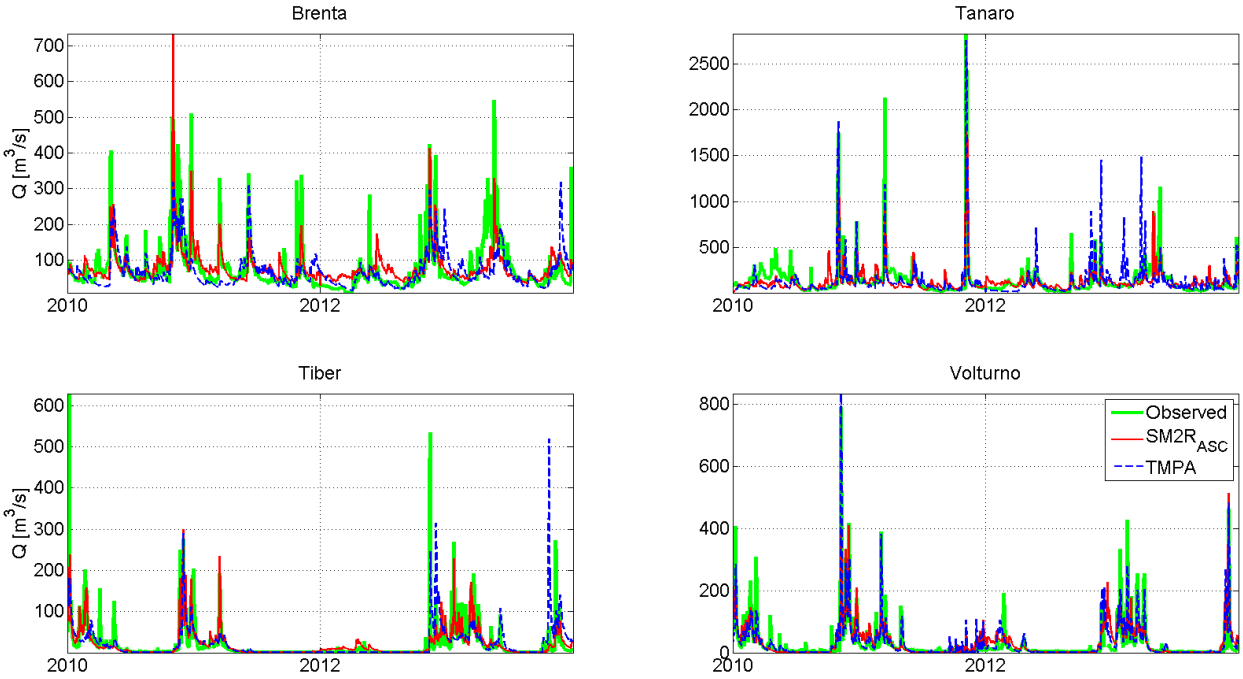

Figure 3.5 - Comparison of observed and simulated daily discharge obtained by forcing MISDc model with the two satellite rainfall products SM2RASC and TMPA for Brenta (up-left), Tanaro (up-right), Tiber (bottom-left) and Volturno (bottom-right) basins, during the entire analysis period (2010-2013).

More specifically, when $SM2R_{ASC}$ is used as input, a deterioration of the results with respect to those obtained by using OBS is found, with *NS* values of 0.63 (0.52) for Brenta, 0.60 (0.48) for Tanaro, 0.66 (0.48) for Tiber and 0.63 (0.48) for Volturno during the period 2010-2011 (2012-2013). The lower scores are probably due to SM2RAIN algorithm limitations, i.e., underestimation of rainfall when the soil is close to saturation and to the presence of mountains and/or snow within the basin that affects the SM data quality (and, hence, of the SM2RAIN-derived rainfall). The first issue can be easily observed over the Tiber basin at the end of 2012, when a discharge peak of over 500 m^3/s is not identified. The latter issue is evident over Brenta and Tanaro basins characterized by higher uncertainty in SM data and a general underestimation of river discharge. In terms of correlation coefficient, $SM2R_{ASC}$ still provides fair *R* values for all the analysed basins: during the calibration (validation) period *R* values greater than 0.73 (0.70) are obtained for the analysed basins. In terms of errors in volume, quite low E_v values are observed during the calibration (validation) period: -2% (-4%) for Brenta, 13% (10%) for Tanaro, 3% (-1%) for Tiber and -3% (-32%) for Volturno. The negative values, mainly obtained during the last two years of the analysis period, highlight an overestimation of discharge.

When MISDc is forced with TMPA, lower *NS* values are obtained, even negative during the validation period. *R* values are greater than 0.60 (0.36) during the calibration (validation) period and an overall discharge underestimation is observed with E_v values lower than 6% and 36% in the calibration and validation period, respectively. It is likely that the lower performance scores are due to the accuracy of the TMPA product, which is highly affected by topographic issue and by the type and intensity of precipitation. Indeed, Ciabatta et al. (2015) highlighted that TMPA product shows

low performance in Southern Italy and in areas characterized by an intense rainfall regime (e.g., Brenta basin). Moreover, the low and even negative scores obtained during the validation period are likely due to the need of a more frequent correction of the bias in order to take into account its variability due also to the changes in the retrieval algorithms and measurement sensors (note that the TMPA product is based on measurements from a constellation of satellite sensors that are changing in time). A monthly analysis (not shown) was also carried out in order to investigate the reasons of the low performance of MISDc using TMPA during the validation period and by analysing both rainfall and discharge data. The analysis has shown that the performance in terms of rainfall reproduction (by using ground observations as benchmark) of TMPA during the validation period are highly variable (much more that in the calibration period), with some months in which the performance reaches very low values (e.g., R<0.2). Therefore, it appears that any error or performance reduction in rainfall estimation have a significant impact on the hydrological simulation and propagates forward in time for several months. As a result, any short period in which rainfall estimates are less accurate produces remarkable errors in the simulation of discharge and it is the main reason for the observed low performance of TMPA in the validation period.
In Italy, just a work by Nikolopoulos et al. (2013) evaluated the reliability of different SRPs for discharge simulation but their study was addressed to the simulation of only a limited number of flood events and not a continuous simulation such as we have performed here. The obtained performances are in agreement anyhow with those obtained by previous studies in different regions worldwide (Artan et al., 2007; Stisen and Sandhot, 2010; Zhao et al., 2015). We note also that the discharge simulation in Mediterranean areas is more complex than that one for large basins in Africa or South Asia that are characterized by a consistent and pronounced seasonal cycle and that are the basins in which most of the studies were carried out by employing SRPs (see Serrat-Capdevilla et al., 2013 for a review). Therefore, the results obtained here highlight that SRPs may be employed with some skill also in smaller basins of the Mediterranean region.

Discharge simulation by using the integrated rainfall datasets

The integration procedure between ground observed and satellite rainfall by using ***Eq. 3.3*** provides improvements in the performance scores, showing *NS* values most of the times (for 3 out 4 basins) higher than those obtained by using observed rainfall, mainly for $SM2R_{ASC}$+OBS product (see bold numbers in ***Table 3.3***). ***Table 3.4*** reports *K* values obtained during the calibration period for each rainfall dataset. The simple integration scheme here proposed involves very high values of *K*, except for TMPA+OBS in the Tanaro basin that shows the lowest *K* value equal to 0.5. It should be noted that the high weight given to ground observations is expected due the high quality of ground observed rainfall datasets used in this analysis.

Basin	$SM2R_{ASC}$+OBS	TMPA+OBS
Brenta	0.8	0.9
Tanaro	0.8	0.5
Tiber	0.7	0.9
Volturno	0.8	0.9

Table 3.4 - Integration coefficient (K) for the considered basins by using as model input the integrated products between the observed and satellite products (SM2RASC+OBS and TMPA+OBS).

As it can be noticed in ***Figure 3.6***, the use of the integrated datasets into MISDc allows to obtain an accurate discharge simulation over the four analysed basins. It is worth to notice that some of the discharge peaks are still not properly identified by the simulated discharge. This is not due to the SRPs quality, as the same events are also not well captured in the simulations carried out by using OBS as input (see ***Figure 3.3***). Therefore, these errors have to be attributed to the MISDc model deficiencies in representing the hydrological behaviour of the basins throughout the year.

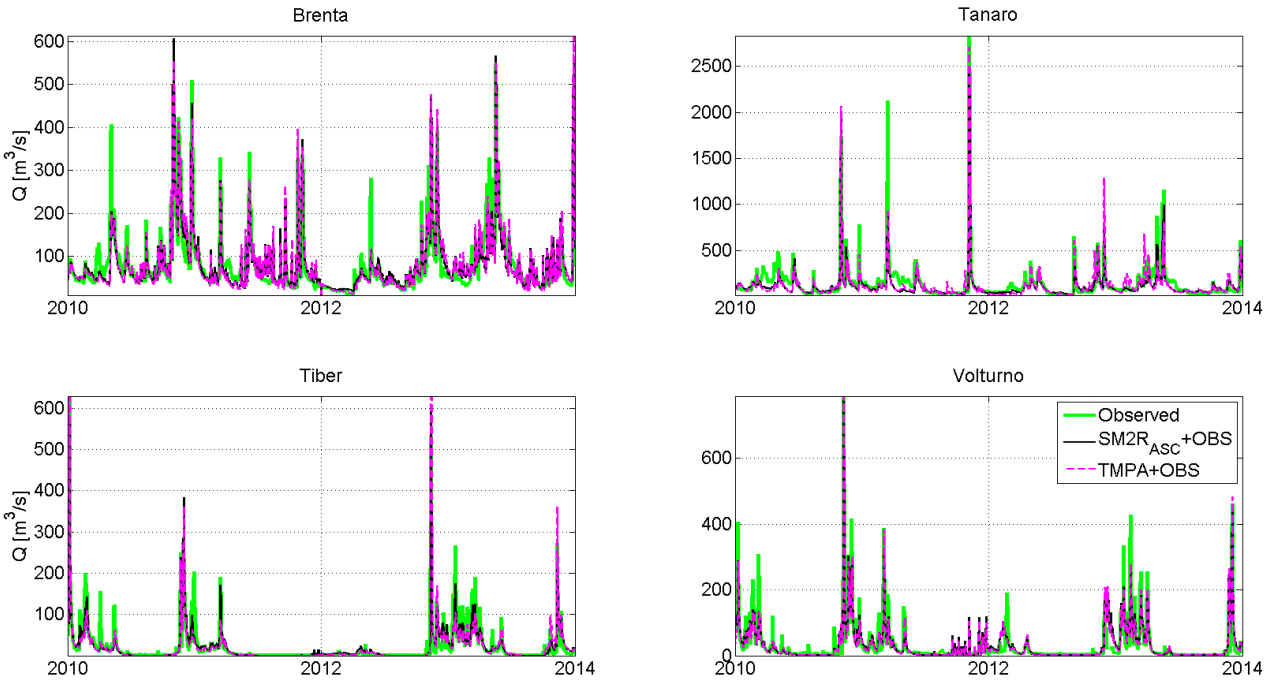

Figure 3.6 - Comparison of observed and simulated daily discharge obtained by forcing MISDc model with the two integrated rainfall products SM2RASC+OBS and TMPA +OBS for Brenta (up-left), Tanaro (up-right), Tiber (bottom-left) and Volturno (bottom-right) basins, during the entire analysis period (2010-2013).

The integration between observed and satellite rainfall improves the model performance for all the basins except Volturno basin. ***Figure 3.7*** shows the mostly positive percentage variations of *NS* values obtained by using OBS and the integrated products over the four basins, both during the calibration and validation period. During calibration, SM2RASC+OBS (TMPA+OBS) provides *NS* values greater than 0.77 (0.75), while during validation *NS* values greater than 0.63 (0.36) are obtained. In terms of correlation, similar results are obtained.

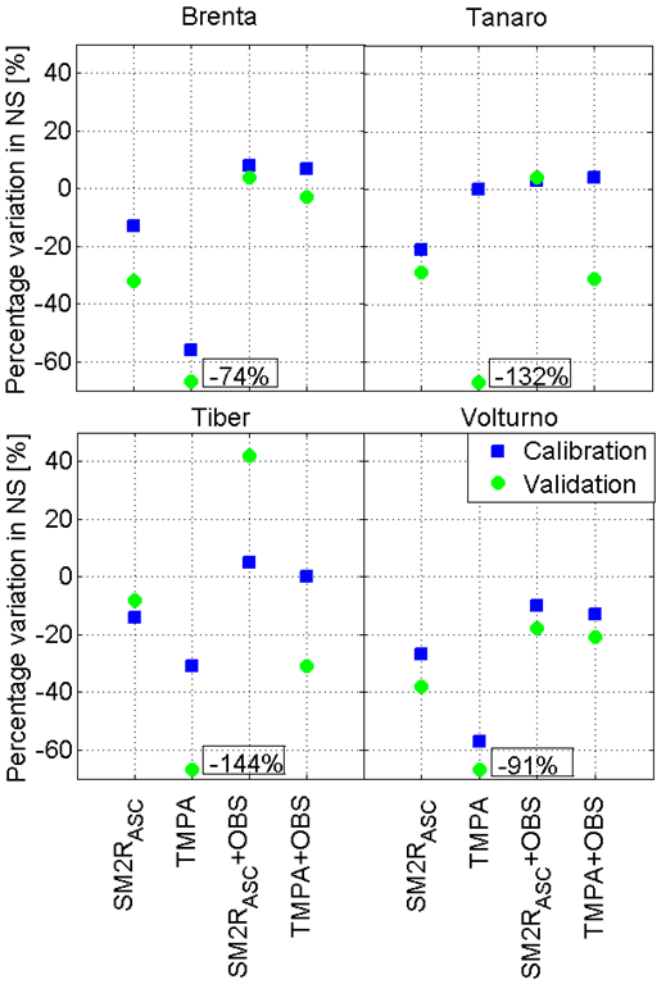

Figure 3.7 - Nash-Sutcliffe efficiency index (NS) percentage variation obtained by forcing MISDc model with SM2RAIN derived rainfall (SM2RASC), TMPA 3B42-RT product (TMPA) and the integrated products between the observed and satellite rainfall data (SM2RASC+OBS and TMPA+OBS) during calibration (blue squares) and validation (green rumbles). The text boxes show the percentage variations in NS obtained for TMPA during the validation period that exceed the axis limit.

That is, $SM2R_{ASC}$+OBS provides *R* values higher than 0.88 and 0.82 during calibration and validation, respectively, while TMPA+OBS dataset yields *R* higher than 0.87 and 0.73. The use of integrated rainfall datasets provides also a reduction of the error in volume, for all basins.

Model performance for flood events

The analysis of the performance is carried out on a total of 43 flood events extracted from the analysed timeseries: 11 for Tanaro basin, 12 for Brenta basin, 10 for Tiber and Volturno basins. The events were extracted by selecting those characterized by a total rainfall of more than 20 mm. An event is distinguished from another if a total rainfall less than 1 mm occurred for at least 6 h. Specifically, the performances are assessed by considering the hydrographs obtained by forcing MISDc with the different rainfall datasets, and thus, no recalibration based on flood events is carried out. In ***Figure 3.8*** the performance scores obtained for each flood event and basin are shown. It can be noticed that if MISDc is forced with OBS data, quite high *NS* values are obtained, except for Tiber basin which is characterized by lower performance scores.

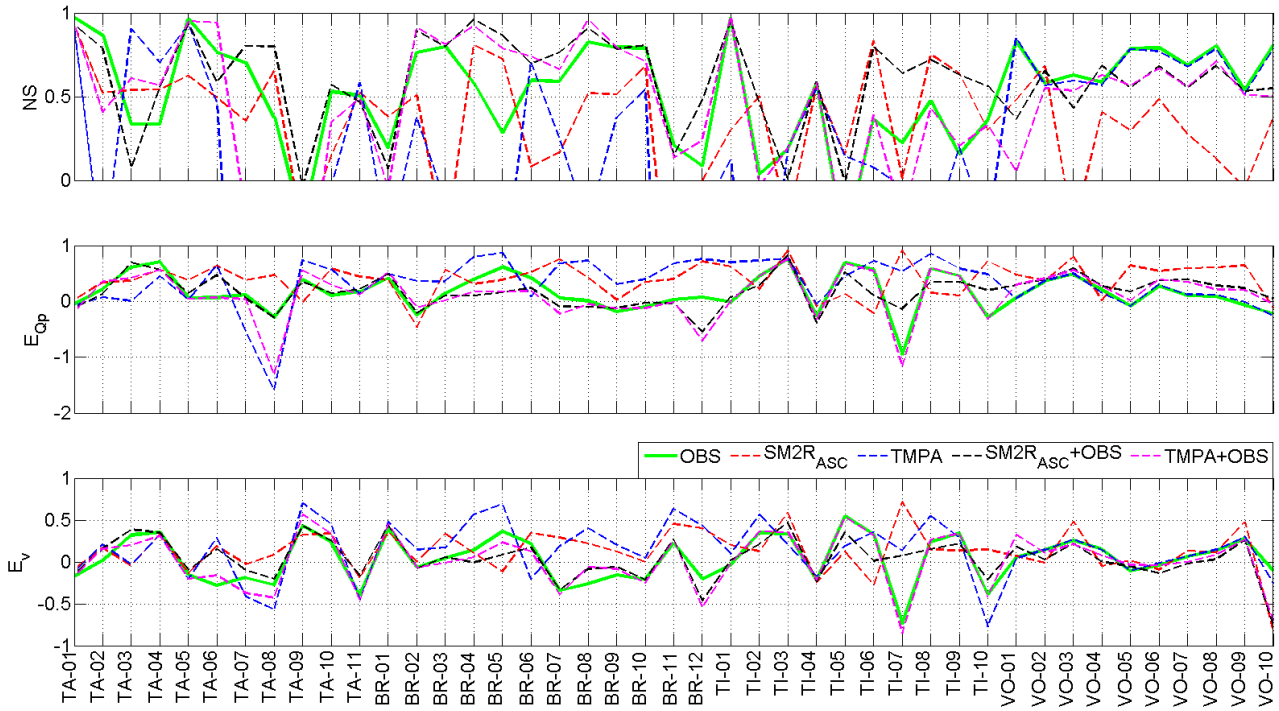

Figure 3.8 - Performance scores obtained during the flood events simulations over the Tanaro (TA), Brenta (BR), Tiber (TI) and Volturno (VO) basins by forcing MISDc model with observed data (OBS, solid green line), SM2RAIN derived rainfall (SM2RASC, dashed red line), TMPA data (TMPA, dashed blue line), integrated product between SM2RASC and OBS data (SM2RASC+OBS, dashed black line) and integrated product between TMPA and OBS data (TMPA+OBS, dashed magenta line). Nash-Sutcliffe efficiency index (NS, upper panel), percentage error in peak discharge (EQp, middle panel) and percentage error on direct runoff volume (Ev, bottom panel). In the upper panel graph, the y-axis is truncated to 0 for visualization purposes.

These results are in agreement with those obtained by Brocca et al. (2011b) in Central Italy and by Massari et al. (2015) throughout the Italian territory who obtained *NS* values at the event-scale ranging between 0.50 and 0.95. If TMPA and SM2R$_{ASC}$ datasets are used as input data, lower performance can be observed with an average reduction of *NS* equal to -40% and -36% for TMPA and SM2R$_{ASC}$, respectively. More in details, TMPA provides the worst performance with several negative NS values over Tanaro and Brenta basins (e.g., event 8 for Tanaro and event 11 for Brenta). SM2R$_{ASC}$ provides *NS* values comparable with those obtained by forcing MISDc with OBS over Tanaro, Brenta and Tiber basins, while *NS* is consistently lower for Volturno basin. The integrated products provide results comparable and sometimes higher than those obtained by using OBS, except for event 8 over Tanaro basin, where TMPA+OBS product yields a *NS* value of about -2.

In terms of E_{Qp}, a general underestimation of peak discharge can be observed by using OBS as input data. Even in this case, the simulations over Tiber basin provide the worst performance scores, with an error of about 50% for events 3, 4, 6, 7, 8 and 9 and about -100% for event 7. TMPA product provides a general underestimation of the discharge peaks over Tanaro, Brenta and Tiber basins. SM2R$_{ASC}$ is characterized by a general underestimation over all the four analysed basins, mainly for

Tiber and Volturno basins. TMPA+OBS and SM2R$_{ASC}$+OBS products provide E_{Qp} values similar to those obtained if MISDc is driven with OBS and even lower error values (with respect to OBS) over Brenta basin. In terms of E_v, OBS data provide the best performance scores, mainly for Volturno basin. TMPA and SM2R$_{ASC}$ products are characterized by a general underestimation for Tanaro, Brenta and Tiber basins while the simulations carried out for Volturno basin provide better results with respect to the other basins, except for event 10.

To sum up, in terms of median *NS* on all the selected flood events, the use of integrated products provides comparable results with those achieved by using OBS with the best performance obtained for Tiber River for SM2R$_{ASC}$+OBS (+54%) and Brenta basin by using TMPA+OBS (+14%) and worst ones obtained for Volturno with TMPA+OBS (-18%). In the remainder of the cases both SM2R$_{ASC}$+OBS and TMPA+OBS yields values close to OBS with better results obtained by SM2R$_{ASC}$+OBS. The poor results obtained for Volturno basin can be explained by the relatively high quality OBS data when they are used as input in MISDc. Similar results are obtained for E_{Qp} (E_v) with an error reduction of about 28% (38%) for Tiber basin by using SM2R$_{ASC}$+OBS and 43% (16%) for Brenta basin by using TMPA+OBS.

If compared with the study by Massari et al. (2014), who forced a rainfall-runoff model over a small catchment in France by using an estimated rainfall product obtained by the application of SM2RAIN to in situ SM observations, a good agreement in the obtained results is observed. Indeed, Massari et al. (2014) found that the use of the SM2RAIN-derived rainfall provides reasonable results but lower than using traditional raingauge observations. However, accordingly our study, the integration of observed (from raingauge) and estimated rainfall (from SM2RAIN) provided the best performance with an increase in the mean *NS* equal to 38% (from 0.48 to 0.66).

4.APPLICATION OF SATELLITE RAINFALL DATA FOR LANDSLIDES PREDICTION

Once the satellite rainfall data are assessed in a thorough way, by considering different scales, periods and methodologies, they are applied for landslide prediction. In this Chapter, the use of satellite rainfall data within a physically-based model is tested. The model is based on the integration of a hydrological module the simulates the soil moisture within a soil column for different soil layers and a stability module that estimates the Factor of Safety (FS) taking into account the soil moisture conditions. The first part of this Chapter describes the developed model, while the second one shows some preliminary results obtained over a study area in Umbria.

4.1 The coupled hydrological-stability distributed model for landslide risk assessment

A physically-based model is developed during this work of thesis with the aim of estimating FS by using satellite rainfall data has input. The model is composed of two main modules: 1) a hydrological module that estimate soil saturation conditions over the analysis area and, 2) a stability module the estimates FS by taking soil moisture into account.

Model description

A coupled hydrological-stability model is developed for testing the capabilities of using satellite rainfall data for landslide risk assessment. The model allows to estimate the FS over the analyzed area, by taking into account the soil saturation conditions, and by using as input data ground (or satellite) rainfall and air temperature observations. The input data are rescaled to a common regular grid, according to their native spatial and temporal resolutions. However, the user is free to set the temporal/spatial resolution of the analysis grid, according to specific needs. The soil saturation conditions and FS estimation is carried out by considering multiple soil layers. In this respect, soil layers within the same soil column are assumed to be parallel to the ground surface. The user can set the number and the thickness of the layers. The model is fully distributed, i.e. the relationships between grid cells are taken into account. A visual representation of the analysis grid is reported in ***Figure 4.1***.

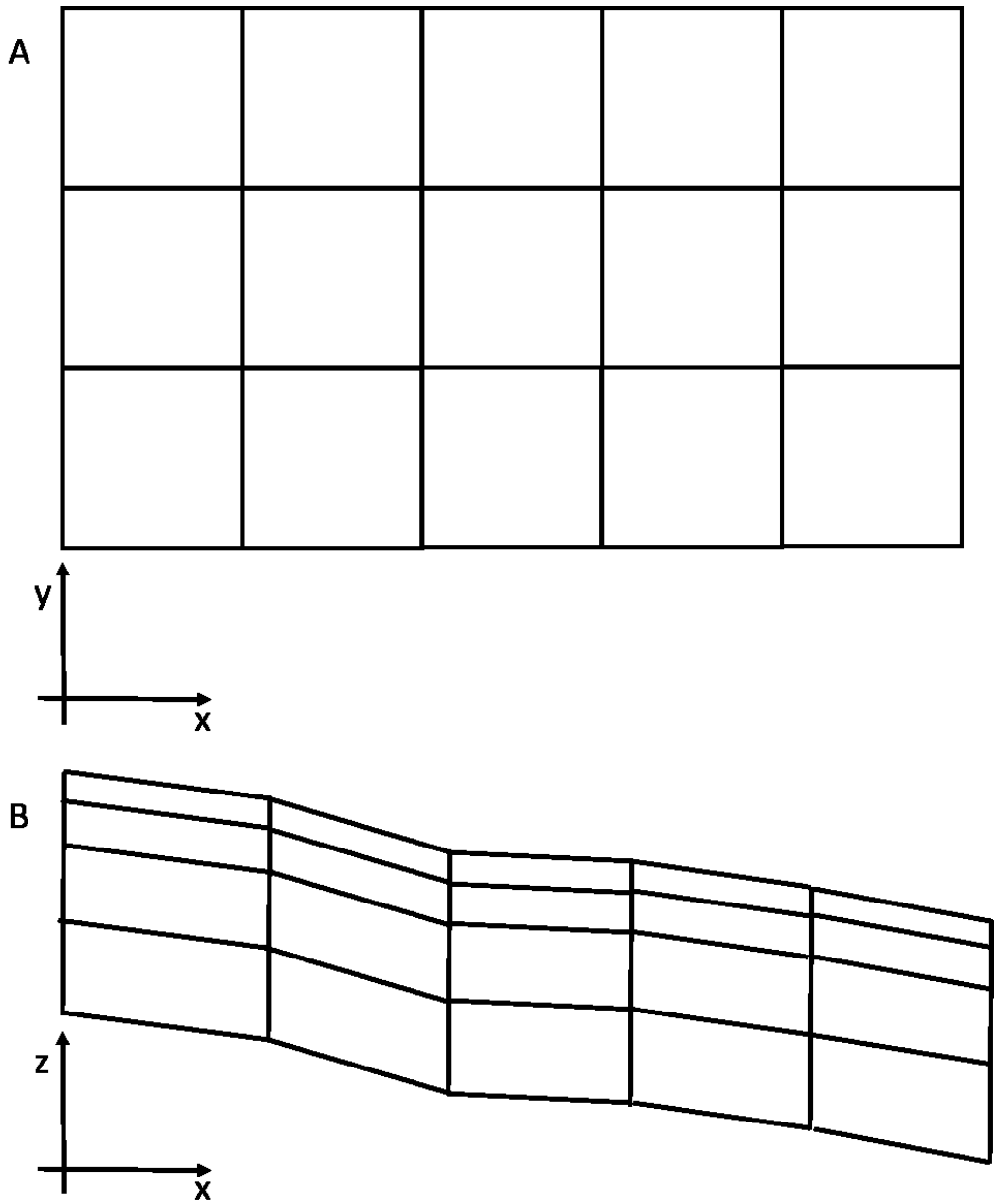

Figure 4.1 – Planar(A) and sectional (B) view of the analysis mesh

The model is composed of three main modules:

1) Input data reading, preprocessing and memory allocation;
2) Soil Water Balance Module (SWBM) for the estimation of soil saturation conditions;
3) Stability module for the estimation of FS.

In the following, a detailed description of the main features of each module is provided. The basic idea of coupling of a hydrological and a geotechnical module is not new, but up to now just few papers report such application. The main idea is based on the works by Valentino et al. (2014) and by Xiaogang et al. (2016), who simulated soil moisture conditions in order to assess slope stability. The developing a new model comes from the need to reduce the number of required parameters and the possibility to be forced with satellite data

Input data reading, pre-processing and memory allocation

The first module of the model reads all the necessary input data and preprocesses them in order to be used within the second and third modules in a common way. Regarding the necessary inputs, the model needs data related to:

1) Topography, usually obtained through a Digital Elevation Model (DEM);
2) Air temperature data, through a ground monitoring network, along with coordinates of measurement points and temporal sampling;
3) Rainfall data, obtained through ground monitoring network or through satellite observations, along with coordinates of measurement points and temporal sampling;
4) Soil texture information, in order to derive the hydraulic properties of the study area;
5) Geotechnical parameters of the study area;

First of all, DEM is loaded and resampled to a different spatial resolution, if required. A spatial sampling of 100 m is used to test the procedure and to assess the stability condition over the study area. The selected resolution is a compromise between the need to provide stability information at medium-high resolution and the computational time required for the simulation. After this step, the model creates a slope layer that has two-fold utility: 1) to identify the slope conditions of the analysis cells and 2) to identify the relationships between each cell, in order to assess the direction of surface and subsurface water flows. This step is carried out by using the d8 algorithm (O'Callaghan and Mark, 1984), in which the water flows from a centered grid point to its neighbor along with the steepest direction, as described in ***Figure 4.2***. The inflow cell is defined by ascribing an index corresponding to flow direction to the centered cell.

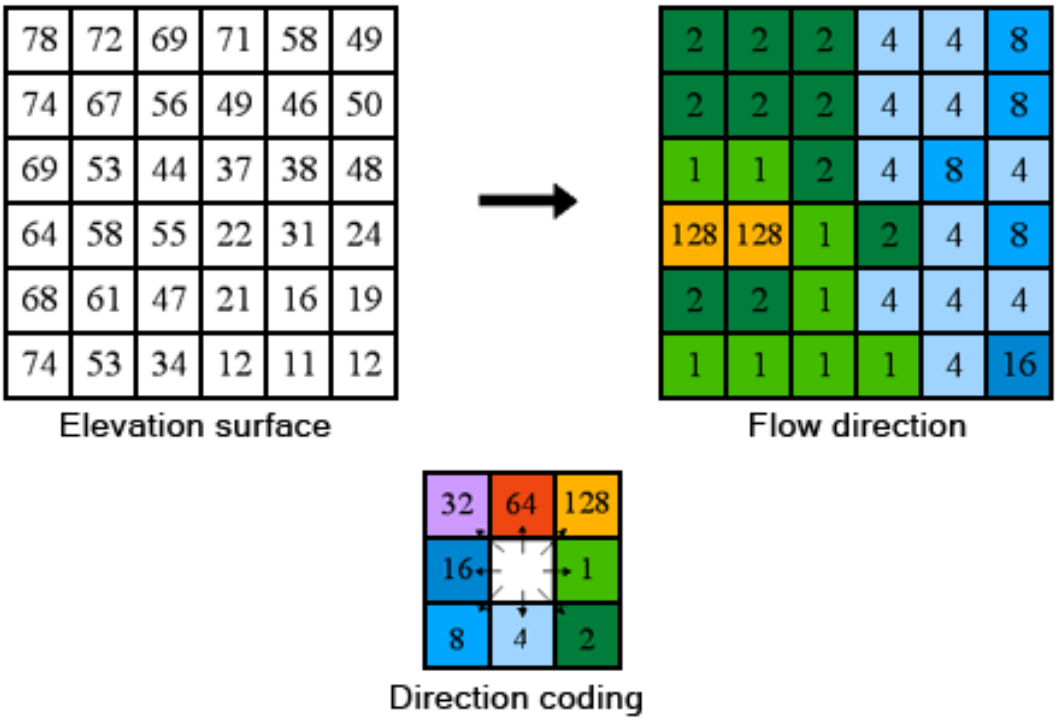

Figure 4.2 – Visual representation of the d8 algorithm

Rainfall and air temperature data, obtained through the regional monitoring network of Umbria region, are loaded along with their spatial coordinates and interpolated over the study area at the defined resolution. The user can set in this step if ground or satellite rainfall data are used as input and the model simulation time step.

The hydrological module

The soil saturation conditions are estimated by running a multi-layer soil water balance model (SWBM) that takes into account several fluxes within the soil column. A visual representation of water fluxes is reported in ***Figure 4.3***.

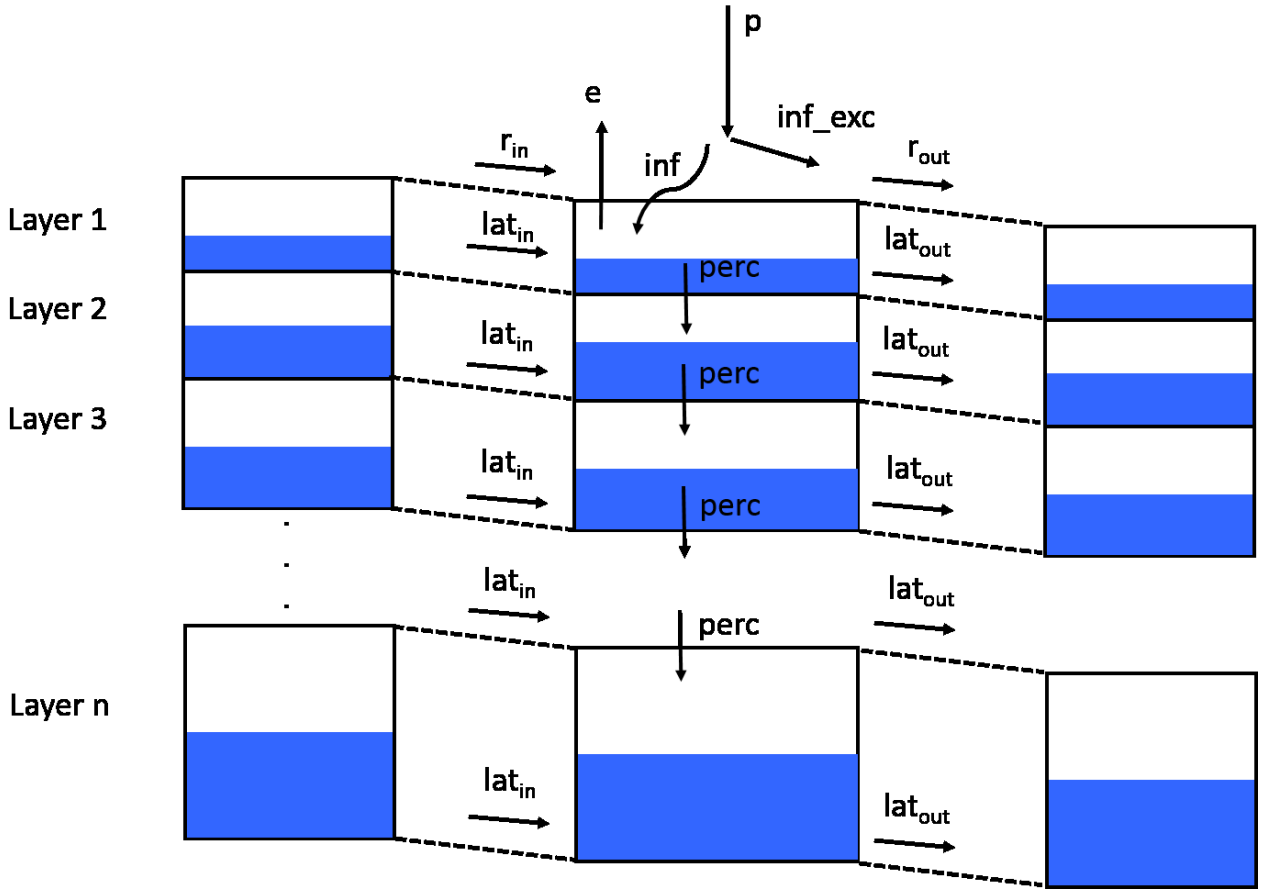

Figure 4.3 – Visual representation of water fluxes considered in the coupled hydrological-stability model.

For the first soil layer, the following water content balance equation holds:

$$\begin{cases} dW_1(t)/dt = f(t) - e(t) - perc_1(t) - lat_{1\,out}(t) + lat_{1\,in}(t), & W_1(t) \le W_{1\max} \\ W_1(t) = W_{1\max}, & W_1(t) > W_{1\max} \end{cases} \tag{4.1}$$

while for the remain soil layers it becomes:

$$\begin{cases} dW_i(t)/dt = perc_{i-1}(t) - lat_{i\,out}(t) + lat_{i\,in}(t) - perc_i(t), & W_i(t) \le W_{i\max} \\ W_i(t) = W_{i\max}, & W_i(t) > W_{i\max} \\ i \ge 2 \end{cases} \tag{4.2}$$

where $W(t)$ is the water amount within the soil, W_{max} is the maximum water capacity of the soil layer, t is the time, $f(t)$ is the infiltration rate, $e(t)$ is the evapotranspiration rate, $perc(t)$ is the deep percolation rate, $lat_{out}(t)$ is the interflow rate exits the soil cell, while $lat_{in}(t)$ is the flow entering the downstream cell and the subscript i indicates the soil layer. In the following, the subscripts are removed for sake of simplicity. W_{max} is defined through the following formulation:

$$W_{\max} = (\theta_{sat} - \theta_{res}) * L \tag{4.3}$$

Where θ_{sat} is the soil water content at saturation, θ_{res} is the residual soil water content and L is the soil layer thickness. The infiltration rate is estimated by adopting the empirical formulation proposed by Georgakakos and Baumer (1996), defined by the following equation:

$$f(t) = p(t) * [1 - (S_e)^{\psi}] \tag{4.4}$$

With

$$S_e = \frac{W(t)}{W_{\max}} \tag{4.5}$$

where $p(t)$ is the precipitation rate, S_e is the saturation degree defined by ***Eq. 4.5*** and ψ is a parameter linked to the non-linearity of the process with value greater than 1.

Evapotranspiration rate is estimated by using a linear equation depending on the potential evapotranspiration, $EPOT(t)$, and the soil saturation:

$$e(t) = EPOT(t) * S_e \tag{4.6}$$

According to the empirical relation of Blaney and Criddle modified by Doorenbos and Pruitt (1997), the potential evapotranspiration rate is estimated through:

$$EPOT(t) = K_c * \{-2 + 1.26 * [\xi * (0.46 * T(t) + 8.13)]\} \tag{4.7}$$

where $T(t)$ is the 2-meters air temperature, ξ is the percentage of daytime hours out the total hours during a year while K_c is a correction factor due to the empirical nature of the formulation.

The deep percolation and interflow rates are estimated by considering the formulation of Famiglietti and Wood (1994):

$$perc(t) = (1 - Nu) * K_s * S_e^{3+2/\Lambda} \tag{4.8}$$

$$lat(t) = Nu * K_s * S_e^{3+2/\Lambda} \tag{4.9}$$

whit Nu defined as:

$$Nu = \sin(\beta) \tag{4.10}$$

where K_s is the saturated hydraulic conductivity and Λ is the pore size distribution index. Nu is a repartition coefficient, introduced in this work, estimated as function of slope, β is the slope angle. Lateral water flow is assumed parallel to the surface. No percolation from the deepest layer is allowed, i.e. an impermeable bedrock is assumed at the end of the soil column.

The surface runoff rate is estimated by summing up the amount of rainfall that does not infiltrate into the soil (infiltration excess) and the water that move upwards from the soil layers for ex-filtration or saturation excess phenomena. The surface water volume is moved to the downstream cell by applying the kinematic model approximated by the Manning's formula, as proposed by Liu and Todini (2002):

$$\frac{\delta V}{\delta t} = r * X^2 - \frac{C * X}{X^{2*\omega}} * V^{\omega} \tag{4.11}$$

with

$$C = \frac{\sqrt{\tan(\beta)}}{\eta} \tag{4.12}$$

and

$$V = r * X^2 \tag{4.13}$$

Where r is the water depth over the surface resulting from precipitation, infiltration excess, saturation excess or surface runoff from the upstream cell, X is the cell dimension, η is the Manning coefficient over land, ω=5/3 and V is the surface water volume over the cell. As in Todini and Ciarapica (2001), the equation solution is carried out by applying the fourth order Runge-Kutta ordinary differential equation solving method.

The volume of water over the surface that does not flow to the downstream cell and remains over the surface, is summed up to rainfall during the next model time step ($t+1$).

The module needs five parameters, the maximum soil water capacity (W_{max}), the soil layer thickness (L), the pore size distribution index (Λ), the empirical correction factor for evapotranspiration (K_c) and the hydraulic conductivity at saturation (K_s). The parameters are assumed to be constant within the soil column, i.e. every layer within a cell has the same textural class, except for K_s. The hydraulic conductivity decreases with depth according to the following power law:

$$Ks_N = Ks_1^{-A*\sum_{j=1}^{N} L_j} \tag{4.14}$$

where A is a reduction coefficient, K_{s1} is the hydraulic conductivity of the first layer, L is the layer thickness and the subscript N stands for the soil layer.

The stability module

Once the soil saturation conditions are estimated within the soil column, the FS can be estimated through the stability module. FS is defined as ratio between resisting and driving forces acting on a slope:

$$FS = \frac{\tau_f}{\tau} \tag{4.15}$$

with

$$\tau_f = c' + (\sigma - u_w) * \tan(\varphi') \tag{4.16}$$

where *c'* is soil cohesion, σ is the total normal stress, u_w is the pore water pressure, φ' is the soil angle of internal friction and τ is the shear stress. Landslide is expected to occur when FS<=1.0, due to increase of driving forces (earthquakes, increase in load) or a reduction of resisting forces (increase in water pressure, weathering). The most used analysis methods for evaluating slope stability are limit equilibrium methods. One of the easiest limit equilibrium method often applied to shallow landslides is the infinite slope. In this method, soil layer thickness is negligible with respect to longitudinal extension of landslide and the failure plan is assumed to be parallel to the slope.

A schematic representation of infinite slope analysis is drawn in ***Figure 4.4***.

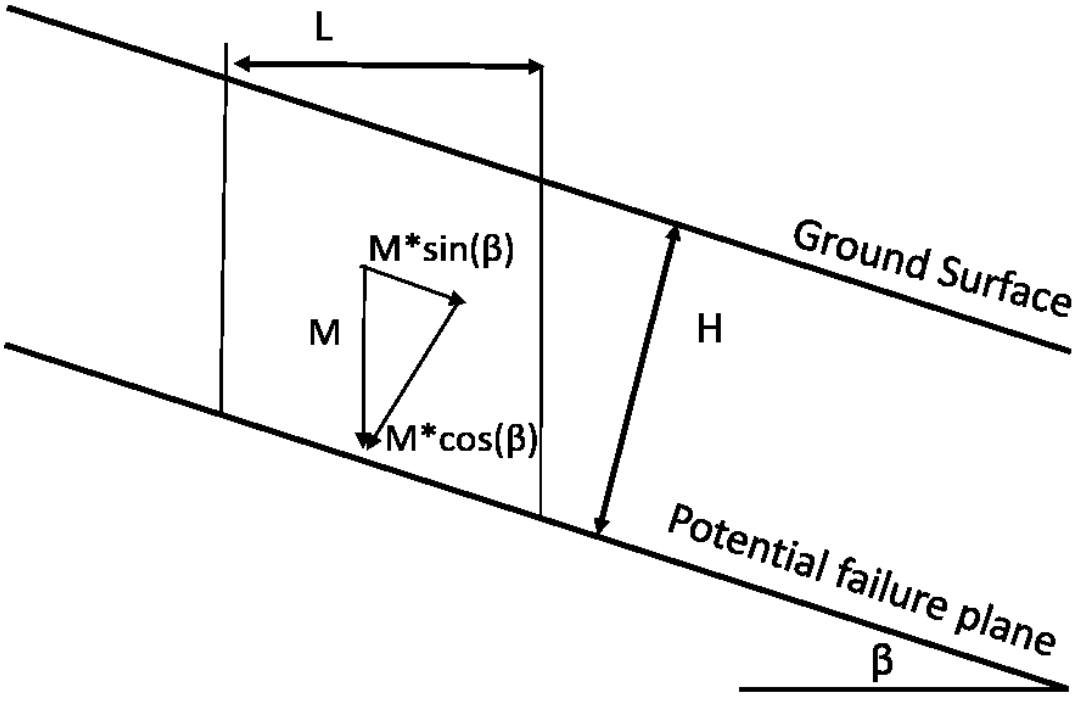

Figure 4.4 – Schematic representation of infinite slope

For various saturation conditions, Lu and Godt (2008) proposed a formulation based on a new definition of the effective stress:

$$\sigma' = (\sigma - u_a) - \sigma^s \tag{4.17}$$

Where u_a is the pore air pressure and σ^s is the suction stress.

Lu and Likos (2004) showed that suction stress can be related to water content through:

$$\sigma^s = -\frac{\theta - \theta_{res}}{\theta_{sat} - \theta_{res}}(u_a - u_w) = S_e(u_a - u_w) \tag{4.18}$$

With S_e expressed by the Soil Water Characteristic Curve proposed by van Genutchen (1980):

$$S_e = \left\{\frac{1}{1 + [\alpha(u_a - u_w)]^n}\right\}^{1-1/n} \tag{4.19}$$

Where α and n are empirical fitting parameters of the soil water characteristic curve proposed by van Genutchen (1980). Then by combining Equation 3.18 and 3.19, suction stress can be expressed, as shown in Lu et al. (2010) by:

$$\sigma^s = -\frac{S_e}{\alpha}(S_e^{\frac{n}{n-1}} - 1)^{\frac{1}{n}} \tag{4.20}$$

Once σ^s is estimated, it can be inserted into the infinite slope stability equation (Lu and Godt, 2008):

$$FS = \frac{\tan(\varphi')}{\tan(\beta)} + \frac{2c'}{\gamma H \sin(2\beta)} - \frac{\sigma_s}{\gamma H}[(\tan(\beta) + \cot(\beta)]\tan(\varphi') \tag{4.21}$$

Where γ is the unit weight of soil, and H is the depth of the failure surface.

Eq. 4.21 allows to estimate FS for the complete range of saturation conditions via infinite slope analysis.

4.2 Application of satellite-based rainfall data for slope analysis in Umbria region

---

The model is tested over a small area in central Italy by using both ground and satellite rainfall data. First, soil moisture simulations are carried out by using the distributed module described in the previous section and then FS is estimated through the stability module. The assessment of the model outputs is made by comparing soil moisture simulations with ASCAT soil moisture product, while the assessment in terms of stability is carried out by considering a limited number of landslide events occurred in the study area.

Results of the application of the coupled hydrological-stability model

In order to test the capabilities of satellite rainfall data in slope stability analysis, the coupled hydrological-stability model described above is applied over a small area of 36 km^2, drawn in ***Figure 4.5***. The study area is located in central Italy and it is characterized by a hilly territory. The northern and eastern sectors of the study area are characterized by the highest slope angles, while in the western part a flat area is presented.

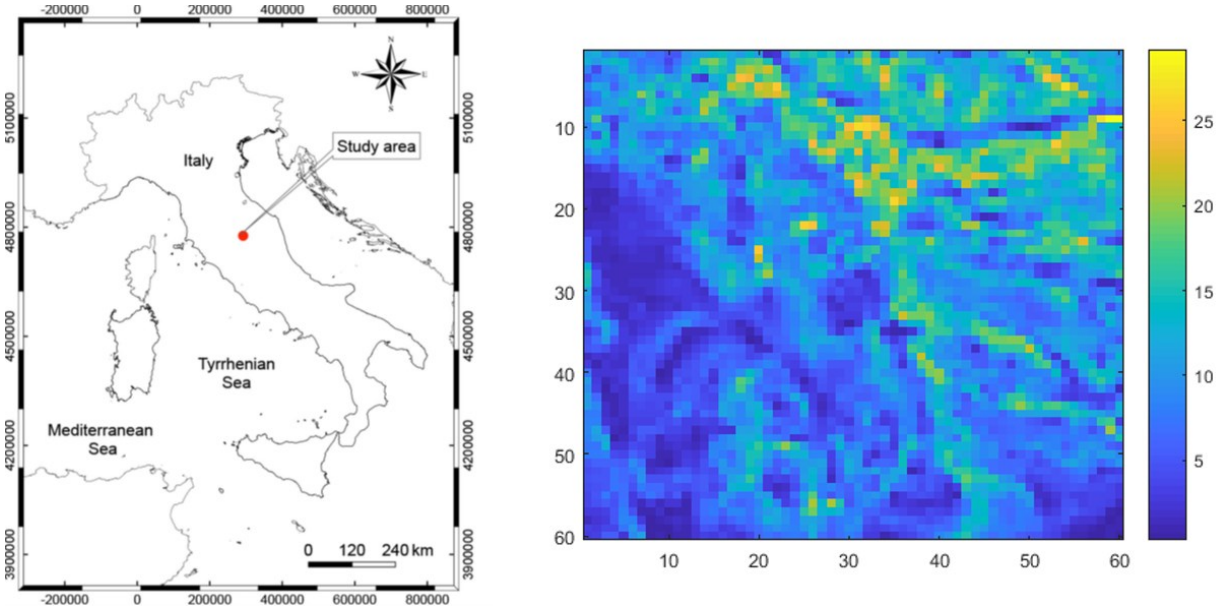

Figure 4.5 – Study area (left) and slope angles (right).

The study area is not fully appropriate as the contribution of cells outside the selected boundaries might occur. The purpose of this case study is only testing the proposed model with ground- and satellite-based rainfall data. In the future, the model will be applied over larger areas and, particularly, to different hydrological basins. As described in the previous section, the model needs several parameters and input data to perform the analysis. To this end, a 20 m DEM is used to define the slope conditions and flow direction, through d8 algorithm. The flow direction layer is displayed in ***Figure 4.6***. The soil textural map of Umbria (Brocca et al., 2016) is used to obtain soil texture information and to derive all the necessary soil hydraulic parameters. The definition of a texture layer allows to define soil hydraulic properties according to values defined in literature following ***Table 4.1*** (Rawls et al., 1982).

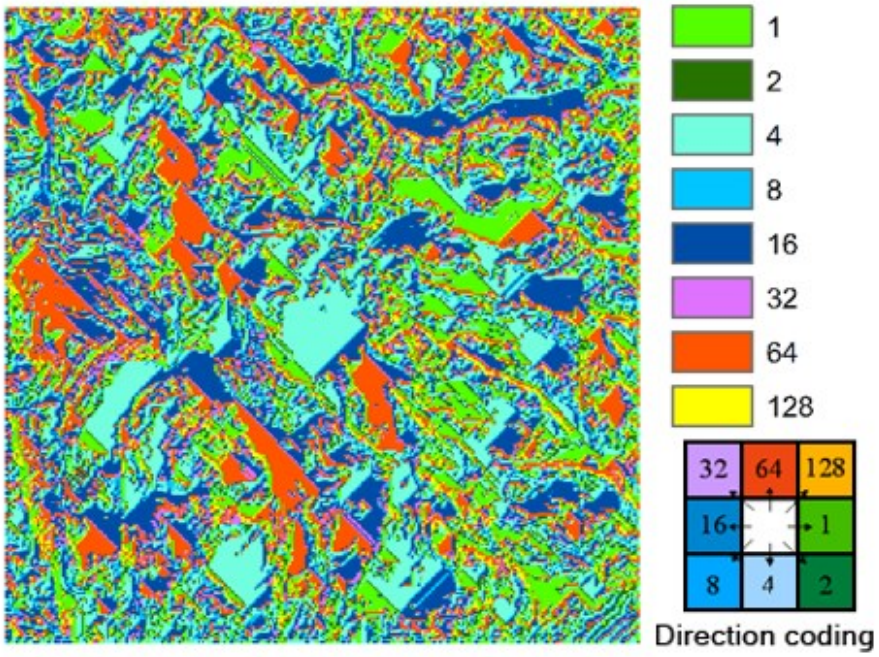

Figure 4.6 – Flow direction layer obtained during the preprocessing step. The colors refer to a direction, as displayed in the direction coding inset.

The soil textural map is obtained through the analysis of more than 1500 soil surveys and it is shown in ***Figure 4.7***.

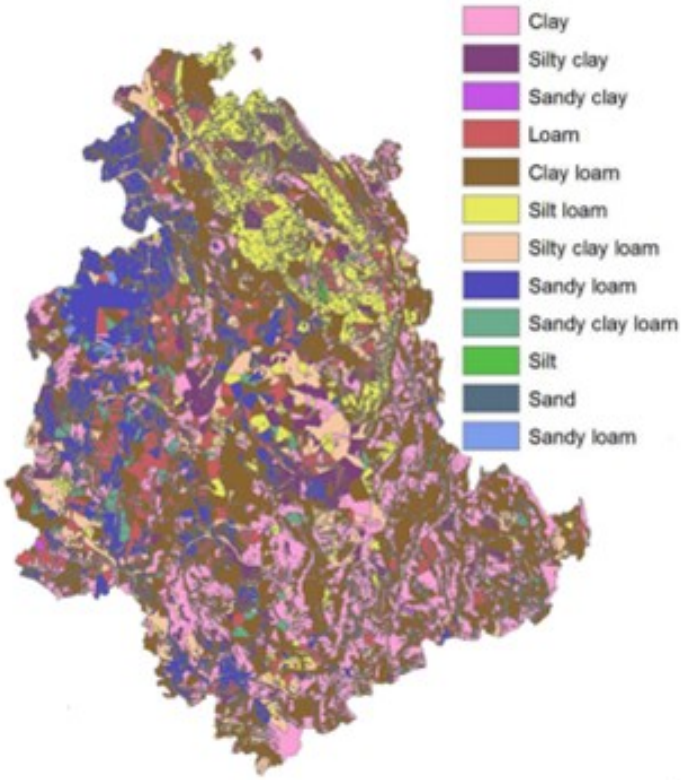

Figure 4.7 – Soil textural map for Umbria region (Modified from Brocca et al., 2016c).

Table 4.1 summarizes the selected parameters values according to the study proposed by Rawls et al. (1982) as a function of soil texture. With respect to ***Eqs 4.4*** and ***4.7***, ψ is set equal to 10 while *Kc* equal to 1.96.

Soil texture	*Θsat [cm³/cm³]*	*Θres [cm³/cm³]*	*Λ [-]*	*Ks [mm/h]*
Silty clay	0.423	0.056	0.15	0.9
Sandy clay	0.321	0.109	0.223	1.2
Silty loam	0.486	0.015	0.234	6.8
Silty clay loam	0.432	0.040	0.177	1.5
Sandy clay loam	0.33	0.068	0.319	4.3
Silty	0.434	0.027	0.252	13.2

Table 4.1 – Values of hydraulic parameters used for the hydrological module according to Rawls et al. (1982).

Figure 48 displays the spatial distribution of soil texture over the study area, obtained through the soil map described in Brocca et al. (2016c).

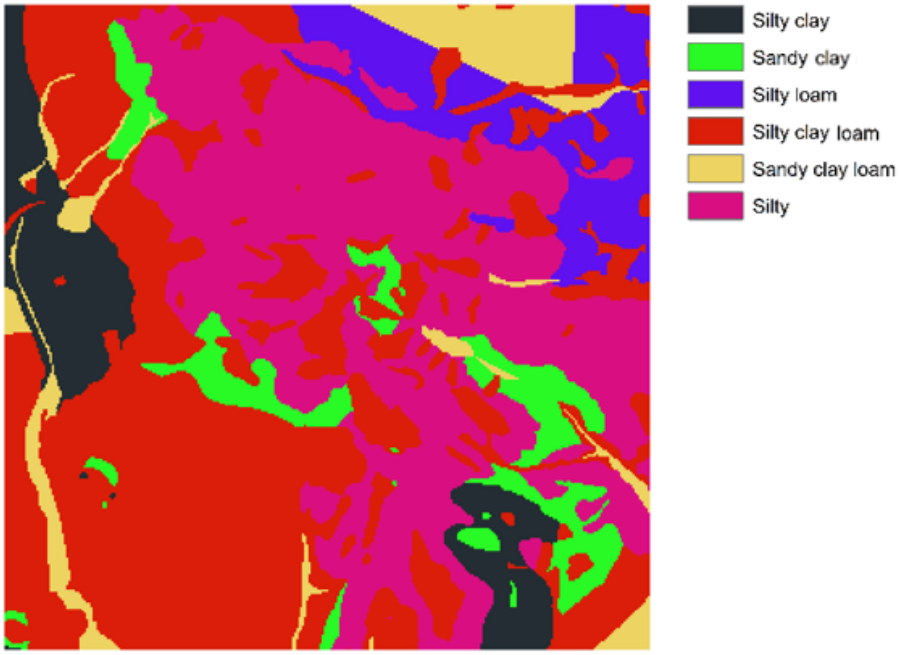

Figure 4.8 – Spatial distribution of soil textures over the study area.

Air temperature data are obtained through the regional monitoring network with a temporal resolution of 30 minutes. Rainfall data are obtained by the raingauges operating in the analysis area (every 30 minutes) and through the TMPA 3B42RT rainfall product (every 3 hours over an area of 25*25 km^2). Both air temperature and rainfall ground data are interpolated over the analysis area

using the inverse distance weighted algorithm. One of the most challenging task in performing a distributed analysis over areas larger than a single slope or plot scale is the definition of geotechnical parameters (mainly cohesion and angle of internal friction). The Department of Civil and Environmental Engineering of the University of Perugia developed a geostatistical approach to obtained such values over large areas from punctual information. Geotechnical parameters for the study area are obtained by applying the methodology described in Fanelli et al. (2016) in which punctual values of angle of internal friction and cohesion are interpolated over large areas through a Kriging technique. The spatial distribution of these two variables for the study area is reported in ***Figure 4.9***.

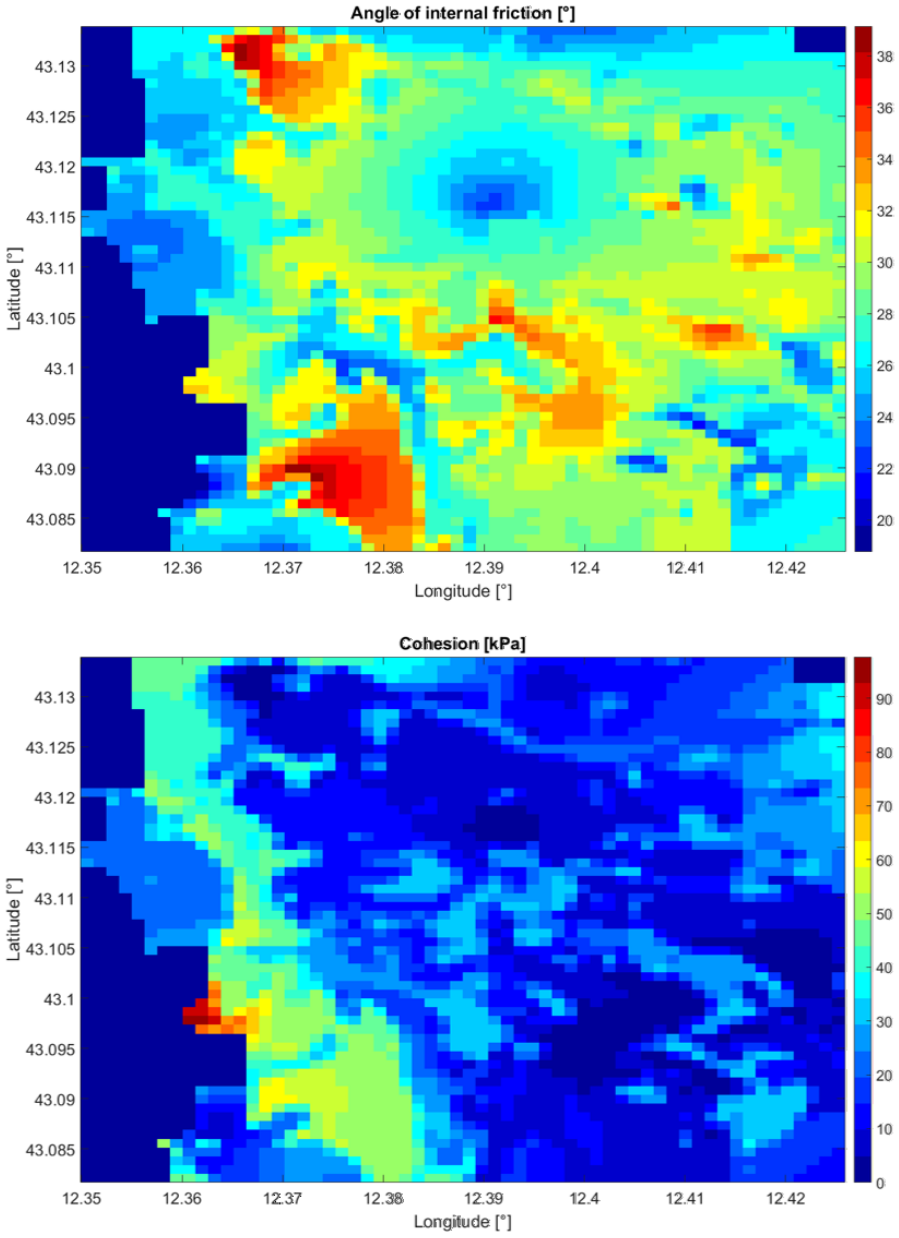

Figure 4.9 – Angle of internal friction (upper panel) and cohesion (lower panel) values for the study area.

In order to evaluate the performance of satellite rainfall products, two different model runs are carried out:1) the model is forced with ground data by considering a temporal resolution of 3 hours

(consistent with satellite data), 2) the model is forced with satellite rainfall data by TMPA 3B42RT. Due to the pixel resolution, rainfall is spatially uniform over the analysis area for each model iteration.

For the sake of brevity, the results obtained by forcing the model with ground rainfall data are hereinafter referred as GROUND, while those obtained with TMPA 3B42RT data are hereinafter referred as SAT. The simulations are carried out by considering 6 soil layers of increasing thickness: 150, 200, 400, 500, 1000 and 1000 mm allowing the estimation of soil moisture and FS up to a depth of 3250 mm. The last soil layer is initialized as fully saturated and the simulation covered the period 1st January 2007 – 31st December 2010. For the purposes of the present work, the module is run over a grid with spacing of 100 m. A soil saturation condition of 50% is set for the 4 shallower soil layers as starting condition, while the 5th soil layer is initialized as fully saturated. As the model run starts in January, it is reasonable to assume saturated conditions for the two last soil layers. A soil saturation profile during the analysis period can be observed in ***Figure 4.10*** for a randomly selected cell.

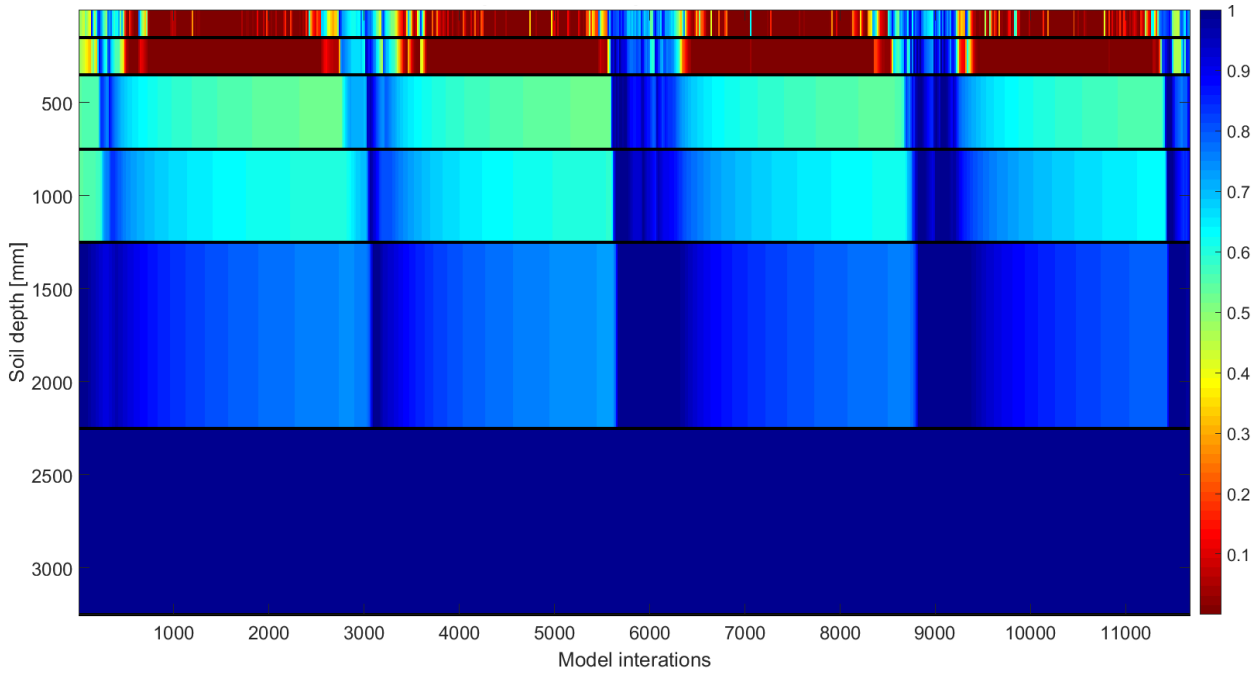

Figure 4.10 – Soil saturation profile for a cell simulated by the hydrological module

The obtained soil moisture profiles by using ground or satellite data are assessed through the comparison with ASCAT soil moisture product (Wagner et al., 2013). The quality of this product is extensively assessed over Italy and in particular over Umbria region by several studies (Brocca et al., 2010; 2011; 2017, Wagner et al., 2013, to name a few). Due to the limited soil thickness investigated by the satellite sensor, only the first 2 layers are compared with ASCAT data. To this end, the exponential filter (Wagner et al., 1999) is applied to raw satellite soil moisture data in order to obtain a Soil Water Index (SWI) related to a thicker soil layer. Constant values of 2 (for the first soil layer) and 5 days (for the second layer) are selected for the T parameter during the entire

analysis period. The comparison is carried out by estimating the correlation coefficient (R) at half-daily temporal resolution. Due to the ASCAT coarse spatial sampling (12.5 km), every grid cell is compared with the same ASCAT pixel.

Figure 4.11 reported the comparison of GROUND and SAT soil moisture simulations with ASCAT SWI data.

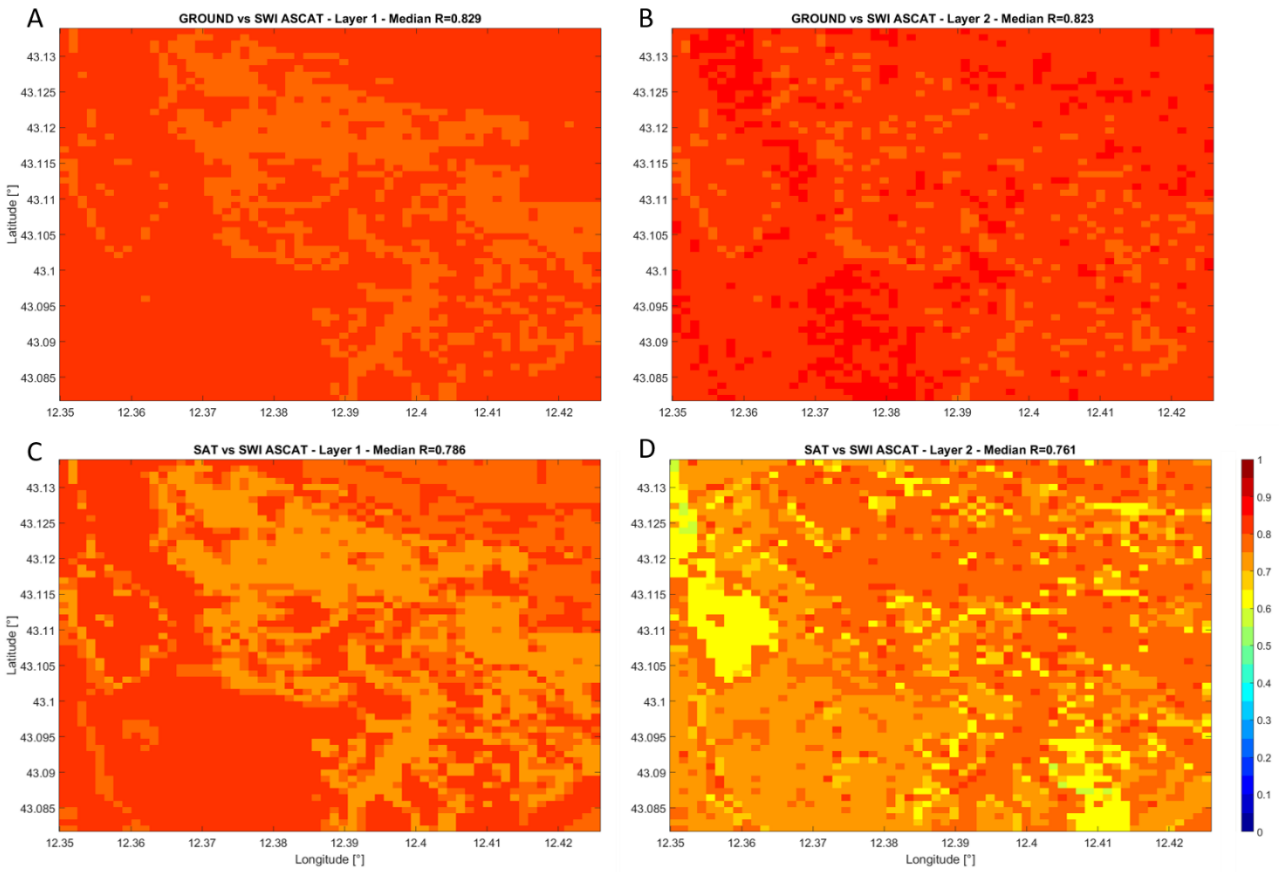

Figure 4.11 – Correlation maps obtained by comparing GROUND and SAT soil moisture simulations with ASCAT SWI estimates for the first (A, C) and second (B, D) soil layers.

As it can be seen from ***Figure 4.11***, both GROUND and SAT soil moisture simulations are in good agreement with ASCAT derived SWI. Median R-values of 0.83 (0.79) and 0.82 (0.76) are obtained by comparing GROUND (SAT) and ASCAT SWI soil moisture estimates over the first two soil layers. The spatial patterns highlighted lower R-values over the steepest regions of the study area for the first soil layer (***Figure 4.11 A*** and ***C***), while for the second soil layer (***Figure 4.11 B*** and ***D***), lower values are obtained over flat areas, especially when SAT soil moisture estimates are compared with ASCAT SWI data. This is mainly due to two major factors: 1) water flow and accumulation towards those sectors and, 2) the spatial resolution of ASCAT soil moisture product, too coarse to highlight wetter conditions over these areas. In order to show the temporal agreement more in details, ***Figure 4.12*** shows the soil moisture time series, provided by GROUND and SAT model simulation and by ASCAT derived SWI, for 3 randomly selected pixels of the analysis grid. The time series are referred to the first soil layer with half-daily temporal resolution.

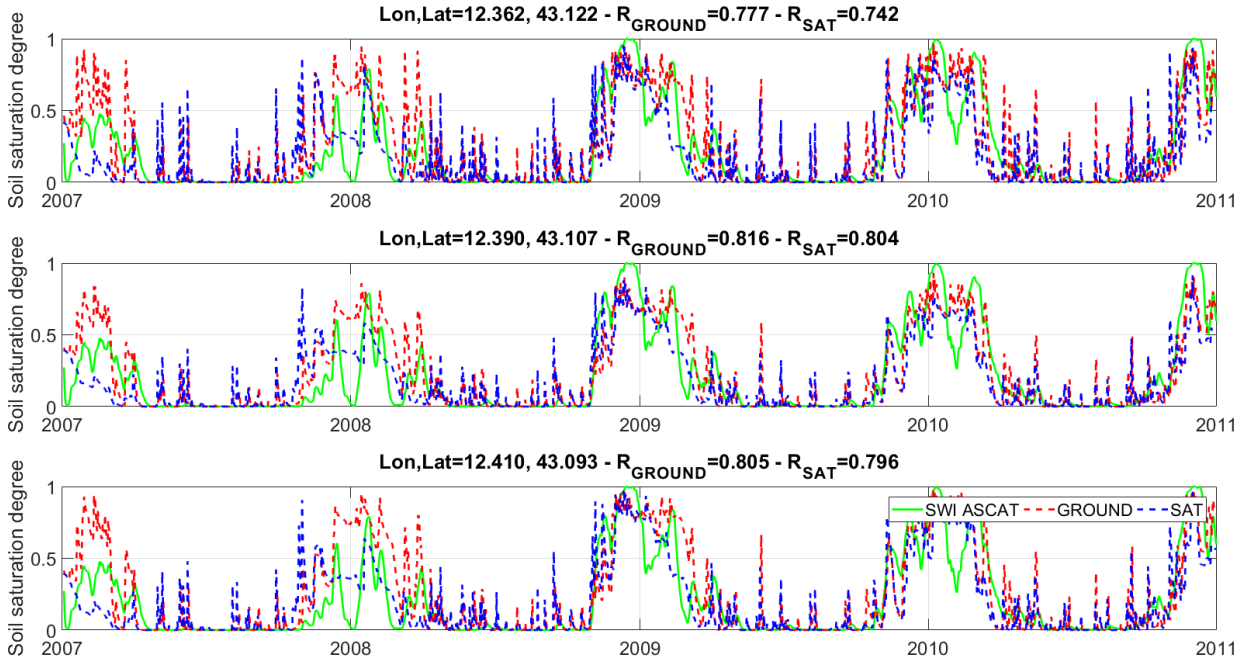

Figure 4.12 – Soil moisture time series for 3 randomly selected pixels over the analysis, obtained through GROUND (red dashed line), SAT (blue dashed line) and SWI ASCAT (green solid line). For each time series the spatial localization is provided along with the temporal correlation (R).

As it can be seen, the temporal patterns provided by GROUND and SAT soil moisture estimates are in good agreement with those provided by SWI ASCAT, with R-values > 0.74. During Summer, both GROUND and SAT estimates provided higher soil moisture values, probably due to short rainfall events, not recognized by the satellite soil moisture sensor, while the agreement is better during Fall and Winter. It is worth noting that landslides usually occur during the wet season, i.e. when the soil moisture conditions are close to saturation. The decrease in correlation during Winter 2008 is due to intense snow events occurred within the study area, impacting the quality of ASCAT soil moisture product.

Due to the good agreement between GROUND, SAT and SWI ASCAT soil moisture estimates, the model is expected to provide reasonable soil moisture simulations, thus allowing to be used for FS estimation through the stability module.

The assessment of FS simulations involved knowledge of landslide events occurred within the study area during the analysis period. Both date of occurrence and spatial localization of landslide events have to be as much accurate as possible. The Civil Protection Service of Umbria region has a landslide catalog used in the present work to test the capabilities of the developed method. Only three landslide events occurred in the study area during the analysis period, as reported in ***Figure 4.13*** and in ***Table 4.2***. The catalog provided the date of occurrence, with daily temporal resolution and the spatial localization of event as punctual coordinates, so no information about the extension (both on the surface and in depth) are available. In order to overcome these limitations, the closest grid point to each landslide site is selected as "investigated pixel" by considering the vales of FS during the entire day of occurrence, i.e. from 00:00 to 23:59.

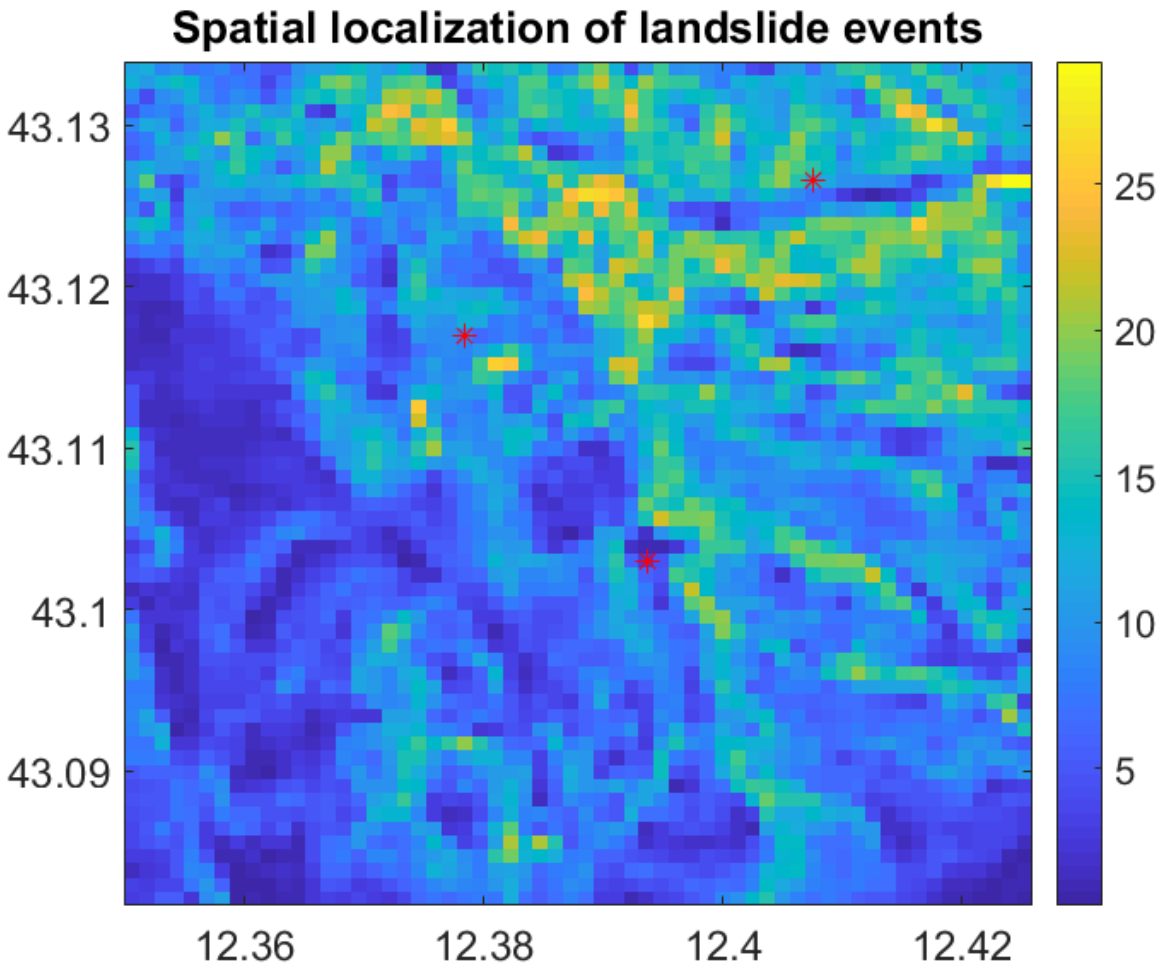

Figure 4.13 – Spatial localization of the 3 landslide events used for the assessment of stability conditions by using GROUND and SAT model runs. The colorbar is referred to the slope angles obtained during the previous steps.

Landslide ID	Date of Occurrence	Longitude [°]	Latitude [°]
1	10 December 2008	12.39	43.10
2	10 April 2009	12.38	43.12
3	10 December 2008	12.41	43.13

Table 4.2 – Date of occurrence and coordinates of the landslide events occurred within the study area.

As described above, the geotechnical parameters (angle of internal friction and cohesion) are obtained from the analysis performed by Fanelli et al. (2016), while a constant value of 20 kN/m^3 is used as unit weight of soil.

In the following the FS obtained by GROUND and SAT model runs are reported for the first two layers of soil for the 3 landslides occurred in the study area. ***Figure 4.14*** draws the SM and FS time series for the three landslide events according to GROUND model run. For visualization purposes, only a small time window is reported. The red area indicates the day of occurrence according to ***Table 4.2***, while the dashed red line indicates the threshold value of FS=1. At it can be seen, if the model is forced with ground rainfall, during the investigated time window, FS shows values very close to 1, i.e. instability conditions, both on the first and the second soil layer. Looking at the landslide event N°1 (***Figure 4.14***, upper panel), the FS reached the value of 1 also before the landslide occurrence. This can be related to four main factors: 1) the use of a 100 m grid that does not allow to simulate in details the soil saturation conditions and impacts the accuracy of geotechnical parameters and slope angles; 2) spatial interpolation of rainfall that creates wetter conditions during the days before the landslides; 3) the parametrization of the model, including the soil layer thickness, and 4) the landslide is reported some days after the real triggering rainfall event.

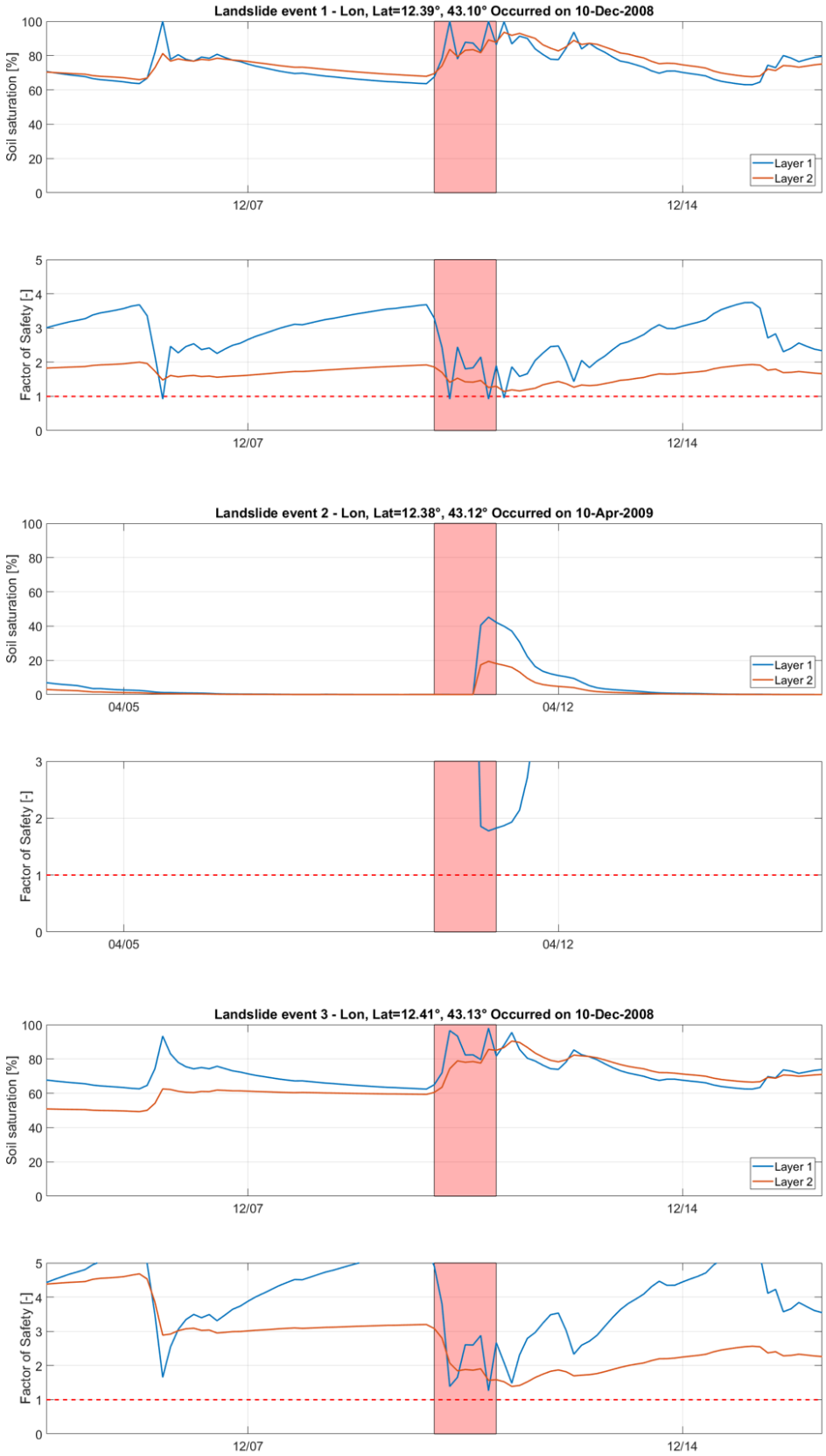

Figure 4.14– Soil moisture and Factor of Safety time series for three landslides events within the study area obtained by forcing the model with ground rainfall data

The event N°2 on 10th April, 2009 occurred during dry conditions. An isolated rainfall event triggered the landslide involving probably just the most superficial soil layer. As it can be seen in Figure 3.12 (middle panel), a minimum FS of 2 is obtained for the first soil layer. Although the model did not identify the landslide event, the decrease of FS during the investigated time window is clearly visible. Further analysis will be carried out by considering this landslide event, applying different parametrization and grid resolution.

The last analyzed event occurred on 10th December, 2008. Similarly to event N°1, during the time window, a strong decrease in FS for the two soil layers is observed. In this case, values very close to 1 are obtained, thus identifying unstable conditions.

The analysis is carried out by forcing the model with rainfall estimates obtained by TMPA 3B42RT. As stated in the previous Chapters of this thesis, this kind of product is chosen to test the feasibility of using satellite rainfall data in an operational framework, as they are provided in near real time. ***Figure 4.15*** draws the SM and FS time series obtained by the SAT model run. This model setting provided very good results, both in terms of soil moisture and FS values. The landslides events N°1 and N°3 are well identified by the model, even if satellite rainfall data are used to force the hydrological module. More in details, for event N°1 and N°3, the model provided better results than those obtained by using ground data, confirming the potential added value of using remotely sensed information for geo-hydrological applications. For the events occurred on 10th December 2008, the FS estimates obtained by the SAT model run identified very well the landslides. Similarly to GROUND run for event N°1, a decrease in FS some days before the event is recognizable, but if satellite data are used, values higher than 1 can be observed in this case. On the

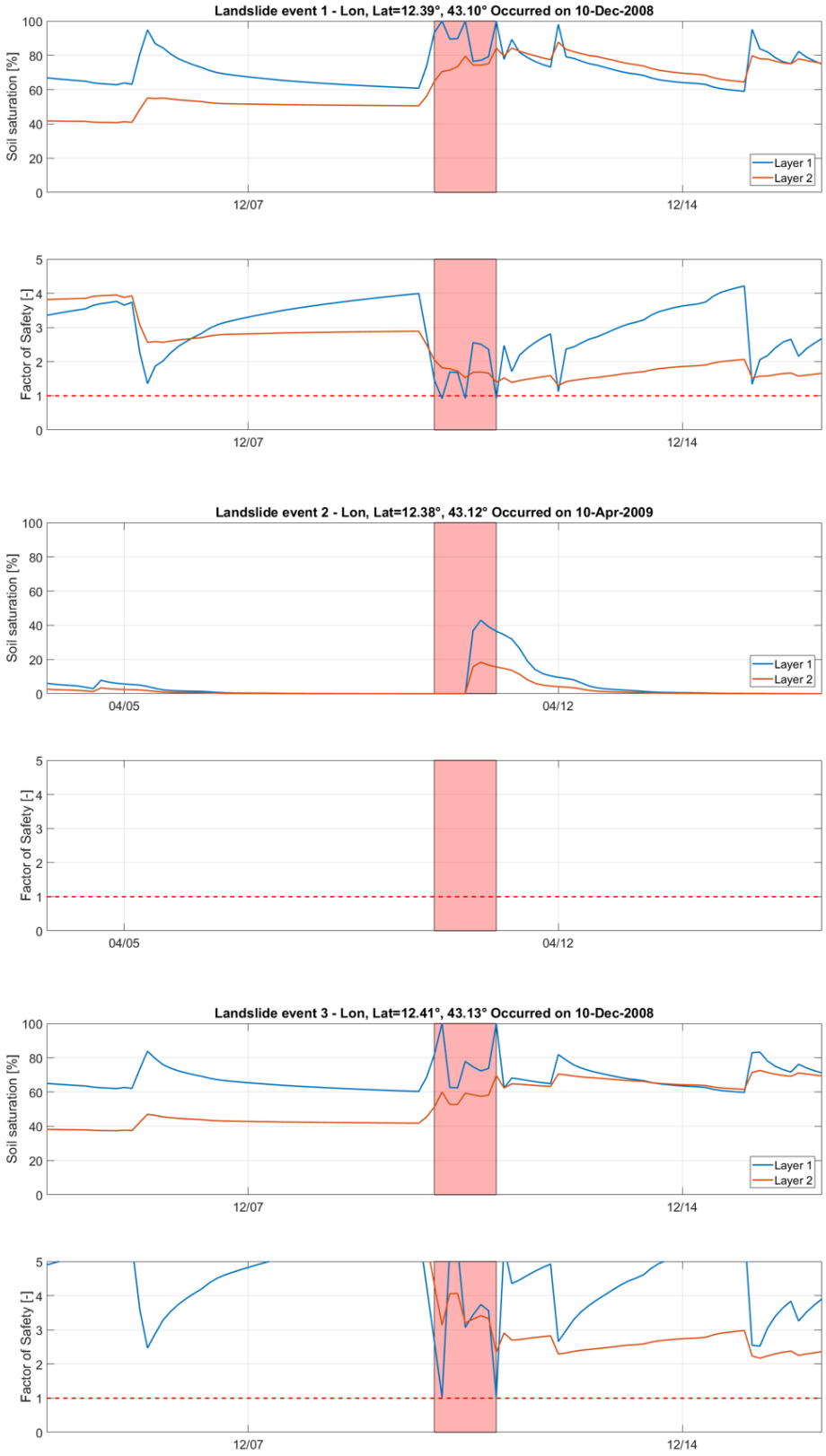

Figure 4.15 – Soil moisture and Factor of Safety time series for the three landslides events analyzed in this work obtained by forcing the model with satellite rainfall data.

other hand, event N°2 is completely missed, even if the rainfall event that probably triggered the landslide is identified and an increase in soil saturation is observed. In this case, the satellite rainfall estimates are characterized by underestimation, impacting the soil moisture simulation and FS estimation.

5.CONCLUSIONS

This work of thesis investigated the feasibility of using satellite rainfall data for landslide risk assessment. Due to their spatial and temporal resolutions, considered too coarse, and the limitations that impact the quality of rainfall estimates from space, this kind of data is scarcely used in hydrological applications, as confirmed by the relative small number of studies available in the scientific literature on this topic.

5.1 Satellite rainfall data validation and integration

State-of-the-art satellite rainfall products are evaluated by considering several statistical and categorical scores with ground and modelled precipitation benchmarks. The analysis carried out over Italy (Ciabatta et al., 2015; 2017) showed that satellite rainfall data can provide reliable estimates, but are characterized by errors that impact the quality of estimates. Indeed, satellite rainfall data show a seasonal dependency on product performance and suffer from topographical effects. These aspects have to be investigated in depth before using satellite rainfall data for any kind of applications. The analysis carried out on a global scale (Ciabatta et al., 2018) highlighted the similar limitations. These works aim to offer a thorough assessment of satellite rainfall products over different climate areas, by considering different periods and benchmarks, in order to provide a complete definition of data error.

This work of thesis also proposed and applied a novel algorithm that allow to estimate rainfall from SM observations. The method, called SM2RAIN, is applied to several satellite SM products (see Ciabatta et al., 2015; 2017; 2018) by considering different spatial and temporal resolution. The algorithm allowed to obtain reliable rainfall estimates, sometime more accurate than those obtained by "top-down". Indeed, the algorithm allows to obtain more reliable rainfall accumulations at ground, "measuring" the amount of rainfall that infiltrates the soil. The analysis and validations carried out for evaluating "bottom-up" rainfall datasets showed that the quality of precipitation estimates are closely related to the quality of the input SM product. Low quality data are obtained over densely vegetated areas, deserts, when the soil is frozen or in presence of snow and over areas characterized by high topographical complexity. The algorithm is also not able to estimate rainfall when the soil is close to saturation.

The integration of multiple satellite rainfall data sources is investigated in order to obtain more reliable precipitation estimates. The results show that integration between different rainfall sources can greatly improve the performance of the parent products (Ciabatta et al., 2017; 2018). By integrating classical satellite and SM-derived rainfall data, products characterized by higher accuracy and reliability than the parent products are obtained. Indeed, the limitations of the two approaches are compensated in the integrated product allowing to improve the estimation of the ground accumulated rainfall thanks to "bottom-up" estimates while, at the same time, overcoming the limitation of rainfall estimates for high intensity rainfall events during wet conditions thanks to "top-down" rainfall products.

5.2 Use of satellite rainfall data for flood estimation

The rainfall products are also applied and used for hydrological applications. In Ciabatta et al. (2016) satellite rainfall data are used to force a hydrological model over several basins in Italy and over the Mediterranean area. The analysis showed that satellite rainfall data (both obtained by "top-down" or "bottom-up" approaches) can offer valuable information over the analyzed basins but BIAS correction and model recalibration are necessary steps that have to be applied before these kind of applications. Indeed, small errors in rainfall estimates can highly impact discharge simulations, also after several days since the rainfall events. Also in this case, the integration of different rainfall products (obtained by ground network, satellite sensors or SM observations) is found to improve discharge simulations, due to the higher quality of the integrated product.

5.3 Use of satellite rainfall data for landslide risk assessment

The impact of using satellite rainfall data is finally tested for landslide risk assessment.

The evaluation is carried out by considering a physically-based model that directly uses remotely sensed rainfall information, specifically developed.

Satellite rainfall estimates obtained through TMPA 3B42RT are used to force an *ad-hoc* developed distributed hydrological-stability model. The model allowed to estimate FS by taking the soil saturation conditions into account. To this end, rainfall data are used to estimate SM conditions over a small area in Umbria, central Italy during the period 1st January 2007 to 31st December 2010. The model is forced also by considering ground rainfall observation as input data. The SM simulations are assessed by comparison with ASCAT SM product, with satisfactorily results. Then, the obtained SM time series are used to estimate FS over the study area. The results provided by forcing the model with ground data allowed to potentially identify 3 out 3 landslide events occurred within the study area, whereas if the model is forced with satellite rainfall data, 2 out 3 events are identified. The results confirm the feasibility of using satellite rainfall data for landslide risk assessment by using a physically-based model with an acceptable level of confidence.

5.4 Final remarks

The results showed in this work are expected to provide useful insights on the use of satellite rainfall data for geo-hydrological applications. The added value of obtaining rainfall data few hours after sensing and the possibility of integration of several data sources could provide a useful tool to Civil Protection services. Although the performance in terms of discharge estimation and landslide occurrence identification are satisfactory, a detailed analysis of errors related to this new source of information over other climatic regions is required.

5.5 Next steps

Further research will be carried out by using the results obtained in this work of thesis as starting point. The impact of spatial/temporal resolution of satellite input data will be carefully addressed, also by considering the recent GPM mission data. The analysis will be carried out by considering a higher resolution analysis grid and over larger areas.

Next analysis steps will involve also the use of integrated rainfall products with high-level merging scheme, in order to force the model with more reliable information. The introduction of a data assimilation module will allow to directly use satellite SM moisture information, taking advantages of the high resolution Sentinel-1 SM product, recently available.

The research will be focused also on the model developed within this work. In particular, the model will be applied over larger areas, in order to better assess the parametrization and formulation applied here, also through hydrovalidation. At the same time, more information about occurred events will be gathered with the final aim to perform a thorough assessment of the proposed modeling chain.

6.APPENDIX

In this part additional material is reported. The validation of satellite rainfall data and the application of SM2RAIN over Australia and India is firstly described. Then, a thorough hydrovalidation of state-of-the-art satellite rainfall products over the Mediterranean area is reported. Lastly, the use of satellite and SM2RAIN-derived rainfall information for landslide prediction through the definition of rainfall thresholds over Italy is assessed.

6.1 Validation over Australia

The validation of satellite rainfall products is carried out over larger areas than the one used for the assessment of the performance described in the previous section. More in details, the results obtained by applying three different satellite rainfall correction and estimation methodologies to SMOS soil moisture data over Australia are here reported. The comparison is carried out against ground- and satellite-based rainfall data sets. This section is based on the following publication:

Brocca, L., Pellarin, T., Crow, W.T., Ciabatta, L., Massari, C., Ryu, D., Su, C.-H., Rudiger, C., Kerr, Y. (2016b). Rainfall estimation by inverting SMOS soil moisture estimates: a comparison of different methods over Australia. Journal of Geophysical Research, 121(20), 12062-12079.

Study area

The main purpose of the study by Brocca et al. (2016b) is to perform a detailed analysis of three different methods that can be used for improving satellite rainfall estimation using remotely sensed soil moisture data, namely, SM2RAIN (Brocca et al., 2014), API-mod (Pellarin et al., 2013), and SMART (Crow et al., 2011). The main benefit of this study is that the three different methods are applied by using the same input data and the same analysis period thus allowing to perform a fair, comprehensive, and robust comparison. The Australian continent is selected as case study because of satellite soil moisture observations from SMOS that are known to be accurate (e.g., Al-Yaari et al., 2014a, 2014b) and also for the availability of the good quality gauge-based product provided by the Australian Water Availability Project (AWAP) which allows for an objective evaluation of the three algorithms. Precipitation across Australia is highly variable due to its significantly different climate zones, ranging from tropical in the northeast, temperate (southeastern and southwestern regions, and Tasmania), arid deserts and savannas (most of central and northern Australia), as well as semiarid regions in the transitional zones. The rainfall pattern is therefore concentric around the extensive arid core of the continent, which generally receives only little precipitation (<60 mm/yr). The northern tropical zone experiences the majority of the annual rainfall events during the summer months (October–March), often exceeding a total depth of 2000 mm, and its winter months are dry. The tropical rain events are mainly driven by the Australian monsoon, tropical depressions, and cyclones. The southeastern mid latitude regions are temperate and have no distinctive dry season. Rain falls mostly during the warm/hot summer through low-pressure systems (e.g., the east coast low) that can bring strong storms with heavy rain, while cold frontal systems are more prominent through the cooler months. The Great Dividing Range, which runs parallel along much of the east coast, is also a likely contributor to wetter temperature summers due to its orographic influence. The southwestern regions are classified temperate but experience dry warm/hot summers (in particular from November to February). In those summer months, the west coast trough can result in large thunderstorms, provided that sufficient moist air is brought into the region. Finally, the stable and dry conditions over large parts of central Australia are attributed to the high-pressure-related subtropical ridge for most times of the year; northern arid regions can, however, occasionally receive convective rainfall during periods of monsoon and depressions in the tropics.

The AWAP rainfall product is generated via spatial analyses on the quality-controlled daily rain gauge measurements from the Australian Bureau of Meteorology daily rain gauge network (accessed online via http://www.bom.gov.au/jsp/awap/rain/archive_recal.jsp). The first analysis

method applied to daily anomalies (given by the ratio of daily rainfall to monthly mean) is based on a two-dimensional Barnes successive correction technique that interpolates point-gauge data by applying a weighted averaging process. Second, the three-dimensional (i.e., latitude, longitude, and altitude) smoothing splines are used for the analysis of monthly climatological averages of rainfall. Both methods generate analysis fields that achieve their smallest errors subject to constraints on the smoothness and the spectrum of the final field. The analysis fields from the anomaly and climatology analyses are combined via simple multiplication. To reduce biases in daily estimates at this step, the daily rainfall analyses are recalibrated so that their sum is equal to the monthly rainfall analyses. AWAP daily rainfall for a given day is the 24 h total rainfall from local time 9 A.M. the day before to 9 A.M. the current day. The rainfall fields are gridded on a 0.05° × 0.05° grid and spatially resampled to the desired 0.25° × 0.25° grid by taking area-weighted averages. This product has known shortcomings (e.g., Contractor et al., 2015). The network has a varying density across the country (and also varies with time), with a strong focus on the urbanized coastal areas along the east, southeast, and southwest, while the network is extremely sparse in central Australia and essentially nonexistent in the barely populated central west. The accuracy of the data varies considerably across Australia (with higher analysis errors in the northern tropics than other regions), since it is limited to what can be resolved by the station network. In central Australia, the network is too sparse to support a daily rainfall analysis, leading to the data "voids" in ***Figure 6.1***, which is considered acceptable, due to the little rainfall occurring in those regions. While the analysis errors tend to increase away from the gauges, the errors also tend to increase in data-rich areas such as in southeast Australia and in regions with strong rainfall gradients and/or with significantly orography; the spatial analysis can lead to smoothing such that grid point values may differ slightly from the exact reading at the contributing stations. The daily spatial analysis of highly convective systems, which are short and variable in length scales in the tropics, is clearly more susceptible to errors due to data smoothing, variability of the Barnes parameters, and the station network density. While the AWAP analysis typically underestimates intensity and frequency of extreme rainfall events, the intensity and frequency of low rainfall events are typically overestimated. On the whole, the mean average error is about 50% of the average daily rainfall, based on cross-validation analysis (Jones et al., 2009). For this study we have masked out the pixels where AWAP contains fewer than 50% of total 1461 analysis days.

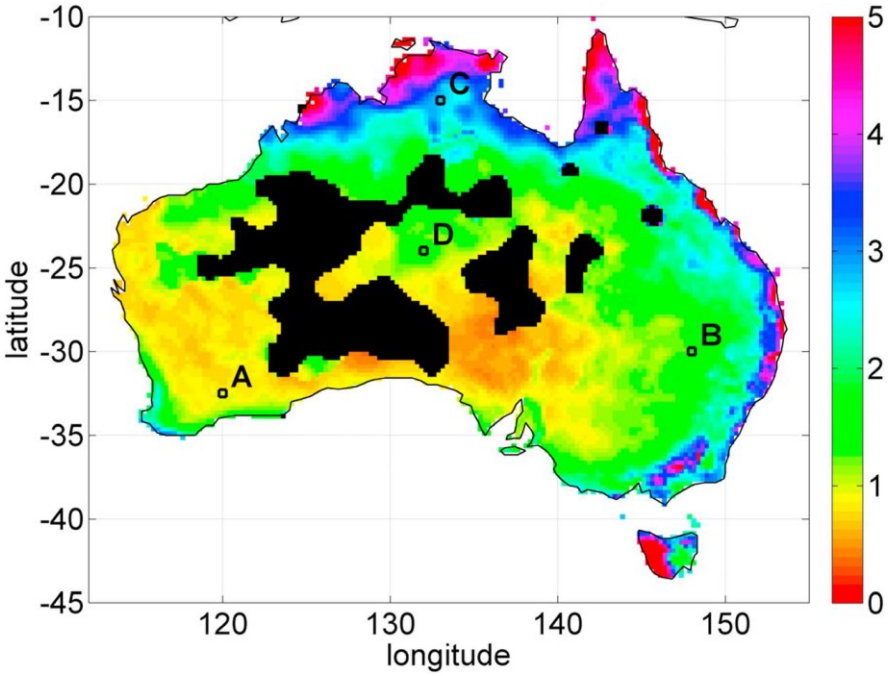

Figure 6.1 - Climatology of the study area expressed as mean daily rainfall rate (mm/d) in the investigated period (from 15 January 2010 to 30 November 2013) obtained by the AWAP data set. The four letters indicate the 1° boxes for which the monthly rainfall time series are shown in Figure 6.6. Black areas represent the zones in which AWAP data are not available.

For the SMOS data set (Kerr et al., 2012), the reprocessed level 3 (L3) data generated with the version 5.51 of the algorithm are taken. The L-Band Microwave Emission of the Biosphere Model (Wigneron et al., 2007) is used for inverting SM from dual-polarized multiangular brightness temperature observations of SMOS; the algorithm details can be found in Kerr et al. (2012). The product is expressed in volumetric terms (m^3/m^3) and is representative of a soil layer of about 3.5 cm. The product is available from January 2010 with a spatial sampling of 0.25°. We note here that the analysis was carried out also with the new SMOS product (version 6.20), only with SM2RAIN, but no significant differences in the results are found. Therefore, we finally decided to use version 5.51 SMOS product. We also underline that in the period January–June 2010 the SMOS data are expected to be of lower quality due to the commissioning phase but removing this period did not have a significant impact on results and hence we preferred to consider the longer period.

The real-time (3B42RT) and the gauge-corrected version 7 (3B42) TMPA products, developed by Huffman et al. (2007), are used in this study. The TMPA algorithm combines infrared information from geosynchronous satellites and several microwave precipitation estimates from active and passive microwave sensors. The 3B42 product is bias adjusted to the monthly Global Precipitation Climatology Centre gauge analyses (Schamm et al., 2013). The real-time product does not include any ground-based information. The TMPA products have coverage of 50°N–50°S and are produced at the 3 h/0.25° temporal/spatial resolution. The accumulated daily rainfall is obtained by aggregating the eight 3 h time windows every day. It should be noted that TMPA data are provided within a time window ±90 min from the nominal time (0000, 0300, …, 2100 UTC), while the satellite soil moisture product and the observed rainfall data set are delivered in local time, i.e.,

UTC + 9 (on average over Australia). Therefore, the daily accumulated rainfall product from 3B42 and 3B42RT represents the total rainfall starting, and ending the next day, at 07:30, with 1.5 h of delay with respect to the other products.

The real-time version of TMPA (3B42RT) is used as input along with SMOS soil moisture observations (ascending plus descending orbits). The gauge-corrected TMPA product, 3B42, is used for a pixel-by-pixel calibration of the parameter values of the three algorithms. The gauge-based AWAP product is finally employed as a separate validation data set (see the diagram in ***Figure 6.2***). We acknowledge that AWAP and 3B42 data sets are not fully independent as the gauge correction of 3B42 product likely includes some of the AWAP gauges. However, as the correction is made at monthly time scale, it is less important at 1 day and 5 days time scales that are considered here for evaluating the candidate algorithms. Due to limitations in the current length of the SMOS soil moisture data set, distinct temporal periods for parameter calibration and model validation are not utilized. Each product is resampled in space to the same computational grid with spacing of 0.25° Equal-Area Scalable Earth (EASE) (EASE grid). The temporal resolution of the obtained rainfall products is daily (9 A.M. to 9 A.M., local standard time, as AWAP). Both the parameter calibration and the performance assessment are carried out for the whole data period, i.e., from 15 January 2010 to 30 November 2013.

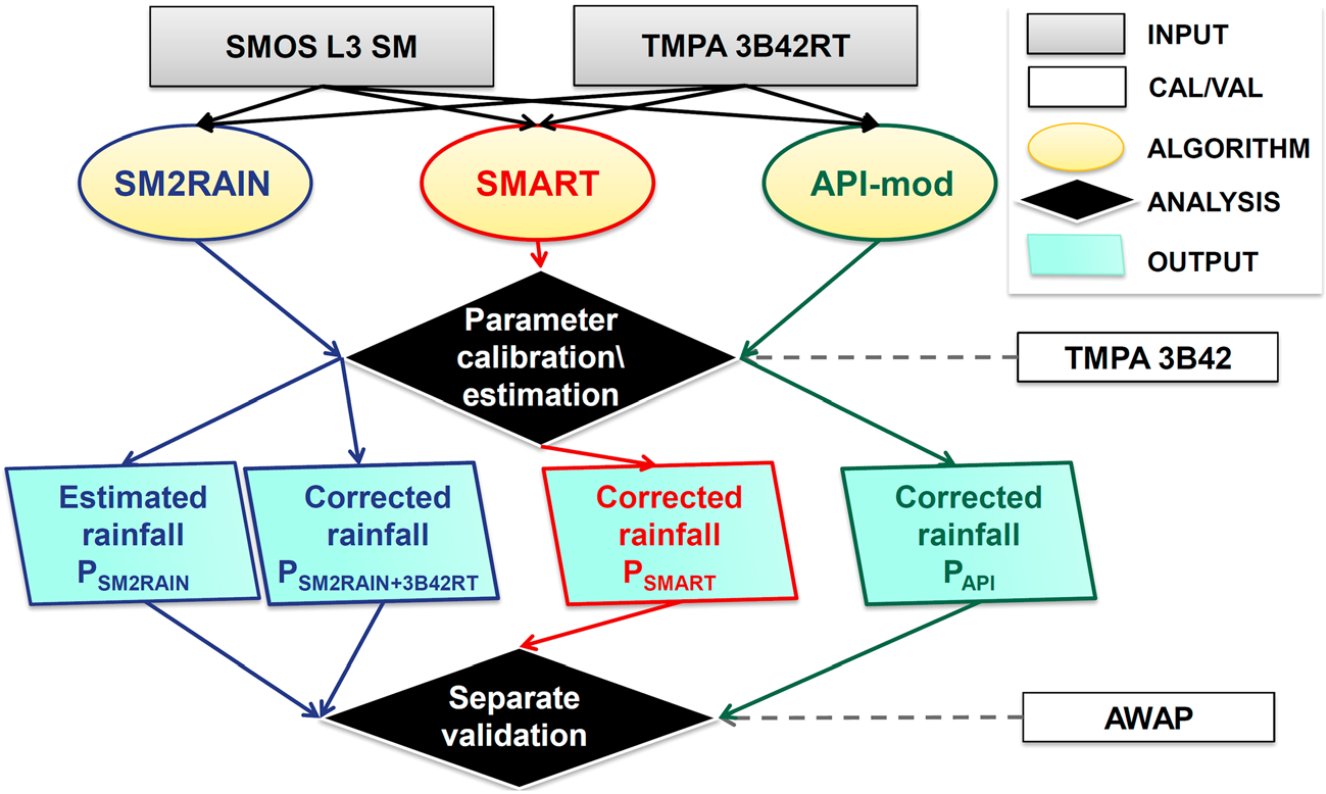

Figure 6.2 - Diagram of the input-output data, algorithms, and processing step carried out in the study for estimating and correcting rainfall through SMOS soil moisture observations. Note that TMPA 3B42 and AWAP data sets are used for parameter calibration/estimation and products validation, respectively.

In the following sections, the main characteristics of each algorithm, and their specific implementation for this study, are summarized. More complete descriptions of each method can be obtained in the cited references.

Rainfall datasets

SM2RAIN

SM2RAIN algorithm is already described in the previous Chapters. In this study SMOS SM data are used to estimate rainfall after some preprocessing steps applied to satellite estimates. the SMOS soil moisture data are first normalized between 0 and 1 by considering the minimum and maximum values of each pixel. Successively, normalized data are interpolated in time at 9 A.M. local time of each day. The obtained time series of relative soil moisture are used as input into the algorithm, and the four parameters (Z*, a, b, and T) are calibrated by minimizing the RMSE between the estimated rainfall and the 3B42 data set at daily time scale. The obtained rainfall product, PSM2RAIN, is in turn merged with 3B42RT through ***Eq. 6.1*** implying the calibration of k parameter; the minimization of RMSE is used also for this step.

$$P_{SM2RAIN+3B42RT}(t) = P_{3B42RT}(t) + k[P_{SM2RAIN(t)} - P_{3B422RT}(t)] \tag{6.1}$$

The second rainfall product is PSM2RAIN+3B42RT, for which the same procedure is applied separately for each pixel of the study area. For simplicity, the two products will be referred as SM2RAIN and SM2RAIN+3B42RT thereinafter.

API-Mod

The API-mod algorithm is based on a simple modification of the Antecedent Precipitation Index (API) initially designed to provide a proxy of the surface soil moisture with a single precipitation observation and a single parameter ι which controls the soil drying-out velocity. The API relationship can be written as

$$API(t) = API(t-1)e^{\frac{\Delta t}{\iota}} + P(t) \tag{6.2}$$

A modification of the API model, API-mod, was introduced in Pellarin et al. (2013). The API-mod includes two more parameters to account for soil saturation (θ_{sat}) and soil layer thickness (d_{soil}). The API-mod algorithm can be expressed as

$$SSM(t) = SSM(t-1)e^{\frac{\Delta t}{\iota}} + [\theta_{sat} - SSM(t-1)][1 - e^{\frac{P(t)}{d_{soil}}}] \tag{6.3}$$

where θ_{sat} [L^3/L^3] is the saturated soil moisture value, d_{soil} is the soil depth [L], P(t) is the rainfall accumulation [L] over a Δt period [T], and ι is a parameter which describes the soil drying-out velocity [T].

A CDF-matching procedure is done in order to avoid any bias between API-mod SSM and SMOS L3SM data. The CDF matching is a pixel-by-pixel procedure and can be expressed as

$$SMOS^{CDF} = p_1 + p_2 SMOS \tag{6.4}$$

With

$$p_2 = \frac{s(API - Mod)}{s(SMOS)} \tag{6.5}$$

$$p_1 = \mu(API - Mod) - p_2\mu(SMOS) \tag{6.7}$$

Where s and μ are the standard deviation and mean of the SM data. The API-mod algorithm provides one rainfall product (***Figure 6.2***), i.e., $P_{API\text{-}mod}$, and requires the calibration of the single parameter τ on a pixel-by-pixel basis; θ_{sat} and d_{soil} parameters are assumed as spatially constant for the whole study area. Before applying the assimilation technique, a preprocessing step is carried out to match SSM, ***Eq. 6.3***, forced with 3B42 daily precipitation and SMOS L3SM data thus obtaining the spatial distribution of p1 and p2 coefficients. Then, for implementing the API-mod methodology, a particle filter assimilation scheme is used. This approach is based on stochastic perturbation of the precipitation forcing that explicitly simulates the consequence of these uncertainties in the soil moisture estimates (Arulampalam et al., 2002; Doucet et al., 2000; Moradkhani et al., 2005; Van Leeuwen, 2009). The random generation is obtained as K = exp(4*_Rand_-2) where *Rand* is a random number uniformly distributed between 0 and 1. Then, each 3 h rainfall estimate is randomly changed using the multiplicative factor K ranging from about 0.13 (e^{-2}) to about 7.3 (e^{2}). The assimilation time period is fixed to five successive SMOS measurements. An ensemble of 100 API-mod simulations is done, and the 10 best simulations are selected based on RMSE minimization between API-mod and SMOS soil moisture at daily time scale. The retrieval accumulation product is calculated as the mean value of the 10 best simulations (average of 10 perturbed precipitation time series). This operation is renewed for the next period of five SMOS measurements and for each 0.25° pixels of Australia. For simplicity, accumulation products $P_{API\text{-}mod}$ acquired above will be referred as API-mod thereinafter.

SMART

The Soil Moisture Analysis Rainfall Tool (SMART, Crow et al., 2009,2011) is based on the sequential assimilation of SMOS soil moisture retrievals into a daily implementation of ***Eq. 6.2*** for the case of P(t) derived from TMPA 3B42RT rainfall accumulations. For each sequential assimilation of a single SMOS retrieval, an increment of water (δ) is either added or subtracted from the analysis background in an attempt to compensate for the impact of random rainfall errors on daily API forecasts. Given their relationship to rainfall errors, these increments can be used to correct satellite-based rainfall accumulations via a simple additive correction (Crow et al., 2009):

$$[P_{SMART}(t)] = [P_{3B42RT}(t)] + \Omega\delta \tag{6.8}$$

where Ω is a temporally fixed (but spatially variable) constant and bracketing "[]" reflects summing within a multiday period. The specific Kalman filter and the API model parameterization applied here follow the one described by Crow et al. (2011) except for three modifications. First, instead of the month-by-month approach recommended by Crow et al. (2011), the preprocessing of SMOS surface soil moisture retrievals is based on the application of a single pixel-wise CDF-rescaling function to transform the distribution of raw SMOS retrievals to match that of the API predictions

obtained from ***Eq. 6.2*** (utilizing 3B42RT rainfall and no data assimilation). This change is made because the 4-year length of the SMOS time series is deemed too short to sample separate rescaling functions for each month. Note that this rescaling approach is similar to that described in ***Eq. 6.4*** for API-mod, except based on the matching of all statistical moments (not just mean and variance). Second, to reflect relatively arid conditions within the Australian continent, the ι in ***Eq. 6.2*** is lowered from the globally fixed value of 6.15 (days) recommended by Crow et al. (2011) to a lower value of 1.96 (days). Third, instead of applying the triple collocation-based approach recommended by Crow et al. (2011), soil moisture retrieval errors in assimilated SMOS soil moisture retrievals are held fixed at a constant value of 0.04 m^3/m^3. This ensures that the data input needs of SMART are consistent with SM2RAIN and API-mod. A temporally constant value of Ω in ***Eq. 6.8*** is calibrated on a pixel-by-pixel basis to minimize the RMSE between [PSMART] and [P3B42] estimates (where brackets indicate either 1-day or 5-day accumulation periods). The SMART algorithm provides a single rainfall accumulation product (***Figure 6.2***), i.e., [PSMART]. The time scale of this product is determined by the accumulation window applied in ***Eq. 6.8***. Past experience with SMART has revealed that it is preferable to apply ***Eq. 6.8*** using a multiday accumulation window rather than applying it at a daily time scale and then aggregating to a multiday period (Crow et al., 2009). Therefore, in order to maximize the 5-day performance of SMART, separate implementations of ***Eq. 6.8***, each with its own unique Ω calibration, were applied to acquire 1 and 5-day SMART rainfall accumulation estimates. Note that such an approach contrasts which that of SM2RAIN and API-Mod, where 5 day accumulations were obtained by simply aggregating 1 day or 3-hourly results (see above). See below and Crow et al. (2011) for additional SMART implementation details. For simplicity, the [PSMART] rainfall accumulation products resulting from the application of ***Eq. 6.8*** will be referred as SMART thereinafter.

Parameter values of rainfall estimation algorithms

Following the procedure described in previous section, the parameter values of each method are computed by using 3B42 as benchmark. ***Table 6.1*** shows the summary statistics of the spatial distribution (median, standard deviation, and 25th and 75th percentiles) of each parameter that is considered to be varying in space for each method. The percentiles are computed on the obtained parameter values and aim at providing an estimate of the frequency distribution of their spatial variability.

The strategy for the parameterization of each method is different. For SM2RAIN and SMART, the parameter values are calibrated based on the explicit minimization of errors (RMSE) with respect to 3B42 retrievals. Specifically, as mentioned above, two separate calibrations are carried out with SMART for 1-day and 5-day rainfall correction. For API-mod, the single parameter ι is parameterized as a function of soil texture information instead of performing a pixel-by-pixel calibration.

For SM2RAIN, the obtained parameter values are quite consistent with those of previous studies by Brocca et al. (2014) and Ciabatta et al. (2015), despite that the application of the exponential filter was not used in those studies. In particular, the Z* parameter is found to be higher than in previous investigations likely due to the application of the exponential filter. Indeed, the filter smooths the soil moisture signal, which in turn becomes representative of a thicker soil layer thus increasing Z*value. Similar considerations can be made for the other parameters. The spatial variability of the parameter values resembles the one found in Brocca et al. (2014) and Ciabatta et al. (2015) as

higher Z* for higher rainfall rates (i.e., northern and eastern Australia; see ***Figure 6.1***) and higher a values along the coasts where the SMOS signal is noisier (Ciabatta et al., 2015).

For the API-mod methodology, similarly to previous studies (Pellarin et al., 2013; Louvet et al., 2015), soil depth (d_{soil}) is fixed to 100 mm and θ_{sat} is fixed to 0.41m^3/m^3, whereas τ is assumed to be related to clay fraction as $\iota = 32 \ln(clay) + 174$ with clay ranging from 0 to 100% (FAO/IIASA/ISRIC/ISSCAS/JRC, 2012). Thus, only three parameters are spatially distributed over Australia in the API-mod method (p1, p2, and ι; see ***Eqs. 6.3*** and ***6.4***).

Parameters		Z* [mm]	a [mm/day]	b [-]	T [days]	k [-]
SM2RAIN	Median	77.2	11.5	5.3	2.9	0.25
	s	135.3	26.9	17.5	6.8	0.18
	25th	48.2	0.0	2.1	1.5	0.11
	75th	125.3	23.4	27.3	6.6	0.38
Parameters		ι [hours]				
API-mod	Median	209.2				
	s	45.4				
	25th	174.0				
	75th	262.3				
Parameters		Ω (1-day) [-]	Ω (5-day) [-]			
SMART	Median	0.15	0.30			
	s	0.14	0.19			
	25th	0.09	0.21			
	75th	0.23	0.41			

Table 6.1 - Summary statistic of the calibration parameters of each method; (s: Standard Deviation; 25th and 75th: Percentiles)

<u>*Results*</u>

Validation results over Australia

Three continuous metrics are used for the evaluation of the performance of the soil moisture-derived rainfall products (and TMPA products): R, RMSE, in mm, the BIAS, computed as relative error on the accumulated rainfall in the entire investigated period, the unbiased RMSE (ubRMSE, in mm), and the mean error (BIAS*, in mm), computed as the long-term mean difference. The ubRMSE is the square root of the difference between $RMSE^2$ and $BIAS^{*2}$, and it provides information regarding the random error only. Additionally, three more categorical metrics are employed: FAR, POD, and TS. See previous section for the definition of the categorical scores. The categorical performance metrics are evaluated for different rainfall thresholds computed as rainfall percentiles (from 0 to 100°) of each pixel in the study area (e.g., Chen et al., 2012; Brocca et al., 2014).

Continuous performance scores (R and RMSE) are computed for both 1-day and 5-day accumulated rainfall, and the summary statistics of their spatial distribution are given in ***Table 6.2***. Specifically, all the performances are referred to the comparison with the AWAP data set, and six different satellite-based rainfall products are analyzed: 3B42, 3B42RT, SM2RAIN, SM2RAIN+3B42RT, API-mod, and SMART. As in ***Table 6.1***, the percentiles are simply computed on the values obtained for each performance score and aim at providing an estimate of their frequency distribution. The performance of 3B42 is reported here as a baseline product. However, we note that 3B42, by retrospectively including ground-based observations, is not comparable with the other products based solely on near-real-time satellite observations. The top down baseline to be compared with SMOS-based rainfall products is the (purely remotely sensed) 3B42RT product. Additionally, the SM2RAIN product should be analyzed separately from the other three products (SM2RAIN+3B42RT, API-mod, and SMART) as it considers only SMOS soil moisture data and does not utilize 3B42RT rainfall improvement. As there is an extreme range of precipitation patterns across Australia, the performances are also computed for each climatic zone. The relative comparison between these zone-specific scores is quite similar to that obtained for the whole Australia with only minor differences (outlined below) and, hence, not shown here for brevity. In terms of correlation, which provides information about the ability of reproducing the relative temporal dynamics of observations, 3B42RT performs quite well for both 1-day and 5-day accumulated rainfall with median R values equal to 0.62 and 0.72, respectively. SM2RAIN provides lower (higher) scores for 1 day (5 day) accumulated rainfall. Indeed, as shown in previous studies (e.g., Brocca et al., 2014), the revisit time of SMOS observations (~2 days in Australia) is not suitable for accurately estimating rainfall at daily time scale. Nevertheless, both SM2RAIN+3B42RT and SMART are found to outperform 3B42RT with consistent results, which are also close to those of 3B42. For SM2RAIN+3B42RT (SMART) the median R values are equal to 0.65 (0.63) and 0.76 (0.76) for 1-day and 5-day accumulated rainfall, respectively, and these values are significantly different from those obtained with 3B42RT (significance level of 0.10, one-tailed test). The performance of API-mod is found to be slightly lower in terms of correlation, specifically for 1-day rainfall estimates. The spatial distribution of the local correlations is shown in ***Figure 6.3*** for 1-day and 5-day accumulated rainfall. ***Figure 6.3*** (left column) represents the correlation maps obtained with 3B42RT, and ***Figure 6.3*** (right column) presents the ratio between the correlations obtained with SMOS-based products and the baseline (3B42RT). Therefore, from left panels of ***Figure 6.3*** the spatial pattern of the performance is shown, while the right panels provide an immediate understanding of the areas where an improvement (blue) and a deterioration (red) of performances occur. For 1-day rainfall it is evident that SM2RAIN+3B42RT and SMART provide a significant improvement of the correlation, mainly in the central part of Australia (arid climate). SM2RAIN and API-mod have lower performance, and only by considering 5-day accumulated rainfall, a widespread improvement related to these two products is observed. Interestingly, the lower performance of the SMOS based rainfall products is found along the coast and particularly in the southeastern (temperate climate) part of Australia (evident for SM2RAIN at 1 day). This region is characterized by a high density of vegetation and the presence of urban areas, and, hence, the lower accuracy of SMOS soil moisture product is expected. In terms of RMSE (see ***Table 6.2***), which aims at characterizing the random error plus the BIAS between observed and estimated rainfall data, the relative performances of the products are different with respect to correlations.

Product		1-day Rainfall			5-day Rainfall			BIAS	|BIAS|
		R	RMSE (mm)	TS	R	RMSE (mm)	TS		
3B42	10^{th}	0.53	3.06	0.3	0.67	6.48	0.53	-0.14	0.02
	50^{th}	0.68	4.73	0.42	0.8	10.7	0.66	0.03	0.09
	90^{th}	0.78	8.69	0.54	0.88	20.08	0.76	0.21	0.25
3B42RT	10^{th}	0.46	3.44	0.27	0.54	8.3	0.48	-0.18	0.05
	50^{th}	0.62	5.59	0.4	0.71	14	0.62	0.2	0.26
	90^{th}	0.73	9.44	0.52	0.83	24.04	0.74	0.7	0.72
SM2RAIN	10^{th}	0.4	2.61	0.27	0.58	6.04	0.46	-0.26	0.02
	50^{th}	0.56	4.4	0.38	0.74	10.71	0.6	0.01	0.12
	90^{th}	0.66	8.5	0.48	0.83	23.37	0.81	0.27	0.37
SM2RAIN+3B42RT	10^{th}	0.51	2.86	0.28	0.61	6.81	0.47	-0.18	0.04
	50^{th}	0.65	4.39	0.4	0.76	11.07	0.6	0.15	0.2
	90^{th}	0.75	8.16	0.52	0.85	20.72	0.78	0.47	0.53
API-mod	10^{th}	0.44	3.29	0.24	0.57	6.57	0.47	-0.21	0.03
	50^{th}	0.58	5.43	0.37	0.73	11.89	0.61	0.07	0.15
	90^{th}	0.69	9.03	0.48	0.83	22.2	0.72	0.37	0.42
SMART	10^{th}	0.48	3.16	0.28	0.62	6.77	0.48	-0.24	0.03
	50^{th}	0.63	5.24	0.39	0.76	12.13	0.63	0.09	0.18
	90^{th}	0.74	9.04	0.5	0.85	22.53	0.81	0.5	0.59

Table 6.2 - Summary statistics of the spatial distribution of performance scores of the different satellite rainfall products in the comparison with AWAP data.

The baseline 3B42RT product has quite large RMSE values (e.g., median RMSE = 5.59mm for 1-day rainfall), partly due to the tendency to overestimate observations (median BIAS = 0.20). Therefore, all SMOS-based rainfall products outperform 3B42RT for both rainfall accumulations. The best performing products are SM2RAIN+3B42RT for 1- day accumulation and SM2RAIN for 5-day accumulations.

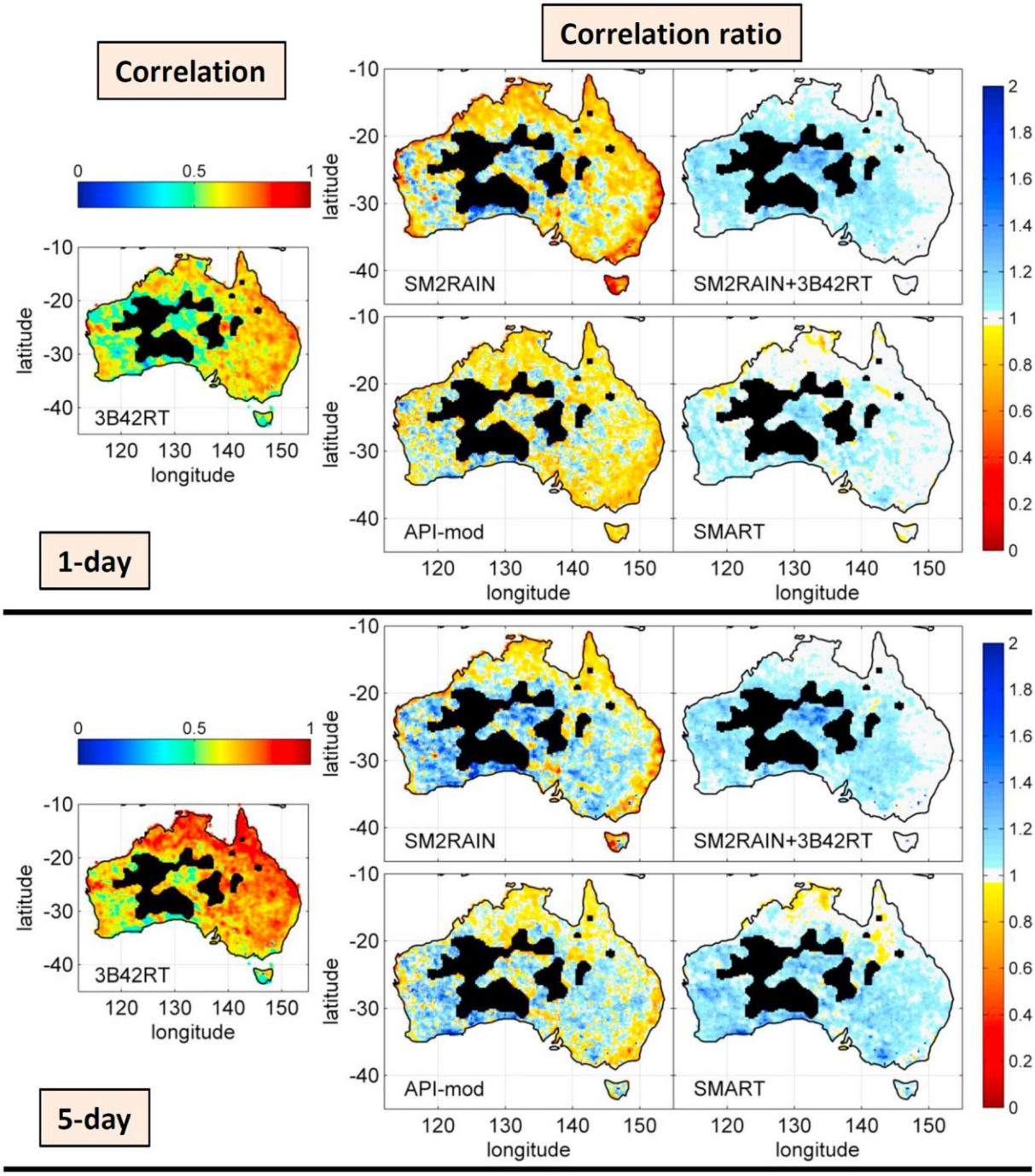

Figure 6.3 - (left column) Pearson's correlation maps between AWAP-observed accumulated rainfall and TMPA 3B42RT product. (right column) Correlation ratio maps between the correlation obtained by comparing the four different SMOS-derived products (SM2RAIN, SM2RAIN+3B42RT, API-mod, and SMART) with AWAP observed rainfall and the correlation obtained with TMPA 3B42RT (left column); red pixels indicate degradation (lower correlations), whereas blue pixels an improvement (higher correlations). The analysis period is from 14 January 2010 to 30 November 2013, and the top (bottom) rows show results for 1 day (5 day) accumulated rainfall. Black areas represent the zones in which AWAP data are not available.

Interestingly, for 1-day rainfall SM2RAIN-related products show performance scores even better than the gauge-corrected 3B42. Differently from the correlations, API-mod provides comparable scores with SMART. The absolute BIAS (last column of ***Table 6.2***) gives nearly the same picture of RMSE with all the SMOS-based products outperforming 3B42RT and the best results for SM2RAIN. ***Figure 6.4***, similarly to ***Figure 6.3***, shows on the spatial distribution of RMSE values obtained through 3B42RT (left column) and the improvement (blue)/deterioration (red) that is found due to the use of SMOS soil moisture data for rainfall estimation/correction (right column). Clearly, all the maps highlight that the use of SMOS largely improves the estimation of rainfall in terms of RMSE, with all the products providing the largest added value in central Australia (arid climate). The overall spatial patterns of RMSE and R values are in good agreement (e.g., low to no improvement along the coast and better scores in central Australia).

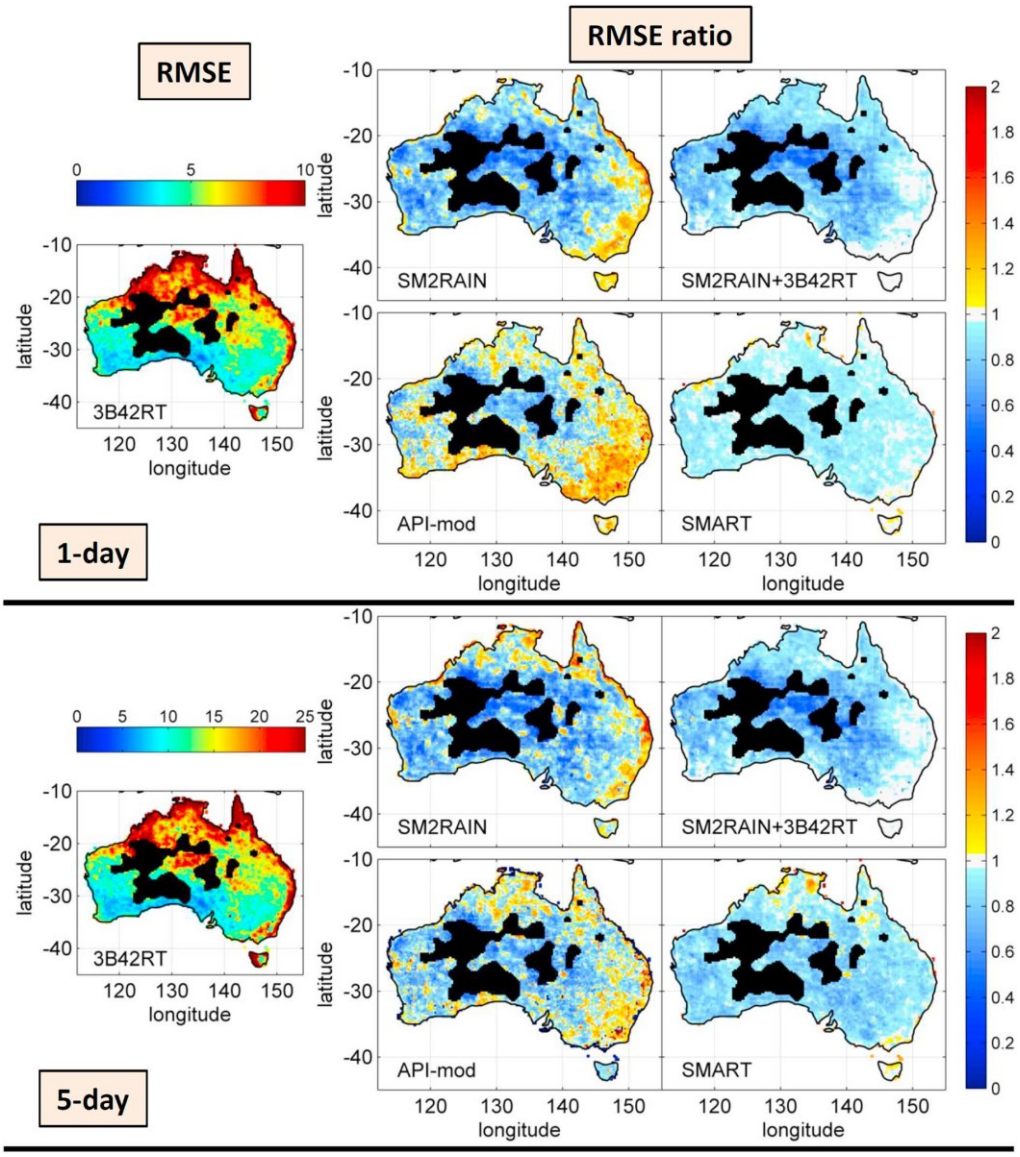

Figure 6.4 - As in Figure 6.3 but for the root-mean-square error (RMSE). Red pixels indicate degradation (higher RMSE), whereas blue pixels indicate an improvement (lower RMSE).

Besides the continuous performance scores, rainfall products should be analyzed in terms of their capacity to detect the occurrence of rainfall events. In ***Table 6.2*** the summary statistics of the TS

values are given for each product. TS integrates POD and FAR scores and is computed in 6.2 for a rainfall threshold of 0.2 mm. 3B42RT provides quite accurate results with median TS values equal to 0.40 and 0.62 for 1-day and 5-day accumulated rainfall, respectively. SMOS-based products generally provide equal or lower performances with the SM2RAIN+3B42RT product giving the best scores for 1-day accumulated rainfall. For 5-day rainfall, SMART has the best scores (except for the 10th percentiles) with median TS of 0.63. ***Figure 6.5*** shows the POD, FAR, and TS values in each panel for both 1-day and 5-day accumulated rainfall. Plots show the median (±1 standard deviation) values of each categorical score and for different rainfall threshold computed as the 10th, 50th, and 90th percentiles of the AWAP-observed rainfall in each pixel. Therefore, the panels show the capability of the products to detect rainfall occurrence for low to high rainfall events (from left to right).

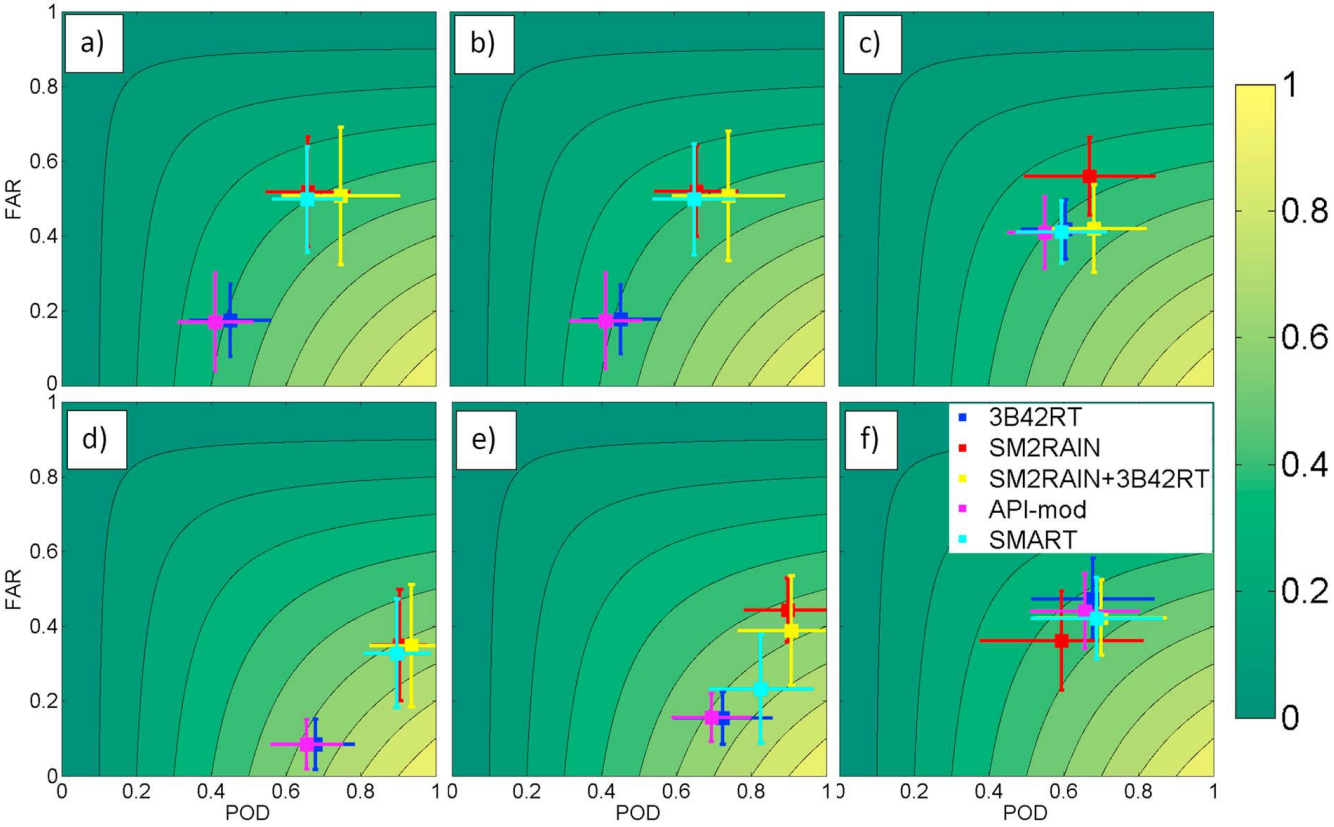

Figure 6.5 - POD (Probability of Detection) versus FAR (False Alarm Ratio) plots for (a, d) 10th, (b, e) 50th, and (c, f) 90th percentile and for 1 day (Figures 6a–6c) and 5 days (Figures 6d–6f) accumulated rainfall. The contour lines indicate TS (Threat Score) values, the horizontal (vertical) bars represent the standard deviation of POD (FAR), and the square is the median value. Squares represent the median POD (FAR) over all pixels for the 10th, 50th, and 90th percentiles at that pixel. Optimal performances are for FAR = 0, POD = 1, and TS = 1. Percentiles represent the rainfall threshold used for the computation of the scores. Therefore, low (high) percentiles indicate the product capability to detect high (low) rainfall intensities.

For 1-day rainfall (***Figures 6.5a–6.5c***), SM2RAIN and API-mod give the lower performance in terms of TS. SMART, SM2RAIN, and SM2RAIN+3B42RT have a quite high probability of falsely identifying rainfall events (high FAR) but a good detection capability (high POD). 3B42RT and API-mod have an opposite behavior with low FAR and relatively low POD values. It should be also

underlined that for 90th percentiles (high rainfall intensities) the product's behavior is more similar and the best product is found to be SM2RAIN+3B42RT. For 5-day rainfall (***Figures 6.5d–6.5f***), the product's performance is better (lower FAR and higher POD) but with a similar pattern of 1-day rainfall. For medium to high rainfall intensities (50th and 90th percentiles, 5-day rainfall), the best product is SMART with values very close to the optimal performance (FAR = 0, POD = 1, TS = 1) for the 50th percentiles. Overall, performances deteriorate from left to right mainly due to the increased difficulty of detecting high-intensity rainfall events. The overall performance of SMOS-based rainfall products is in agreement with previous studies by Chen et al. (2012), Brocca et al. (2014), and Ciabatta et al. (2015) who found that the soil moisture correction improves POD and deteriorates FAR, with a corresponding slight increase in TS.

Monthly scale analysis

The temporal pattern of observed (AWAP) and estimated (SMOS-based) rainfall is analyzed for the four 1° domains identified in ***Figure 6.1***. In particular, ***Figure 6.6*** shows monthly rain time series of all products (5-day SMART simulation are considered here). The main purpose of ***Figure 6.6*** is to visualize explicitly the capability of the different rainfall products to reproduce the total volume of rainfall. The agreement with observations at monthly time scale is very good for all products with the exception of SM2RAIN in ***Figure 6.6c*** (underestimation) and 3B42RT and SMART in ***Figure 6.6d***. The figures highlight that the temporal dynamic of SMART and 3B42RT is very similar (e.g., ***Figure 6.6d***), while the other three SMOS-based products (SM2RAIN, SM2RAIN+342RT, and API-mod) are more independent from 3B42RT.

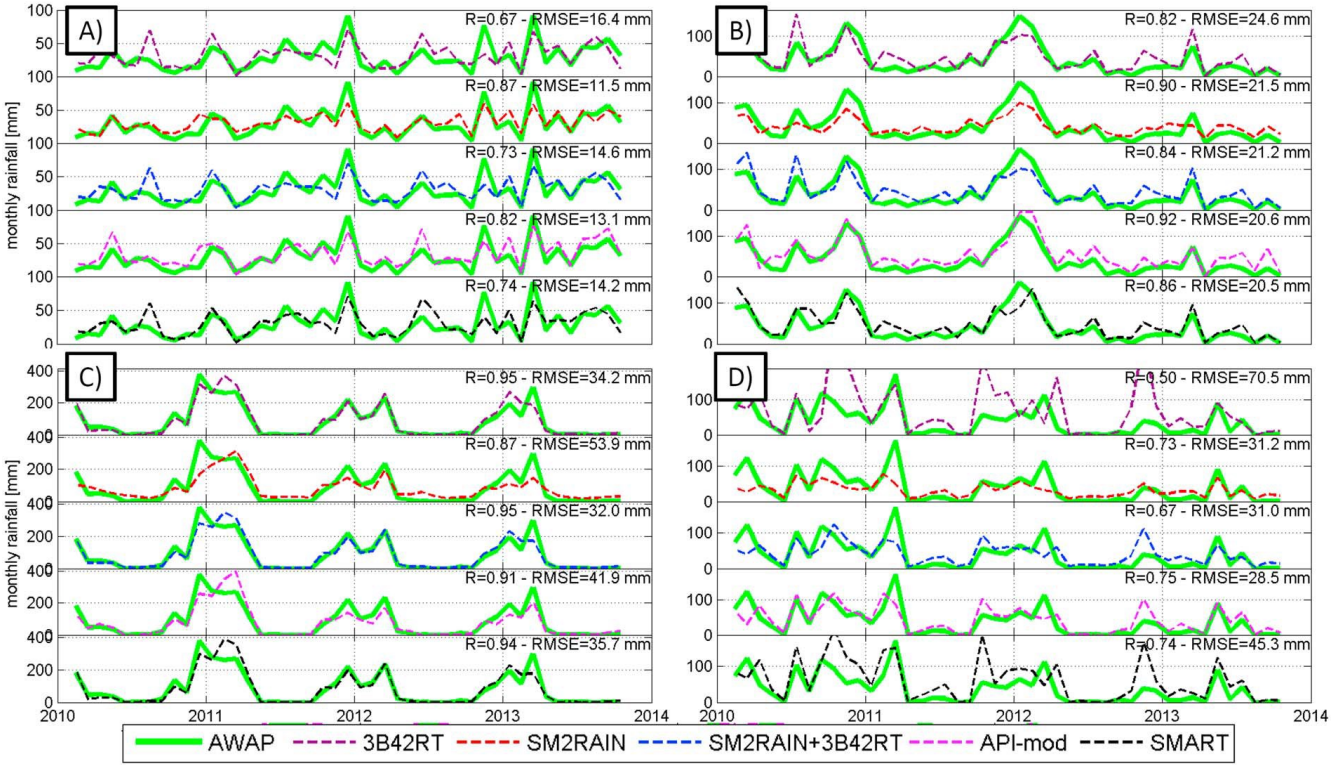

Figure 6.6 - Time series of monthly rainfall obtained from observations (AWAP), the real-time TMPA product (3B42RT), and the SMOS-derived products (SM2RAIN, SM2RAIN+3B42RT, API-mod, and SMART) for the four boxes shown in Figure 6.1 (R: Pearson's correlation coefficient; RMSE: root-mean-square error).

6.2 Validation over India

The section focused on the integration of multiple satellite SM products for obtaining a unique, superior rainfall product via SM2RAIN. The study is carried out over India and Italy, by considering five different satellite SM products and two different gauge-based rainfall datasets as benchmark. Moreover, a comparative analysis is carried out by comparing the SM-derived rainfall data with the Integrated Multi-satellitE Retrievals for GPM (IMERG) precipitation product (Huffman et al., 2014). This section is based on the publication:

Tarpanelli, A., Massari, C., Ciabatta, L., Filippucci, P., Amarnath, G., Brocca, L. (2017). Exploiting a constellation of satellite soil moisture sensors for accurate rainfall estimation. Advances in Water Resources, 108, 249-255.

Study area

The study areas, India and Italy, are chosen for two main reasons. First, a dense rainfall network is available for the period under investigation in both countries. In India, the observed dataset is derived by the India Meteorological Department (IMD) that provides daily rainfall data from 1901 to the present day. The observed rainfall dataset for Italy is obtained by the spatial interpolation of more than 3000 rain gauges over the territory (Ciabatta et al., 2015). Both datasets are available at 0.25°daily spatial/temporal resolution. Second, the two countries are characterized by different geographic scale, varied topography and diverse climate conditions. A large part of India is located within the semi-arid tropics and much of the countries relies on tropical monsoon supporting rainforests in the southwest and the island territories (Peel et al., 2007). Differently, climate in Italy ranges from humid subtropical climate in the northern areas and Mediterranean climate along the coastal areas and southern regions (Ciabatta et al., 2015).

Due to the detailed analysis carried out over Italy, in the following only the results obtained over India will be reported.

Satellite soil moisture and rainfall products

Five active and passive microwave satellites sensors constitutes the "constellation" from which we obtained the different SM products. These products are used as input into the SM2RAIN algorithm for the estimation of rainfall. In the following, a brief list with the main characteristics of each sensor is provided (see also ***Table 6.3***):

1) The Advanced SCATterometer (ASCAT) onboard Metop-A and Metop-B satellites is a scatterometer operating at C-band (5.255 GHz). It provides a SM product characterized by ~25 km and daily spatial-temporal resolution (Wagner et al., 2013). In this study, the SM product provided within the EUMETSAT H-SAF project (http://hsaf.meteoam.it/) denoted as H109 is used.

2) The Advanced Microwave Scanning Radiometer 2 (AMSR2) onboard the Global Change Observation Mission for Water satellite is a radiometer operating in the microwave range 6.925-89.0 GHz. At the bands used for SM estimation (C- and X-bands), the spatial-temporal resolution is ~25 km and daily (Kim et al., 2015). In this study, we focused on the X-band SM product (X-band is found to outperform C-band, not shown for brevity) obtained by the application of the Land Parameter Retrieval Model to AMSR2 brightness temperature data (Parinussa et al., 2015).

3) The Soil Moisture Active and Passive (SMAP) mission SM product is obtained by L-band radiometer observations (1.4 GHz) with ~36 km and 2 days spatial-temporal resolution (Entekhabi et al., 2010). In this study, the version 3 of the Level 3 SM retrievals are used (SMAP_L3_SM_P).

4) The Soil Moisture and Ocean Salinity (SMOS) mission provides a SM product through a radiometer operating at L-band (1.4 GHz) with ~50 km of spatial resolution and 2 days of temporal resolution (Kerr et al., 2012). In this study, version RE04 (level 3) provided by the Centre Aval de Traitement des Données SMOS (CATDS) is used.

5) RapidScat, onboard the International Space Station, is a scatterometer operating at Ku-band (13.4 GHz) in HH and VV polarization over the ± 50° latitude band. It provides data with ~25 km of spatial resolution and temporal resolution depending on the latitude varying from nearly daily in Italy to once every two days in southern India. It is worth to notice that RapidScat does not provide an official SM product. In this study, the backscatter data are used as proposed in Brocca et al. (2016a) for obtaining a RapidScat-based SM product.

For the sake of simplicity, the rainfall products derived by each SM product are referred with the name of the sensor/mission, i.e., ASCAT, AMSR2, SMAP, SMOS, and RapidScat.

SENSOR	SATELLITE	STARTING MONTH	BAND	SPATIAL RESOLUTION	REVISIT TIME
ASCAT	Metop-A, Metop-B	Jan 2007	C (5.255 GHz)	25 km	1 day
AMSR2	Global Change Observation Mission for Water	Jul 2012	X (10.65 GHz)	25 km	1 day
Radiometer	Soil Moisture Active and Passive mission	Apr 2015	L (1.4 GHz)	36 km	2 days
MIRAS	Soil Moisture Ocean Salinity Mission	Jan 2010	L (1.4 GHz)	50 km	2 days
RapidSCAT	International Space Station	Nov 2014	Ku (13.4 GHz)	25 km	1-2 days

Table 6.3 - Main characteristics of the satellite soil moisture products employed in this study.

The merging procedure is feasible if the datasets are consistent each other in terms of spatial-temporal resolution and coverage. Therefore, all the satellite SM products are spatially resampled at 0.25° and temporally interpolated at daily scale at 0000 UTC +3.5 hours (+1 hour) for India (Italy), i.e., at the spatial and temporal resolution (and sampling) of ground observations. As the satellite missions are characterized by different operative periods, a common time window from April to December 2015 is considered in which all satellite SM products are available.

In order to assess the capabilities of the SM-based rainfall products, a comparative analysis is carried out with the rainfall estimates obtained by GPM mission (Hou et al., 2014). The Integrated Multi-satellitE Retrievals for GPM (IMERG) precipitation products, released in early 2015 (Huffman et al., 2014), is available at 0.1° x 0.1° spatial and half-hourly temporal resolutions in three modes, based on latency and accuracy: "early" run (6 h after observation), "late" run (18 h after observation) and "final" run (four months after the observation month). The IMERG "late" run (hereinafter IMERG-lr) product, aggregated at 1-day and 0.25° temporal/spatial resolution, is used here.

SM2RAIN algorithm

The SM2RAIN algorithm is applied separately to the five SM products, by considering a pixel-by-pixel calibration and the minimization of the root mean square error (RMSE) between ground-based and SM2RAIN rainfall estimates as objective function. The short period of analysis (mainly due to the recent SMAP mission) does not allow to consider a calibration and validation period. However, it does not influence the concept of the study that is to demonstrate the benefit derived from integration of multiple SM products for rainfall estimation. For further details of SM2RAIN, the reader is referred to the previous sections. In the application of SM2RAIN to the five SM products, some differences in the processing exist and below they are specified. In the SMAP SM product only the descending orbits are used; therefore, SM2RAIN is simply applied to a single SM time series. The ASCAT SM product incorporates measurements derived by sensors onboard Metop-A and Metop-B satellites, ascending/descending orbits. SM2RAIN is applied to the SM time series integrating both sensors and orbits, as the SM time series are highly consistent. Differently, in the case of AMSR2 and SMOS satellites, the SM products based on ascending and descending orbits present some differences and, hence, SM2RAIN is applied separately to the two orbits. Similarly, also for RapidScat the HH and VV polarizations are considered separately. For obtaining a single rainfall product from each sensor, a first merging is carried out between the two rainfall products (two orbits or polarizations) obtained by AMSR2, SMOS and RapidScat through the merging procedure described below.

Merging procedure

The merging procedure uses a linear combination of all the satellite rainfall products derived from SM observations. The weights of the linear combination are constant in time and varying in space (pixel-by-pixel), with the constrain that the sum of the weights is equal to one. The weights are computed by minimizing *RMSE* between the observed and the estimated rainfall, i.e., the merged product hereinafter referred as MERGING.

Performance indices

The capability to reproduce the observed temporal pattern of rainfall is evaluated through the calculation of the same performance indices used in the previous work by Brocca et at. (2016b) at daily time scale: Pearson coefficient of correlation, *R*, the mean relative error, *BIAS*, and the unbiased root mean square error, *ubRMSE*, computed as:

$$ubRMSE = \sqrt{RMSE^2 - BIAS^2} \tag{6.9}$$

Additionally, three categorical metrics are evaluated for each point and for different rainfall thresholds (Chen et al., 2012; Brocca et al., 2014): *POD*, *FAR* and *TS*.

Performance assessment

Figure 6.7 shows the spatial distribution of the performance metrics R, ubRMSE and absolute BIAS, between observed and estimated daily rainfall in India. As expected, lower performances are observed in Northern India due to the complex topography, and higher accuracy is obtained in the arid and semi-arid parts of western India. Result are consistent with the study by Brocca et al. (2014) who found better performance scores in arid and semi-arid areas and lower in mountainous regions. Among the five SM products, AMSR2 provides the better results with median R of 0.57

and median ubRMSE of 7.7 mm/day. ASCAT and SMAP have slightly lower performances with median R=0.53 and 0.49, respectively. The lower accuracy of RapidScat is likely due to the impact of vegetation that is not properly accounted in the retrieval algorithm (Brocca et al., 2016a). For SMOS the radio frequency interferences that affected large parts of India in 2015 (Koster et al., 2016) are the most likely responsible of the obtained low performances.

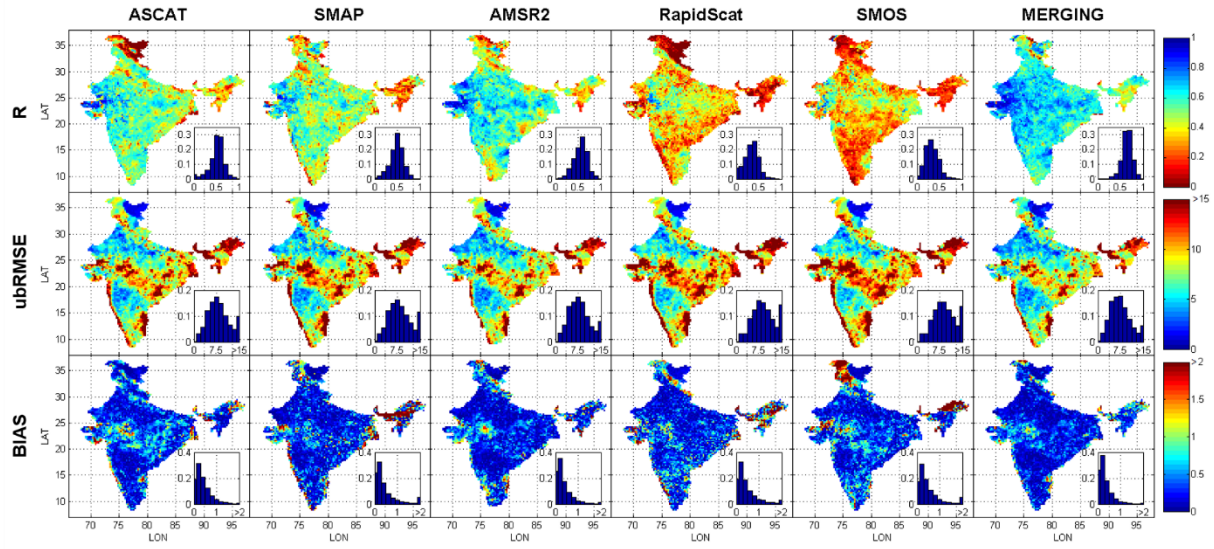

Figure 6.7 - Pearson correlation, R (upper panels), unbiased Root Mean Square Error (ubRMSE, middle panels) and absolute BIAS (lower panel) maps obtained from the comparison of daily rainfall products derived from ASCAT, SMAP, AMSR2, RapidScat, SMOS and after the merging procedure (MERGING) against ground-observed data at 0.25°/daily spatial/temporal resolution. The insets in each sub-figure show the corresponding frequency distribution.

In terms of ubRMSE, the maps show similar spatial patterns that are mainly driven by the rainfall amount, i.e., higher error where it rains more. By comparing absolute BIAS and ubRMSE, it is evident that the random component is dominating the error (ubRMSE>>BIAS, ~30 times) in accordance with previous investigations in Australia (Brocca et al., 2016b).

The large differences among the results of single SM products do not affect the integrated product, MERGING (see ***Figure 6.7***). Indeed, the weaknesses of each single product are significantly reduced, providing high correlations (median R=0.65) and low ubRMSE (7.1 mm/day), even outperforming IMERG-lr product (median R / ubRMSE = 0.56 / 9.7 mm/day). The percentage increase in the performance of the merged product is equal to +45% (-14%) in terms of R (ubRMSE) with respect to the average values of single products. The analysis of the weights enables to evaluate the impact of each rainfall product to the final MERGING (not shown for brevity): on average AMSR2, ASCAT and SMAP contributes 41, 27 and 21%, respectively, whereas for RapidScat and SMOS the contribution is lower (11%).

Figure 6.7 shows the performance metrics obtained by the different SM-based products, as well as the merged product, grouped by rainfall intensity (computed on the observed dataset). Specifically, we considered three type of rainfall events: drizzle (≤5 mm/day), moderate (5-15 mm/day) and heavy (≥15 mm/day). In terms of correlation, better performances are obtained for drizzle and heavy rainfall events while for the other metrics a comparison between event types is not appropriate (errors are lower for lower rainfall intensities).

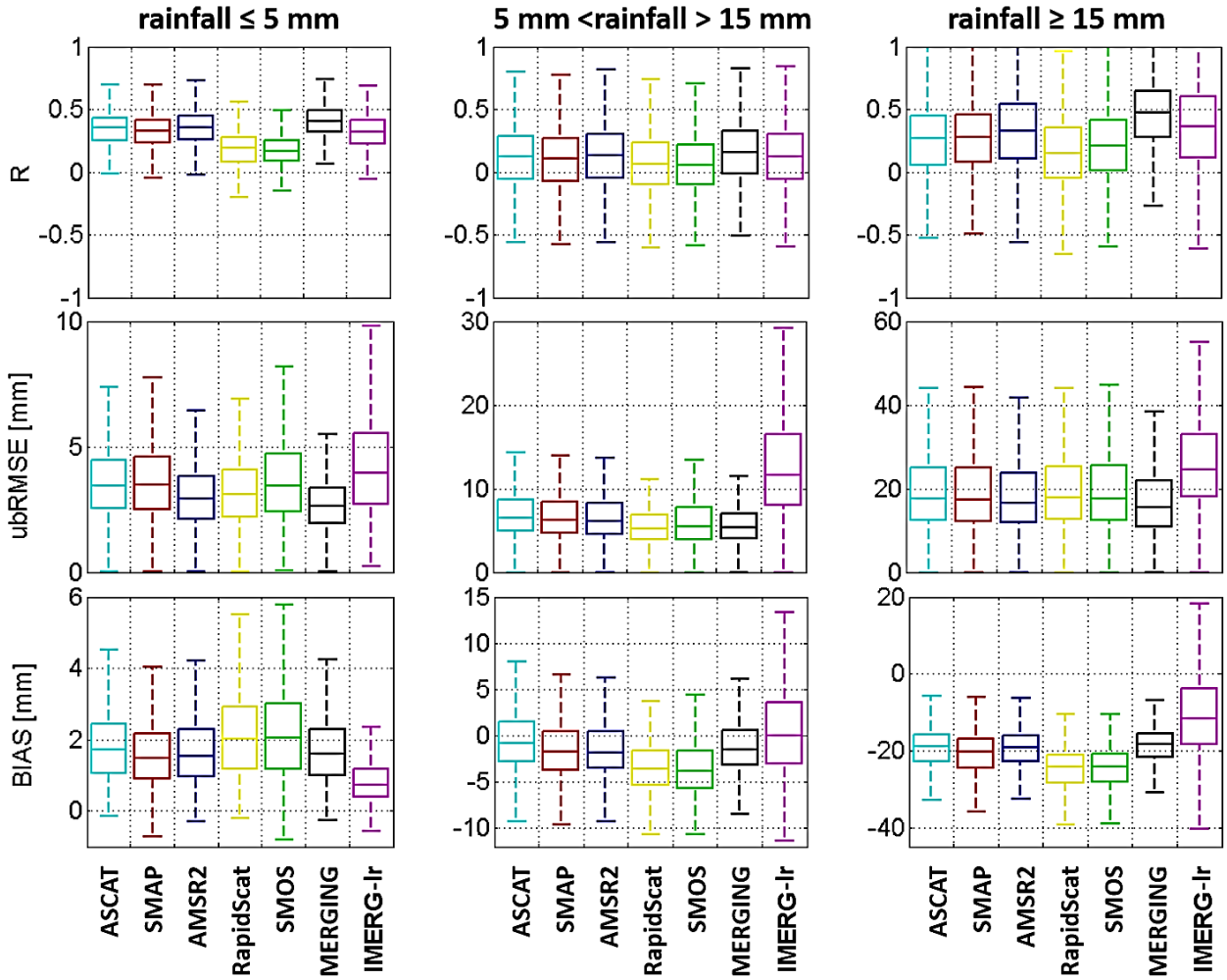

Figure 6.7 - Box plot of summary statistics for 1-day rainfall estimates grouped by rainfall intensity, i.e., <5 mm (drizzle events), 5-15 mm (moderate rainfall events), >15 mm (heavy rainfall events), computed on the ground observed data in India. Note that y-axis have different ranges to better visualize the differences in the performance between datasets. In the box plots the min/max, 25/75° percentiles and the median values are shown (R: Pearson correlation coefficient; ubRMSE: unbiased Root Mean Square Error, BIAS: mean error).

The merged product (MERGING) is always outperforming the others, including IMERG-lr, except for the BIAS. The larger differences are observed for moderate and heavy rainfall events in terms of ubRMSE and for low and heavy rainfall events in terms of R. All the products overestimate low rainfall events (positive BIAS) and underestimate moderate and, particularly, heavy events. Indeed, the median BIAS for heavy events is equal to -18 and -11 mm for MERGING and IMERG-lr, respectively.

Categorical scores assessment

The capability to detect the occurrence of rainfall events is investigated through the computation of categorical scores. ***Figure 6.8*** shows POD, FAR and TS for daily accumulated rainfall and for three rainfall thresholds (0, 5, and 15 mm/day) in order to assess the detection capability from low to high rainfall events. In India (***Figure 6.8***), by analysing TS-values, we obtained that MERGING product performs worse than IMERG-lr for low rainfall threshold (>0 mm/day), mainly due to the

overestimation of rainfall as identified by high POD and FAR values. Differently, for rainfall threshold >5 and >15 mm/day, MERGING product outperforms IMERG-lr.

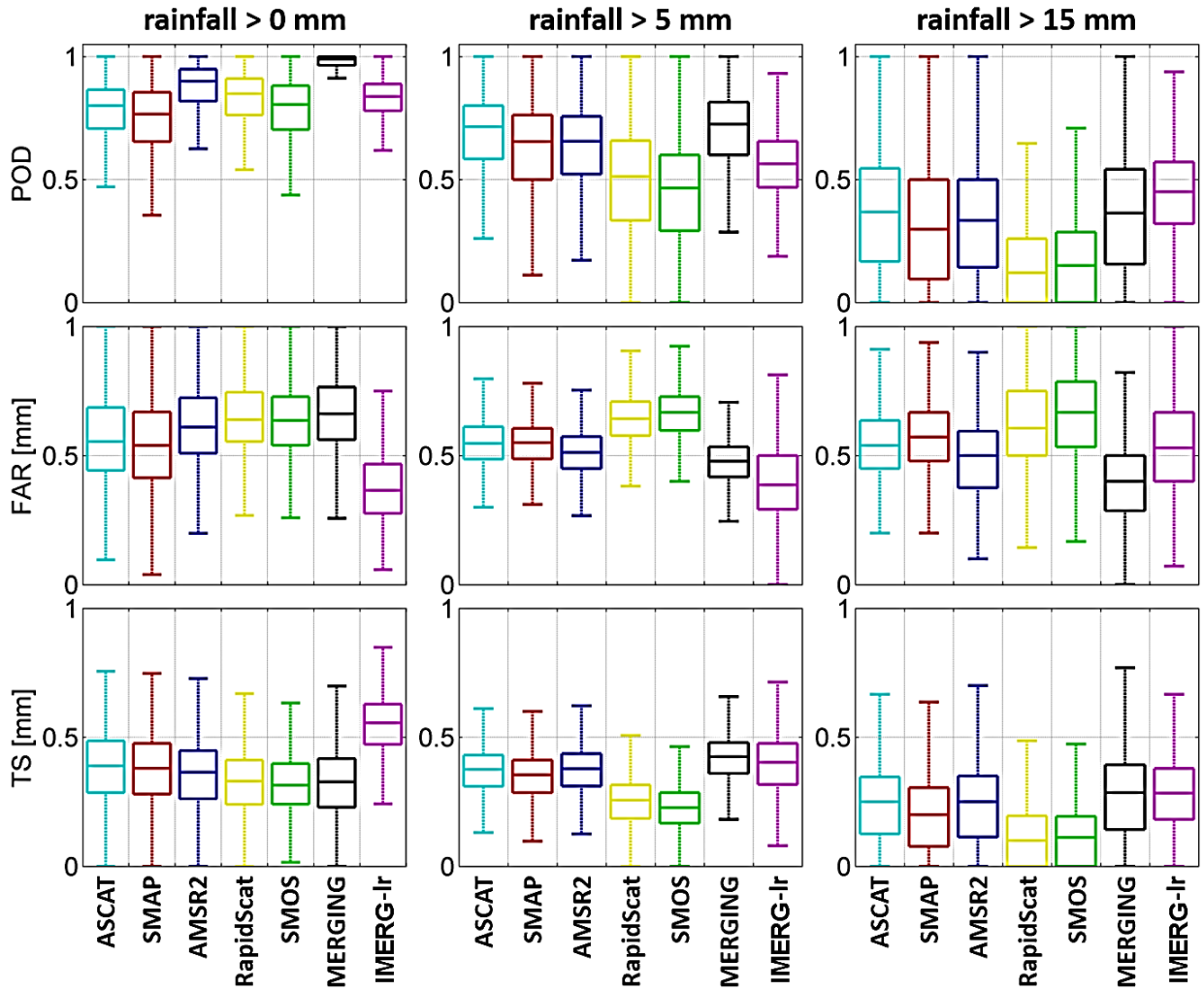

Figure 6.8 - Box plot of the categorical metrics POD (Probability of Detection), FAR (False Alarm Ratio) and TS (Threat Score) values, for daily rainfall estimates grouped by rainfall intensity, i.e. >0 mm, >5 mm and >15 mm, and computed on the ground observed data in India. In the box plots the min/max, 25°/75° percentiles and the median values are shown.

6.3 Rainfall-runoff modelling over the Mediterranean area

This section presented the results of a hydrological validation carried out over the Mediterranean area. The analysis involved both classical and SM2RAIN-derived rainfall products over 15 basins with different climatic and physiographic features. As benchmark, a high quality rainfall product is used to force a semi-distributed model in order to obtain baseline simulations. The analysis highlighted the needed of BIAS correction and model recalibration, underlining also the beneficial effect of integration between rainfall products. This section in based on the publication:

Camici, S., Ciabatta, L., Massari, C., Brocca L. (2018). How reliable are satellite precipitation estimates for driving hydrological models: a verification study over the Mediterranean area. Journal of Hydrology, under review.

The study by Camici et al. (2018) analyzed 15 catchments draining into the Mediterranean Sea (***Figure 6.9***). The Mediterranean region, is characterized by complex topography ranging from the Alpine Mountains, the Italian and Balkan peninsulas, northern Spain, and southern France containing about a hundred peaks higher than 4000 meters, to the Great European Plain most of which lies below 152 meters in elevation. Due to the topographic complexity, the climate is generally characterized by hot dry summers and humid cool winters with an intricate spatial/temporal variability. A clear contrast exists between the rainier northern part of the study region (Southern Europe) and the drier southern area (North Africa, Iberian Peninsula) and between the western sides (rainsides) of the Iberian, Italian and Balkan peninsulas and their eastern sides (rainshadows). The mean annual precipitation averaged over the study area is P = 593 ± 203 mm year−1, but it has a strong spatial variability ranging from 20 mm year−1 (North Africa) to 1500 mm year−1 (Alps). A significant seasonal variability exists, with the early winter and late autumn months (November and December) being the wettest with precipitation amounts larger than 60 mm month−1 (Hatzianastassiou et al., 2016).

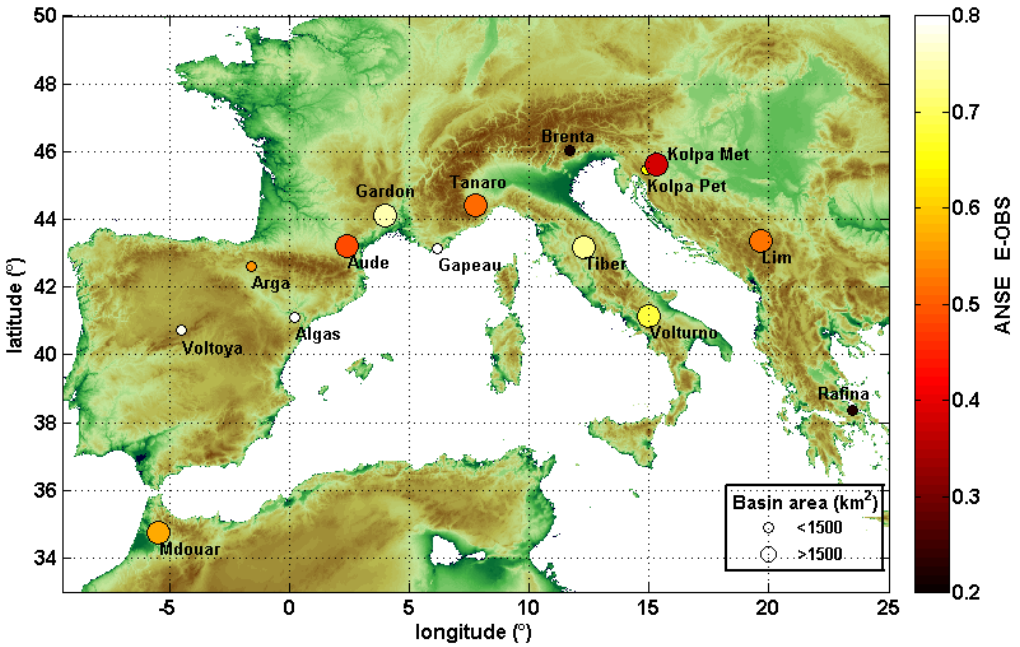

Figure 6.9 - Study basins and relative ANSE index obtained by considering E-OBS rainfall dataset in the calibration period. For each catchment, the related dots vary in dimension depending on the area.

Table 6.4 summarizes the main characteristics of the study catchments, with area ranging from 100 km2 for Rafina basin in Greece to about 5000 km2 for the Tiber river in Italy, mean basin elevation from 86.5 m.a.s.l. (lowland basin) to 1362 m.a.s.l. (mountainous basin) and topographic complexity index (i.e., the normalized standard deviation of elevation within a DEM grid cell derived from the GTOPO30 global digital elevation model, Wagner et al., 2013) varying from 4.8 (Algas at Batea, small topographic complexity) to 32.3 (Brenta at Berzizza, high topographic complexity).

#	Study basins	Country	Area (km^2)	Topographic complexity index	Mean basin elevation (m.a.s.l.)	Available observed discharge data
1	Rafina @ Fladar	Greece	109	11.80	86.5	2009-2014
2	Voltoya @ Mediana	Spain	140	7.60	1116.0	2004-2011
3	Algas @ Batea	Spain	335	4.80	255.0	2002-2011
4	Gapeau @ Hyeres	Fance	451	9.80	163.0	2000-2008
5	Kolpa @ Petrina	Slovenia	460	13.40	629.0	2000-2012
6	Arga @ Arazuri	Spain	741	7.80	558.7	2001-2014
7	Brenta @ Berzizza	Italy	1506	32.30	1362.0	2010-2013
8	Gardon @ Russan	France	1530	9.70	514.4	2009-2013
9	Aude @ Carcassonne	France	1770	9.20	105.0	2000-2012
10	Mdouar @ Elmakhazine	Morocco	1800	8.90	304.3	2000-2011
11	Kolpa @ Metlika	Slovenia	2002	10.00	197.0	2007-2012
12	Volturno @ Solopaca	Italy	2580	14.80	610.8	2010-2013
13	Lim @ Prijepolje	Serbia	3160	17.00	612.0	2007-2010
14	Tanaro @ Asti	Italy	3230	18.90	927.4	2010-2013
15	Tiber @ Monte Molino	Italy	4820	10.80	434.7	2000-2015

Table 6.4 - Main characteristics of the study basins.

Note that, the topographic complexity of the Mediterranean region ranges from zeros to 40 and a threshold value of 10 can be assumed to exactly discern between alpine mountainous or lowland areas. Therefore, the selected catchments together form a representative sample of the different climatic and physiographic conditions of the Mediterranean.

Datasets

The datasets used in this study include both ground-based and satellite observation products.

Ground-based observations

Ground-based observations include rainfall, temperature and discharge data. As ground-based reference product for precipitation and mean temperature, we used the European high-resolution

gridded data sets, E-OBS (Haylock et al., 2008), developed as part of the EU-FP6 ENSEMBLES project. The rainfall and temperature provided by E-OBS are available at daily time step for the period 1950 up to now. Given the relatively high density of the raingauges and thermometers used by this product, it can be considered a reasonable reference for comparing the performance of each SRP within the hydrological simulations.

Discharge data, interpolated at hourly time step, are available for all the study catchments as described in ***Table 6.4***. Only 4 out of 15 catchments have a limited observation period (4 years), whereas for about half of the basins the length of discharge observations is greater than 8 years.

Satellite rainfall observation products

Four different rainfall datasets derived from satellite sensors are used (***Table 6.7***). Among the classical "top-down" satellite precipitation products, which sense the cloud properties to retrieve precipitation, we used TMPA 3B42RT, CMORPH, PERSIANN satellite products.

#	Satellite-only datasets	Spatial/ temporal resolution	Time period
1	TMPA RT (3B42RT V7)	0.25° / 3-hour	Mar 2000 – Dec 2015
2	CMORPH	0.25° /3-hour	Jan 1998 – Jan 2015
3	PERSIANN	0.25° / 3-hour	Mar 2000 – Dec 2015
4	$SM2RAIN_{CCI}$ (EU dataset)	0.25° / 24-hour	Jan 2007 – Dec 2015
#	**Large scale gauge based dataset**	**Spatial/ temporal resolution**	**Time period**
1	E-OBS	0.22° / 24-hour	1950– 2015

Table 6.7 - Main characteristics of the satellite datasets used in this study.

TMPA 3B42RT, provided by the National Aeronautics and Space Administration (NASA, http://disc.sci.gsfc.nasa.gov/), is available from 1997 onward with 3 h temporal resolution and a spatial sampling of 0.25° for the ±50° north-south latitude band. The retrieval algorithm takes advantages of multiple microwave sensors, i.e. the TRMM Microwave Imager (TMI), the Precipitation Radar (PR), the Special Sensor Microwave Imager (SSM/I), the Advanced Microwave Scanning Radiometer - Earth Observing System (AMSR-E) and the Advanced Microwave Sounding Unit B (AMSU-B). The TMPA 3B42RT estimates are obtained through a three-step process: (1) the passive microwave (PMW) estimates are calibrated with sensor-specific versions of the Goddard Profiling Algorithm (GPROF; Kummerow et al., 1996) and combined, (2) Infrared rainfall (IR) estimates are created using the PMW estimates for calibration, and (3) PMW and IR estimates are then combined.

CMORPH is available at different spatial and temporal resolutions. Here we used the raw version provided by the CPC (ftp://ftp.cpc.ncep.noaa.gov) with a spatial sampling of 0.25° every 3 hours. The product is available from March 2000 onward on the +60°/-60° latitude and is obtained by using the same microwave sensors used for TMPA 3B42RT. However, unlike TMPA 3B42RT here the infrared data are used to propagate the rainfall estimates within the times between two successive microwave satellite overpasses.

PERSIANN is provided by the Center for Hydrometeorology and Remote Sensing (CHRS, http://chrsdata.eng.uci.edu/) at the University of California, Irvine (UCI) with a spatial sampling of

0.25° and a 3-hourly temporal resolution. PERSIANN product uses the artificial neural network technique to estimate rainfall rate from geostationary infrared data with. Rainfall is estimated by training the infrared data to the collocated microwave estimates, when available (Hsu et al., 1997; Sorooshian et al. 2000).

In addition to these classical SRPs, we used the SM2RAIN$_{CCI}$ rainfall product (Ciabatta et al., 2018) obtained by applying the SM2RAIN algorithm (Brocca et al., 2014) to the ESA CCI satellite soil moisture products. In particular, within the ESA CCI initiative (http://www.esa-soilmoisture-cci.org/) three different SM datasets are provided: 1) the Active (obtained by merging only active sensors observations), 2) the Passive (obtained by merging only passive sensors observations), and, 3) Combined (obtained by merging the Active and Passive datasets) (Liu et al, 2011). The datasets are available from 1978 until 2015 at 0.25° of spatial resolution on a daily basis. Detailed information regarding the ESA CCI SM products can be found in Liu et al. (2011, 2012), Wagner et al., (2012) and in Dorigo et al., (2017). To obtain the SM2RAIN$_{CCI}$ rainfall product only the active and the passive ESA CCI satellite soil moisture products are combined by a scheme developed by Kim et al. (2015). The product is characterized by the same temporal and spatial sampling of the ESA CCI products (i.e., 0.25°degrees and on a daily basis). Major details about the SM2RAIN$_{CCI}$ rainfall performances can be found in Ciabatta et al. (2018).

For sake of simplicity, hereinafter the TMPA 3B42RT, CMORPH, PERSIANN and SM2RAIN$_{CCI}$ satellite-based datasets are referred to as TMPA, CMOR, PERS and SM2R$_{CCI}$, respectively.

Workflow

The algorithms and the models applied for the purpose of hydrological validation of SRPs are described in details in this section. In particular, as several studies have shown that local adjustments of SRPs, as well as specific rainfall-runoff model calibration, are necessary steps to produce reliable hydrological simulation (Harris et al., 2007; Immerzeel and Droogers, 2008; McCabe et al., 2008; Pan et al., 2008), a bias correction approach is applied to SRPs prior to use them to force the hydrological model. Details about the bias correction approach are given in the following.

Bias correction of satellite rainfall time series

The quantile mapping (QM) approach is applied to bias correct the cumulative density function (CDF) of TMPA, CMOR, PERS, and SM2R$_{CCI}$ (Ciabatta et al., 2018) according to E-OBS. The choice of using QM approach is based on the results of Thiemig et al. (2013) who demonstrated that a more sophisticated QM bias-correction method is able to provide better hydrological performance than simpler bias-correction methods. Largely applied in hydrologic and climate impact studies, this method match, besides the mean and variance, all the statistical moments of SRPs (as the skewness and the tails of the CDF) to the observed data (Camici et al., 2014).

For the SRPs for the calibration/validation period (cal/val), the method can be written as:

$$\mathrm{SRP}_{QM,k}^{cal/val} = F_{OBS_k^{cal}}^{-1}\left(F_{SRP_k^{ca/val}}\left(\mathrm{SRP}_k^{cal/val}\right)\right) \tag{6.10}$$

where $F^{-1}_{OBS^{cal}_{k}}$ is the inverse CDF (or quantile function) of the observations for the day k, $F_{SRP^{cal}_{k}}$ is the CDF of the raw SRPs, both in the calibration period. As concerns the quantile function $F^{-1}_{OBS^{cal}_{k}}$ different parametric or non-parametric transformations can be adopted (Gudmundsson et al., 2012). In this study a two-order polynomial function is applied in which the parameters – estimated in the calibration period – are then adopted also to bias correct the SRPs in the validation period. Given the high presence of zero values in the precipitation signal the application of the QM method can lead to negative rainfall values (Wang and Chen, 2014). To overcome this issue, QM is applied at daily time step, i.e., by considering accumulated raw SRPs and E-OBS rainfall values at daily time step. The daily bias-corrected values are then re-distributed to the eight 3-hourly temporal intervals according to their original temporal pattern. Although this expedient allows to limit significantly the problem of zeros rainfall values, it does not guarantee missing residual negative values in the bias-corrected SRPs. Thus, these values were simply assumed equal to zero which results in a non-perfect bias correction.

Integration of SRPs

The integration of the single rainfall datasets is implemented by using the following scheme:

$$SRP_1(t)+SRP_2(t) = SRP_1(t)+K*[\ SRP_2(t)-SRP_1(t)] \quad (6.11)$$

where $SRP_1(t)+SRP_2(t)$ is the integrated rainfall product, SRP_1 and SRP_2 are two single satellite-based rainfall products selected among the bias corrected TMPA, PERS, CMOR and $SM2R_{CCI}$ rainfall. K is the gain parameter ranging between 0.05 to 0.95 in order to assure that an integrated product is always obtained from ***Eq. 6.11***. In particular, when K= 0.05 almost only the SRP_1 is used, for K= 0.95 almost only SRP_2. K is calibrated by maximizing ANSE index between observed and simulated discharge in the calibration period. The same K value is then applied in the validation period to integrate the SRPs mentioned above.

Continuous hydrological model (MISDc)

MISDc (Brocca et al. 2011) is a one-layer semi-distributed model that entails two main components: 1) a soil water balance model to simulate the soil moisture temporal pattern and 2) a semi-distributed event-based rainfall-runoff model for flood simulation. MISDc couples a routing module with a single layer soil water balance model. The soil water balance module computes the evapotranspiration, the percolation, the infiltration and the rainfall excess (through the Soil Conservation Service – Curve Number, SCS-CN, method) rates. The discharge is estimated by routing the surface runoff, the saturation excess and the subsurface runoff to the outlet section. The model uses 8 parameters, i.e., the maximum soil water capacity, the pore size distribution index, the saturated hydraulic conductivity, the fraction of percolated water that generates baseflow, the lag-area relationship coefficient, a correction parameter for the evapotranspiration, the initial abstraction coefficient of the SCS-CN method and the coefficient of the relationship relating SM to the initial condition of the SCS-CN method. The model is written in MATLAB® language and is freely available at: http://hydrology.irpi.cnr.it/download-area/midsc-code/.

MISDc model is successfully applied for flood simulation in many basins in Italy (Brocca et al., 2011; 2013a, Massari et al., 2015, Masseroni et al., 2017) and Europe (Brocca et al., 2013b) and used within climate change impact studies (Camici et al., 2014).

Experimental design

Prior to consider the hydrological evaluation of SRPs it is useful to assess the quality of SRPs themselves. For that, at first an intercomparison of rainfall datasets is carried out by using the daily E-OBS data as reference. Then, we perform discharge simulation by running the MISDc model for each of the considered forcing datasets (previous *Datasets* section). As the shorter observation period has a sufficient duration (4 years, see ***Table 6.7***), for each catchment discharge data are split exactly in two parts: the first half period is used for calibration and the second one for validation.

First MISDc is calibrated and validated for each catchment by using as input the mean areal E-OBS rainfall and temperature data. As all the analyzed catchments have a sub-daily concentration time, to guarantee meaningful hydrological simulations all runs are carried out at three-hourly time step, i.e. the maximum temporal resolution of the SRPs. For that, for each day the total E-OBS rainfall amount is split over eight 3-hourly temporal intervals with constant rainfall rate.

After that, the single bias corrected SRPs and the integrated ones (see *Integration of SRPs* section) are used to drive MISDc model. In these runs the model parameter values are recalibrated separately for each SRPs. Having the $SM2R_{CCI}$ rainfall product a daily temporal resolution, it is here used only within the integration procedure and not used to simulate discharge time series.

Six integrated products are considered in this study that can be divided in two main groups. The first group includes integration between only classical "top-down" SRPs, i.e. TMPA+CMOR; TMPA+PERS; CMOR+PERS; the second group considers integration between "top-down" and "bottom-up" SRPs, i.e., TMPA+$SM2R_{CCI}$, CMOR+$SM2R_{CCI}$, PERS+$SM2R_{CCI}$. In particular, to allow the integration between the 3-hourly "top-down" products and the daily $SM2R_{CCI}$ product, for each day the total $SM2R_{CCI}$ rainfall amount is re-distributed over eight 3-hourly temporal intervals according to the temporal pattern of the partner product.

Performance metrics

The assessment of the different SPRs was made by calculating the Pearson correlation coefficient, R, the bias and the root mean square error, RMSE, between the daily E-OBS and the single/integrated satellite rainfall data averaged over the area of each basin.

The suitability of the gauged-based versus single/integrated satellite-based rainfall products for flood modelling is evaluated by computing the modified Nash-Sutcliffe efficiency (NSE) adapted for high flow conditions, ANSE (Hoffmann et al., 2004), between the observed and simulated discharge both in the calibration and validation periods. Simulations providing ANSE values greater than 0.5 were reasonably assumed good in terms of reproducing observed (high-flow) discharge time series. Additionally, the Kling-Gupta efficiency (KGE, Gupta et al., 2009; Kling et al., 2012), which was found to be more robust than NSE, was considered here for assessing model performance for medium-flow conditions.

Results

This section describes the results about the assessment of the different SPRs. Then the suitability of SRPs for hydrological modeling is investigated. At first, MISDc is driven by E-OBS, to simulate benchmark discharge time series that are compared with the ones obtained by the different SRPs and the integrated products.

Rainfall assessment

Results about rainfall scores for the calibration/validation periods are illustrated in ***Figure 6.10***. Boxplot with thin/thick lines refer to calibration/validation periods, respectively. It can be noted that the performances of the single and integrated products are very similar each other both in calibration and validation period. All the considered products show daily correlation values on average equal to 0.6 both in calibration and validation periods and, among the integrated products, the TMPA+SM2R$_{CCI}$ and CMOR+SM2R$_{CCI}$ show a slightly better agreement with observed data (mean R=0.62).

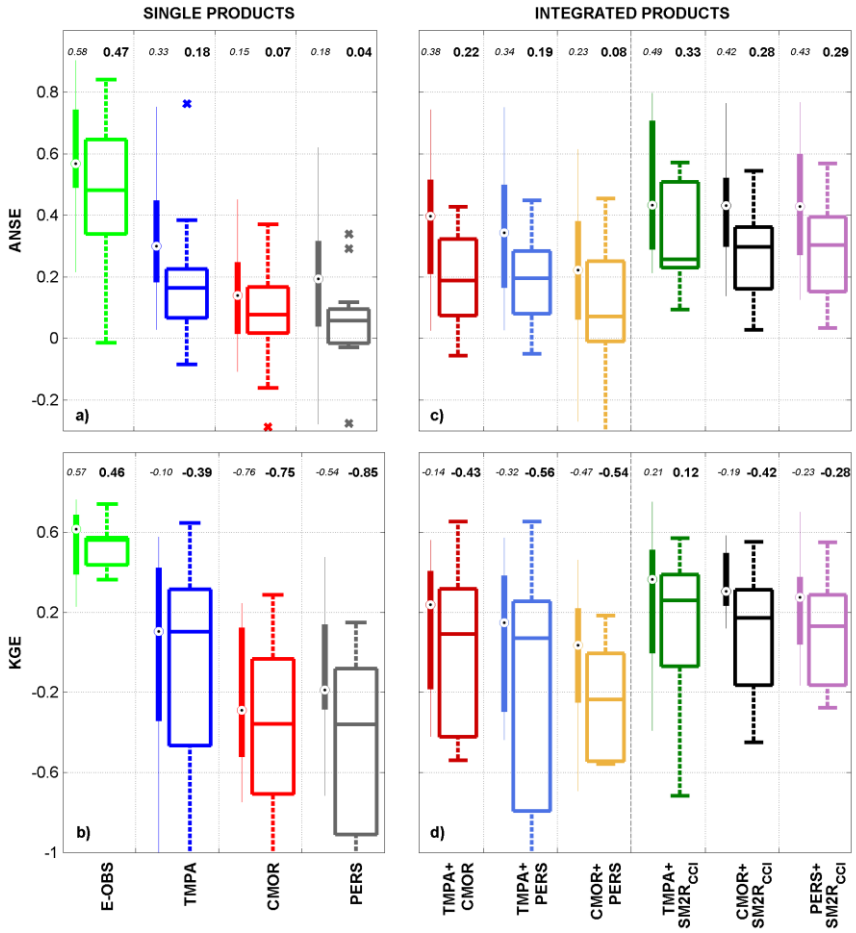

Figure 6.10. Performances in terms of ANSE (Nash–Sutcliffe efficiency for high-flow conditions) and KGE (Kling-Gupta efficiency, for medium flow conditions) of the different parent (a, b) and integrated (c, d) rainfall products in reproducing the observed discharge for all the study catchments in the calibration (thin boxplot) /validation period (thick boxplot). Cross symbols represent outlier values, the bold numbers indicate the mean values for each rainfall product.

Relatively larger differences are obtained in terms of RMSE and bias for the single products with SM2R$_{CCI}$ having the highest RMSE and bias. Nevertheless, in terms of RMSE the first group of integrated products (i.e., TMPA+CMOR, TMPA+PERS, CMOR+PERS) perform worse than the second group (i.e., the one containing SM2R$_{CCI}$) with general lower values for both groups of the integrated products with respect to the parent products. Conversely, the first group of integrated products outperforms the second one with respect to the bias likely due to the high bias of SM2R$_{CCI}$. Note that, as mentioned in the *Bias correction of satellite rainfall time series* section the bias correction procedure adopted during the calibration period is affected by the necessity to set

negative rainfall values equal to zero thus the bias differences shown in ***Figure 6.10*** should not surprise. R, RMSE and BIAS of the products do not show remarkable changes as a function of the basin area while some changes can be observed in terms of topographic complexity and mean basin elevation. As expected, basins over flat areas perform better than mountainous basins.

Discharge simulation with E-OBS rainfall data

We test the reliability of MISDc by using E-OBS ground-based rainfall. ***Figure 6.9*** illustrates the related performances in terms of ANSE obtained for all the study catchments over the calibration period while ***Table 6.8*** reports the ANSE values both for calibration/validation periods. Overall MISDc model provides relatively good performances with ANSE values greater than 0.5. Exceptions are represented by the Rafina basin, probably due to the low E-OBS raingauge density in the investigated period, and by Kolpa Metlika and Brenta mountainous catchments for which the snowmelt process, not simulated by MISDc, may play an important role in the flood formation. Based on that, we can reasonably state that the geomorphological characteristics of the basins have a negligible effect on the model performance while raingauge density and model structure errors might play an important role.

#	Study basins	CALIBRATION PERIOD				VALIDATION PERIOD			
		E-OBS	TMPA	CMOR	PERS	E-OBS	TMPA	CMOR	PERS
1	Rafina	0.22	0.18	0.14	0.07	-0.01	***0.76***	*0.19*	*0.06*
2	Voltoya	0.79	0.64	0.30	0.38	0.75	0.25	**0.37**	0.12
3	Algas	0.80	0.39	0.20	0.20	0.12	-0.05	0.08	0.05
4	Gapeau	**0.90**	0.35	0.21	0.22	**0.84**	0.16	0.08	0.07
5	Kolpa	0.65	0.16	0.01	-0.01	0.52	0.01	0.04	0.00
6	Arga	0.55	0.07	0.01	0.04	0.58	0.10	0.01	-0.03
7	Brenta	0.22	0.20	-0.11	-0.28	0.40	0.18	-0.29	-0.34
8	Gardon	0.75	0.46	0.04	0.04	0.72	-0.09	0.07	0.06
9	Aude	0.48	0.21	0.26	0.07	0.67	0.22	0.07	-0.02
10	Mdouar	0.57	0.42	0.22	0.47	0.55	0.23	0.21	0.29
11	Kolpa	0.38	0.03	0.00	-0.01	0.32	0.07	-0.03	0.08
12	Volturno	0.68	0.28	0.39	0.33	0.44	0.16	0.11	0.10
13	Lim	0.53	0.30	0.05	0.19	0.29	0.07	-0.16	-0.28
14	Tanaro	0.51	***0.75***	**0.45**	***0.62***	0.48	0.17	0.08	0.03
15	Tiber	0.73	0.54	0.14	0.28	0.39	0.38	0.20	**0.34**
Average		0.58	0.33	0.15	0.18	0.47	0.18	0.07	0.04

Table 6.8 - ANSE index obtained by forcing MISDc hydrological model with E-OBS and satellite (TMPA, CMOR, PERS) rainfall data during the calibration and the validation periods. In bold font the best performances score for each basin are reported while the scores are in italic font if better than those obtained with ground observed data (E-OBS).

The results above are confirmed also in the validation period as summarized in ***Table 6.8***. Indeed, ANSE index shows only slight reductions for all the study catchments except for Rafina, Algas and Tiber basins where the performances significantly worsen. This is likely due to the sensitivity of ANSE index in reproducing high flood events that could differ in magnitude between calibration and validation period. In general, the mean ANSE value in the validation period decreases on average of about 18% over the study area. These outcomes demonstrating the suitability of E-OBS rainfall dataset for discharge simulation, hence it will be hereinafter assumed as a baseline to compare the simulations that use SRPs.

Discharge simulation with single SRPs

The performances in terms of ANSE and KGE of the different rainfall products in reproducing the observed discharge data over the entire study area are illustrated in ***Figure 6.11a, b***, both in the calibration and validation periods (ANSE values of each basin are detailed in ***Table 6.8***).

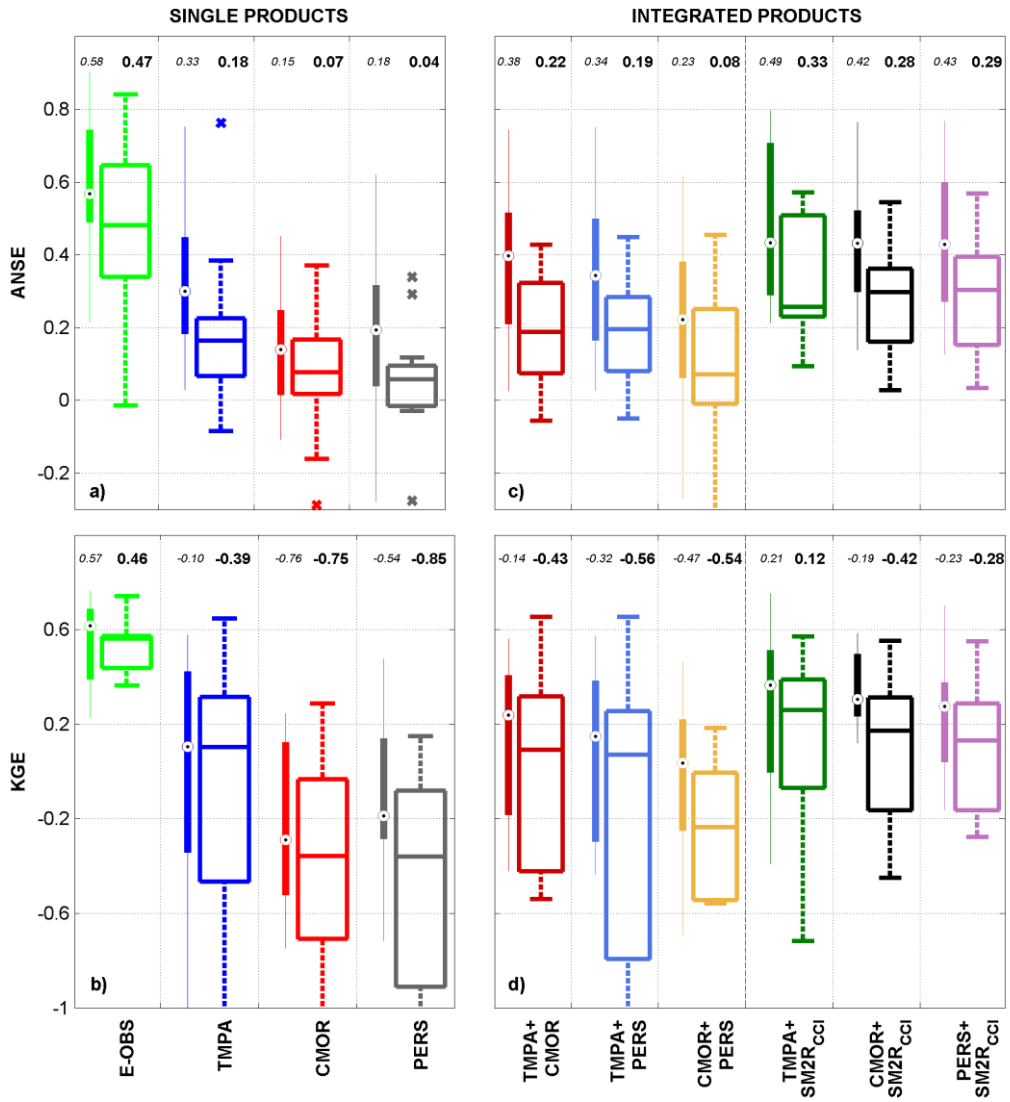

Figure 6.11 Performances in terms of ANSE (Nash–Sutcliffe efficiency for high-flow conditions) and KGE (Kling-Gupta efficiency, for medium flow conditions) of the different parent (a, b) and integrated (c, d) rainfall products in reproducing the observed discharge for all the study catchments in the calibration (thin boxplot) /validation period (thick boxplot). Cross symbols represent outlier values, the bold numbers indicate the mean values for each rainfall product.

From ***Table 6.8*** it can be noted that with respect to E-OBS, satellite rainfall data perform worst both in calibration and validation periods. Mean ANSE value are equal to 0.33, 0.15, 0.18, for TMPA, CMOR, PERS, respectively, in the calibration period and to 0.18, 0.07, 0.04, respectively, in the validation period. Among all the products, TMPA works better both in calibration and validation periods even though, as already highlighted, for some basins unreliable simulation characterized by ANSE values lower than zero are obtained. Similar considerations can be drawn from the analysis of KGE-values (***Figure 6.11b***). Here, E-OBS performs satisfactorily both in calibration (mean KGE=0.57) and validation (0.46) whereas SRPs significantly worse.

This is mainly due to the difficult in using SRPs for smaller basins (e.g., KGE-values equal to -1.14, -0.38, -2.62, -0.44 are obtained through TMPA in calibration for Rafina, Voltoya, Algas and Gapeau, respectively) whereas the performances increase for larger basins (e.g. TMPA provides KGE equal to 0.58 in calibration for Tiber basin). The relatively low performance in terms of KGE can be partly explained by the choice of the cost function (i.e., ANSE) within the calibration step, which favors a better reproduction of high flows but does not guarantee the same optimality in terms of medium flow and bias.

In general, these outcomes prove that for using SRPs in hydrological modelling, bias correction and model recalibration are not always sufficient to achieve satisfactory performances mainly in smaller basins which represent the main target for flood modelling in the Mediterranean area.

Discharge simulation with integrated SRPs

The parent SRPs are integrated according to group 1 (TMPA+CMOR; TMPA+PERS; CMOR+PERS) and group 2 (TMPA+SM2R$_{CCI}$, CMOR+SM2R$_{CCI}$, PERS+SM2R$_{CCI}$) and results are summarized for the entire study area in ***Figure 6.11c*** and ***Table 6.9*** in terms of ANSE values and in ***Figure 6.11d*** in terms of KGE index. Although on average E-OBS dataset remain the best performing rainfall products, the added-value of the integrated products against single SRPs is noticeable. For the group 1, the performances of integrated products are closely linked to the ones of the parent rainfall datasets. Lower performances are found for CMOR+PERS whereas the integrated products that consider TMPA show greater ANSE indexes. In particular, the best results are obtained by considering the integration between TMPA and CMOR with mean ANSE values equal to 0.38 and 0.22 in calibration and validation, respectively. The performances significantly increase by considering the group 2, i.e., the integration with SM2R$_{CCI}$. Indeed, ANSE values are greater than zeros for all the study catchments and, above all for TMPA+SM2R$_{CCI}$, they become closer to the ones obtained with the E-OBS rainfall data with mean ANSE values of 0.49 and 0.33 in calibration and validation periods, respectively. The performances drop when medium-flow conditions are analyzed for all the integrated products except for the TMPA+SM2R$_{CCI}$ product. This outcome is quite expected being the hydrological model calibrated to reproduce high flood events.

A more in-depth analysis is carried out in order to investigate the advantages of using integrated SRPs, also in relation with the topographic basin characteristics. The scatterplots on the first column of ***Figure 6.12*** show the added value of satellite rainfall integration with respect to the use of single rainfall products. For all the study catchments, small benefits are gained from the integration of CMOR with TMPA (***Figure 6.12a***). Due to the lower CMOR performances, the ANSE values obtained by considering TMPA alone are very similar to the ones obtained by considering the integrated product and ANSE values are aligned along the bisector line both for the calibration and validation period.

#	Study basins	CALIBRATION PERIOD						VALIDATION PERIOD					
		TMPA+ CMOR	TMPA+ PERS	CMOR+ PERS	TMPA+ SM2R$_{CCI}$	CMOR+ SM2R$_{CCI}$	PERS+ SM2R$_{CCI}$	TMPA+ CMOR	TMPA+ PERS	CMOR+ PERS	TMPA+ SM2R$_{CCI}$	CMOR+ SM2R$_{CCI}$	PERS+ SM2R$_{CCI}$
1	Rafina	*0.46*	0.12	0.14	*0.27*	*0.26*	*0.25*	**0.79**	0.32	**0.45**	0.40	0.09	0.09
2	Voltoya	0.67	0.67	0.58	0.70	**0.76**	**0.77**	0.33	0.28	0.16	0.45	0.47	0.41
3	Algas	0.40	0.38	0.20	***0.80***	0.62	0.58	-0.06	-0.05	0.05	0.12	0.10	0.18
4	Gapeau	0.35	0.35	0.22	0.40	0.43	0.43	0.16	0.16	0.07	0.09	0.03	0.03
5	Kolpa	0.15	0.16	0.01	0.24	0.14	0.13	0.02	0.03	0.03	0.16	0.30	0.29
6	Arga	0.07	0.13	0.04	0.22	0.16	0.15	0.10	0.16	-0.03	0.25	0.34	0.32
7	Brenta	0.18	0.19	-0.27	*0.43*	*0.38*	*0.35*	0.19	0.19	-0.38	0.26	0.14	0.16
8	Gardon	0.58	0.51	0.36	0.63	0.62	0.61	0.25	0.28	0.33	**0.57**	0.30	0.30
9	Aude	0.43	0.21	0.29	0.21	0.38	0.13	0.38	0.22	0.07	0.22	0.21	0.15
10	Mdouar	0.41	0.48	0.46	0.42	0.29	0.48	0.23	0.26	0.28	0.26	0.34	0.31
11	Kolpa	0.03	0.03	0.00	0.34	0.33	*0.41*	0.06	0.07	-0.02	0.31	0.28	0.35
12	Volturno	0.38	0.33	0.39	0.49	0.53	0.48	0.11	0.11	0.11	0.57	0.37	**0.57**
13	Lim	0.29	0.34	0.19	*0.72*	0.48	*0.63*	0.06	-0.01	-0.27	0.53	**0.54**	0.54
14	Tanaro	***0.74***	***0.75***	***0.61***	*0.75*	0.48	*0.62*	0.31	0.38	0.05	0.25	0.26	0.08
15	Tiber	0.53	0.54	0.28	0.71	0.43	0.40	0.43	**0.45**	0.34	0.54	0.46	0.54
Average		0.38	0.34	0.23	0.49	0.42	0.43	0.22	0.19	0.08	0.33	0.28	0.29

Table 6.9 - ANSE index obtained by forcing MISDc hydrological model with integrated satellite rainfall data during the calibration and the validation periods. In bold font the best performances score for each basin are reported while the scores are in italic font if better than those obtained with ground observed data (E-OBS).

Conversely, the added-value of SM2R$_{CCI}$ is noticeable for almost all the basins: ANSE values are spread above the bisector line both for TMPA+SM2R$_{CCI}$ (***Figure 6.12c***) and CMOR+SM2R$_{CCI}$ (***Figure 6.12e***). These outcomes are very important as they demonstrate the potential of the integration between top-down and bottom-up satellite precipitation products. In particular, it can be noted that TMPA works better than TMPA+SM2R$_{CCI}$ only for the smaller basins in the study area, Rafina and Gapeau characterized by similar topographic complexity and mean basin elevation (Table 1) whereas the added-value of the TMPA+SM2R$_{CCI}$ product is particular evident for Algas, Brenta, Kolpa at Metlika, Voltuno and Lim basins. By analysing these results in terms of the basins characteristics (as listed in ***Table 6.6***) we did not observe any influence of either the basin area, nor the topographic complexity or the mean elevation of the basin. For instance, the small and mountainous Voltoya basin (#2 in ***Table 6.6***) or the large lowland Tiber river basin (#15 in ***Table 6.6***) are opposite cases where it is proved that integrated satellite rainfall data can be useful tools for flood modelling. Similar conclusions can be drawn by inspecting the scatterplot of ***Figure 6.12e***: for 9 out of 15 basins, ANSE values obtained by considering the integrated product are doubled

with respect to the ones obtained by considering CMOR alone, while no connections between basin characteristics and performances can be found.

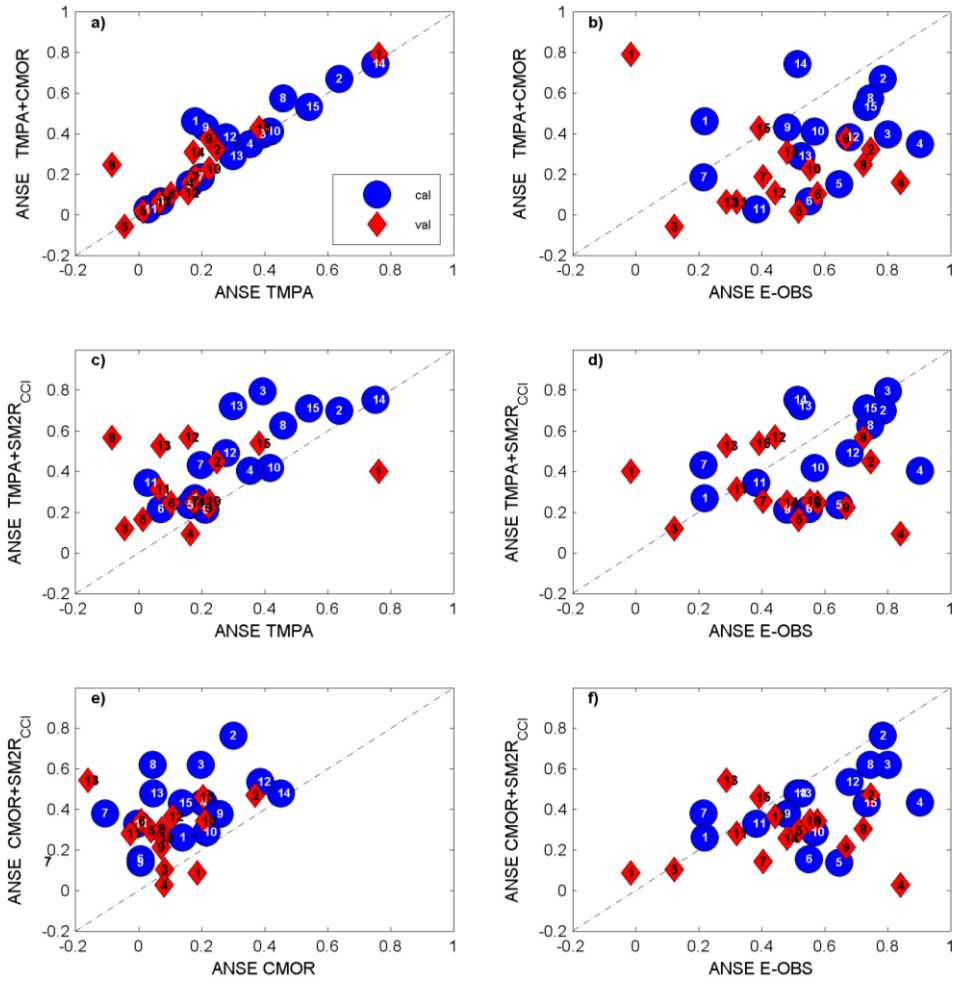

Figure 6.12 - Comparison in terms of ANSE index: performances of integrated versus parent satellite rainfall products/E-OBS data (first column/ second column) in reproducing observed discharge data. Blue dots and the red diamonds refer to calibration/validation periods, numbers indicate the basins as listed in Table 6.9.

These findings highlight that the basin characteristics exert a small influence on the hydrological performance and that the connection between the rainfall quality and the performance in hydrological modelling is not straightforward due the potential interactions between the model and the specific SRP (as also demonstrated by Qi et al., 2015). For instance, products characterized by a low bias such as those of group 1 (i.e., those obtained by integrating between the classical SRPs, see ***Figure 6.12***), provide worse simulation results with respect to the ones of group 2 (those integrated products using SM2R$_{CCI}$). This raises the interesting issue whether bias and correlations (and RMSE) are useful scores to indicate potentially good or worse hydrological performance and whether the basin characteristics can condition the choice of the specific rainfall source to use. This topic, that is beyond the scope of the paper, will be further investigated in the future. An additional analysis is carried out to display the relative performance of the integrated SRPs with respect to E-OBS in flood simulation (***Figure 6.12b, d, f***). Especially through TMPA+SM2R$_{CCI}$ product (***Figure 6.12d***), in calibration (validation period), for 7 (6) out 15 of the investigated basins ANSE indexes

are equal or even higher than the ones obtained through E-OBS rainfall data. This suggests that integrated SRPs can be potentially used in place of ground observed rainfall data for flood modelling over poorly gauged areas (e.g., Rafina) and for lowland large basins (i.e., Volturno, Lim and Tiber basins) in the Mediterranean area. To clearly support this statement, ***Figure 6.13*** shows observed and simulated discharge time series obtained by forcing MISDc model through TMPA, TMPA+SM2R$_{CCI}$, and E-OBS rainfall data for four basins representative of the topographic characteristics of the study area: Algas at Batea, Brenta at Berzizza, Kolpa at Metlika and Tiber at Monte Molino river basins.

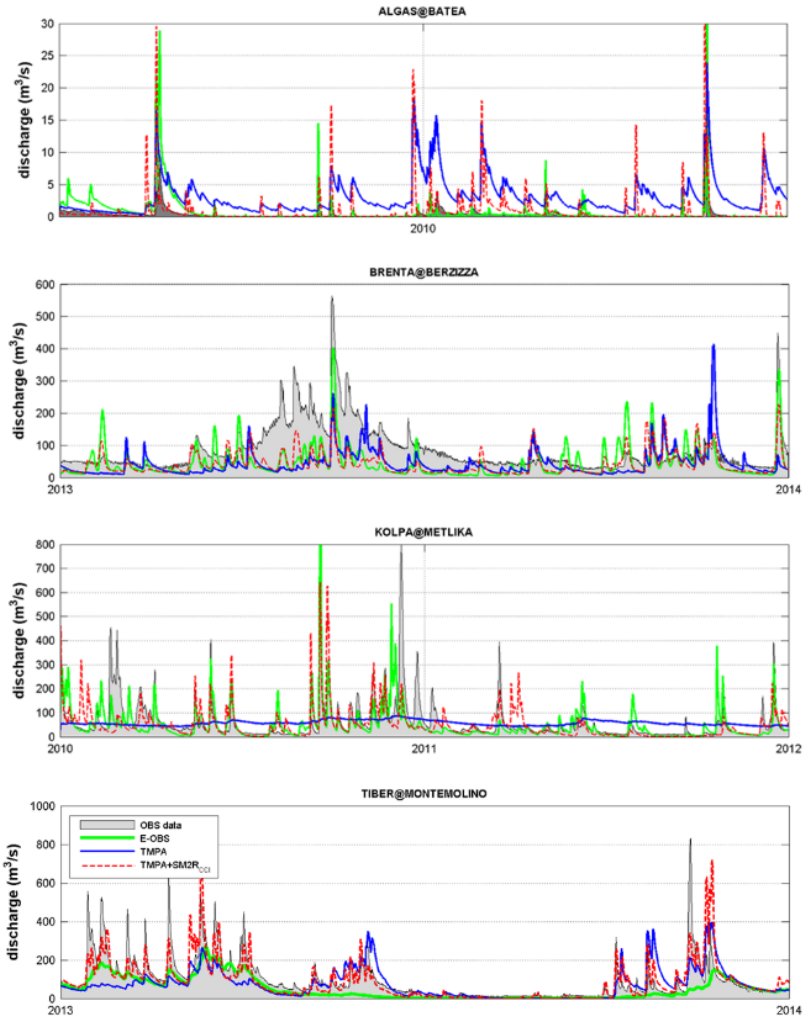

Figure 6.13 - Discharge time series for some study catchments obtained by forcing MISDc model through E-OBS, TMPA and TMPA+SM2RCCI rainfall products. For sake of visualization, for each basin only short time windows on the validation period are shown.

For sake of visualization, for each basin only short time windows on the validation period are displayed. Here, we can see that TMPA product alone does not provide reasonable reproduction of the observed discharges for Algas and Kolpa but when the latter is integrated with SM2R$_{CCI}$ we can obtain even better simulations than those obtained with E-OBS (e.g., see Tiber basin). These results support those showed by Ciabatta et al., (2016) for four basins over Italy, i.e. better hydrological performances were obtained by forcing MISDc model with integrated rainfall products instead of ground data.

6.4 Use of satellite rainfall data with empirical rainfall thresholds

Besides the use of satellite rainfall data within a physically-based methodology, this source of information is used to test the capabilities in landslide risk assessment by means of empirical rainfall threshold. Classical and SM2RAIN-derived satellite rainfall products are used to identify rainfall thresholds for the possible occurrence of landslides in Italy. This section reported the results showed in the publication:

Brunetti, M.T., Melillo, M., Peruccacci, S., Ciabatta, L., Brocca, L. (2018). How far are we from the use of satellite rainfall products in the prediction of landslides? Remote Sensing of Environment, under review.

Study area

Italy is a boot-shaped peninsula that extends for about 300,000 km^2 in the Mediterranean Sea including the major islands of Sicily and Sardinia (***Figure 6.14***). Given its location and latitude, climate varies largely from northern to southern Italy. The coldest period occurs in December and January, the hottest in July and August. In the northern part of Italy, which includes the Po River Valley and the Alps mountain range, the climate is typically cold in winter and warm in summer with abundant rain. Snowfalls are common in autumn and spring over 1500 m on the Alps.

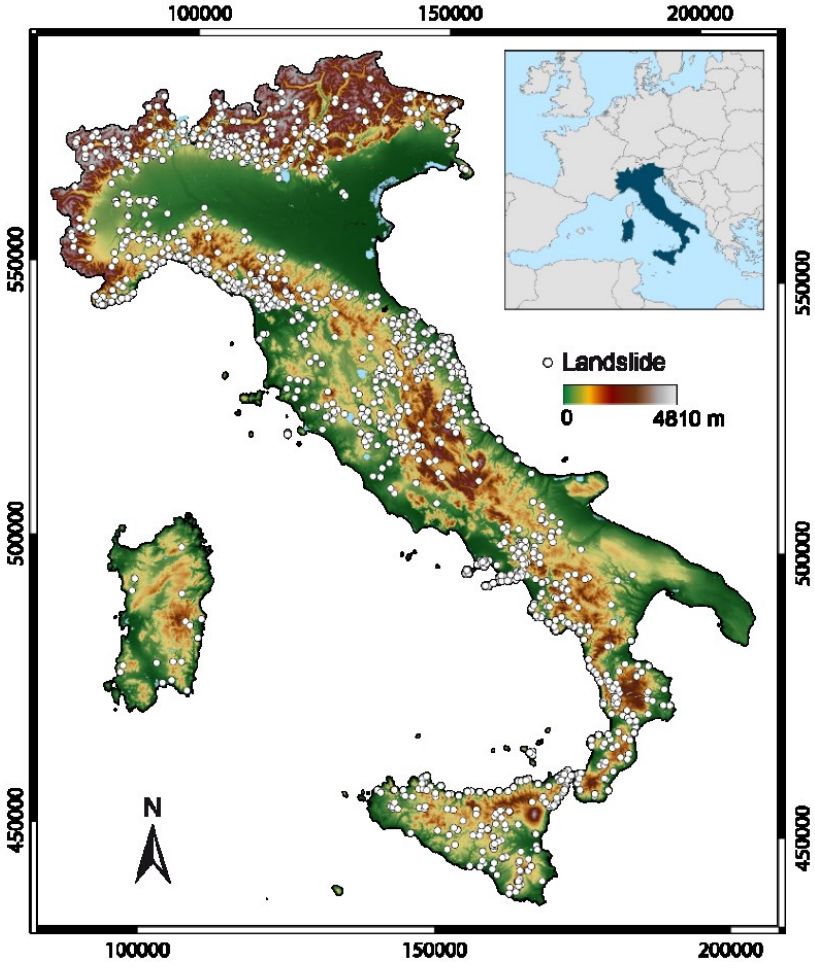

Figure 6.14 - Map of Italy showing the distribution of the rainfall-induced landslides in the period 2008-2014 (white dots).

Along the peninsula and in the islands the climate is temperate, with cold winters and dry summers with mean temperature increasing going southward. Mean annual precipitation ranges from less than 400 mm in Sicily and Sardinia, to more than 2000 mm in the northern Apennines and the eastern Alps. Generally, November is the wettest and July the driest month (Desiato et al., 2015). Except for the Po River Valley and narrow coastal belts, the Italian mainland is generally hilly and mountainous. The topography causes widespread and frequent landslides, actually more than half a million recognized and mapped (Trigila et al., 2015). Most of the failures occur after intense or prolonged rainfall (Guzzetti et al., 1994; Guzzetti and Tonelli, 2004).

Landslide and rainfall data

Landslide information was obtained from a catalogue of rainfall events responsible for failures in Italy collected by Peruccacci et al. (2017). We used a subset of 1414 rainfall-induced landslides in the 7-year period between 2008 and 2014 that matches the time interval of reliable rainfall information available from satellite estimates (Ciabatta et al., 2015).

Landslide information was derived from digital and printed newspapers, blogs, technical documents, and landslide event reports. The documented rainfall-induced landslides were mapped as single points, using Google Earth™ (white dots in ***Figure 6.14***).

Each landslide in the catalogue has a temporal accuracy in three classes. The first class contains failures for which the exact time (hourly) of occurrence is known, while the second and the third classes include landslides for which the part of the day or the day of occurrence was inferred, respectively.

As mentioned above, we used here one rain gauge and four satellite-based rainfall data sets. The rain gauge based product, hereinafter OBS, is obtained from the Italian Civil Protection Department meteorological monitoring network. This data set is obtained by interpolating via an advanced kriging technique the data from about 3000 rain gauges available throughout the Italian territory (Pignone et al., 2010). The data set provides hourly rainfall observations over a grid with spacing of 10 km (Ciabatta et al. 2017). The daily rainfall estimates are obtained by simply summing the 24 hourly data within each day., although this source of information is impacted by spatial representation issues, here, we consider OBS data set as “ground-truth”.

The TMPA 3B42-RT product (Huffman et al., 2007, hereinafter 3B42-RT), version 7 (http://trmm.gsfc.nasa.gov), is obtained by combining rainfall estimates from various satellite sensors. The multisatellite platform uses the TRMM Microwave Imager (TMI), the Special Sensor Microwave Imager (SSM/I) on board the Defense Meteorological Satellite Program (DMSP) satellites, the Advanced Microwave Scanning Radiometer EOS, AMSR-E, and the Advanced Microwave Sounding Unit-B (AMSU-B) on board the National Oceanic and Atmospheric Administration (NOAA) satellite series. In addition, the 3B42-RT product also uses Geostationary (GEO) Infrared data, characterized by higher spatial and temporal resolution than the microwave data, through a constellation of GEO satellites. The 3B42-RT product is provided by the National Aeronautics and Space Administration (NASA) with a temporal resolution of 3 hours and a spatial resolution of 0.25° for the ±50° north–south latitude band with a latency of about 8 hours. The product is interpolated over the 10 km grid by using the nearest neighbor approach.

The SM2RASC product is obtained through the application of the SM2RAIN (Brocca et al., 2013, 2014) algorithm to the ASCAT SM data set. The SM data are obtained from the Metop-A and –B

satellite, and they are characterized by a spatial resolution of 25 km, enhanced to 12.5 after observation resampling, and a daily temporal resolution. The SM2RASC product is specifically developed for Italy during the period 2008-2015 over the 12.5 km grid with daily temporal resolution. More in details, the algorithm is applied to the H109 product provided by the H SAF project (http://hsaf.meteoam.it/) and is calibrated during the period 2013-2014 against ground-based observations. Due to the temporal resolution of SM2RASC, the product shows limitations in the definitions of shorter precipitation events (at sub-daily). The algorithm also is not able to estimate rainfall where the soil is close to saturation, as in such conditions, no variation of the soil water content can be observed during a rainfall event. Finally, the quality of rainfall estimation is strictly related to the quality of SM input data. SM retrievals over complex topography or densely vegetated areas are characterized by low quality and should be used carefully. Nevertheless, the product showed good capabilities in identify rainfall at daily temporal resolution, as shown in Ciabatta et al. (2015; 2017).

PERSIANN (Hsu et al., 1997) data set uses the artificial neural network technique to estimate rainfall rate from geostationary infrared data at each 0.25° pixel at different time steps, for the ± 60° latitude band. In this work, the 3-hour time step was chosen. Rainfall estimation is carried out by training the infrared data to the collocated microwave estimates, when available The product is developed by the Center for Hydrometeorology and Remote Sensing of University of California, Irvine, and it is available since March 2000 (http://chrsdata.eng.uci.edu/) about 2 days after observations.

CMORPH rainfall estimates are obtained by exploiting the same microwave sensors used for 3B42-RT rainfall product, while the infrared data are used to fill the gap at the times between two successive microwave satellite overpasses, through morphing technique. The product is provided by the Climate Prediction Center (CPC) of the National Oceanic and Atmospheric Administration (NOAA) at the spatial resolutions of 0.25° and 8 km on a daily, 3-hourly or 30 minutes basis for the ± 60° latitude band. Here we used the high resolution product (8 km at the equator every 30 minutes) obtained via interpolation of the coarser resolution product. For further details regarding CMORPH rainfall product, the readers are referred to Joyce et al. (2004). The product is provided about 18 hours after observation.

The accuracy of the 3B42-RT, PERSIANN and CMORPH depends mostly on the quality of the passive microwave precipitation retrievals, and particularly on the availability of frequent satellite overpasses over the region of interest (Nijssen and Lettenmaier, 2004). If the overpasses frequency is not sufficiently high, a rainfall event could me underestimated or completely missed.

Algorithm for rainfall event reconstruction

The algorithm proposed by Melillo et al. (2015) was exploited to calculate the rainfall responsible for the observed landslides. For the purpose, the algorithm analyzed the daily rainfall obtained from ground-based stations and satellite sensors, and reconstructed distinct rainfall events (RE) in terms of their duration D (in h) and cumulated rainfall E (in mm), i.e. (D, E) pairs. In particular, to separate two consecutive rainfall events the algorithm requires a minimum dry period (i.e., a period without rainfall or with a negligible amount of rainfall). The length of the dry period varies depending on the local seasonal and climatic conditions. Specifically, dry periods of 48 h (two days) and 96 h (four days) were used to identify rainfall events in the warm and in the cold season,

respectively (Peruccacci et al., 2017). After reconstructing RE, and with the information on the occurrence day of each landslide and on the rainfall of the pixel containing the landslide, the algorithm identified the rainfall events responsible for each failure (RE*). Note, that when the landslide occurs after the end of the event the corresponding RE* is equivalent to RE. Otherwise, the duration of RE* is shorter than that of RE, and the cumulated rainfall is lower (Melillo et al., 2015). For each data set, we discarded RE* having a delay between the rainfall ending time and the landslide occurrence time longer than 48 h. This should prevent the use of wrong information (i.e., incorrectly dated landslides) in the definition of the thresholds.

The reconstructed RE* for OBS, SM2RASC, 3B42-RT, and MERGED data sets were analyzed to define empirical rainfall thresholds for the possible initiation of landslides in Italy. Note that the number of RE* is less than the number of landslides since in some cases the rainfall measured before the failure was null.

Method for calculation and selection of ED rainfall thresholds

To calculate the empirical cumulated event rainfall-rainfall duration (*ED*) thresholds for the four data sets, we adopted the well-established frequentist method proposed by Brunetti et al. (2010), and modified by Peruccacci et al. (2012). The method assumes in a Cartesian plane the threshold curve of the form:

$$E = (\chi \pm \Delta\chi) D^{(\varepsilon \pm \Delta\varepsilon)} \tag{6.12}$$

where E is the cumulated rainfall (in mm), D the rainfall duration (in hours), χ is a scaling constant (the intercept), ε is the shape parameter (that defines the slope of the power law curve), and $\Delta\chi$ and $\Delta\varepsilon$ represent the uncertainties of χ and ε, respectively. The method determines thresholds for any exceedance probability level, e.g., a threshold at 5% probability level leaves 5% of the (D, E) pairs with landslides below the curve.

In order to determine the threshold exceedance probability providing the best performance in landslide forecasting we used the following validation procedure. For each rainfall data set (OBS, SM2RASC, 3B42-RT, CMORPH, and PERSIANN), we constructed synthetic series randomly selecting 85% of rainfall events with landslides (RE*). Then, we used the remaining 15% of RE* to assess the threshold performance. For the purpose, rainfall thresholds were used as binary classifiers of rainfall events that triggered (RE*) or did not trigger landslides. In a *DE* plane, a RE* located above the threshold is a true positive (TP), and below the threshold is a false negative (FN). Analogously, a rainfall event without landslides above the threshold is a false positive (FP), and below is a true negative (TN). We repeated 100 times the random selection of rainfall events, and we got a contingency table with the mean values of TP, FN, FP and TN.

As the threshold exceedance probability rises, the number of FN increases, and the number of TP decreases correspondingly. Conversely, when using thresholds at low exceedance probability, the number of FP increases and the number of TN decreases. When using the thresholds in a landslide warning system, FP results in “false alarms” and FN in “missed alarms”. It is worth noting that FP can be overrated by the lack of information on landslide occurrence i.e., landslides may have occurred but not reported. Consequently, even the number of TN can be overestimated (Gariano et al., 2015).

In addition, we would notice that the validation of the rainfall thresholds for the possible occurrence of slope failures is a complicated issue; at first glance, the occurrence of a rainfall-induced landslide is a stochastic mechanism, i.e. the same rainfall conditions may trigger a landslide in an area and may not in a different place. The prediction of rainfall-induced landslide does not depend exclusively upon correct rainfall forecasts (and measurements), it is instead largely influenced by the local characteristics of the terrain (slope, soil type, soil moisture, etc.), which are mostly unknown for large areas.

From the contingency table, we obtained, the POD (Probability Of Detection) and the POFD (Probability Of False Detection skill scores:

$$POD = \frac{TP}{TP + FN} \tag{6.13}$$

$$POFD = \frac{FP}{FP + TN} \tag{6.14}$$

More specifically, POD (or Hit Rate) is the fraction of RE* above the threshold, i.e. predicted correctly, and POFD (or False Alarm Rate) is the fraction of RE above the threshold, i.e. predicted incorrectly. We used POD and POFD to draw the receiver operating characteristic (ROC) curves (Fawcett, 2006) and to calculate the HK (POD-POFD) skill score (Hanssen and Kuiper, 1965). The quality of the satellite-based rainfall products is evaluated comparing the ROC curves and the HK skill score whose optimal value is 1.

Results

In the following, we assessed the capability of the satellite-based rainfall products to forecast rainfall-induced landslides using the ground-based rainfall product as a reference. Based on the statistical criteria described above, we compared the performances of SM2RASC, 3B42-RT, CMORPH, and PERSIANN data sets. In addition, we evaluated the best performing threshold for each product simulating their use in a landslide warning system. As a preliminary analysis, we investigated the performance of the three satellite rainfall products against ground observations for the whole period of analysis. Specifically, we computed the temporal Pearson correlation between OBS and satellite-based daily rainfall for each pixel (***Figure 6.15***). The correlation maps clearly show that the SM2RASC product (***Figure 6.15a***) has improved performances with respect to the other products when compared with ground observations.

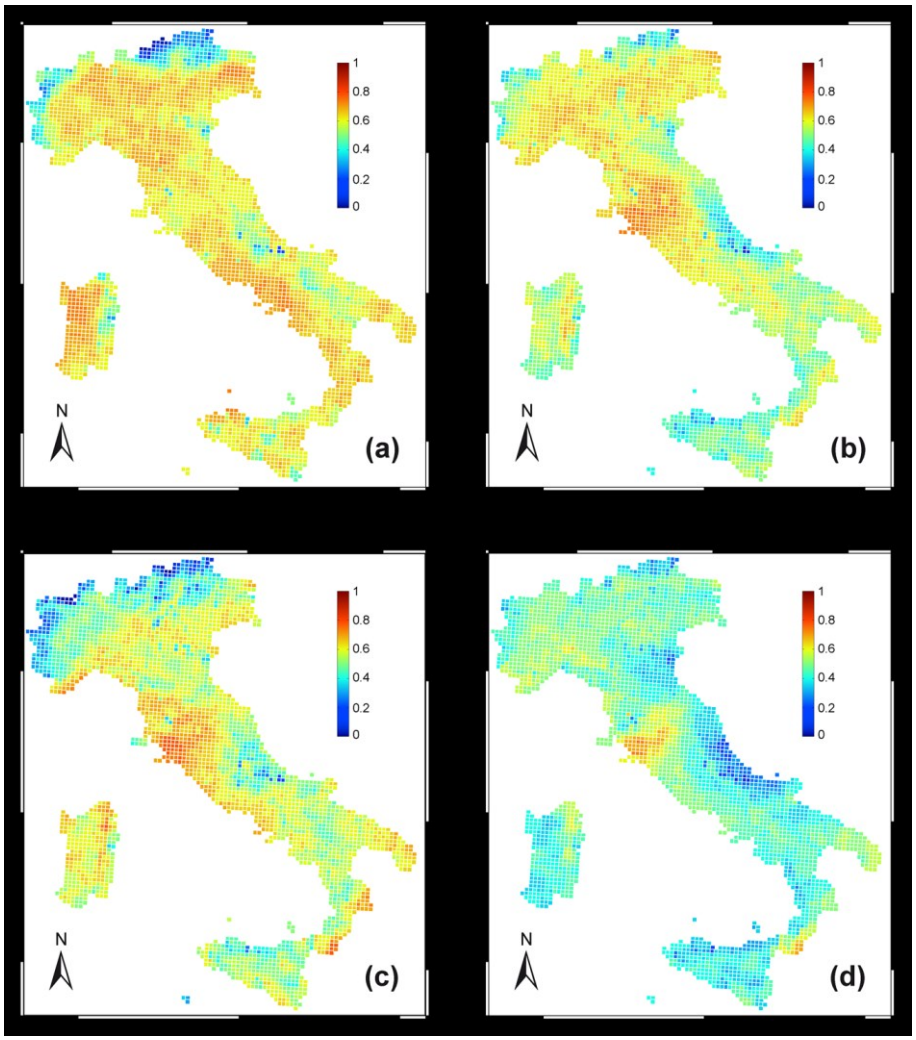

Figure 6.15 - Maps of Pearson correlation between ground-based rainfall observations and (a) SM2RASC, (b) 3B42-RT, (c) CMORPH and (d) PERSIANN satellite rainfall products.

Figure 6.16 shows the empirical cumulative distribution functions (ECDF) of the duration *D* (***Figures 6.16a*** and 6.16***b***) and of the cumulated rainfall *E* (***Figures 6.16*** and ***6.16d***) for RE and RE* calculated using the ground-based and satellite-based data sets.

Inspection of ***Figures 6.16a*** and ***6.16b*** reveals that OBS and SM2RASC rainfall events (RE and RE*) exhibit a similar distribution of *D*, whereas 3B42-RT, CMORPH and PERSIANN rainfall events have a shorter duration. As expected, the duration of RE* is generally longer than that of RE (as shown by quantile values in the inset tables), since the cumulated rainfall in short duration precipitation events is usually not adequate to trigger a landslide. The ECDF curves of the cumulated rainfall *E* for the three satellite products (***Figures 6.16c*** and 6.16***d***) are higher than that of OBS. This means that rainfall events are characterized by lower *E* values as shown also by the quantile values (see inset tables in ***Figures 6.16c*** and ***6.16d***). The ECDF curve of SM2RASC is the closest to the OBS one, whereas those of 3B42-RT, CMORPH and PERSIANN are characterized by lower E values. As expected, satellite products underestimate the rainfall measured by the ground-based observations.

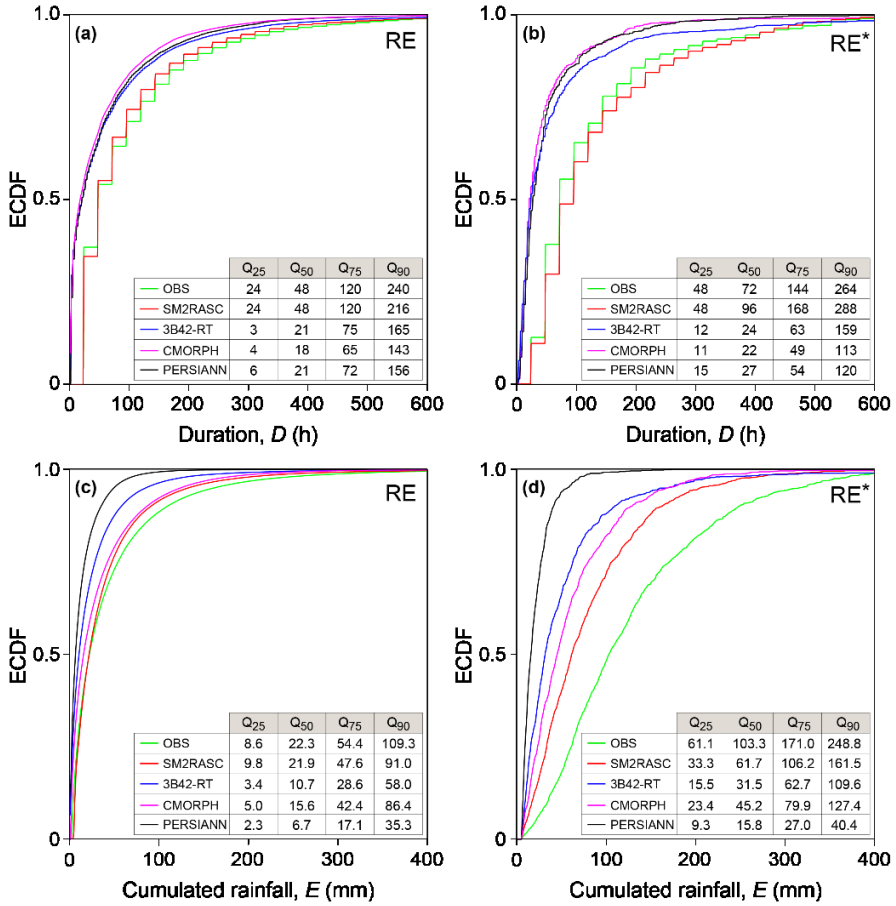

Figure 6.16 - Empirical cumulative distribution function (ECDF) of (a) the rainfall duration D and (b) the cumulated rainfall E of the reconstructed rainfall events for OBS (green curves), SM2RASC (red curves), 3B42-RT (blue curves), CMORPH (magenta curves) and PERSIANN (black curves) data sets. Inset tables list relevant quantile values of D and E.

Using the frequentist method on the synthetic series on 85% of the reconstructed RE*, we calculated the mean *ED* rainfall thresholds at different exceedance probabilities for the four data sets. An example of thresholds for the OBS data set is shown in ***Figure 6.17***.

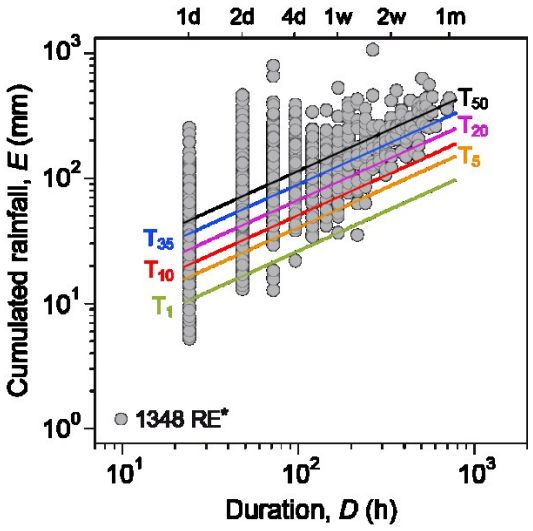

Figure 6.17 - Example of ED rainfall thresholds calculated using RE at exceeding probabilities from 1% (T_1) to 50% (T_{50}) for the OBS data set. Grey dots are the (D, E) pairs.*

Using 15% of the remaining RE*, we simulated the application of the thresholds in a virtual landslide warning system. ***Figure 6.18*** portrays, as an example, the classification of rainfall events in the four contingencies (TP, FP, FN and TN) based on the 50% rainfall thresholds for the four data sets. Each graph in ***Figure 6.18*** represents one out of 100 synthetic series. We applied the classification illustrated in ***Figure 6.18*** to the different exceedance probability levels shown in ***Figure 6.17*** and built the corresponding ROC curves. For civil protection purposes, the priority is to minimize the number of missed alarms (FN) and secondary to limit false alarms (FP), which implies maximizing POD and minimizing POFD skill scores.

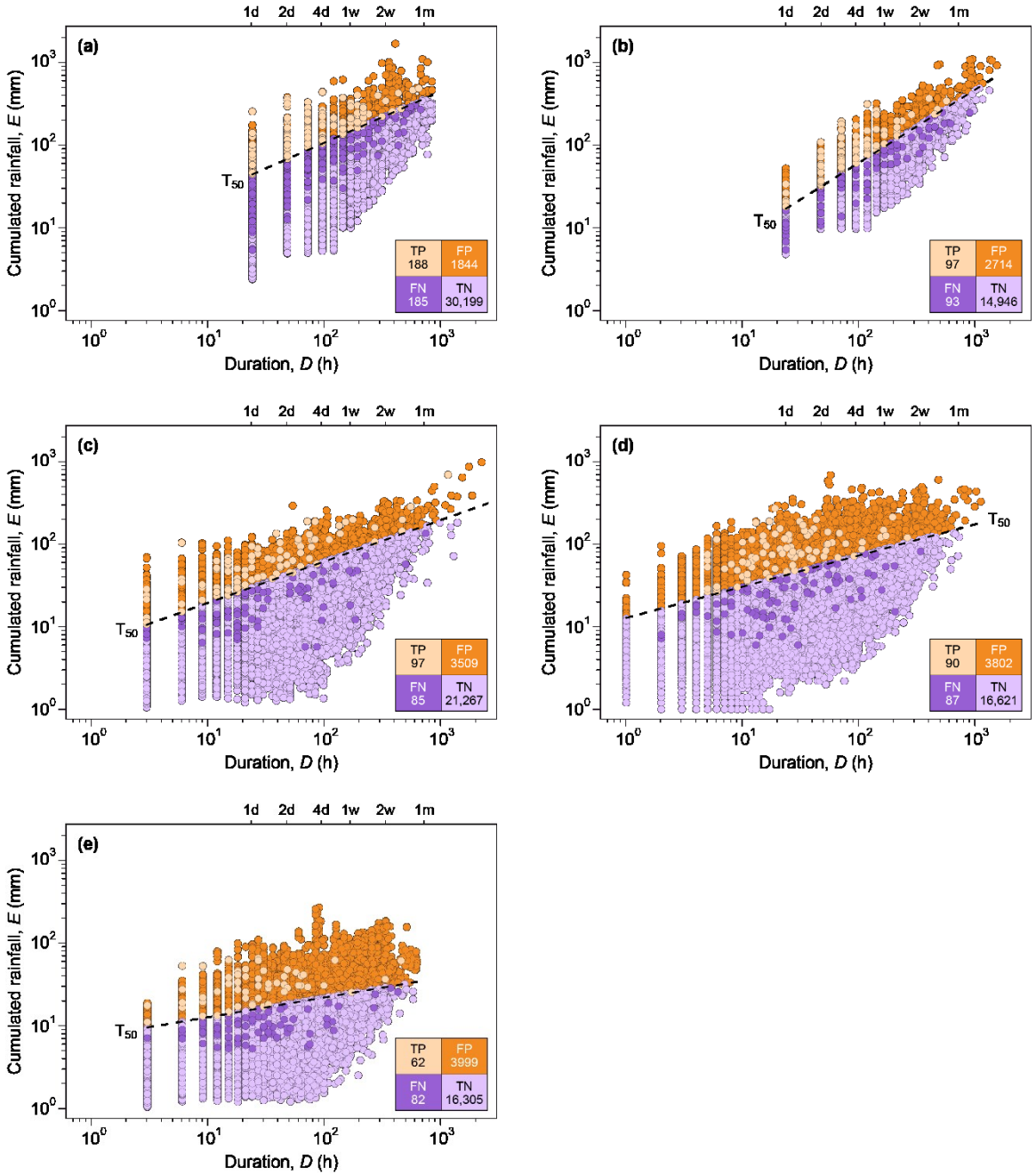

Figure 6.18 - Rainfall duration vs. cumulated event rainfall conditions in Italy in the period 2008-2014, compared with thresholds at 50% (T50%) exceedance probability level (dashed black lines) for (a) OBS, (b) SM2RASC, (c) 3B42-RT, (d) CMORPH and (e) PERSIANN. Legend: TP, True Positives; TN, True Negative; FP, False Positive; FN, False Negative.

Applying the classification illustrated in ***Figure 6.18*** to the different non-exceedance probability levels shown in ***Figure 6.17***, we found POD and POFD skill scores. For civil protection purposes, the priority is to minimize the number of missed alarms (FN) and secondary to limit false alarms (FP), which implies maximizing POD and minimizing POFD skill scores, i.e. maximizing HK. ***Figure 6.19*** shows for each data set the POD, POFD and HK values at different non-exceedance probability.

(a) OBS

(%)	POD	POFD	HK
3	0.97	0.48	0.49
5	0.95	0.41	0.54
10	0.91	0.31	0.60
15	0.88	0.24	0.63
20	0.83	0.20	0.63
25	0.78	0.16	0.62
30	0.75	0.13	0.62
35	0.70	0.11	0.59
40	0.63	0.09	0.54
45	0.58	0.07	0.51
50	0.50	0.06	0.45

(b) SM2RASC

(%)	POD	POFD	HK
3	0.97	0.77	0.20
5	0.95	0.69	0.26
10	0.90	0.57	0.33
15	0.85	0.49	0.37
20	0.82	0.42	0.40
25	0.77	0.36	0.41
30	0.72	0.31	0.41
35	0.67	0.26	0.40
40	0.62	0.22	0.40
45	0.56	0.19	0.38
50	0.51	0.15	0.36

(c) 3B42-RT

(%)	POD	POFD	HK
3	0.97	0.61	0.36
5	0.96	0.56	0.40
10	0.91	0.46	0.44
15	0.87	0.40	0.48
20	0.82	0.35	0.48
25	0.74	0.30	0.44
30	0.70	0.26	0.43
35	0.68	0.23	0.45
40	0.63	0.20	0.43
45	0.55	0.17	0.39
50	0.53	0.14	0.39

(d) CMORPH

(%)	POD	POFD	HK
3	0.97	0.67	0.30
5	0.96	0.61	0.35
10	0.90	0.51	0.39
15	0.85	0.44	0.42
20	0.80	0.38	0.42
25	0.74	0.34	0.40
30	0.71	0.30	0.41
35	0.65	0.27	0.38
40	0.63	0.24	0.39
45	0.59	0.21	0.37
50	0.51	0.19	0.32

(e) PERSIANN

(%)	POD	POFD	HK
3	0.99	0.58	0.41
5	0.99	0.54	0.45
10	0.92	0.45	0.46
15	0.83	0.40	0.44
20	0.76	0.36	0.41
25	0.72	0.32	0.40
30	0.67	0.29	0.38
35	0.60	0.26	0.34
40	0.51	0.24	0.28
45	0.48	0.22	0.26
50	0.43	0.20	0.23

Figure 6.19 - Values of the POD, POFD and HK skill scores at varying the threshold non-exceedance probability for the five data sets. Values in red are those which maximize HK.

Following this criterion for each data set we selected the threshold probability level that maximizes the HK skill score. For OBS and the satellite-based data sets 3B42-RT and CMORPH, the highest HK was obtained with the threshold at 15% non-exceedance probability that also maximize POD values. Using the same criteria, for SM2RASC the most suitable threshold is at 25%, and for PERSIANN is at 10%. Using POD and POFD, we also built the ROC. ***Figure 6.20*** shows the comparison of the ROC curves for the five data sets. As expected, OBS gives the best performance at all the non-exceedance probability levels. Among the curves of satellite-based rainfall data, 3B42-RT is performing better for non-exceedance probability higher than 4%, while PERSIANN is the worst above 7%.

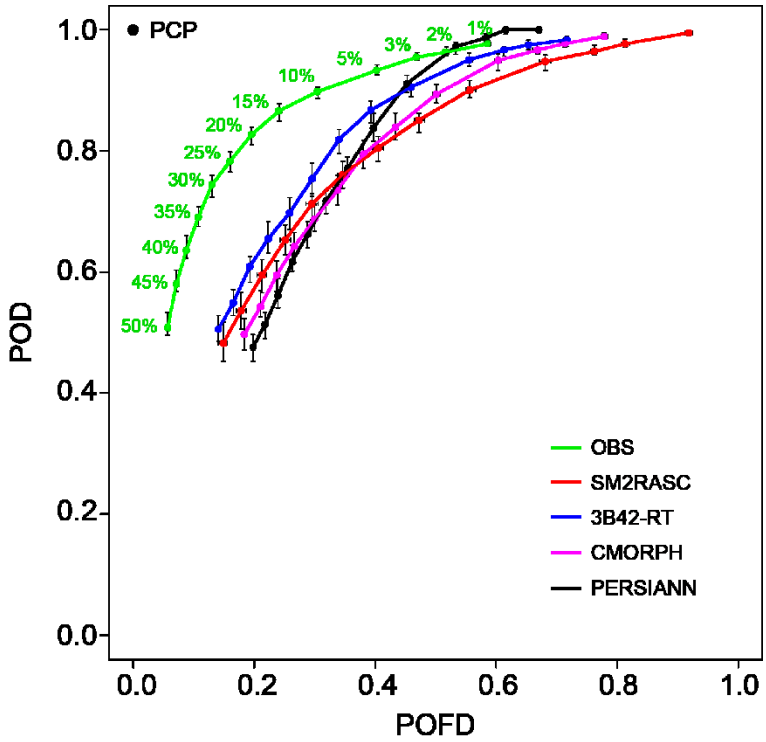

Figure 6.20 - ROC curves built by skill scores obtained varying the threshold exceedance probability for OBS (green), SM2RASC (red), 3B42-RT (blue), CMORPH (magenta) and PERSIANN (black) data sets. Horizontal and vertical bars represent the range of variation of POFD and POD for the 100 runs in which RE are randomly selected.*

This results highlighted that satellite rainfall products considered here are able to satisfactorily predict landslide occurrence in Italy, and the lower performance with respect to ground observations are due to the high-quality of OBS data set (based on ~3000 rain gauges). Due to the low latency associated with satellite rainfall products, this source of information could be applied with beneficial effect in real-time early warning system.

7.REFERENCES

Adler, R. F.; Huffman, G. J.; Chang, A.; Ferraro, R.; Xie, P.-P.; Janowiak, J.; Rudolf, B.; Schneider, U.; Curtis, S.; Bolvin, D.; Gruber, A.; Susskind, J.; Arkin, P.; Nelkin, E. The Version-2 Global Precipitation Climatology Project (GPCP) Monthly Precipitation Analysis (1979–Present). J. Hydrometeorol. 2003, 4, 1147–1167.

Albergel, C., Rudiger, C., Pellarin, T., Calvet, J.C., Frtiz, N., Froissard, F., Suquia, D., Petitpa, A., Piguet, B., Martin, E. (2008). From near-surface to root-zone soil moisture using an exponential filter: An assessment of the method based on in-situ observations and model simulations. Hydrol. Earth Syst. Sci., 12, 1323-1337.

Al-Yaari, A., Wigneron, J.P., Ducharne, A., Kerr, Y., De Rosnay, P., de Jeu, R.A.M., Govind, A., Al Bitar, A., Albergel, C., Munoz-Sabater, J., Richaume, P., Mialon, A. (2014a). Global-scale evaluation of two satellite-based passive microwave soil moisture datasets (SMOS and AMSR-E) with respect to Land Data Asssimilation System estimates. Remote Sensing of Environment, 149, 181-195.

Al-Yaari, A., Wigneron, J.P., Ducharne, A., Kerr, Y., Wagner, W., De Lannoy, G., Reichle, R., Al Bitar, Dorigo, W., Richaume, P., Mialon, A. (2014b). Global-scale comparison of passive (SMOS) and active (ASCAT) satellite-based microwave soil moisture retrievals with soil moisture simualtions (MERRA-Land). Remote Sensing of Environment, 152, 614-626.

Arkin PA, Meisner BN. (1987). The relationship between large-scale convective rainfall and cold cloud over the western hemisphere during 1982–1984. Monthly Weather Review, 115: 51–74.

Artan, G., Gadain, H., Smith, J.L., Asante, K., Bandaragoda, J., Verdin, J.P. (2007). Adequacy of satellite derived rainfall data for stream flow modeling. Nat. Hazards, 43, 167-185.

Arulampalam, M. S., Maskell, S., Gordon, N., & Clapp, T. (2002). A tutorial on particle filters for online nonlinear/non-Gaussian Bayesian tracking. IEEE Transactions on Signal Processing, 50, 174–188.

Baum, R.L., Godt, J.W. (2010). Early warning of rainfall-induced shallow landslides and debris flows in the USA. Landslides 7, 259-272.

Beck, H.E., van Dijk, A.I.J.M., Levizzani, V., Schellekens, J., Miralles, D.G., Martens, B., de Roo, A. (2017). MSWEP: 3-hourly 0.25° global gridded precipitation (1979–2015) by merging gauge, satellite, and reanalysis data, Hydrology and Earth System Sciences, 21, 589–615, doi:10.5194/hess-21–589-2017, 2017.

Bober, W. (2013). Introduction to Numerical and Analytical Methods with MATLAB for Engineers and Scientists. CRC Press, Inc.: Boca Raton, FL, USA.

Brocca, L., Ciabatta, L., Massari, C., Camici, S., Tarpanelli, A. (2017). Soil moisture for hydrological applications: open questions and new opportunities. Water, 9(2), 140, doi:10.3390/w9020140.

Brocca, L., Ciabatta, L., Moramarco, T., Ponziani, F., Berni, N., Wagner, W. (2016c). Use of satellite soil moisture products for the operational mitigation of landslides risk in central Italy. In: G.P. Petropoulos, P. Srivastava, Y. Kerr (eds.), Satellite Soil Moisture Retrievals: Techniques & Applications. Elsevier, Amsterdam, Chapter 12, 231-247, ISBN: 978-0-12-

803388-3, doi:10.1016/B978-0-12-803388-3.00012-7. http://dx.doi.org/10.1016/B978-0-12-803388-3.00012-7

Brocca, L., Pellarin, T., Crow, W.D., Ciabatta, L., Massari, C., Ryu, D., Su, C.H., Rüdiger, C., Kerr, Y. (2016b), Rainfall estimation by inverting SMOS soil moisture estimates: A comparison of different methods over Australia, J. Geophys. Res. Atmos., 121, doi:10.1002/2016JD025382.

Brocca, L., Massari, C., Ciabatta, L., Wagner, W., Stoffelen, A. (2016a). Remote sensing of terrestrial rainfall from Ku-band scatterometers. IEEE Journal of Selected Topics in Applied Earth Observations and Remote Sensing, 9(1), 533-539.

Brocca, L.; Massari, C.; Ciabatta, L.; Moramarco, T.; Penna, D.; Zuecco, G.; Pianezzola, L.; Borga, M.; Matgen, P.; Martínez-fernández, J. (2015). Rainfall estimation from in situ soil moisture observations at several sites in Europe: an evaluation of the SM2RAIN algorithm. *Journal of Hydrology and* Hydromechanics, 63(3), 201-209.

Brocca, L., Ciabatta, L., Massari, C., Moramarco, T., Hahn, S., Hasenauer, S., Kidd, R., Dorigo, W., Wagner, W., & Levizzani, V. (2014). Soil as a natural rain gauge: Estimating global rainfall from satellite soil moisture data. Journal of Geophysical Research-Atmospheres, 119, 5128-5141.

Brocca, L., Moramarco, T., Melone, F., & Wagner, W. (2013a). A new method for rainfall estimation through soil moisture observations. Geophysical Research Letters, 40, 853-858.

Brocca, L., Moramarco, T., Dorigo, W., Wagner, W. (2013b). Assimilation of satellite soil moisture data into rainfall-runoff modeling for several catchments worldwide. Proceedings 2013 IEEE International Geoscience and Remote Sensing Symposium (IGARSS), 2281-2284, doi:10.1109/IGARSS.2013.6723273.

Brocca L., Hasenauer, S., Lacava, T., Melone, F., Moramarco, T., Wagner, W., Dorigo, W., Matgen, P., Martinez.Fernandez, J., Llorens, P., Latron, J., Martin, C., Bittelli, M. (2011a). Soil moisture estimation through ASCAT and AMSR-E sensors: an intercomparison and validation study across Europe. Remote Sensing of Environment, 115, 3390-3408.

Brocca, L., Melone, F., Moramarco, T. (2011b). Distributed rainfall-runoff modelling for flood frequency estimation and flood forecasting. Hydrological Processes, 25 (18), 2801-2813.

Brocca, L., Melone, F., Moramarco, T., Wagner, W., Hasenauer, S. (2010). ASCAT Soil Wetness Index validation through in-situ and modeled soil moisture data in central Italy. Remote Sensing of Environment, 114 (11), 2745-2755.

Brocca, L., Melone, F., Moramarco, T., Singh, V.P. (2009). A continuous rainfall –runoff model as a tool for the critical hydrological scenario assessment in natural channels. In: M. Taniguchi, W.C. Burnett, Y. Fukushima, M. Haigh, Y. Umezawa (Eds), From headwater to the ocean. Hydrological changes and managements, Taylor & Francis Group, London, 175-179.

Brocca, L., Melone, F., Moramarco, T. (2008). On the estimation of antecedent wetness conditions in rainfall-runoff modelling. Hydrological Processes, 22 (5), 629-642.

Brunetti, M.T., Melillo, M., Peruccacci, S., Ciabatta, L., Brocca, L. (2018). How far are we from the use of satellite rainfall products in the prediction of landslides? Remote Sensing of Environment, under review.

Brunetti, M.T., Perruccacci, S., Rossi, M., Luciani, S., Valigi, D., Guzzetti, F. (2010). Rainfall thresholds for the possible occurrence of landslides in Italy. Natural Hazards and Earth System Sciences 10, 447-458. http://dx.doi.org/10.5194/nhess-10-447-2010.

Camici, S., Brocca, L., Melone, F., Moramarco, T. (2014). Impact of climate change on flood frequency using different climate models and downscaling approaches. Journal of Hydrologic Engineering, 19(8), 04014002, doi:10.1061/(ASCE)HE.1943-5584.0000959.

Camici, S., Ciabatta, L., Massari, C., Brocca, L. (2018). How reliable are satellite precipitation estimates for driving hydrological models: a verification study over the Mediterranean area. submitted to Journal of Hydrology.

Chen, F. W., & Staelin, D. H. (2003). Airs/amsu/hsb precipitation estimates. Geoscience and Remote Sensing, IEEE Transactions on, 41(2), 410-417.

Chen, M.; Shi, W.; Xie, P. and CPC Precipitation Working Group CPC/NCEP/NOAA; (2008a) CPC Unified Gauge-based Analysis of Global Daily Precipitation. 2008 Western Pacific Geophysics Meeting Cairns, Australia, 29 July - 1 August.

Chen, M.; Shi, W.; Xie, P.; Silva, V. B. S.; Kousky, V. E.; Higgins, R. W.; Janowiak, J. E. (2008b) Assessing objective techniques for gauge-based analyses of global daily precipitation. J. Geophys. Res. Atmos, 113, 1–13.

Chen, F., Crow, W.T., Holmes, T.H. (2012): Improving longterm, retrospective precipitation datasets using satellite-based surface soil moisture retrievals and the soil moisture analysis rainfall tool. J. Appl. Remote Sens., 6, 063604.

Ciabatta, L., Massari, C., Brocca, L., Gruber, A., Reimer, C., Hahn, S., Paulik, C., Dorigo, W., Kidd, R., Wagner, W. (2018). SM2RAIN-CCI: a new global long-term rainfall data set derived from ESA CCI soil moisture. Earth System Science Data, 10, 267-280. https://doi.org/10.5194/essd-10-267-2018.

Ciabatta, L., Marra, A.C., Panegrossi, G., Casella, D., Sanò, P., Dietrich, S., Massari, C., Brocca, L. (2017). Daily precipitation estimation through different microwave sensors: verification study over Italy. Journal of Hydrology, 545:436-450.

Ciabatta, L., Brocca, L., Massari, C., Moramarco, T., Gabellani, S., Puca, S., Wagner, W. (2016a). Rainfall-runoff modelling by using SM2RAIN-derived and state-of-the-art satellite rainfall products over Italy. International Journal of Applied Earth Observation and Geoinformation, 48, 163-173.

Ciabatta, L., Massari, C., Brocca, L., Reimer, C., Hann, S., Paulik, C., Dorigo, W., Wagner, W. (2016b) Using Python® language for the validation of the CCI soil moisture products via SM2RAIN. PeerJ Preprints, 4:e2131v2, doi:10.7287/peerj.preprints.2131v2.

Ciabatta, L., Camici, S., Brocca, L., Ponziani, F., Stelluti, M., Berni, N., Moramarco, T. (2016c). Assessing the impact of climate-change scenarios on landslide occurrence in Umbria region, Italy. Journal of Hydrology, 541, 285-295.

Ciabatta, L., Brocca, L., Massari, C., Moramarco, T., Puca, S., Rinollo, A., Gabellani, S., Wagner, W. (2015). Integration of satellite soil moisture and rainfall observations over the Italian territory. Journal of Hydrometeorology, 16(3), 1341-1355.

Contractor, S., Alexander, L.V., Donat, M.G., Herold, N. (2015). How Well Do Gridded Datasets of Observed Daily Precipitation Compare over Australia? Advances in Meteorology, 2015, Article ID 325718, 15 pages.

Crow, W.T., van den Berg, M.J., Huffman, G.J., & Pellarin, T. (2011). Correcting rainfall using satellite-based surface soil moisture retrievals: The Soil Moisture Analysis Rainfall Tool (SMART). Water Resources Research, 47.

Crow, W.T., & Bolten, J.D. (2007). Estimating precipitation errors using spaceborne surface soil moisture retrievals. Geophysical Research Letters,34

Crow, W.T., Huffman, G.J., Bindlish, R., & Jackson, T.J. (2009). Improving Satellite-Based Rainfall Accumulation Estimates Using Spaceborne Surface Soil Moisture Retrievals. Journal of Hydrometeorology, 10, 199-212

Dee, D. P.; Uppala, S. M.; Simmons, a. J.; Berrisford, P.; Poli, P.; Kobayashi, S.; Andrae, U.; Balmaseda, M. a.; Balsamo, G.; Bauer, P.; Bechtold, P.; Beljaars, a. C. M.; van de Berg, L.; Bidlot, J.; Bormann, N.; Delsol, C.; Dragani, R.; Fuentes, M.; Geer, a. J.; Haimberger, L.; Healy, S. B.; Hersbach, H.; Hólm, E. V.; Isaksen, L.; Kållberg, P.; Köhler, M.; Matricardi, M.; McNally, a. P.; Monge-Sanz, B. M.; Morcrette, J.-J.; Park, B.-K.; Peubey, C.; de Rosnay, P.; Tavolato, C.; Thépaut, J.-N.; Vitart, F. (2011). The ERA-Interim reanalysis: configuration and performance of the data assimilation system. Q. J. R. Meteorol. Soc., 137, 553–597.

Desiato, F., Fioravanti, G., Fraschetti, P., Perconti, W., Piervitali, E. (2015). Valori climatici normali di temperatura e precipitazione in Italia. ISPRA, Stato dell'Ambiente 55/2014, ISBN 978-88-448-0689-7, (in Italian).

Dilley, M., Chen, R.S., Deichmann, U., Lerner-Lam, A.L., Arnold, M., Agwe, J., Buys, P., Kjevstad, O., Lyon, B., Yetman, G. (2005). Natural disaster hotspots: A global risk analysis. Washington, DC: World Bank. http://documents.worldbank.org/curated/en/621711468175150317/Natural-disaster-hotspots-A-global-risk-analysis.

Dinku, T., Ceccato, P., Grover‐Kopec, E., Lemma, M., Connor, S. J., Ropelewski, C. F. (2007). Validation of satellite rainfall products over East Africa's complex topography. Int. J. Remote Sens., 28, 1503‐1526.

Doorenbos J, Pruitt WO. (1977). Background and development of methods to predict reference crop evapotranspiration (ETo). In Crop Water Requirements. FAO Irrigation and Drainage Paper No. 24, FAO: Rome; 108–119 (Appendix II).

Dorigo, W.A., Gruber, A., De Jeu, R.A.M., Wagner, W., Stacke, T., Loew, A., Albergel, C., Brocca, L., Chung, D., Parinussa, R.M., Kidd, R. (2015). Evaluation of the ESA CCI soil moisture product using ground-based observations. Remote Sensing of Environment, doi: 10.1016/j.rse.2014.07.023. 686.

Dorigo, W.A., Scipal, K., Parinussa, R.M., Liu, Y.Y., Wagner, W., de Jeu, R.A.M., Naeimi, V. (2010). Error characterisation of global active and passive microwave soil moisture datasets. Hydrology and Earth System Sciences, 14-12, 2605-2616.

Dorigo, W.A., Wagner, W., Albergel, C., Ablrecht, F., Balsamo, G., Brocca, L., Chung, D., Ertl, M., Forkel, M., Gruber, A., Haas, E., Hamer, P., Hirschi, M., Ikonen, J., de Jeu, R., Kidd., R., Lahoz, W., Liu, Y.Y., Miralles, D., Mistelbauer, T., Nicolai-Shaw, N., Parinussa, R., Pratola, C., Reimer, C., van der Schalie, R., Seneviratne, S.I., Smolander, T., Lecomte, P. (2017). ESA CCI Soil Moisture for improved Earth system understating: state-of-the-art and future decision. Submitted to Remote Sensing of Environment.

Doucet, A., Godsill, S., & Andrieu, C. (2000). On sequential Monte Carlo sampling methods for Bayesian filtering. Statistics and Computing,10, 197–208.

Draper, C., Walker, J. P., Steinle, P., De Jeu, R. A. M., & Holmes, T. R. H. (2009). An evaluation of AMSR-E derived soil moisture over Australia. Remote Sensing of Environment, 113(4), 703–710

Ebert, E.E., Janowiak, J., Kidd, C. (2007). Comparison of near real time precipitation estimates from satellite observations and numerical models. Bull. Amer. Meteor. Soc., 88, 47-64.

Entekhabi, D., Njoku, E.G., Neill, P.E., Kellogg, K.H., Crow, W.T., Edelstein, W.N., et al., (2010). The soil moisture active passive (SMAP) mission. Proceedings of the IEEE 98(5), 704–716. doi:10.1109/JPROC.2010.2043918.

Famiglietti, JS, Wood, EF. (1994). Multiscale modeling of spatially variable water and energy balance processes. Water Resources Research, 11, 306-3078.

Fanelli, G., Salciarini, D., Tamagnini, C. (2016). Reliable soil property maps over large areas: a case study in central Italy. Journal of Environmental and Engineering Geoscience, 22 (1), 37-52.

FAO/IIASA/ISSCAS/JRC (2012). Harmonized World Soil Database (version 1.2). Food Agriculture Organizzation, Rome, Italy and IIASA, Laxenburg, Austria.

Farahmand, A. and AghaKouchak, A. (2013). A satellite-based global landslide model. Natural Hazards and Earth System Science, 113, 1259-1267.

Fawcett, T. (2006). An introduction to ROC analysis. Pattern Recognition Letters 27, 861-874. http://dx.doi.org/10.1016/j.patrec.2005.10.010.

Fischer, E. M., Knutti, R., (2015) Anthropogenic contribution to global occurrence of heavy-precipitation and high-temperature extremes, Nature Climate Change, 5, 560–564.

Gariano, S.L., Brunetti, M.T., Iovine, G., Melillo, M., Peruccacci, S., Terranova, O., Vennari, C., Guzzetti, F. (2015). Calibration and validation of rainfall thresholds for shallow landslide

forecasting in Sicily, southern Italy. Geomorphology 228, 653-665. http://dx.doi.org/1016/j.geomorph.2014.10.019.

Gariano, S.L., Guzzetti, F. (2016). Landslides in a changing climate. Earth-Science Reviews 162, 227-252.

Georgakakos, K, Baumer OW. (1996). Measurement and utilization of on-site soil moisture data. Journal of Hydrology. 184:131-152.

Gruber, A., Dorigo, W. Crow, W., Wagner, W. (2017). Triple collocation based merging of satellite soil moisture retrievals". IEEE Transactions on Geoscience and Remote Sensing, 55, 12; 6780 – 6792.

Gudmundsson, L., Bremnes, J. B., Haugen, J. E. Engen-Skaugen, T. (2012). Technical Note: Downscaling RCM precipitation to the station scale using statistical transformations–a comparison of methods. Hydrology and Earth System Sciences, 16(9), 3383-3390.

Gupta, H. V., Kling, H., Yilmaz, K. K., & Martinez, G. F. (2009). Decomposition of the mean squared error and NSE performance criteria: Implications for improving hydrological modelling. Journal of Hydrology, 377(1), 80-91.

Guzzetti, F., Cardinali, M., Reichenbach, P. (1994). The AVI Project: A bibliographical and archive inventory of landslides and floods in Italy. Environmental Management 18, 623-633. http://dx.doi.org/10.1007/bf02400865.

Guzzetti, F., Tonelli, G. (2004). Information system on hydrological and geomorphological catastrophes in Italy (SICI): a tool for managing landslide and flood hazards. Natural Hazards and Earth System Science 4, 213-232. http://dx.doi.org/10.5194/nhess-4-213-2004

Guzzetti, F., Stark, C.P., Salvati, P. (2005). Evaluation of flood and landslide risk to the population of Italy. Environmental Management 36(1), 15-36.

Harris, A.; Rahman, S.; Hossain, F.; Yarborough, L.; Bagtzoglou, A. C.; Easson, G. (2007) Satellite-based Flood Modeling Using TRMM-based Rainfall Products. Sensors, 7, 3416–3427.

Hatzianastassiou, N., Papadimas, C. D., Lolis, C. J., Bartzokas, A., Levizzani, V., Pnevmatikos, J. D., & Katsoulis, B. D. (2016). Spatial and temporal variability of precipitation over the Mediterranean Basin based on 32-year satellite Global Precipitation Climatology Project data, part I: evaluation and climatological patterns. International Journal of Climatology.

Haylock, M.R., N. Hofstra, A.M.G. Klein Tank, E.J. Klok, P.D. Jones, M. New. (2008): A European daily high-resolution gridded dataset of surface temperature and precipitation. J. Geophys. Res (Atmospheres), 113, D20119, doi:10.1029/2008JD10201.

Herold, N., Behrangi, A., Alexander, L., V. (2017). Large uncertainties in observed daily precipation extremes over land. Journal of Geophysical Research (Atmospheres), 122-2, 668-981.

Hoffmann, L., Idrissi, A. E., Pfister, L., Hingray, B., Guex, F., Musy, A., Humbert, J., Drogue, G. and Leviandier, T. (2004). Development of regionalized hydrological models in an area with short hydrological observation series, River Research and Applications, 20, 243-254.

Hong, Y., Adler, R., Huffman, G. (2006). Evaluation of the Potential of NASA Multi-satellite Precipitation Analysis in Global Landslide Hazard Assessment. Journal of Geophysical Research, 33 (22).

Hong, Y., Adler, R., Huffman, G. (2007). An experimental global monitoring system for rainfall-triggred landslides using satellite remote sensing information. IEEE Transactions on Geoscience and Remote Sensing, 45 (6), 1671-1680.

Hou, A.Y., Kakar, R.K., Neeck, S., Azarbarzin, A.A., Kumerrow, C.D., Kojima, M., Oki, R., Nakamura, K., Iguchi, T. (2014). The global precipitation measurement mission. Bulletin of the American Meteorological Society, 95, 701–722. doi:10.1175/BAMS-D-13-00164-1.

Hsu, K.L., Gao, X.G., Sorooshian, S., & Gupta, H.V. (1997) Precipitation estimation from remotely sensed information using artificial neural networks. Journal of Applied Meteorology, 36, 1176-1190.

Huffman GJ, Adler RF, Arkin P, Chang A, Ferraro R, Gruber A, Janowiak J, McNab A, Rudolf B, Schneider, U. (1997). The Global Precipitation Climatology Project (GPCP) combined precipitation dataset. Bulletin of the American Meteorological Society, 78: 5–20.

Huffman, G. J., Adler, R. F., Bolvin, D. T., Gu, G., Nelkin, E.J., Bowman, K. P., Hong, Y., Stocker, E. F., and Wolff, D. B. (2007). The TRMM Multisatellite Precipitation Analysis (TMPA): quasi-global, multiyear, combined-sensor precipitation estimates at fine scales, J. Hydrometeorol., 30(8), 38–55.

Huffman, G.J., Bolvin, D.T., Braithwaite, D., Hsu, K., Joyce, R., Xie, P. (2014). NASA Global Precipitation Measurement (GPM) Integrated Multi-satellitE Retrievals for GPM (IMERG). Algorithm Theoretical Basis Document (ATBD), version 4.4, NASA, p. 30.

Immerzeel, W. W., & Droogers, P. (2008). Calibration of a distributed hydrological model based on satellite evapotranspiration. Journal of hydrology, 349(3), 411-424.

ISPRA (2015). Dissesto idrogeologico in Italia: pericolosità e indicatori di rischio. Rapporto 2015, http://www.isprambiente.gov.it/files/pubblicazioni/rapporti/rapporto-233-2015/Rapporto_233_2015.pdf.

Jones, D.A., Wang, W., Fawcett, R. (2009). High-quality spatial climate data-sets dor Australia. Australian Meteorological and Oceanogrphic Journal, 58, 233-248.

Joyce, R. J., Janowiak, J. E., Arkin, P. A., and Xie, P. (2004). CMORPH: a method that produces global precipitation estimates from passive microwave and infrared data at high spatial and temporal resolutions, J. Hydrometeorol., 5, 487–503.

Keefer D.K., Wilson R.C., Mark R.K., Brabb E.E., Brown W.M.-III, Ellen S.D., Harp E.L., Wieczorek G.F., Alger C.S., Zatkin R.S. (1987). Real-time landslide warning during heavy rainfall. Science 238, 921–925.

Kerr, Y. H.; Waldteufel, P.; Richaume, P.; Wigneron, J. P.; Ferrazzoli, P.; Mahmoodi, A.; Al Bitar, A.; Cabot, F.; Gruhier, C.; Juglea, S. E.; Leroux, D.; Mialon, A.; Delwart, S. (2012). The SMOS Soil Moisture Retrieval Algorithm IEEE Transactions on Geoscience and Remote Sensing, 50(5), 1384-1403.

Kidd C. (1998). Passive microwave rainfall monitoring using polarization-corrected temperatures. International Journal of Remote Sensing 19: 981–996.

Kidd, C.; Huffman, G. (2011). Review Global precipitation measurement. 353, 334–353.

Kidd, C.; Levizzani, V. (2011). Status of satellite precipitation retrievals. Hydrol. Earth Syst. Sci., 15, 1109–1116.

Kidd, C., P. Bauer, J. Turk, G. J. Huffman, R. Joyce, K. L. Hsu, and D. Braithwaite (2012): Intercomparison of high-resolution precipitation products over the northwest Europe. J. Hydrometeor., 13, 67–83, doi:10.1175/JHM-D-11-042.1.

Kidd, C., Becker, A., Huffman, G. J., Muller, C.L., Joe, P., Skofronick-Jackson, G., Kirschbaum, D.B. (2017): So, How Much of the Earth's Surface IS Covered by Rain Gauges?, B. Am. Meteorol. Soc., 98, 69–78.

Kim, S., Parinussa, R. M., Liu, Y. Y., Johnson, F. M., Sharma, A. (2015). A framework for combining multiple soil moisture retrievals based on maximizing temporal correlation. Geophysical Research Letters, 42(16), 6662-6670.

Kirschbaum, D., Adler, R., Hong, Y., Hill, S., Lerner-Lam, A. (2010). A global landslide catalog for hazard applications: method, results and limitations. Natural Hazards, 52 (3), 561-575.

Kirschbaum, D., Adler, R., Hong, Y., Kumar, S., Peters-Lidard, C., Lerner-Lam, A. (2011). Advances in landslide nowcasting: evaluation of a global and regional modeling approach. Environmental Earth Science, 66 (6), 1683-1696.

Kirschbaum, D., Stanley, T., Simmons, J. (2015). A dynamic landslide hazard assessment system for Central America and Hispaniola. Natural Hazards and Easrth System Science, 15, 2257-2272.

Kirschbaum, D., T. Stanley, and S. Yatheendradas, (2016). Modeling landslide susceptibility over large regions with fuzzy overlay. Landslides, 13, 485–496.

Kling, H., Fuchs, M., & Paulin, M. (2012). Runoff conditions in the upper Danube basin under an ensemble of climate change scenarios. Journal of Hydrology, 424, 264-277.

Kongoli, C.; Ferraro, R. R.; Pellegrino, P.; Meng, H.; Dean, C. (2007). Utilization of the AMSU high frequency measurements for improved coastal rain retrievals. Geophys. Res. Lett., 34, L17809.

Koster, R.D., Brocca, L., Crow, W.T., Burgin, M.S., De Lannoy, G.J.M. (2016). Precipitation Estimation Using L-Band and C-Band Soil Moisture Retrievals. submitted to Water Resources Research. Water Resour. Res., 52, doi:10.1002/2016WR019024.

Kubota, T., Shige, S., Hashizume, H., Aonashi, K., Takahashi, N., Seto, S., Hirose, M., Takayabu, Y. N., Nakagawa, K., Iwanami, K., Ushio, T., Kachi, M., and Okamoto, K. (2007). Global

precipitation map using satellite-borne microwave radiometers by the GSMaP Project: production and validation, IEEE Trans. Geosci. Remote Sens., 45, 2259–2275,

Kucera, P.A., E.E. Ebert, F.J. Turk, V. Levizzani, D. Kirschbaum, F.J. Tapiador, A. Loew, M. Borsche, (2013). Precipitation from space: Advancing earth system science. Bull. Amer. Meteor. Soc., 94, 365-375.

Kummerow, C.; Hong, Y.; Olson, W. S.; Yang, S.; Adler, R. F.; McCollum, J.; Ferraro, R.; Petty, G.; Shin, D.-B.; Wilheit, T. (2007). The Evolution of the Goddard Profiling Algorithm (GPROF) for Rainfall Estimation from Passive Microwave Sensors. J. Appl. Meteorol., 40, 1801–1820.

Kummerow, C. (1998). Beamfilling Errors in Passive Microwave Rainfall Retrievals. J. Appl. Meteorol. 37, 356–370. doi:10.1175/1520.

Lagomarsino D., Segoni S., Fanti R., Catani F. (2013). Updating and tuning a regional scale landslide early warning system. Landslides 10, 91–97.

Li, L., Gaiser, P.W., Gao, B.C., Bevilacqua, R.M., Jackson, T.J., Njoku, E.G., Rudiger, C., Calvet, J.C., Bindlish, R. (2010). WindSat global soil moisture retrieval and validation. IEEE Transactions on Geoscience and Remote Sensing, 48 (5), 2224-2241.

Liao, Z., Hong, H., Wang, J., Fukuoka, H., Sassa, K., Karnawati, D., Fathnani, F. (2010). Prototyping an experimental early warning system for rainfall-induced landslides in Indonesia using satellite remote sensing and geospatial datasets. Landslides, 7(3), 317-324.

Liao, Z., Hong, Y., Kirschbaum, D., Liu, C. (2012). Assessment of shallow landslides from Hurricane Mitch in central America using a physically based model. Environmental Earth Sciences 66 (6), 1697-1705.

Liu, Y.Y., Dorigo, W.A., Parinussa, R.M., de Jeu, R.A.M., Wagner, W., McCabe, M.F., Evans, J.P., van Dijk, A.I.J.M. (2012). Trend-preserving blending of passive and active microwave soil moisture retrievals, Remote Sensing of Environment, 123, 280-297, doi: 10.1016/j.rse.2012.03.014.

Liu, Y. Y., Parinussa, R. M., Dorigo, W. A., De Jeu, R. A. M., Wagner, W., van Dijk, A. I. J. M., McCabe, M. F., Evans, J. P. (2011). Developing an improved soil moisture dataset by blending passive and active microwave satellite-based retrievals. Hydrology and Earth System Sciences, 15, 425-436, doi:10.5194/hess-15-425-2011.

Liu, Z. and Todini, E. (2002). Towards a comprehensive physically-based rainfall-runoff model, Hydrol. Earth Syst. Sci., 6, 859-881, https://doi.org/10.5194/hess-6-859-2002.

Louvet S., Pellarin T., al Bitar A., Cappelaere Bernard, Galle Sylvie, Grippa M., Gruhier C., Kerr Yann, Lebel Thierry, Mialon A., Mougin E., Quantin G., Richaume P., de Rosnay P. (2015). SMOS soil moisture product evaluation over West-Africa from local to regional scale. Remote Sensing of Environment, 156, 383-394.

Lu, N. and Godt, J. (2008). Infinite slope stability under steady unsaturated seepage conditions. Water Resources Research 44 (11).

Lu, N., Likos, W.J. (2004). Unsaturated soil mechanics. Wiley Eds. ISBN: 978-0-471-44731-3, 584 pages.

Lu, N., Godt, J., Wu, D. (2010). A closed-form equation for effective stress in unsaturated soil. Water Resources Research 46 (5).

Massari, C., Crow, W.D., Brocca, L., (2017). An assessment of the accuracy of global precipitation estimates without gauge observations. Hydrol. Earth Science Discuss, doi:10.5194/hess-2017-163.

Massari, C., Brocca, L., Ciabatta, L., Moramarco, T., Gabellani, S., Albergel, C., de Rosnay, P., Puca, S., Wagner, W. (2015). The use of H-SAF soil moisture products for operational hydrology: flood modeling over Italy. Hydrology, 2 (1), 2-22.

Massari, C., Brocca, L., Moramarco, T., Tramblay, Y., Didon Lescot, J.-F. (2014). Potential of soil moisture observations in flood modelling: estimating initial conditions and correcting rainfall. Advances in Water Resources, 74, 44-53.

Masseroni, D., Cislaghi, A., Camici, S., Massari, C., Brocca, L. (2017). A reliable rainfall-runoff model for flood forecasting: review and application to a semiurbanized watershed at high flood risk in Italy. Hydrology Research, in press, doi:10.2166/nh.2016.037.

McCabe, M. F., Wood, E. F., Wójcik, R., Pan, M., Sheffield, J., Gao, H., & Su, H. (2008). Hydrological consistency using multi-sensor remote sensing data for water and energy cycle studies. Remote Sensing of Environment, 112(2), 430-444.

McColl, K. A., Vogelzang, J., Konings, A. G., Entekhabi, D., Piles, M., & Stoffelen, A. (2014). Extended triple collocation: Estimating errors and correlation coefficients with respect to an unknown target. Geophysical Research Letters, 41(17), 6229–6236. https://doi.org/10.1002/2014GL061322.

Melillo, M., Brunetti, M.T., Peruccacci, S., Gariano, S.L., Guzzetti, F. (2015). An algorithm for the objective reconstruction of rainfall events responsible for landslides. Landslides 12, 311-320. http://dx.doi.org/10.1007/s10346-014-0471-3.

Melone, F., Corradini, C., Singh, V.P. (2002). Lag prediction in ungauged basins: an investigation through actual data of the upper Tiber River valley. Hydrological Processes, 16, 1085-1094.

Moradkhani, H., Hsu, K. -L., Gupta, H., & Sorooshian, S. (2005). Uncertainty assessment of hydrologic model states and parameters: Sequential data assimilation using the particle filter. Water Resources Research, 41, W05012. http://dx.doi.org/10.1029/2004WR003604.

Mugnai, A., and Coauthors. (2013a). Precipitation products from the hydrology SAF. Nat. Hazards Earth Syst. Sci., 13, 1959-1981.

Mugnai, A., Smith, E.A., Tripoli, G.J., Bizzarri, B., Casella, D., Dietrich, S., Di Paola, F., Panegrossi, G., Sanò, P. (2013b). CDRD and PNPR satellite passive microwave precipitation retrieval algorithms: EuroTRMM/EURAINSAT origins and H-SAF operations. Nat. Hazards Earth Syst. Sci., 13, 887-912.

Nikolopoulos, E.I., Anagnostou, E.N., Borga, M. (2013). Using high-resolution satellite rainfall products to simulate a major flash flood event in northern Italy. Journal of Hydrometeorology, 14(1), 171-185.

Nijssen, B., & Lettenmaier, D.P. (2004). Effect of precipitation sampling error on simulated hydrological fluxes and states: Anticipating the Global Precipitation Measurement satellites. Journal of Geophysical Research-Atmospheres, 109.

O'Callaghan, J.F. and Mark, D.A. (1984) The Extraction of the Drainage Networks from Digital Elevation Data. Computer Vision, Graphics, and Image Processing, 28, 323-344.

Owe, M., de Jeu, R.A.M., Walker, J. (2001). A methodology for surface soil moisture and vegetation optical depth retrieval using the microwave polarization difference index, IEEE Trans. Geosci. Remote Sens., 39, 1643–1694.

Owe, M., De Jeu, R.A.M., Holmes, T.R.H. (2008). Multi-sensor historical climatology of satellite derived global land surface moisture. J. Geophys. Res., 113, F01002.

Pan, M., Wood, E. F., Wójcik, R., & McCabe, M. F. (2008). Estimation of regional terrestrial water cycle using multi-sensor remote sensing observations and data assimilation. Remote Sensing of Environment, 112(4), 1282-1294.

Panegrossi G., D. Casella, S. Dietrich, A. C. Marra, L. Milani, M. Petracca, P. Sanò, A. Mugnai (2014). CDRD and PNPR passive microwave precipitation retrieval algorithms: extension to the MSG full disk area, Proc. 2014 EUMETSAT Meteorological Satellite Conference, Geneva, Sept. 2014, https://www.eumetsat.int/website/home/News/ConferencesandEvents/DAT_2076129.html

Parinussa, R., Holmes, T.R.H., de Jeu, R. (2012). Soil moisture retrievals from the Windsat spaceborne polarimetric microwave radiometer. IEEE Transactions on Geoscience and Remote Sensing 50(7): 2683-2694.

Parinussa, R. M., Holmes, T. R. H., Wanders, N., Dorigo, W. A., de Jeu, R. A. M. (2015). A preliminary study toward consistent soil moisture from AMSR2. Journal of Hydrometeorology, 16, 932–947, doi:10.1175/JHM-D-13-0200.1.

Peel, M. C., Finlayson, B. L., McMahon, T. A. (2007). Updated world map of the Köppen-Geiger climate classification. Hydrology and Earth System Sciences Discussions, 4(2), 439-473.

Pellarin, T., Louvet, S., Gruhier, C., Quantin, G., & Legout, C. (2013). A simple and effective method for correcting soil moisture and precipitation estimates using AMSR-E measurements. Remote Sensing of Environment, 136, 28-36

Pellarin, T., Tran, T., Cohard, J.M., Galle, S., Laurent, J.P., de Rosnay, P., & Vischel, T. (2009). Soil moisture mapping over West Africa with a 30-min temporal resolution using AMSR-E observations and a satellite-based rainfall product. Hydrology and Earth System Sciences,13, 1887-1896

Peruccacci, S., Brunetti, M. T., Luciani, S., Vennari, C., Guzzetti, F. (2012). Lithological and seasonal control on rainfall thresholds for the possible initiation of landslides in central Italy. Geomorphology 139, 79-90. http://dx.doi.org/10.1016/j.geomorph.2011.10.005.

Peruccacci, S., Brunetti, M.T., Gariano, S.L., Melillo, M., Rossi, M., Guzzetti, F. (2017). Rainfall thresholds for possible landslide occurrence in Italy. Geomorphology 290, 39-57. https://doi.org/10.1016/j.geomorph.2017.03.031

Peterson, T. C.; Easterling, D. R.; Karl, T. R.; Groisman, P.; Nicholls, N.; Plummer, N.; Torok, S.; Auer, I.; Boehm, R.; Gullett, D.; Vincent, L.; Heino, R.; Tuomenvirta, H.; Mestre, O.; Szentimrey, T.; Salinger, J.; Førland, E. J.; Hanssen-Bauer, I.; Alexandersson, H.; Jones, P.; Parker, D. (1998). Homogeneity adjustments of in situ atmospheric climate data: a review. Int. J. Climatol., 18, 1493–1517.

Piciullo, L., Gariano, S.L., Melillo, M., Brunetti, M.T., Peruccacci, S., Guzzetti, F., Calvello, M. (2016). Definition and performance of a threshold-based regional early warning model for rainfall-induced landslides. Landslides, 14, 995-1008.

Pignone, F., N. Rebora, F. Silvestro, and F. Castelli (2010). GRISO–Rain. Operational Agreement 778/2009 DPC-CIMA, Year-1 Activity Rep. 272/2010, CIMA Research Foundation, Savona, Italy, 353 pp.

Ponziani, F., Pandolfo, C., Stelluti, M., Berni, N., Brocca, L., Moramarco, T. (2012). Assessment of rainfall thresholds and soil moisture modeling for operational hydrogeological risk prevention in the Umbria region (central Italy). Landslides, 9, 229-237.

Posner, A.J., Georgakakos, K.P. (2015). Soil moisture and precipitation thresholds for real-time landslide prediction in El Salvador. Landslides, 12, 1179-1196.

Qi, W., Zhang, C., Fu, G., Sweetapple, C., Zhou, H. (2016). Evaluation of global fine-resolution precipitation products and their uncertainty quantification in ensemble discharge simulations. Hydrol. Earth Syst. Sci. 20, 903–920. doi:10.5194/hess-20-903-2016.

Rawls W.J., Brakensiek D.L., Saxton K.E. (1982). Estimation of soil water properties. TRANSACTION of the ASAE, vol.25, n°.5, pp.1316-1320 & 1328.

Ray, R.L., Jabobs, J.M. (2007). Relatioship amog remotely sensed soil moiture, precipitation and landslide events. Natural Hazards, 43, 211-222.

Ray, R.L., Jacobs, J.M., Cosh, M.H. (2010). Landslide susceptibility mapping using downscaled AMSR-E soil moisture: a case study from Cleveland Corral, California, US. Remote Sensing of Environment, 114, 2624-2636.

Rossi, M., Peruccacci, S., Brunetti, M.T., Marchesini, I., Luciani, S., Ardizzone, F., Balducci, V., Bianchi, C., Cardinali, M., Fiorucci, F., Mondini, A.C., Reichenbach, P., Salvati, P., Santangelo, M., Bartolini, D., Gariano, S.L., Palladino, M., Vessia, G., Viero, A., Antronico, L., Borselli, L., Deganutti, A.M., Iovine, G., Luino, F., Parise, M., Polemio, M., Guzzetti, F. (2012). SANF: National warning system for rainfall-induced landslides in Italy. In: Eberhardt, E., Froese, C., Turner, A.K., Leroueil, S. (Eds.), Landslides and engineered slopes: Protecting society through improved understanding. Taylor & Francis Group, London. ISBN: 978-0-415-62123-6, pp. 1895-1899.

Rossi, M., Luciani, S., Valigi, D., Kirschbaum, D., Brunetti, M.T., Peruccacci, S., Guzzetti, F. (2017). Statistical approaches for the definition of landslide rainfall thresholds and their uncertainty using rain gauge and satellite data. Geomorphology, 285, 16-27.

Rudolf, B., and U. Schneider (2005). Calculation of gridded precipitation data for the global land-surface using in-situ gauge observations. Proc. Second Workshop Int. Precipitation king Group, Monterey, CA, NRL/EUMETSAT, 231–247.

Salvati, P., Bianchi, C., Fiorucci, F., Giostrella, P., Marchesini, I., Guzzetti, F. (2014). Perception of flood and landslide risk in Italy: a preliminary analysis. Natural Hazards and Earth System Sciences 14, 2589-2603.

Sanò, P., Panegrossi, G., Casella, D., Di Paola, F., Milani, L., Mugnai, A., Petracca, M., and Dietrich, S (2015a). The Passive microwave Neural network Precipitation Retrieval (PNPR) algorithm for AMSU/MHS observations: description and application to European case studies. Atmos. Meas. Tech., 8, 837-857.

Sanò, P., D. Casella, G. Panegrossi, A. C. Marra, M. Petracca, and S. Dietrich. (2015b). The Passive Microwave Neural Network Precipitation Retrieval (PNPR) for the Cross-track Scanning ATMS Radiometer, EUMETSAT Meteorological Satellite Conference, Toulouse, Sept. 2015.

Sanò, P., G. Panegrossi, D. Casella, A. C. Marra, F. Di Paola, and S. Dietrich (2016), The new Passive microwave Neural network Precipitation Retrieval (PNPR) algorithm for the cross-track scanning ATMS radiometer: description and verification study over Europe and Africa using GPM and TRMM spaceborne radars, Atmos. Meas. Tech., 9, 5441-2460.

Schamm, K.; Ziese, M.; Becker, a.; Finger, P.; Meyer-Christoffer, a.; Schneider, U.; Schröder, M.; Stender, P. (2013). Global gridded precipitation over land: a description of the new GPCC First Guess Daily product. Earth Syst. Sci. Data, 6, 49–60.

Schamm, K., Ziese, M., Raykova, K., Becker, A., Finger, P., Meyer-Christoffer, A., Schneider, U. (2015): GPCC Full Data Daily Version 1.0 at 1.0°: Daily Land-Surface Precipitation from Rain-Gauges built on GTS-based and Historic Data. DOI: 10.5676/DWD_GPCC/FD_D_V1_100.

Segoni, S., Lagomarsino, D., Fanti, R.,Moretti, S., Casagli, N. (2015). Integration of rainfall thresholds and susceptibility maps in the Emilia Romagna (Italy) regional-scale landslide warning system. Landslides 12, 773-785.

Seo, D. J. (1998). Real-time estimation of precipitation fields using radar precipitation and rain gauge data. J. Hydrol., 208, 37– 52.

Serrat-Capdevila, A.; Valdes, J. B.; Stakhiv, E. Z. (2014). Water Management Applications for Satellite Precipitation Products: Synthesis and Recommendations. JAWRA J. Am. Water Resour. Assoc., 50, 509–525.

Sorooshian, S., K. Hsu, X. Gao, H.V. Gupta, B. Imam, and D. Braithwaite (2000). Evaluation of PERSIANN System Satellite-Based Estimates of Tropical Rainfall. Bulletin of American Meteorology 81(9), 2035-2046.

Stampoulis, D.; Anagnostou, E. N. (2012). Evaluation of Global Satellite Rainfall Products over Continental Europe. J. Hydrometeorol., 13, 588–603.

Stanley, T., Kirschbaum, D. (2017). A heuristic approach to global landslide susceptibility mapping. Natural Hazards, 87, 145-164.

Stisen, S., Sandholt, I. (2010). Evaluation of remote-sensing-based rainfall products though predictive capability in hydrological runoff modelling. Hydrological Processes, 24,879-891.

Stoffelen, A. (1998): Toward the true near-surface wind speed: Error modeling and calibration using triple collocation, Journal of Geophysical Research, 103, 7755, doi:10.1029/97JC03180.

Tarnavsky, E., Mulligan, M., Ouessar, M., Faye, A., Black, E. (2013). Dynamic Hydrological Modeling in Drylands with TRMM Based Rainfall. Remote Sensing, 5(12), 6691-6716.

Tarpanelli, A., Massari, C., Ciabatta, L., Filippucci, P., Amarnath, G., Brocca, L. (2017). Exploiting a constellation of satellite soil moisture sensors for accurate rainfall estimation. Advances in Water Resources, 108, 249-255.

Thiemig, V., Rojas, R., Zambrano-Bigiarini, M., & De Roo, A. (2013). Hydrological evaluation of satellite-based rainfall estimates over the Volta and Baro-Akobo Basin. Journal of Hydrology, 499, 324-338.

Tian, Y., Peters-Lidard, C.D., Eylander, J.B., Joyce, R.J., Huffman, G.J., Adler, R.F., Hsu, K.-L., Turk, F.J., Garcia, M., Zeng, J. (2009). Component analysis of errors in Satellite-based precipitation estimates. J. Hydrometeor., 114(D24).

Todini, E. and Ciarapica, L. (2001). The TOPKAPI model. Chapter 12 in Mathematical Models of Large Watershed Hydrology, V.P. Singh et al. (Eds.). Water Resources Publications, Littleton, Colorado.

Trigila, A., Iadanza, C. Bussettini, M., Lastoria, B., Barbano, A. (2015). Dissesto idrogeologico in Italia: pericolosità e indicatori di rischio. Rapporto 2015, Istituto Superiore per la Protezione e la Ricerca Ambientale – ISPRA, Rapporti 233/2015, 162 pp. (in Italian).

Turk, F. J., Rohaly, G. D., Hawkins, J., Smith, E. A., Marzano, F. S., Mugnai, A., and Levizzani, V. (2000). Meteorological applications of precipitation estimation from combined SSM/I, TRMM and infrared geostationary satellite data, in: Microwave Radiometry and Remote Sensing of the Earth's Surface and Atmosphere, edited by: Pampaloni, P. and Paloscia, S., VSP Int. Sci. Publ., Zeist, The Netherlands, 353–363.

Valentino, R., Meisina, C., Montrasio, L., Losi, G.L., Zizioli, D. (2014). Predictive power evaluation of physically-based model for shallow landslides in the area of Oltrepò Pavese, Northern Italy. Geotech. Geol. Eng., 32 (4), 783-805.

Van Genutchen, M.T. (1980). A closed-form equation for predicting the hydraulic conductivity of unsaturated soils. Soil Science Society of America, 44 (5), 892-898.

Van Leeuwen, P. J. (2009). Particle filtering in geophysical systems. Monthly Weather Review, 137(12), 4089–4114.

Wagner, W., Hahn, S., Kidd, R., Melzer, T., Bartalis, Z., Hasenauer, S., Figa, J., de Rosnay, P., Jann, A., Schneider, S., Komma, J., Kubu, G., Brugger, K., Aubrecht, C., Zuger, J., Gangkofner, U., Kienberger, S., Brocca, L., Wang, Y., Bloeschl, G., Eitzinger, J., Steinnocher, K., Zeil, P., Rubel, F. (2013). The ASCAT soil moisture product: Specifications, validation results, and emerging applications. Meteorologische Zeitschrift, 22(1), 5-33.

Wagner, W., Dorigo, W., de Jeu, R., Fernandez, D., Benveniste, J., Haas, E., Ertl, M. (2012). Fusion of active and passive microwave observations to create an Essential Climate Variable data record on soil moisture, ISPRS Annals of the Photogrammetry, Remote Sensing and Spatial Information Sciences (ISPRS Annals), Volume I-7, XXII ISPRS Congress, Melbourne, Australia, 25 August-1 September 2012, 315-321.

Wagner, W., G. Lemoine, H. Rott (1999) A Method for Estimating Soil Moisture from ERS Scatterometer and Soil Data, Remote Sensing of Environment, 70, 191-207.

Wanders, N., Pan, M., Wood, E.F. (2015). Correction of real-time satellite precipitation with multi-sensor satellite observations of land surface variables. Remote Sensing of Environment, 160, 206-221.

Wang, Lin, and Wen Chen. (2014). Equiratio cumulative distribution function matching as an improvement to the equidistant approach in bias correction of precipitation. Atmospheric Science Letters 15.1: 1-6.

Wigneron, J.P., Kerr, Y., Waldteufel, P., Saleh, K., Escorihuela, M.J., Richaume, P., Ferrazzoli, P., de Rosnay, P., Gurney, R., Calvet, J.C., Grant, J.P., Guglielmetti, M., Hornbuckle, B., Matzler, C., Pellarin, T., & Schwank, M. (2007). L-band Microwave Emission of the Biosphere (L-MEB) Model: Description and calibration against experimental data sets over crop fields. Remote Sensing of Environment, 107, 639-655.

He, X., Hong, Y., Vergara, H., Zhang, K., Kirstetter, P.E., Gourley, J.J., Zhang, Y., Qiao, G., Liu. C. (2016). Development of a coupled hydrological-geotechnical framework for a rainfall-induced landslides prediction. Journal of Hydrology, 543, 395-405.

Xie P, Arkin PA. (1997). Global precipitation: a 17-year monthly analysis based on gauge observations, satellite estimates, and numerical model outputs. Bulletin of the American Meteorological Society, 78: 2539–2578.

Zhan, W.; Pan, M.; Wanders, N.; Wood, E. F. (2015). Correction of real-time satellite precipitation with satellite soil moisture observations. Hydrol. Earth Syst. Sci. Discuss., 12, 5749–5787.

Zhao, H., Yang, S., Wang, Z., Zhou, X., Luo, Y., Wu, L. (2015). Evaluating the suitability of TRMM satellite rainfall data for hydrological simulation using a distributed hydrological model in the Weihe River catchment in China. Journal of Geographical Sciences, 25(2), 177-195.

8.PUBLICATIONS

Under review

Bauer-Marschallinger, B., Naeimi, V., Cao, S., Paulik, C., Schaufler, S., Stachl, T., Modanesi, S., **Ciabatta, L.**, Massari, C., Brocca, L., Wagner, W. (2018). Towards global soil moisture monitoring with Sentinel-1: harnessing assets and overcoming obstacles. submitted to *IEEE Transactions on Geoscience and Remote Sensing*.

Bauer-Marschallinger, B., Paulik, C., Hochstöger, S., Mistelbauer, T., Modanesi, S., **Ciabatta, L.**, Massari, C., Brocca, L., Wagner, W. (2018). Soil moisture from fusion of scatterometer and sar: closing the scale gap with temporal filtering. submitted to *Remote Sensing*.

Camici, S., **Ciabatta, L.**, Massari, C., Brocca, L. (2018). How reliable are satellite precipitation estimates for driving hydrological models: a verification study over the Mediterranean area. submitted to *Journal of Hydrology*.

Jalilvand, E., Tajrishy, M., Brocca, L., Massari, C., Hashemi, S.A.G., **Ciabatta, L.** (2018). Estimating the drainage rate from surface soil moisture drydowns: application of DfD model to in situ soil moisture data. submitted to *Journal of Hydrology*.

Published in peer-reviewed journals

Brunetti, M.T., Melillo, M., Peruccacci, S., **Ciabatta, L.**, Brocca, L. (2018). How far are we from the use of satellite data in landslide forecasting? *Remote Sensing of Environment*, 210, 65-75, doi:10.1016/j.rse.2018.03.016.

Ciabatta, L., Massari, C., Brocca, L., Gruber, A., Reimer, C., Hahn, S., Paulik, C., Dorigo, W., Kidd, R., Wagner, W. (2018). SM2RAIN-CCI: a new global long-term rainfall data set derived from ESA CCI soil moisture. *Earth System Science Data*, 10, 267-280, doi:10.5194/essd-10-267-2018.

Massari, C., Camici, S., **Ciabatta, L.**, Brocca, L. (2018). Exploiting satellite-based surface soil moisture for flood forecasting in the Mediterranean area: state update versus rainfall correction. *Remote Sensing*, 10(2), 292, doi: 10.3390/rs10020292.

Santi, E., Paloscia, S., Pettinato, S., Brocca, L., **Ciabatta, L.**, Entekhabi, D. (2018). On the synergy of SMAP, AMSR2 and SENTINEL-1 for retrieving soil moisture. *International Journal of Applied Earth Observation and Geoinformation*, 65, 114-123, doi:10.1016/j.jag.2017.10.010.

Santi, E., Paloscia, S., Pettinato, S., Brocca, L., **Ciabatta, L.**, Entekhabi, D. (2018). Integration of microwave data from SMAP and AMSR2 for soil moisture monitoring in Italy. *Remote Sensing of Environment*, 212, 21-30, doi:10.1016/j.rse.2018.04.039.

Brocca, L., Crow, W.T., **Ciabatta, L.**, Massari, C., de Rosnay, P., Enenkel, M., Hahn, S., Amarnath, G., Camici, S., Tarpanelli, A., Wagner, W. (2017). A review of the applications of ASCAT soil moisture products. *IEEE Journal of Selected Topics in Applied Earth Observations and Remote Sensing*, 10(5), 2285-2306, doi:10.1109/JSTARS.2017.2651140.

Brocca, L., **Ciabatta, L.**, Massari, C., Camici, S., Tarpanelli, A. (2017). Soil moisture for hydrological applications: open questions and new opportunities. *Water*, 9(2), 140, doi:10.3390/w9020140.

Ciabatta, L., Marra, A.C., Panegrossi, G., Casella, D., Sanò, P., Dietrich, S., Massari, C., Brocca, L. (2017). Daily precipitation estimation through different microwave sensors: verification study over Italy. *Journal of Hydrology*, 545, 436-450, doi: 10.1016/j.jhydrol.2016.12.057.

Massari, C., Su, C.-H., Brocca, L., Sang, Y.F., **Ciabatta, L.**, Ryu, D., Wagner, W. (2017). Near real time de-noising of satellite-based soil moisture retrievals: An intercomparison among three different techniques. *Remote Sensing of Environment.*, 198, 17-29, doi:10.1016/j.rse.2017.05.037.

Tarpanelli, A., Massari, C., **Ciabatta, L.**, Filippucci, P., Amarnath, G., Brocca, L. (2017). Exploiting a constellation of satellite soil moisture sensors for accurate rainfall estimation. *Advances in Water Resources*, 108, 249-255, doi: 10.1016/j.advwatres.2017.08.010.

Brocca, L., Pellarin, T., Crow, W.T., **Ciabatta, L.**, Massari, C., Ryu, D., Su, C.-H., Rudiger, C., Kerr, Y. (2016). Rainfall estimation by inverting SMOS soil moisture estimates: a comparison of different methods over Australia. *Journal of Geophysical Research*, 121(20), 12062-12079, doi:10.1002/2016JD025382.

Brocca, L., Massari, C., **Ciabatta, L.**, Wagner, W., Stoffelen, A. (2016). Remote sensing of terrestrial rainfall from Ku-band scatterometers. *IEEE Journal of Selected Topics in Applied Earth Observations and Remote Sensing*, 9(1), 533-539, doi:10.1109/JSTARS.2015.2508065.

Ciabatta, L., Brocca, L., Massari, C., Moramarco, T., Gabellani, S., Puca, S., Wagner, W. (2016). Rainfall-runoff modelling by using SM2RAIN-derived and state-of-the-art satellite rainfall products over Italy. *International Journal of Applied Earth Observation and Geoinformation*, 48, 163-173, doi:10.1016/j.jag.2015.10.004.

Ciabatta, L., Camici, S., Brocca, L., Ponziani, F., Stelluti, M., Berni, N., Moramarco, T. (2016). Assessing the impact of climate-change scenarios on landslide occurrence in Umbria region, Italy. *Journal of Hydrology*, 541, 285-295, doi:10.1016/j.jhydrol.2016.02.007.

Santi, E., Paloscia, S., Pettinato, S., Brocca, L., **Ciabatta, L.** (2016). Robust assessment of an operational algorithm for the retrieval of soil moisture from AMSR-E data in central Italy. *IEEE Journal of Selected Topics in Applied Earth Observations and Remote Sensing*, 9(6), 2478-2492, doi:10.1109/JSTARS.2016.2575361.

Brocca, L., Massari, C., **Ciabatta, L.**, Moramarco, T., Penna, D., Zuecco, G., Pianezzola, L., Borga, M., Matgen, P., Martínez-Fernández, J. (2015). Rainfall estimation from in situ soil moisture observations at several sites in Europe: an evaluation of SM2RAIN algorithm. *Journal of Hydrology and Hydromechanics*, 63(3), 201-209, doi:10.1515/johh-2015-0016.

Ciabatta, L., Brocca, L., Massari, C., Moramarco, T., Puca, S., Rinollo, A., Gabellani, S., Wagner, W. (2015). Integration of satellite soil moisture and rainfall observations over the Italian territory. *Journal of Hydrometeorology*, 16(3), 1341-1355, doi:10.1175/JHM-D-14-0108.1.

Massari, C., Brocca, L., **Ciabatta, L.**, Moramarco, T., Gabellani, S., Albergel, C., de Rosnay, P., Puca, S., Wagner, W. (2015). The use of H-SAF soil moisture products for operational hydrology: flood modelling over Italy. *Hydrology*, 2(1), 2-22, doi:10.3390/hydrology2010002.

Brocca, L., **Ciabatta, L.**, Massari, C., Moramarco, T., Hahn, S., Hasenauer, S., Kidd, R., Dorigo, W., Wagner, W., Levizzani, V. (2014). Soil as a natural rain gauge: estimating global rainfall from satellite soil moisture data. *Journal of Geophysical Research*, 119(9), 5128-5141, doi:10.1002/2014JD021489.